Constraints on the physical properties and chemical evolution of star-forming gas in primeval galaxies

Julia Gutkin

To cite this version:

Julia Gutkin. Constraints on the physical properties and chemical evolution of star-forming gas in primeval galaxies. Astrophysics [astro-ph]. Université Pierre et Marie Curie - Paris VI, 2016. English. NNT : 2016PA066255 . tel-01443650

HAL Id: tel-01443650
https://theses.hal.science/tel-01443650

Submitted on 10 Jul 2017

École Doctorale d'Astronomie et Astrophysique d'Île-de-France
UNIVERSITÉ PARIS VI - PIERRE & MARIE CURIE

DOCTORATE THESIS

to obtain the title of Doctor of the
University of Pierre & Marie Curie in Astrophysics

Presented by
Julia Gutkin

Constraints on the physical properties and chemical evolution of star-forming gas in primeval galaxies

Thesis Advisor: Stéphane Charlot

prepared at Institut d'Astrophysique de Paris, CNRS (UMR 7095),
Université Pierre & Marie Curie (Paris VI)
with financial support from the
European Research Council grant 'ERC NEOGAL'

Composition of the jury

Reviewers:	Alessandro Bressan	-	SISSA, Trieste, Italy
	Bruno Guiderdoni	-	CRAL, Observatoire de Lyon, France
Advisor:	Stéphane Charlot	-	IAP, Paris, France
President:	Patrick Boissé	-	IAP, Paris, France
Examinators:	Jarle Brinchmann	-	Leiden Observatory, The Netherlands
	Elisabetta Caffau	-	Observatoire de Paris, France

To my family.

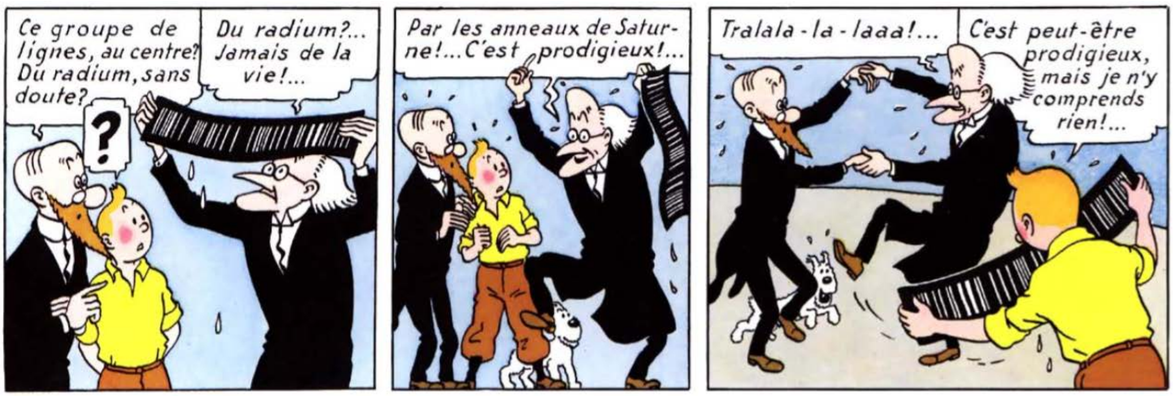
Ce groupe de lignes, au centre? Du radium, sans doute?
?
Du radium?... Jamais de la vie!...
Par les anneaux de Saturne!... C'est prodigieux!...
Tralala - la - laaa!...
C'est peut-être prodigieux, mais je n'y comprends rien!...

Abstract

The emission from interstellar gas heated by young stars in galaxies contains valuable clues about both the nature of these stars and the physical conditions in the interstellar medium. In particular, prominent emission lines produced by H II regions, diffuse ionized gas and a potential active galactic nucleus in a galaxy are routinely used as global diagnostics of gas metallicity and excitation, dust content, star formation rate and nuclear activity. Modeling the emission of ionized gas in galaxies is therefore an essential means of investigating the physical parameters of both the gas itself and the sources of ionization. The rest-frame ultraviolet and optical spectral regions are particularly rich in spectral diagnostics useful to constrain the physical properties and chemical enrichment of the gas in galaxies at all cosmic epochs. This is important, because galaxies are being detected at always higher redshift and upcoming observations with large telescopes, such as the *James Webb Space Telescope*, will gather high-quality spectra of thousands of high-redshift galaxies; as an example, the NIRSpec spectrograph will collect detailed information about the rest-frame ultraviolet and optical emission from large samples of galaxies out to the epoch of cosmic reionization. In this context, the development of sophisticated models is required to analyze these observations and interpret in a reliable way the emission-line spectra of primeval galaxies in terms of constraints on star formation and interstellar gas parameters. In particular, the models should be optimized for studies of the ultraviolet – in addition to optical – nebular properties of chemically young galaxies, in which heavy-element abundances are expected to differ substantially from those in star-forming galaxies at lower redshifts.

In this thesis, I present a new model of nebular emission from star-forming galaxies, which I have developed by combining updated stellar population synthesis models with a standard photoionization code. I detail the main features of this new model, such as the recent advances in the theories of stellar interiors and atmospheres it incorporates to interpret the ionizing radiation from star-forming galaxies, and the careful treatment of individual abundances and depletion onto dust grains, which allows one to properly explore the signatures of non-solar metal abundance ratios, and then the properties of chemically young galaxies out to the reionization epoch.

I present the public comprehensive grid of photoionization models I have computed, including full ranges of stellar and interstellar parameters. This grid allows one to characterize the nature of star formation and chemical enrichment in a wide range of galaxy types, in particular in chemically young galaxies at high redshifts. I describe the ability of the models to account simultaneously for observational trends followed by star-forming galaxies in several ultraviolet and optical diagnostic line-ratio diagrams, and I explore the influence of the various adjustable model parameters on predicted line-luminosity ratios. As an application, I use this comprehensive grid of models to investigate the limitations of standard recipes based on the direct-T_e method to measure element abundances from emission-line luminosities.

I also describe how the combination of this model with calculations of narrow-line emitting regions from active galactic nuclei computed using the same photoionization code allows one to define new ultraviolet and optical emission-line diagnostics to discriminate between star

formation and nuclear activity in galaxies.

Finally, I show how the new model presented in this thesis has already been used successfully to interpret the rest-frame ultraviolet and optical line emission of different types of high-redshift star-forming galaxies, mainly lensed dwarf star-forming galaxies at redshift between 2 and 7.

The grid of photoionization models presented in Chapter 3 is available electronically from http://www.iap.fr/neogal/models.html.

Résumé

L'émission du gaz interstellaire chauffé par les jeunes étoiles dans les galaxies contient de précieux indices sur la nature de ces étoiles et les conditions physiques du milieu interstellaire. En particulier, les raies d'émission saillantes produites par les régions H II, le gaz diffus ionisé et un éventuel noyau actif sont couramment utilisées comme traceurs de la métallicité et de l'excitation du gaz, de son contenu en poussière, son taux de formation stellaire et l'activité nucléaire. Modéliser l'émission du gaz ionisé dans les galaxies est en ce sens un moyen essentiel pour étudier les paramètres physiques du gaz lui-même mais aussi des sources d'ionisation. Les régions spectrales ultraviolette et optique sont particulièrement riches en diagnostics spectraux utiles pour contraindre les propriétés physiques et l'enrichissement chimique du gaz des galaxies à toutes les époques cosmiques. Cette caractéristique est importante puisque les galaxies sont observées à des décalages spectraux vers le rouge toujours plus élevés, et les observations à venir avec les grands téléscopes comme le *James Webb Space Telescope* vont recueillir des spectres de haute qualité de milliers de galaxies lointaines ; à titre d'exemple, le spectrographe NIRSpec recueillera des informations détaillées sur l'émission intrinsèque aux longueurs d'onde ultraviolettes et optiques de grands échantillons de galaxies jusqu'à l'époque de la réionisation. Dans ce contexte, le développement de modèles sophistiqués est nécessaire pour analyser ces observations et interpréter précisemment les spectres de raies d'émission de galaxies primordiales en termes de contraintes sur la formation stellaire et les paramètres du gaz interstellaire. Les modèles devront être particulièrement optimisés pour l'étude des propriétés nébulaires ultraviolettes – en plus de celles optiques – de galaxies chimiquement jeunes, dont les abondances en éléments lourds sont supposées être sensiblement différentes de celles de galaxies formant des étoiles à plus faibles décalages spectraux.

Dans cette thèse, je présente un nouveau modèle d'émission nébulaire de galaxies à formation d'étoiles, que j'ai développé en combinant un modèle récent de synthèse de populations stellaires avec un code classique de photoionisation. Je détaille les principales caractéristiques de ce nouveau modèle, comme les récentes avancées dans les théories d'intérieurs stellaires et d'atmosphères que le modèle intègre pour interpréter le rayonnement ionisant de galaxies à formation d'étoiles, et le traitement sophistiqué des abondances individuelles et des déplétions sur les grains de poussière qui permet d'explorer de façon appropriée les signatures des rapports non solaires d'abondances de métaux, et donc les propriétés des galaxies chimiquement jeunes à l'époque de la réionisation.

Je présente la grille exhaustive publique de modèles de photoionisation que j'ai créée, explorant de larges éventails de paramètres stellaires et interstellaires. Cette grille permet de caractériser la nature de la formation stellaire et l'enrichissement chimique pour de nombreux types de galaxies, en particulier pour les galaxies chimiquement jeunes à hauts décalages spectraux. Je décris la capacité des modèles à reproduire simultanément les caractéristiques observationnelles de galaxies à formation d'étoiles dans plusieurs diagrammes de rapports de raies ultraviolettes et optiques, et j'explore l'influence des différents paramètres ajustables des modèles sur les prédictions de rapports de luminosités de raies. Comme application, j'utilise cette grille complète de modèles pour étudier les limites de recettes classiques fondées sur la

mesure directe de température électronique pour mesurer les abondances d'éléments à partir des luminosités des raies d'émission.

Je décris également comment la combinaison de ces modèles avec des modèles de régions d'émission de raies étroites autour de noyaux actifs de galaxies, effectués avec le même code de photoionisation, permet de définir de nouveaux diagnostics de rapports de raies d'émission ultraviolettes et optiques pour distinguer la formation stellaire et l'activité nucléaire dans les galaxies.

Enfin, je montre comment le nouveau modèle présenté dans cette thèse a déjà été utilisé pour interpréter avec succès les raies d'émission ultraviolettes et optiques de différents types de galaxies formant des étoiles à hauts décalages spectraux, principalement des galaxies naines lentillées à formation stellaire à des décalages spectraux entre 2 et 7.

La grille de modèles de photoionisation présentée dans le Chapitre 3 est disponible en ligne sur `http://www.iap.fr/neogal/models.html`.

Contents

List of Figures

List of Tables

CHAPTER 1

Introduction

Contents

> This chapter is an introduction to the specific topics that are required to be understood for this work. I start by briefly summarizing the first steps of the early Universe, in which I am particularly interested, as the goal of my work is to spectroscopically characterize the most distant star-forming galaxies. I also present generalities about the chemical composition of galaxies. Then, I focus on H II regions, their nature and emission (lines and continuum). Finally, I describe in more details emission lines, which are valuable tools to explore the physical properties of both nearby and more distant galaxies.

1.1 The early Universe

1.1.1 First steps

The Universe has begun to expand and cool from a hot and dense initial state 13.8 billions years ago. Its complex present-day structure has formed hierarchically, from small scales to bigger ones. I briefly summarize here the crucial steps that happened during the first billion year of the life of our Universe, as shown in Fig. 1.1.

- ***Recombination***: Around $z \sim 1100$, corresponding to 370 000 years after the Big Bang, the temperature of the Universe becomes low enough for neutrons and protons to combine and form ionized deuterium. These ionized atoms then attract free electrons to form first neutral atoms: this is the *recombination process*. As free electrons are bound to protons, light is no more stopped due to Thomson scattering by free electrons, and the Universe can become transparent to radiation. This is the decoupling of matter and radiation, signing the end of the opaque Universe and the emission of the first light freely traveling: the Cosmic Microwave Background (hereafter CMB), observed with satellites like the Cosmic Microwave Background Explorer (COBE), the Wilkinson Microwave Anisotropy Probe (WMAP) and Planck.

- ***Dark Ages***: The Universe then enters into the *Dark Ages*, until around a few hundred million years after the Big Bang. This period characterizes the Universe when it is transparent, but before the formation of any source of light. Indeed, after the first photons are emitted as CMB during the recombination period, no more light is produced until the formation of the first stars.

- ***Reionization***: Stars start to form a few hundred million years after the Big Bang (see details about their formation in Section 1.1.2). The first stars should be extremely massive (see below), with temperatures hot enough to make them emit strong radiation at wavelengths capable of stripping electrons out of the surrounding neutral matter. This causes most of the neutral hydrogen to be reionized, and the Universe becomes once again an ionized plasma. This is the era of *cosmic reionization*. Understanding the physical processes responsible for the reionization of the Universe at the end of the Dark Ages is one of the main current problems in astrophysics. According to recent results, this relatively rapid process occurred over the redshift range $6 \lesssim z \lesssim 10$ (Collaboration et al., 2015; Robertson et al., 2015), i.e., between a few million and one billion years after the Big Bang, until the Universe was fully ionized at $z \sim 6$ (e.g. Fan, Carilli & Keating, 2006). Star-forming galaxies and active galactic nuclei (hereafter AGN) are thought to be main drivers of cosmic reionization, but their relative roles in contributing to the ionizing radiation is still scarcely known (e.g., Haardt & Salvaterra, 2015). The observed drop in the number density of bright quasars at redshifts $z \gtrsim 3$ suggests an insufficient contribution by AGN to the observed ionization of the intergalactic medium at high redshift. As a consequence, early star-forming galaxies have been favoured as the main drivers of cosmic reionization (e.g. Cowie, Barger & Trouille, 2009; Willott et al., 2010; Fontanot, Cristiani & Vanzella, 2012), although quasars, mini-quasars and a faint AGN population could also play a significant role (e.g. Volonteri & Gnedin, 2009; Fiore et al., 2012; Haardt & Salvaterra, 2015; Hao, Yuan & Wang, 2015). Exploring the physical properties of the first star-forming galaxies is essential to understand this early period.

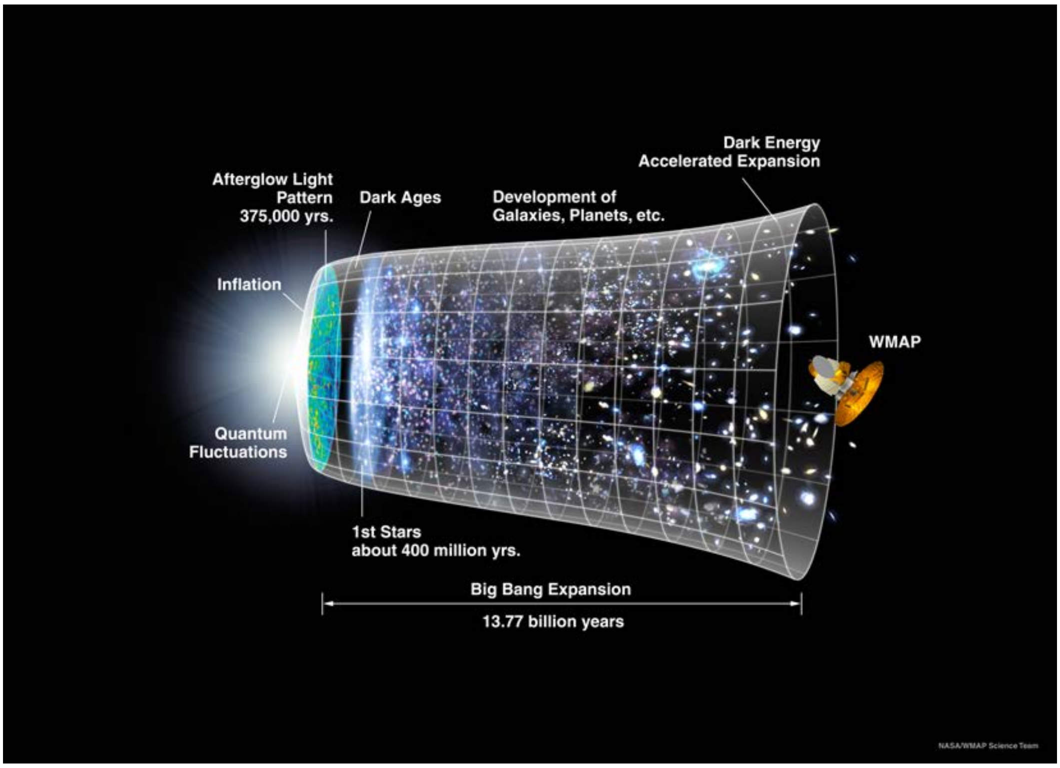

Figure 1.1: Chronology of the Universe over 13.8 billion years, from the Big Bang to nowadays. (Credit: *WMAP*)

1.1.2 Stars and galaxies

The physics of galaxies is a complex area of current astrophysics, which we must understand to be able to describe the fate of baryons in the Universe. A galaxy forms when gas becomes dense enough to sink and cool into the potential well of a dark matter halo and form stars, as follows.

- ***Population III stars***: The very first stars, generally referred to as "population III" (or simply 'Pop III') stars, form in the collapse of primordial gas clouds at the end of the Dark Ages of the Universe. These stars are expected to arise in low-mass dark-matter minihaloes ($< 10^6\,\mathrm{M}_\odot$), at redshift $z \sim 20-30$, and to be mainly composed of hydrogen and helium (and traces of lithium): their metallicity is expected to be extremely low, almost null (up to $10^{-4} Z_\odot$, Schneider et al. 2002). At this early epoch, the primordial gas is not enriched yet in metals, and since gas cooling occurs mainly through radiative deexcitation of collisionally excited metal transitions, the temperature remains too high for the gas to fragment efficiently. This is why the first stars are expected to be massive, around several hundred solar masses (Bromm, Coppi & Larson, 1999; Abel, Bryan & Norman, 2000). These massive stars evolve rapidly until they explode as Type-II (core-collapse) supernovae, returning metals to the interstellar medium (hereafter ISM) (Abel, Bryan & Norman, 2002), particularly 'α elements', i.e., mostly oxygen, sulphur, nitrogen, silicon and magnesium (see details in Section 1.1.3). The metals expelled depend on the initial mass of the stars (as described in Heger & Woosley 2002).

- ***Population II stars***: The first supernova explosions may reheat the surrounding gas and even expel some from the protogalaxy. Metal-enriched gas can cool down more efficiently and form stars of lower masses than during the first stellar generation: this is the birth of "population II" stars. The descendants of these stars, with metallicities between 10^{-3} and 10^{-1} times the solar metallicity, can be found today for example as old cool stars in the bulges and halos of spiral galaxies, such as the Milky Way.

- ***Population I stars***: Finally, less massive, longer-lived stars also contribute to the enhancement of the ISM in metals through the explosion of Type-Ia (binary system with a white dwarf) supernovae, which synthesize large quantities of iron and other iron-peak elements. The ulterior collapse of gas enriched by these different stellar generations leads to the formation of "population I" stars, to which our Sun belongs. Such stars exhibit larger metallicity, typically solar-like ($\geq 10^{-1}\,Z_{\odot}$), as can be found for example in the discs of spiral galaxies today.

In the end, the heavy elements coming from the burned-out deep interiors of stars of different masses pollute galaxies (as well as the intergalactic medium). The details of this pollution encode the signatures of the past history of star formation of galaxies, which to be understood requires models to interpret the light emitted from galaxies in terms of the chemical composition of the stars and gas within them.

In this context, the study of the very first galaxies is a subject of greatest interest for the next decade, especially given that these may be the primary source of reionization of the Universe (Section 1.1.1). One of the most efficient ways to study primeval galaxies is via spectroscopic observations, which allow the investigation of the relative strengths of the many emission lines present at rest-frame ultraviolet and optical wavelengths. These are a rich source of diagnostics and at the same time brighter and hence more easily observable than the continuum. In fact, spectroscopic analyses of emission-line strengths using photoionization models have proven to be an optimal way of interpreting the signatures of different ionizing sources in galaxies. To this end, I focus in this thesis on the interpretation of the emission-line spectrum emitted by ionized gas in galaxies. My goal is to develop a state-of-the-art model to interpret the emission-line signatures of gas of different chemical compositions in galaxies at different cosmic epochs, and thus trace the early history of chemical enrichment during the first episodes of galaxy evolution following the end of the Dark Ages.

It is worth examining the observational means at hand. Unfortunately, present-day telescopes are not able yet to gather high-quality spectra of primeval galaxies, which are too distant and too faint.

With current observing facilities, near-infrared spectroscopy enables studies of galaxies out to redshifts $z \sim 1-3$ at rest-frame ultraviolet and optical wavelengts (e.g., Shapley et al., 2003; Pettini & Pagel, 2004; Hainline et al., 2009; Erb et al., 2010; Richard et al., 2011a; Guaita et al., 2013; Steidel et al., 2014; Stark et al., 2014; Shapley et al., 2015); however, detections at higher redshifts, out to $z \sim 6$, are often limited to only small samples of gravitationally lensed sources (e.g., Fosbury et al., 2003; Bayliss et al., 2014; Stark et al., 2015a,b; Zitrin et al., 2015; Sobral et al., 2015; Stark et al., 2016). In the near future, thanks to the advent of very large telescopes – such as the *James Webb Space Telescope* (hereafter *JWST*), various *Extremely Large Telescopes* (ELTs) and the *Square Kilometer Array* (SKA) – we will soon directly detect light from primeval galaxies and collect thousands of such observations. In particular, a main motivation for my work is that the Near-Infrared Spectrograph NIRSpec developed by the European Space Agency (ESA) for the *JWST* will soon gather high-quality, rest-frame ultraviolet and optical spectra of thousands of large samples of galaxies near the reionization epoch. The *JWST*, which is scheduled for launch in 2018, will be operated for at least five years. The emission-line signatures of primeval galaxies that will be observed in this way will reveal exquisite detail about the physical conditions and chemical composition of primordial gas.

The interpretation of these future high-quality spectra requires models capable of describing the nebular emission from galaxies with pristine chemical composition. The results obtained from spectral analyses using such models on the abundance of different chemical elements will provide valuable constraints on the early chemical enrichment and indirectly on the stellar initial mass function (hereafter IMF) in the first galaxies.

1.1.3 Chemical composition of galaxies

To constrain the past history of star formation, gas accretion and outflow of a galaxy, it is necessary to accurately measure the relative abundances of different chemical elements, and thus exploit the fact that elements are produced by different types of stars and supernovae arising on different timescales. The thermonuclear reactions taking place in stellar interiors produce metals, which for massive stars lead to the classical "onion-like" structure shown in Fig. 1.2. The pollution of the ISM when a supernova explodes is linked to this stellar nucleosynthesis. The enrichment is different according to the type of supernova, as briefly mentioned in Section 1.1.2 above. Type II supernovae, which are the final evolutionary stages of massive stars ($M \geq 8\,M_{\odot}$), explode on a short timescale ($\sim$ 10 Myr) after the onset of star formation and enrich primarily the ISM in α elements (e.g., O, Ne, Mg, Si, S, Ca, Ti), which are those composing the different layers of the massive star in Fig. 1.2. On the other hand, Type Ia supernovae, which are the final evolutionary stages of accreting white dwarfs, explode on a longer timescale (between a few 10^8 yr and $\sim$ 1 Gyr) and produce massively iron-peak elements (e.g., Mn, Fe, Ni).

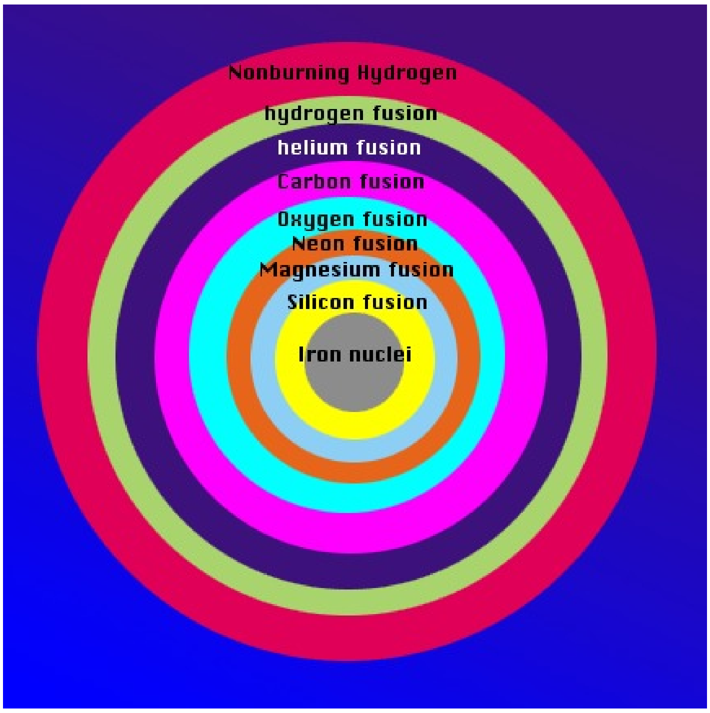

Figure 1.2: Stellar nucleosynthesis: chemical elements composing massive stars, in an "onion-like" structure.

Hence, the explosions of Type II and Type Ia supernovae occur on different timescales, and the chemical composition of their ejecta is different, which will produce different ratios of α elements over iron-peak elements in galaxies with different star formation histories. For example, if some primeval galaxies form a large fraction of stars in a rapid episode (lasting around 10 Myr) of intense star formation at high redshift, before their ISM can be enriched in iron-peak elements by Type Ia supernovae, they may evolve today in galaxies exhibiting enhanced [α/Fe][1] ratios: this is the reason why the chemical composition of the first stars to have formed in galaxies are typically expected to be "α-enhanced". We can thereby expect primeval galaxies to exhibit specific signatures in diagnostics line-ratio diagrams (see Sections 1.3.2, 3.3 and 3.4). This is not the case for more evolved galaxies, which are typically expected to have "scaled-solar" chemical compositions. The enrichment in heavy elements is thus a crucial tracer of the history of star formation of a galaxy, and that is why we must be able to accurately measure the relative abundances of different chemical elements (see Section 1.3.1).

To interpret the emission-line signatures of gas ionized by young stars in terms of the chemical composition of a galaxy, one may appeal to a photoionization code (see Section 2.2). However, current studies of this kind generally rely on the assumption that the interstellar gas

---

[1] The notation [α/Fe] is a commonly used abundance indicator: it is the logarithmic ratio of the α-element abundance to the iron abundance, with respect to the solar ratio, expressed as $[\alpha/Fe] = \log_{10}\left(\frac{N_\alpha}{N_{Fe}}\right) - \log_{10}\left(\frac{N_\alpha}{N_{Fe}}\right)_\odot$

has scaled-solar abundances of heavy-elements. That is, the relative ratios of heavy elements are taken to be the same as in the Sun, at any metallicity (solar or not). This assumption cannot be made to interpret the emission-line properties of high-redshift galaxies, in which the abundance ratios of heavy elements are expected to be non-solar, as described above. A main feature of my work is to overcome this limitation by developing models allowing one to properly explore the emission-line signatures of non-solar metal abundance ratios, and hence, the properties of chemically young galaxies out to the reionization epoch.

1.2 Nebular emission from ionized gas

In my thesis, I focus primarily on the emission-line spectrum produced by star-forming galaxies (except in Chapter 4). I provide here a basic introduction to the properties of H II regions ionized by young stars in a galaxy and to nebular emission in general.

1.2.1 Basic properties of HII regions

H II regions are extensive, diffuse nebulae – i.e., regions of interstellar gas – associated with regions of recent massive-star formation. They are concentrated in the spiral arms of galaxies, and have often irregular morphology and variable size, depending on the structure of their parent molecular cloud (see some examples of such H II regions in Fig. 1.3). In 1939, Bengt Strömgren first described the general properties of H II regions (Strömgren, 1939). He established the link between the rate of ionizing photons, the hydrogen density and the size of an H II region. Each H II region typically contains one or more hot, massive young O-B stars, with effective temperature ranging typically between T=30,000 and 50,000 K. These stars are the main sources of ionizing radiation in the region: the ionizing photons they emit transfer energy to the nebula through photoionization (see Section 1.2.2 next). In an H II region, the ultraviolet radiation field is so intense that the surrounding hydrogen gas is nearly fully ionized (i.e., in the form of H^+), hence the name H II region. The "Strömgren sphere" is the ionized region formed around the central source, which is separated from the outer neutral gas cloud by a thin transition beyond which no further ionizing photon arrives because they have been all absorbed by hydrogen atoms inside the Strömgren sphere. The typical mass of an H II region is 10^2 to $10^4\,M_\odot$; the typical hydrogen density is around $10^3 - 10^4\,\mathrm{cm}^{-3}$ in compact H II regions, and more modest in giant extragalactic H II regions $\sim$ 10 to 10^2 atoms cm^{-3} (e.g., Hunt & Hirashita, 2009); a diffuse H II region is therefore large, from around 1 to hundreds of parsecs. An H II region can also contain dust, and it typically exhibits a complex spectrum including lines and continuum, which I describe below (see Section 1.2.3).

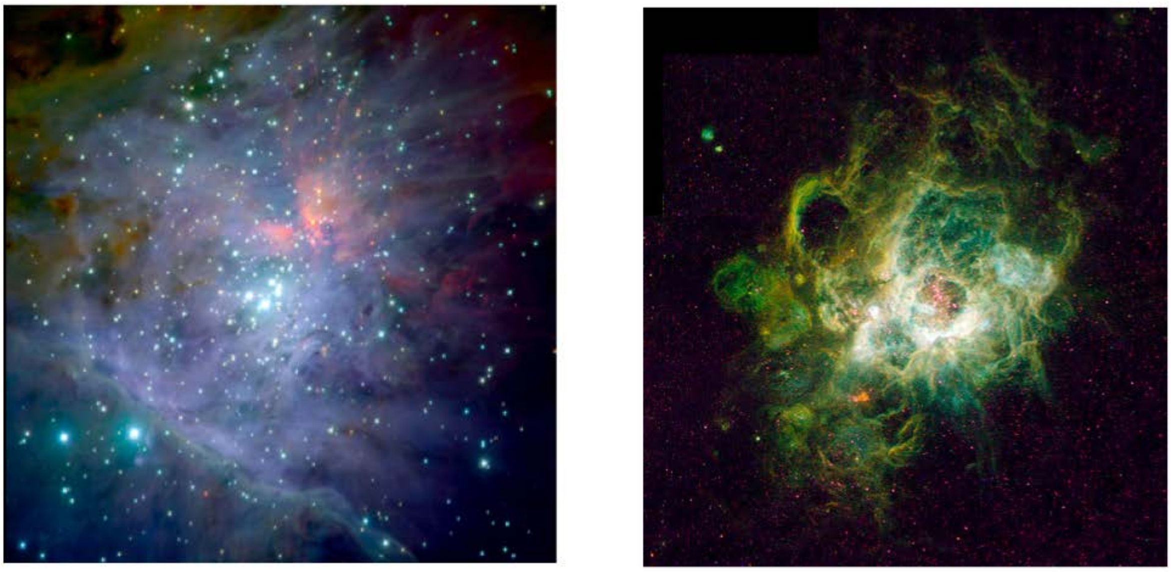

Figure 1.3: Examples of ionized regions: NGC 1976, Orion Nebula (left) and NGC 604, H II region in the Triangulum galaxy (right) (Credit: *ESO*).

1.2.2 Photoionization and recombination processes

I now describe the main general physical processes operating in these ionized regions of the ISM in galaxies, most importantly photoionization and recombination, as well as the different components of the spectra emerging from H II regions and their physical origin: emission lines (recombination lines, collisionally excited lines) and continuum (free-free continuum, free-bound continuum, two-photon process, dust).

In an H II region, the energy of the ultraviolet photons emitted by the ionizing source is transferred to the surrounding gas by photoionization. More precisely, the central star (or the cluster of young massive stars in the center of the cloud) is hot enough ($T \geq 30,000\,\mathrm{K}$) to emit ionizing photons. These are photons with energy above the ionization threshold, i.e., in the case or hydrogen, greater than the H-ionization potential of 13.6 eV (corresponding to wavelengths $\lambda \leq 912\,\mathrm{\AA}$). These photons are called “Lyman-continuum photons” and are on the extreme ultraviolet side of the electromagnetic spectrum. If there is enough matter, the gas extends beyond the Strömgren radius and the nebula is called *ionization bounded*, as all the ionizing photons have been absorbed by ionized species. Otherwise, the nebula is truncated inside the Strömgren radius and is referred to as a *density bounded* nebula. A photoionization leads to the release of a photoelectron. This thermal electron tends to be recaptured by an ion, i.e., in the case of hydrogen, a proton H^+ floating in the cloud: this is the recombination process, which produces a new neutral hydrogen atom. Fig. 1.4 illustrates the photoionization and recombination processes that determine the properties of H II regions.

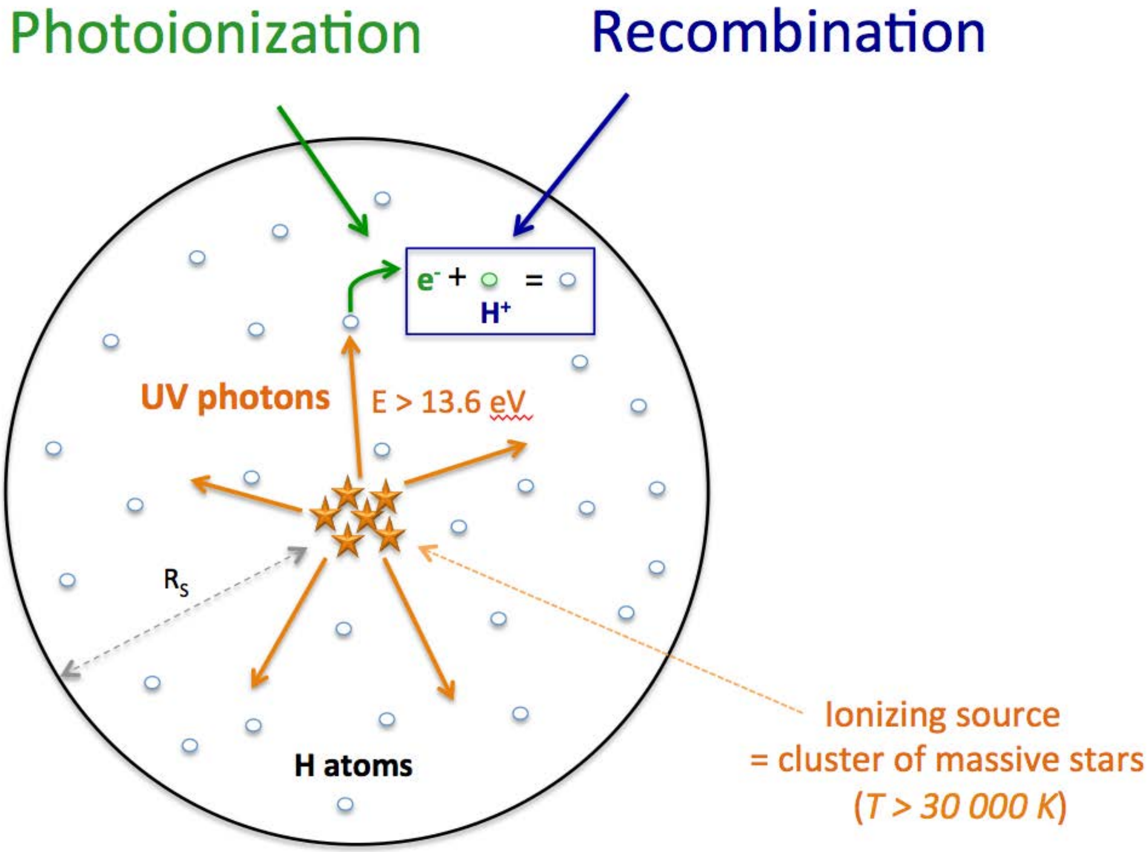

Figure 1.4: Schematic representation of photoionization and recombination processes in an H II region

During recapture, the electron can land on any excited level of the newly formed H atom and then decay to lower and lower levels through radiative transitions. During each de-energizing of the radiative cascade, a photon is emitted with a particular wavelength, which will contribute to the intensity of the corresponding *emission line* in the spectrum of the H II region: this is referred to as an “H I recombination line” (see Section 1.2.3; Fig. 1.6).

An equilibrium stage is established if, for each species, the rate of ionization equals that of recombination. For an ionization-bounded H II region composed of hydrogen, we can write the balance of the total number of ionizing photons emitted per unit time (by stars and during recombination to the ground level) with the total number of recombinations:

$$Q(\mathrm{H}^0) + \int n(\mathrm{H}^+) n_e \epsilon \alpha_1(\mathrm{H}, T_e) dV = \int n(\mathrm{H}^+) n_e \epsilon \alpha_{\mathrm{tot}}(\mathrm{H}, T_e) \mathrm{d}V, \qquad (1.1)$$

where $Q(\mathrm{H}^0)$ is the total number of ionizing photons produced per second, $n(\mathrm{H}^+)$ the number density of protons, n_e the electronic density, ϵ the volume filling factor of the nebular gas, $\alpha_1(\mathrm{H}, T_e)$ the H-recombination coefficient of a transition to the ground level and $\alpha_{\mathrm{tot}}(\mathrm{H}, T_e)$

the total H-recombination coefficient. For an H II region with constant density and filling factor, we will see in Chapter 3 that we can thus derive the Strömgren radius by means of equation (3.6).

Ionized-gas regions are traditionally divided into two types: the optically thin one, corresponding to *case A* recombination (all Lyman-line photons produced though recombination escape from the nebula before they are reabsorbed by another atom); and the optically thick one, corresponding to *case B* recombination (all Lyman line photons are re-absorbed by other atoms until they finally cascade down to the $n = 2$ level and produce either a Lyman α photon or a two-photon decay; Section 1.2.3). The latter is the most common case in the Universe, and the one I will consider in my work. It is worth noting that, in Case B recombination, every ionization must eventually produce a decay to the $n = 2$ state, accompanied by the emission of an optical "Balmer-line" photon. Hence the number of Balmer-line photons is directly related to the number of ionizing photons from the central source.

Likewise, if an atom of helium in the nebula is photoionized and creates an He^{+} ion, the photoelectron will be recaptured and contribute to the He I recombination spectrum (the energy of first ionization for helium is 24.6 eV, so the central stars must be hot enough to produce such energetic photons); in the most highly ionized regions, we can even find He^{2+} ions, which recombine and emit an He II recombination spectrum (the energy of second ionization is 54.4 eV, the incident photons must thus be really energetic). Much weaker recombination lines can also be emitted by elements other than H and He (i.e. metals, for instance C, N, O) such as C III and C IV emission lines.

To summarize, therefore, throughout an H II region, H is fully ionized, He can be singly or even doubly ionized, and other elements, such as carbon, oxygen, nitrogen, magnesium, silicon, sulfur, etc., can be multiply ionized. The details depend primarily on the nature of the ionizing source, i.e. the cluster of massive stars.

1.2.3 Spectra: lines and continuum

An H II region is characterized by a specific emission spectrum. This spectrum presents an important emission-line component, including strong recombination lines of hydrogen and helium, but also collisionally excited lines of ions of common elements; these lines are superimposed on a continuous spectrum, as I now describe.

We can start by showing in Fig. 1.5 the spectrum of the Sun observed by Joseph von Fraunhofer in 1814. He discovered the continuum and superimposed absorption lines (in black), of which he classified more than 500, and which represent today a ubiquitous means of investigation in spectroscopic astrophysics. He deepened his work for a few years and observed spectra of the moon, Venus, Mars and stars other than the Sun.

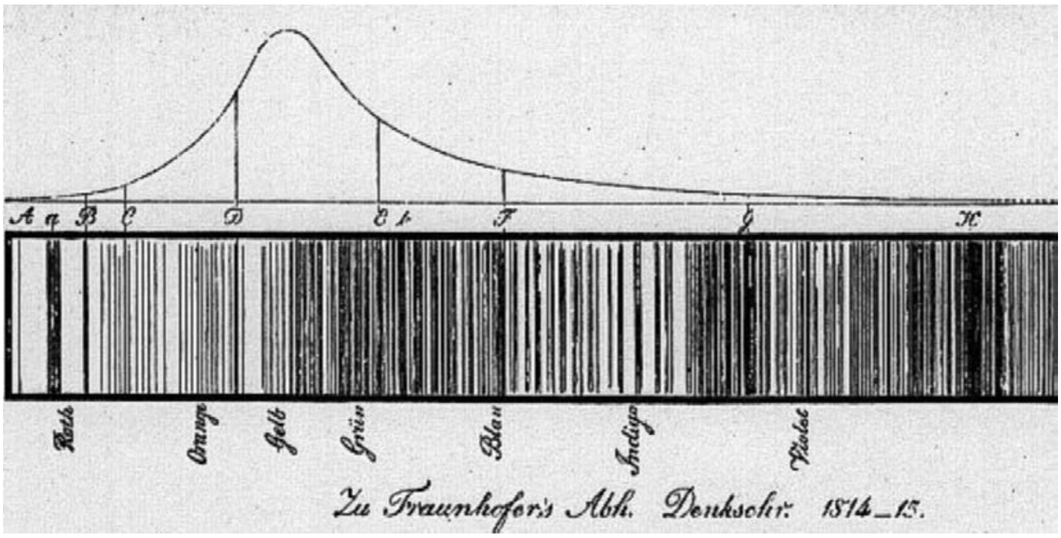

Figure 1.5: The spectrum of the Sun observed by Joseph von Fraunhofer in 1814. We can see the Sun's continuum spectrum, on which are superimposed the dark lines corresponding to the different known chemical elements. The curve above shows overall brightness.

Lines

Recombination lines As we have just seen, recombinations following the ionization of neutral gas by the energetic photons from hot stars produce prominent H I recombination lines in the spectrum of an H II region. The line nomenclature depends on the energy level down to which the electron cascades: "Lyman" lines are emitted when the electron reaches the energy level $n = 1$, "Balmer" lines when it reaches the level $n = 2$, "Paschen" lines the level $n = 3$, and so on (see Fig. 1.6).

The strongest H-recombination line (aside from the ultraviolet Lyman α line at 1216 Å) is the Balmer Hα line, with a wavelength of 6563 Å. It occurs when a hydrogen electron falls from the third to second lowest energy level. We also have the Hβ line at 4861 Å in the blue range ($n = 4$ to $n = 2$ transition), Hγ at 4340 Å in the violet range ($n = 5$ to $n = 2$), and so on. As I mentioned previously, because of the ionization of He gas, we can also find He recombination lines, such as He I 5876 Å (which is weaker than H-recombination lines), and even He II 4686 Å in higher-ionization nebulae.

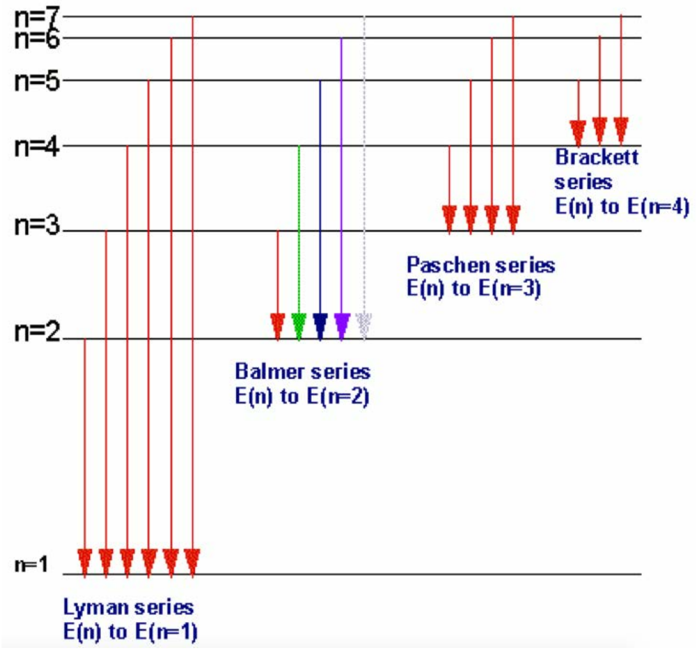

Figure 1.6: Electronic transitions of the hydrogen atom: depending on the energy level the electron cascades down to, we refer to “Lyman” lines when the electron reaches the energy level n = 1, “Balmer” lines when it reaches the level n = 2, “Paschen” lines the level n = 3, and so on.

Collisionally excited lines The emission spectrum of an H II region is also characterized by the presence of collisionally excited lines. Metals present in the H II region (i.e., chemical elements heavier than H and He), in either atomic or ionized state, can be excited through collisions with thermal electrons. In the atom or ion, an electron passes from a lower to an upper energy level and can end up on an excited metastable energy level with a long lifetime. Usually, in such cases, in “normal” gas density conditions, the spontaneous de-energizing from that level has no time to happen, as the atom or ion can be collisionally deexcited on a short timescale (without the emission of a photon). In an H II region, however, the density is so low that even over the lifetime of the metastable energy level, collisions between the atom or ion and an electron are quite unlikely. This is why the electron has time to spontaneously de-energize from its metastable state to a lower level: the emitted radiation gives rise to a “forbidden line” in the spectrum. Such lines are designed in square bracket. In an H II region, we find forbidden lines of common species, such as the strong doublets of [O II] at 3726 Å and 3729 Å, [O III] at 4959 Å and 5007 Å, [N II] at 6548 Å and 6583 Å and [S II] at 6717 Å and 6731 Å. We note that, depending on the spontaneous transition probabilities, we also find semi-forbidden lines, designed by a single bracket, for some elements such as carbon, oxygen and silicon (e.g., C III], O III] and Si III]).

To summarize, therefore, the gas in an H II region is ionized and heated by an energetic central source. This gas emits radiation both via recombination (mostly hydrogen and helium recombination lines) and through the radiative decay of collisionally excited metals (which can lead to permitted, semi-forbidden or forbidden lines). To summarize and illustrate this, I present an example of emission-line spectrum of an H II region in Fig. 1.7: this is the optical spectrum of an H II region observed in the galaxy NGC 2541. We can see in particular strong recombination lines of hydrogen (in the Balmer series, i.e., from energy levels n $\geq$ 3 to n = 2), and strong forbidden lines of a few heavier elements (oxygen, neon). These are among the emission-line features I compute in my work to model the nebular emission from star-forming galaxies.

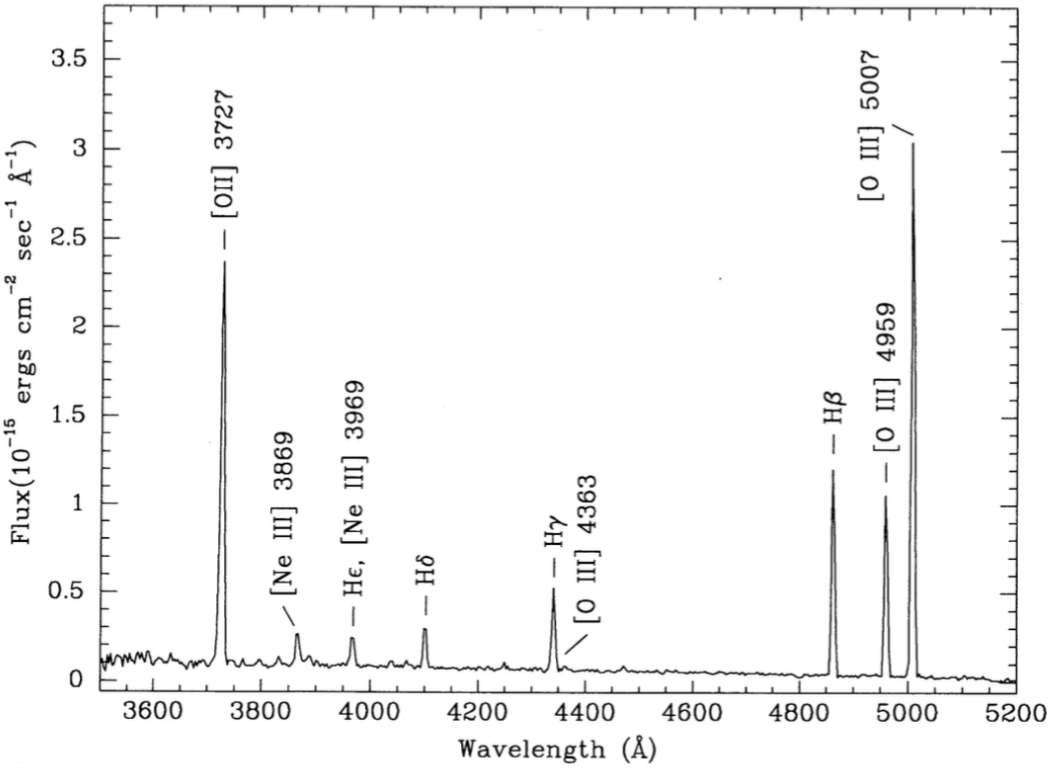

Figure 1.7: Example of a typical H II region spectrum observed in the spiral galaxy NGC 2541. We can see the strong emission lines of hydrogen, oxygen and neon that dominate the spectrum (Zaritsky, Kennicutt & Huchra, 1994).

Continuum

An H II region also emits continuum radiation across the entire electromagnetic spectrum. This arises from free-free radiation, free-bound transitions and a component due to the presence of dust in the ionized region.

Free-free continumm Free-free emission is produced when free electrons pass close to ions without being caught: the electrons are slowed down, scattered off by the ions, and we know that any decelerating charge in space radiates electromagnetic energy: this is the Brehmsstrahlung radiation, as illustrated by Fig. 1.8.

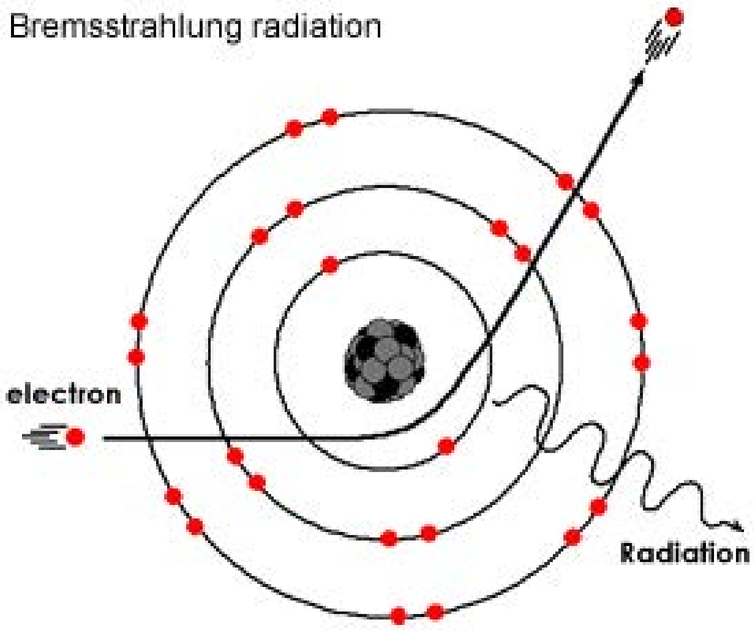

Figure 1.8: Brehmsstrahlung radiation, produced when free electrons pass close to ions without being caught.

This emission involves a transition of the electron from one free kinetic energy state to another. The result for an H II region is a continuum extending across the entire electromagnetic spectrum. It is the main component of the radio continuum of an H II region. This type of emission is one of the different contributions to the continuum in the spectrum of an H II region.

Free-bound continuum Another component of the continuum is the free-bound radiation, or recombination continuum. This is produced during the recapture of a free electron to a bound state of an atom (see Section 1.2.2). Fig. 1.9 shows the free-free and free-bound emission of hydrogen gas at a temperature of 7×10^3 K. The free electrons that are recaptured by ions initially have a range of energies (usually drawn from the thermal distribution), and according to the energy level on which they land, we can see different discontinuities in the spectrum: the "Balmer discontinuity" (recombination on the level $n = 2$), the "Paschen discontinuity" (recombination on the level $n = 3$), and so on. These discontinuities appear in the spectrum as an edge followed by a continuum of emission to higher and higher energies in Fig. 1.9.

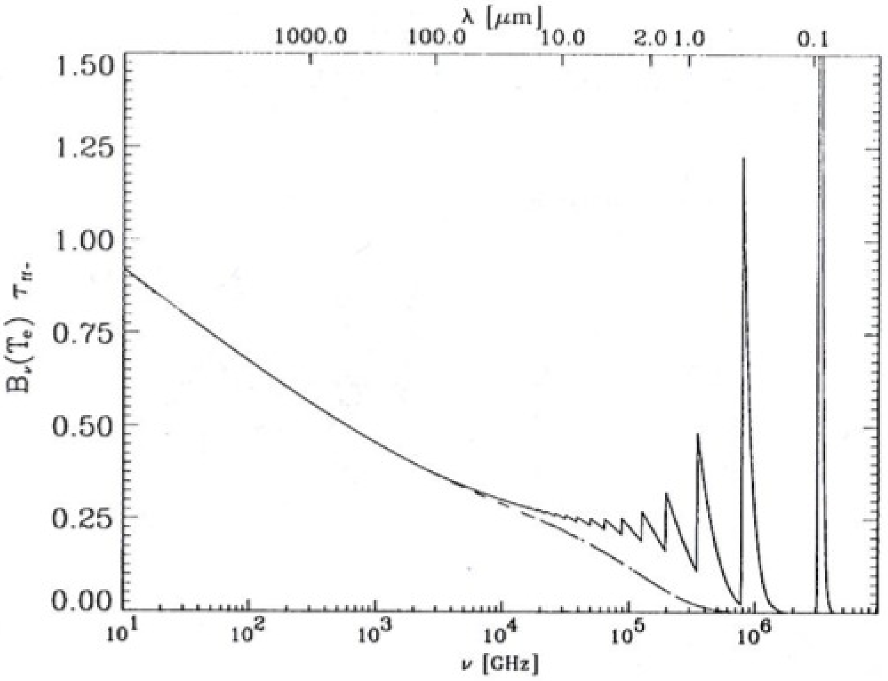

Figure 1.9: Free-free and free-bound emission for hydrogen gas of 7×10^3 K (Credit: Lequeux 2005).

Two-photons process This is a spontaneous transition into a virtual level between the first two excited states of an atom, which leads to the emission of two photons rather than a single one; the total energy of the two photons is then equal to the energy of the transition. The probability for such a double emission to occur is weak, but it cannot be ignored for the de-energizing from a metastable level when there are few collisions in the region. This continuum emission arises from any metastable excited state, particularly in the case of neutral hydrogen, when the electron ends up, by direct recombination or by cascades following recombinations to higher levels, into a metastable 2s ^2S excited state: the only downward radiative transition from this state is a two-photon decay in the 1s ground state. A similar process also happens in neutral helium.

This continuum emission becomes important at ultraviolet wavelengths, where it is stronger than the free-free and free-bound continuum.

Dust H II regions contain dust, which can scatter and absorb the light emitted by the ionizing hot stars. The energy absorbed by dust is reradiated in the mid and far infrared. This gives rise to a thermal continuum, which is an additional component of the continuum spectrum of an H II region. I provide further details on this in Section 3.2.4.

1.3 Emission-line diagnostics

The detection of emission lines produced by ionized gas in star-forming galaxies provides insight into the physical properties of stars and the interstellar medium, such as the gas electronic temperature and chemical composition, of particular interest to me, but also the properties of the ionizing stars and the gas kinematics (Rubin et al., 1985). In this section, I give an overview of abundance determination in H II regions, which is one of the most important applications we can perform based on emission-line measurements. I also introduce emission line-ratio diagnostic diagrams, which I will widely use in the following chapters.

1.3.1 Abundance determination in HII regions

Nebular emission lines have been used to derive abundances in extragalactic H II regions since the 1940s (Aller, 1942). Indeed, as collisional emission lines are strongly sensitive to the local thermodynamic state of the gas (see Figs 1.10 and 1.11), temperature and density determinations using emission lines allow measurements of ionic abundance ratios, and hence, elemental abundances relative to hydrogen.

Two main types of approach exist: the so-called "direct method" and statistical approaches.

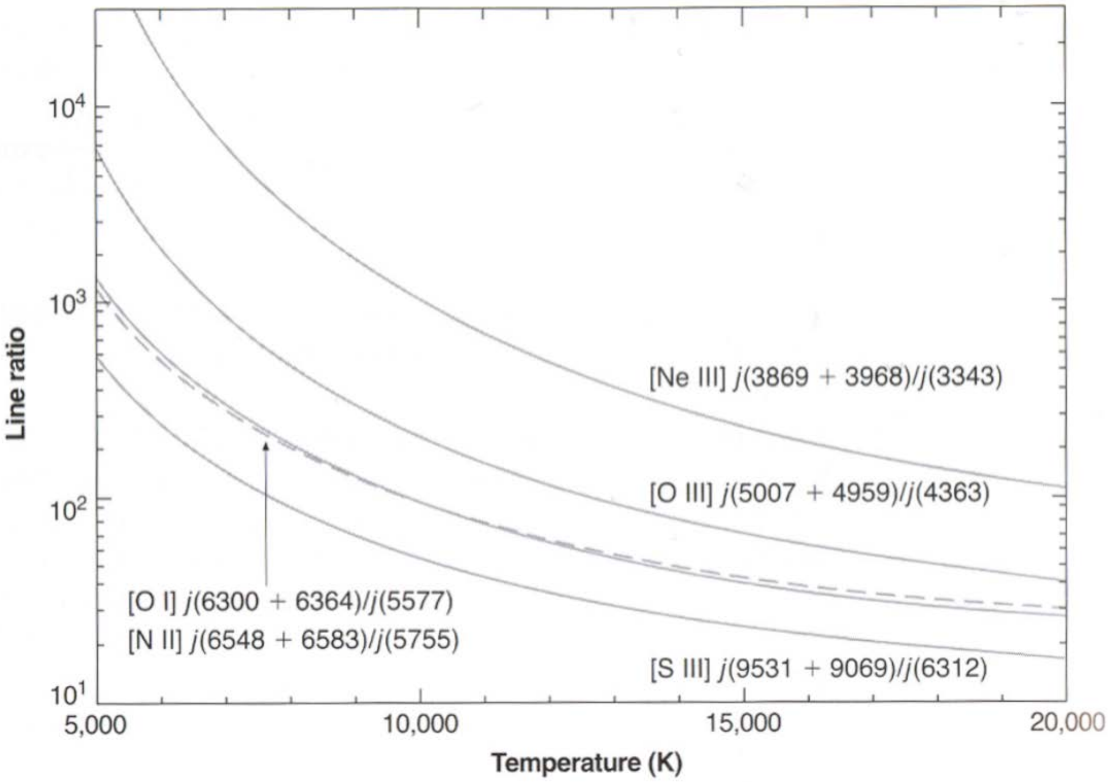

Figure 1.10: Dependence of some line ratios on the electronic temperature (Osterbrock & Ferland, 2006).

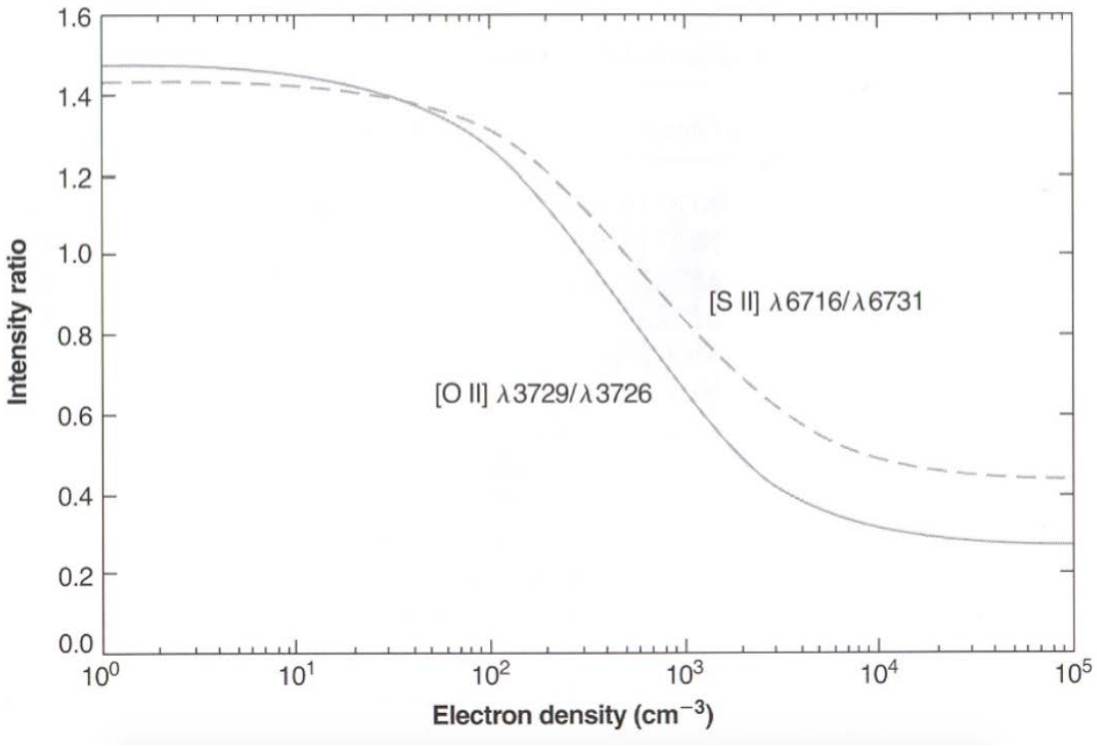

Figure 1.11: Dependence of some optical line ratios of forbidden lines on the electronic density (Osterbrock & Ferland, 2006).

Direct method

The best methods to measure chemical abundances from optical nebular emission lines are generally considered to be those involving an estimate of the thermodynamic state of the ionized gas – in terms of temperature and density. This can be achieved by using the intensity ratio of two lines of the same ion with different excitation levels to derive the electronic temperature T_e (we note that, while intensity ratios of recombination lines do not strongly depend on T_e, those involving collisionally excited, optical and ultraviolet line do if the line excitation levels are different). Some widely used line ratios for T_e estimates are [O III]λ4363/λ5007, [N II]λ5755/λ6584 and [S III]λ6312/λ9532. Estimates of the electronic density n_e can be achieved using the intensity ratio of two lines of the same ion arising from levels with the same excitation energy but different radiative transition probabilities or collisional deexcitation rates, such as for instance [S II]λ6717/λ6731, [O II]λ3729/λ3726 and C III]λ1909/λ1907.

Once both the electronic temperature and density in the ionized gas are inferred from observed emission-line ratios, we can compute the emission coefficient of a collisionally excited ionic line (which is a function of T_e and n_e) and infer the corresponding ionic abundance ratio to H^+, for example O^{2+}/H^+, using the intensity ratio of this line to Hβ, e.g.,

$$\mathrm{O^{2+}/H^{+}} = \frac{[\mathrm{O\,III}]\lambda 5007\,/\,\mathrm{H}\beta}{j_{[\mathrm{O\,III}](\mathrm{T_e,n_e})}\,/\,j_{\mathrm{H}\beta(\mathrm{T_e})}} \tag{1.2}$$

where $j_{[\mathrm{O\,III}](\mathrm{T_e,n_e})}$ and $j_{\mathrm{H}\beta(\mathrm{T_e})}$ are, respectively, the emission coefficients of [O III]λ5007 and Hβ.

It is further possible to derive the total abundance of a given chemical element relative to hydrogen by applying a ionization correction factor to account for the unseen stages of ionization (see Section 3.5). I will provide more details about this direct method and its limitations in Section 3.5.1.

Strong-line method

The lines required to reliably measure the electronic temperature, such as [O III]λ4363, are typically weak and cannot always be observed in external galaxies. For this reason, other statistical approaches have been developed to measure metal abundances based on ratios of prominent emission lines, generally termed “strong-line methods”, as first proposed by Pagel et al. (1979). In these methods, the abundance of an element is usually inferred from theoretical calibrations of strong-line ratios using photoionization models. For example, it is customary to estimate the oxygen abundance O/H by computing the ratio of combined $\mathrm{O^+}$ and $\mathrm{O^{2+}}$ lines to Hβ, i.e., $\mathrm{R_{23}} = ([\mathrm{O\,II}]\lambda 3727 + [\mathrm{O\,III}]\lambda\lambda 4959,5007)/\mathrm{H}\beta$. It is worth noting that in this method, the solution is not unique because the ratio $\mathrm{R_{23}}$ behaves differently depending on the metallicity regime, as shown by Fig. 1.12. At low metallicity, $\mathrm{R_{23}}$ increases with metallicity (as the oxygen abundance rises), while at higher metallicity, it starts to drop with increasing metallicity (as cooling through the infrared lines becomes more efficient; see Section 3.3.3). Other lines must then be investigated to settle the metallicity regime. I will develop on this approach using the CLOUDY photoionization code to compute abundances of heavy elements (Section 2.2).

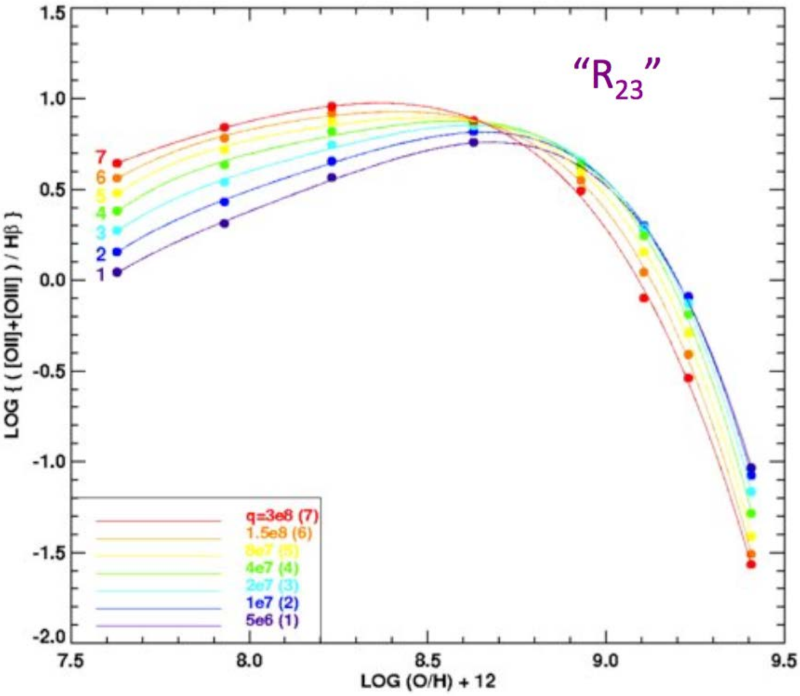

Figure 1.12: Dependence of the R$_{23}$ ratio ([O II]λ3727+[O III]$\lambda\lambda$4959, 5007)/Hβ on the oxygen abundance 12+log(O/H), in the absence of redenning (Kewley & Dopita, 2002). The curves of different colours correspond to different ionization parameters.

It is worth noting that, even in the direct method, photoionization models are traditionally invoked to compute the abundances of other heavy elements, based on that of the first ion measured. In the example of the O^{2+} ion given above (equation 1.2), photoionization models are required to estimate the electron temperatures and ionization corrections for other ions, based on those corresponding to the O^{2+} ionization zone (e.g., Izotov et al., 2006). Absolute abundances computed in this way are therefore tied to the assumptions inherent in standard photoionization models about abundance ratios, which are generally taken to be scaled-solar, and may also be prone to biaises arising from the specific electronic density and ionization structure of these models. There is an inconsistency, therefore, in using any of these standard approaches (direct and strong-line methods) to constrain the presumably non-solar abundance ratios of high-redshift galaxies. One of the goal of my thesis is to address this issue (see Section 3.5).

1.3.2 Emission line-ratio diagrams

The sensitivity of individual emission-line intensities to the nature of the ionizing radiation (stars of different mass and composition, AGN, shocks; see Chapter 3) and the physical parameters of interstellar gas (density, excitation, chemical composition, etc.) has led to the development of emission line-ratio diagnostic diagrams. In practice, the method consists in plotting a ratio of two emission lines – produced in partially ionized zones – as a function of another such ratio. This approach was first advertised by Baldwin, Phillips & Terlevich (1981), who used line ratios based on several strong optical lines, such as [O II]λ3727, [O III]λ5007, Hβ, [N II]λ6584 and Hα, to distinguish between different types of ionizing sources, as exemplified in Fig. 1.13. We note that the [O III]λ5007/Hβ and [N II]λ6584/Hα ratios shown in this figure both involve lines with very close wavelengths, in order to limit sensitivity to reddening and spectrophotometric calibration.

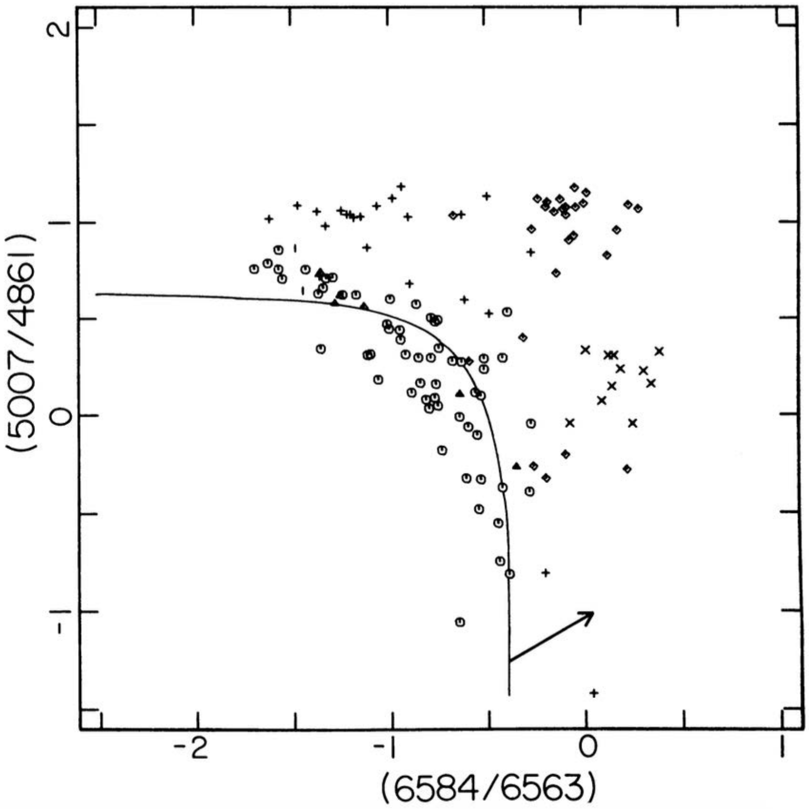

Figure 1.13: The original BPT diagram, plotting the intensity ratios of [O III]λ5007/Hβ against [N II]λ6584/Hα (Baldwin, Phillips & Terlevich, 1981), for H II regions and planetary nebulae. The emission-line intensity ratios are expressed in logarithms.

In Chapters 3 and 4 below, I will describe different line-ratio diagrams at optical and ultraviolet wavelengths and show how these can be useful to characterize the nature of the ionizing source and the physical conditions in the ISM in distant galaxies.

1.3.3 Other use of emission lines

In addition to abundance determinations and diagnostic line-ratio diagrams, I briefly list here other wide uses of emission-lines measurements.

- Both recombination and collisionally excited lines allow estimates of the star formation rate (SFR) in galaxies, since the rate of ionizing photons is directly proportional to the SFR, at fixed IMF. Widely used, approximate formulae to convert observed emission-line luminosities into a star formation rate are those proposed by Kennicutt (1998): for Hα,

  $$\mathrm{SFR}\ (M_\odot\ yr^{-1}) = 7.9\times10^{-42}\ L(\mathrm{H}\alpha)\ (\mathrm{ergs\ s^{-1}}) = 1.08\times10^{-53}\ Q(H^0)\ (\mathrm{s^{-1}}), \tag{1.3}$$

  where $L(\mathrm{H}\alpha)$ is the Hα luminosity assuming case B recombination and, as before, $Q(H^0)$ is the rate of ionizing photons; and for [O II]λ3727,

  $$SFR\ (M_\odot\ yr^{-1}) = (1.4\pm0.4)\times10^{-41}\ L[OII]\ (\mathrm{ergs\ s^{-1}}). \tag{1.4}$$

  We note that the model presented in Chapter 3 allows more refined SFR estimates from emission-line measurements than provided by these formulae.

- Emission-line redshifts and intensity profiles further inform us about gas dynamics in galaxies. Radial velocities and velocity gradients may be inferred by fitting line profiles, when the intrinsic shape of the line is well known (e.g., Mink & Wyatt, 1995). If not, cross-correlation methods can be used to compare observed emission-line profiles with model predictions. Emission lines such as Hα and [N II]λ6584 are standard probes in such studies.

- Strong emission lines can also be used to derive spectroscopic redshifts. For instance, the spectroscopic redshift survey of star-forming galaxies ZFIRE has derived spectroscopic redshifts of a few hundred galaxies, using a combination of nebular emission lines such as Hα, [N II], Hβ, [O II], [O III], and [S II] (Nanayakkara et al., 2016).

1.4 Outline

In this thesis, I present a new model of nebular emission from star-forming galaxies, which I have developed to interpret simultaneously the signatures of stars, gas and dust in the integrated emission-line spectra of galaxies.

In Chapter 2, I describe the main features of the two building blocks of this model: the stellar population synthesis code GALAXEV and the photoionization code CLOUDY, which I combine to compute entire – i.e. stellar and nebular – spectral energy distributions of galaxies.

Then, in Chapter 3, I detail the new approach I have designed to study the chemical properties of ionized gas with non-scaled-solar abundances ratios of heavy elements. This self-consistent modelling allows me to identify the influence of some main model parameters on the nebular emission from star-forming gas by exploring the signatures of changes in the chemical composition of gas ionized by young stars in primeval galaxies on the intensity ratios of selected prominent ultraviolet and optical emission lines (diagnostic line-ratio diagrams). I also show how the modelling approach I have developed allows one to overcome the limitations of standard recipes to measure element abundances from emission-line luminosities. The grid of photoionization models presented in this chapter is available electronically from `http://www.iap.fr/neogal/models.html` (Gutkin, Charlot & Bruzual, 2016).

In Chapter 4, I combine this grid of photoionization models with calculations of narrow-line emitting regions from active galactic nuclei computed using the same photoionization code to define new ultraviolet and optical emission-line diagnostics to discriminate between star formation and nuclear activity in galaxies (Feltre, Charlot & Gutkin, 2016).

Finally, this work overcomes important limitations of existing methods and allows one to interpret in a reliable way the emission-line spectra of chemically young galaxies in terms of constraints on gas parameters. In Chapter 5, I show several examples of the success of these models in interpreting observations of high-redshift star-forming galaxies gathered by some of today's most powerful telescopes (Stark et al., 2014, 2015a,b, 2016).

To conclude, in Chapter 6, I summarize the main features of my work and its implications for future studies.

CHAPTER 2

Tools

Contents

> To link observations of galaxies at all cosmic epochs with theories of galaxy formation, we need to develop sophisticated models to interpret in a reliable way the light emitted by galaxies in terms of stellar population, gas and dust parameters. In this chapter, I describe the two main tools I use in my work to compute complete spectral energy distributions of galaxies: stellar population synthesis codes (Section 2.1), which allow one to compute the contribution by stars of all masses and ages to the emission from a galaxy, and photoionization codes (Section 2.2), which allow one to compute the transfer of radiation from an ionizing source through the ISM. These are the main building blocks of my work, which I combine in an external code to model spectral energy distributions of any type of star-forming galaxy, as we shall see in Chapter 3.

The spectral energy distribution of a galaxy characterizes the light emitted by stars at all wavelengths: it is the total number of photons emitted at each wavelength by the galaxy. This is the sum of the emission from all the stellar populations and from the gas ionized by young massive stars throughout the galaxy. In practice, the emission from a stellar population englobes the light from stars of all masses born at any past epoch, which are still alive;

the emission from each star is characterized by a continuum and specific absorption-line signatures, which encode valuable information about the age and metallicity of that star. On top of this stellar emission, the emission from the ionized gas in H II regions adds emission lines and a nebular continuum, as seen in Section 1.2.3. To compute consistently the entire spectral energy distribution of a galaxy, the most natural way is to combine a population synthesis code – to model the stellar content – with a photoionization code – to describe the emission of the gas ionized by hot massive stars. In my work, I compute such complete spectral energy distributions of galaxies by combining the stellar population synthesis code GALAXEV (Bruzual & Charlot, 2003, Charlot & Bruzual, in preparation) with the photoionization code CLOUDY (Ferland et al., 2013), both in their latest version.

2.1 Stellar population synthesis codes

2.1.1 Generalities

I consider observations of galaxies at ultraviolet-to-near infrared wavelengths, where the stellar content dominates integrated galaxy spectra. Stars are a particularly important component of galaxies: their observability from the ground at visible wavelengths make them privileged tracers of galaxy physical properties. To properly model the spectral evolution of stellar populations inside galaxies, it is common to appeal to stellar population synthesis codes. These allow one to compute the contributions by stars born at any epoch to the spectral energy distribution of a galaxy, by summing the individual spectra (observed or modelled) of stars of all masses, ages and metallicities. In this way, we may interpret observed galaxy spectral energy distributions – and luminosities and colours – by comparing them with stellar population synthesis models.

In pioneer studies, observed galaxy spectra were reproduced using linear combinations of individual stellar spectra of various types taken from a comprehensive library (e.g., Spinrad & Taylor, 1971; Faber, 1972; O'Connell, 1976; Turnrose, 1976). In this approach, however, the number of free parameters is generally too large to be properly constrained by observations. More recent models rely on the evolutionary population synthesis technique (introduced by Tinsley 1978), according to which the evolution in time of the integrated light of a stellar population is computed as a function of a few main adjustable parameters: the stellar IMF and the star formation and chemical enrichment histories. Among existing stellar population synthesis codes, we can cite Tinsley (1978); Bruzual A. (1983); Arimoto & Yoshii (1987); Guiderdoni & Rocca-Volmerange (1987); Buzzoni (1989); Bruzual A. & Charlot (1993); Bressan, Chiosi & Fagotto (1994); Worthey (1994); Leitherer & Heckman (1995); Fioc & Rocca-Volmerange (1997); Maraston (1998); Vazdekis (1999); Bruzual & Charlot (2003); Maraston (2005); Eldridge, Izzard & Tout (2008); Conroy & Gunn (2010); Maraston & Strömbäck (2011) (see also Charlot & Bruzual, in preparation, and Wofford et al. 2016 for a comparison of the predictions from several codes).

There are different types of evolutionary stellar population synthesis models:

(i) Most existing codes rely on the *isochrone synthesis* technique (introduced by Charlot & Bruzual, 1991), which exploits the fact that any stellar population can be expanded in a series of "simple stellar populations" (hereafter SSPs), i.e., individual stellar generations. The contribution to the integrated spectrum of a stellar population by stars of a given age is computed by integrating the flux emitted by stars of all masses along the isochrone at that age.

(ii) Another, more approximate approach consists in computing the flux emitted by stars of a given age without computing the full isochrone, but by integrating the flux contributed by stars beyond the main-sequence[1] turnoff (corresponding to the mass completing core-hydrogen burning) based on the amount of hydrogen and helium available for nuclear burning in subsequent phases; this is the *fuel consumption theorem* (e.g., Maraston, 2005, and references therein), which neglects the dispersion of stellar masses beyond the main sequence.

To model the emission from an SSP, three main components are required, which I now describe:

1. a prescription for the evolving properties (e.g., luminosity, effective temperature, gravity) of stars of given initial mass and chemical composition in the Hertzsprung-Russell (H-R) diagram ("evolutionary tracks");
2. the mass distribution of newly born stars (IMF);
3. a library of individual stellar spectra to characterize the emission of each single star.

2.1.2 Stellar evolutionary tracks

The initial mass of a star has a major influence on its evolution, massive stars evolving faster than low-mass ones. Fig. 2.1 illustrates the evolution of stars with initial masses between 0.1 $\mathrm{M}_\odot$ (very low-mass stars) and 120 $\mathrm{M}_\odot$ (massive stars) in the H-R diagram, for fixed solar metallicity $Z_\odot$. The black line indicates the zero-age main sequence (ZAMS). In the next paragraphs, I briefly summarize the main stages characterizing the evolution of stars in different mass ranges in this diagram: very low-mass stars, with masses $m \lesssim 0.3\,\mathrm{M}_\odot$; low-mass stars, with $0.3 \lesssim m \lesssim 2\,\mathrm{M}_\odot$; intermediate-mass stars, with $2 \lesssim m \lesssim 8\,\mathrm{M}_\odot$; and massive stars, with $m \gtrsim 8\,\mathrm{M}_\odot$. The transition masses between these ranges depend slightly on metallicity, the values mentioned here corresponding to the solar metallicity $Z_\odot$.

---

[1] The main sequence is the region of the Hertzsprung-Russell (bolometric luminosity versus effective temperature) diagram populated by stars burning hydrogen in their cores.

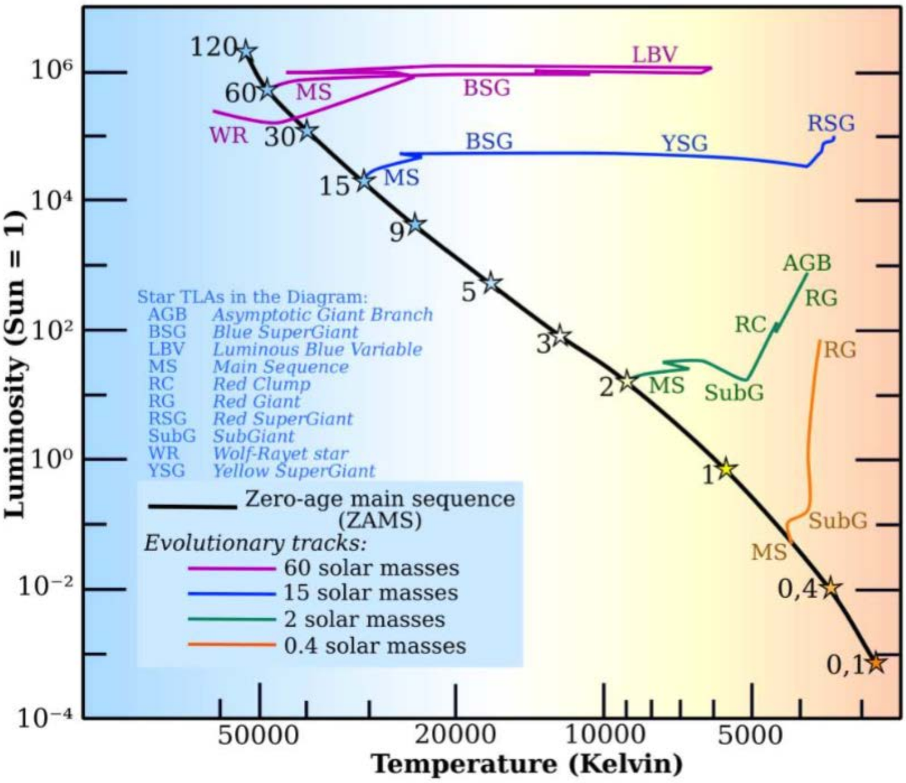

Figure 2.1: Evolutionary tracks of stars with initial masses between 0.1 $M_\odot$ (very low-mass stars) and 120 $M_\odot$ (massive stars) in the Hertzsprung-Russell diagram, for fixed solar metallicity $Z_\odot$. The zero-age main sequence is represented by the solid black line, as well as the main stages of four typical-mass stars during their lifetimes. The effective temperature is given in K, and the bolometric luminosity is in solar luminosity units.

Very low-mass stars ($m \lesssim 0.3\,M_\odot$): a star with an initial mass less than $0.08\,M_\odot$ never reaches a sufficiently high temperature to burn hydrogen in its core. Stars of such low mass and down to about 0.01–$0.06\,M_\odot$ could still burn deuterium and lithium and slowly contract while degenerate electrons gain pressure enough to reach hydrostatic equilibrium; the temperature cools down and the star becomes a *brown dwarf.*

If the star has an initial mass in the range $0.08 \lesssim m \lesssim 0.3\,M_\odot$, the temperature required to start hydrogen burning can be reached, but not helium burning. Once hydrogen is exhausted, the star is expected to slowly cool as a helium *white dwarf.* The lifetime of a very low-mass star typically exceeds the age of our Universe, 13.8 Gyr.

Low-mass stars ($0.3 \lesssim m \lesssim 2\,M_\odot$): while the main-sequence lifetime of a star less massive than about $0.9\,M_\odot$ is greater than 13.8 Gyr, it drops to only about 1 Gyr for a $2\,M_\odot$ star. At the end of main sequence evolution, the hydrogen core is completely exhausted, and H starts burning in a shell around the He core. As this core starts to contract, more energy is produced, leading to a higher temperature of the external envelope of the star and then to its expansion; the surface temperature drops and the luminosity increases: this is the "red giant branch" (RGB), stars in this phase dominating the spectra of stellar populations at old ages. During this phase, more and more helium is produced around the He core, increasing its mass and density. Stars less massive than about $2\,\mathrm{M}_\odot$ do not produce enough gravitational pressure to initiate quietly He burning. Instead, He is compacted into degenerate matter, and the temperature and density of the core keep increasing until the temperature becomes high enough (around $10^8\,\mathrm{K}$) to ignite He burning in an intense flash, called the "helium flash". When all helium in the core is converted into carbon and oxygen, He-burning continues in an outer shell, causing the expansion of the star: this is the "asymptotic giant branch" (AGB). During the "early AGB" (E-AGB) phase (Iben & Renzini, 1983), only helium burns in a shell. This lasts during a short period ($\sim$ 10 **Myr**), until the end of He-burning and the re-ignition of H-burning in outer layers, when the He shell nears the base of the H shell. This marks the beginning of the "thermally pulsing AGB" (TP-AGB) phase, where helium from H-shell burning builds up and eventually re-ignites He-shell burning, causing the star to expand and cool, which shuts off H-shell burning, etc. During these pulses (which last around 0.2 to 2 Myr, Vassiliadis & Wood 1993, Table 1), core material can be dredged up to the surface by convection and released into the ISM in the form of stellar winds (see Section 1.1.3). After the star has lost most of its envelope in this way, and only the core regions remain, it evolves as a planetary nebula and a *white dwarf*.

Intermediate-mass stars ($2 \lesssim m \lesssim 8\,\mathrm{M}_\odot$): the evolution of an intermediate-mass star is similar to that of a low-mass star, except that, in this case, the gravitational pressure is high enough for helium burning to ignite quietly on the RGB. After core-helium exhaustion, the evolution on the AGB depends on whether or not the temperature reached (which is linked to the initial mass and chemical composition of the star) is high enough to ignite core-carbon burning (in a flash, in a partially degenerate carbon-oxygen core). If so – as is expected for initial stellar masses between 5 and $8\,\mathrm{M}_\odot$ (Marigo, 2001), the star will eventually explode as a *supernova*. Otherwise, the star evolves as a *white dwarf*.

High-mass stars ($m \gtrsim 8\,\mathrm{M}_\odot$): this stellar mass range – corresponding to stars with main-sequence lifetimes less than about 40 Myr – is essential to my work, as high-mass stars are the primary sources of ionizing photons in star-forming galaxies (Hollenbach & Tielens, 1999; Schaerer et al., 2011; Dale, Ercolano & Bonnell, 2012; Cai et al., 2014; Kimm & Cen, 2014; Yu, Wang & Li, 2015). Unlike low- and intermediate-mass stars, massive stars go through the quiet ignition of nuclear burning of all elements until the formation of a nickel-iron core. This core, sitting at the center of the star, is surrounded by shells burning successively lighter elements. Since Fe and Ni have the highest binding energy per nucleon of all elements, energy cannot be produced any further by fusion in the core. The core grows, until it collapses gravitationally, explodes as a supernova and pollutes the ISM with large amounts of metals and dust (Schneider, Ferrara & Salvaterra, 2004; Sarangi & Cherchneff, 2015; Dale, Ercolano & Bonnell, 2013). The remnant is either a *neutron star* (for an initial stellar mass $m \lesssim 20\,\mathrm{M}_\odot$) or a *black hole* (for a more massive star). The evolution of massive stars is particularly complex, as some stars rapidly lose mass in strong winds (hot, massive blue supergiants and Wolf-

Rayet stars), leading to the release of strong ionizing radiation. The models used in my work include a state-of-the-art treatment of the evolution through such phases (Bressan et al., 2012; Chen et al., 2015, see Sections 2.1.5 and 3.2.1 for details). Fig. 2.2 (taken from Chen et al. 2015) shows an example of evolutionary tracks of stars with masses between 20 and 350 $M_\odot$ in the H-R diagram, for solar metallicity.

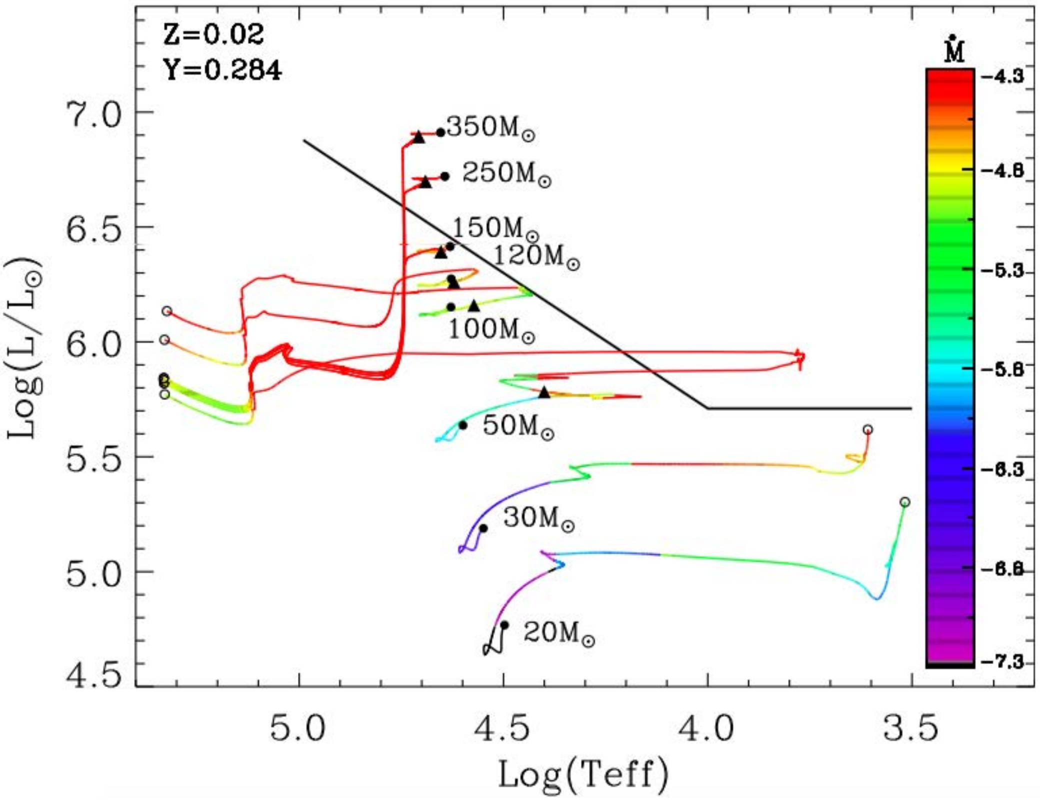

Figure 2.2: Evolutionary tracks of 8 massive stars in Hertzsprung-Russell diagram, for initial stellar masses from 20 $M_\odot$ to 350 $M_\odot$ at a fixed stellar metallicity Z=0.020. The solid and empty black points represent the ZAMS and the central carbon ignition (where the tracks end) respectively, while the triangles indicate the begining of the Wolf-Rayet phase (Credit: Chen et al., 2015).

From the evolutionary tracks of stars in all mass ranges in the H-R diagram, we can compute isochrones joining the positions of stars in a full range of masses at a given time and for a given metallicity. These are required for computing the spectral evolution of stellar populations via the isochrone synthesis technique described earlier in this section.

2.1.3 Stellar Initial Mass Function

The number of stars populating different mass bins along an isochrone in the H-R diagram depends on the initial mass function, which describes the mass distribution of newly born stars. Several parameterizations of the IMF had been investigated since the mid-20th century. We can cite the pioneer, single power-law formula of Salpeter (1955), followed by more complex parametrizations based on either observational or theoretical work (Miller & Scalo, 1979; Kennicutt, 1983; Scalo, 1986; Kroupa, Tout & Gilmore, 1993; Kroupa, 2001; Chabrier, 2003). In this thesis, I adopt the mass distribution of newly born stars corresponding to the Galactic-disk IMF of Chabrier (2003), truncated at 0.1 and either 100 or 300 $M_\odot$ (the upper cutoff of the stellar IMF is one of the adjustable parameters I consider in Section 3.3.1). This IMF presents a turnover at low masses: it is a log-normal function at stellar masses less than 1 $M_\odot$ and a power law (similar to the Salpeter 1955 function) at higher masses,

$$\phi(\log m) \propto \begin{cases} \exp\left[-\frac{(\log m - \log m_c)^2}{2\sigma^2}\right], & \text{for } m \leq 1\mathrm{M}_\odot, \\ m^{-1.3}, & \text{for } m > 1\mathrm{M}_\odot, \end{cases} \tag{2.1}$$

with $m_c = 0.08\,M_\odot$ and $\sigma = 0.69$. Fig. 2.3 illustrates the difference between this IMF (solid red line) and the Salpeter (1955) IMF (dashed blue line).

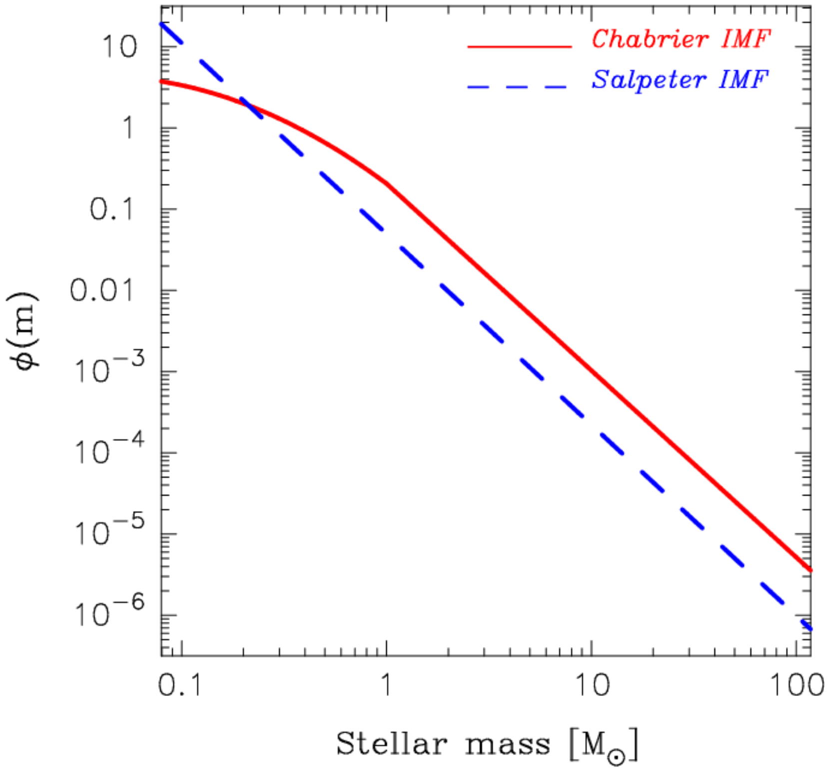

Figure 2.3: Comparison of the Chabrier (2003) IMF (solid red line), with the Salpeter (1955) IMF (dashed blue line), both normalized to unit stellar mass. The IMF is defined such that $\phi(m)dm$ is the fraction of stars born with masses between m and $m + dm$ (Credit: Shimizu & Inoue, 2013).

2.1.4 Library of stellar spectra

The last ingredient to compute the spectral evolution of SSPs with a stellar population synthesis code is a library of individual stellar spectra. This is required to describe the light emitted by each star along an isochrone in the H-R diagram. These individual spectra should include full ranges of stellar parameters (bolometric luminosity, effective temperature, gravity). Two types of stellar spectra libraries can be assembled: empirical (i.e. observational) and theoretical libraries.

- Empirical libraries collect real observations of a few hundreds to a thousand of stellar spectra, mostly observed in our Milk-Way and in nearby galaxies like the Magellanic Clouds. Among the most widely used libraries of observed stellar spectra, we can cite Pickles (Pickles, 1998), ELODIE (Prugniel & Soubiran, 2001; Prugniel et al., 2007), STELIB (Le Borgne et al., 2003), UVES POP (Jehin et al., 2005), MILES (Sánchez-Blázquez et al., 2006; Cenarro et al., 2007; Prugniel, Vauglin & Koleva, 2011), IndoUS/CFLIB (Valdes et al., 2004; Wu et al., 2011), NGSL (Gregg et al., 2004; Koleva & Vazdekis, 2012), XSL (Chen et al., 2011) and IRTF (Rayner, Cushing & Vacca, 2009). These libraries allow one to describe the emission of a wide range of stars of the H-R diagram, but not all stars. Indeed, empirical libraries rely on observations of nearby stars, and hence, they do not include stellar categories not found in the local Universe, such as chemically young massive stars, which are nevertheless necessary for studies of high-redshift stellar populations. Empirical libraries thus do not cover large enough ranges of stellar parameters, and a possible strategy is to combine them with theoretical models to assemble a full range of spectral energy distributions.

- To overcome the lack of spectra for some specific stellar types or extend existing spectra outside the available wavelength range (in particular into the ultraviolet), one must appeal to theoretical libraries. The latter can be computed across any wavelength range with arbitrary resolution, and for all types of stars with any set of parameters. They rely on model atmospheres, which solve the hydrodynamic equations of the gas by accounting for convection and radiative transfer and predict stellar magnitudes and colours. Among them, we can cite ATLAS9 (Kurucz, 1970, 1979, 2005; Castelli & Kurucz, 2004) for stars with negligible mass-loss, MARCS (Gustafsson et al., 1975, 2008) and PHOENIX (Hauschildt, Baron & Allard, 1997; Hauschildt, Allard & Baron, 1999; Hauschildt et al., 1999; Allard et al., 2012) for cool giants, while for hotter stars significantly losing mass there are WM-BASIC (Pauldrach, Puls & Kudritzki, 1986), CMFGEN (Hillier & Miller, 1998) and PoWR (Gräfener, Koesterke & Hamann, 2002; Hamann & Gräfener, 2003, 2004; Hamann, Gräfener & Liermann, 2006; Sander, Hamann & Todt, 2012; Hainich et al., 2014). Several theoretical librairies of synthetic stellar spectra are available for stellar population synthesis models (e.g., Coelho et al., 2005; Martins et al., 2005; Munari et al., 2005; Bertone et al., 2008).

  It is worth noting that the stellar population synthesis code I use in this thesis (see Section 2.1.5 next) appeals to a mix of empirical libraries, at near-ultraviolet, optical and near-infrared wavelengths, and theoretical libraries, to extend the wavelength range, in particular at far-ultraviolet and ionizing wavelengths.

2.1.5 In this work (galaxev)

In this thesis, I adopt the latest version of the Bruzual & Charlot (2003) stellar population synthesis code GALAXEV (Charlot & Bruzual, in preparation), which is a widely used tool to compute the ultraviolet-to-near infrared spectral energy distributions of galaxies. This model reproduces in detail typical observed galaxy spectra extracted from the Sloan Digital Sky Survey (Stoughton et al., 2002). The version of the code used in this thesis incorporates recent important progress in the treatment of the interiors and atmospheres of massive hot stars, including Wolf-Rayet stars, as well as of AGB stars. In brief, here are the main characteristics of the key ingredients implemented in this code, of interest to the work presented in the next chapters (I also provide more details in Section 3.2.1).

- I use models incorporating evolutionary tracks computed using the PARSEC code of Bressan et al. (2012), for initial stellar masses of up to 350 $M_\odot$ (Chen et al., 2015), and including the evolution through the Wolf-Rayet phase.
- The mass distribution of newly born stars follows the Galactic-disk IMF of Chabrier (2003), as described in Section 2.1.3 above.
- Concerning libraries of stellar spectra, I appeal whenever possible to the Miles library (Sánchez-Blázquez et al., 2006; Cenarro et al., 2007; Prugniel, Vauglin & Koleva, 2011), with stellar parameters determined by Prugniel, Vauglin & Koleva (2011). Since these spectra do not include the ultraviolet range, I use the GALAXEV extension of the Miles library into the ultraviolet wavelength range based on the UVBLUE spectral library (Bertone et al., 2008). The spectra of hot O-B stars rely on the Tlusty models (Hubeny & Lanz, 1995; Lanz & Hubeny, 2003, 2007), while those of Wolf-Rayet stars rely on the PoWR models (Gräfener, Koesterke & Hamann, 2002; Hamann & Gräfener, 2003, 2004; Hamann, Gräfener & Liermann, 2006; Sander, Hamann & Todt, 2012; Hainich et al., 2014).

With these ingredients, I use the GALAXEV code to compute the spectral energy distributions of galaxies with any star formation and chemical enrichment histories using the isochrone synthesis technique, as outlined in Chapter 3 (see equation 3.1).

2.2 Photoionization codes

Photoionization codes are useful tools commonly used by the astronomical community to describe the properties of gas irradiated by an ionizing source (e.g., in planetary nebulae, H II regions, and around an AGN), which take into account the different spectral components involved (outlined in Section 1.2.3). These codes solve numerically the ionization and thermal structures of an ionized cloud and output the nebular-continuum and emission-line spectra.

2.2.1 Generalities

Most photoionization codes are static and treat gas in thermal equilibrium and ionization balance (see equation 1.1). Although the most widely used photoionization code is CLOUDY (Ferland et al., 2013), several other similar codes exist.

The first photoionization codes date back to the late 1960's and were mainly dedicated to studies of low-density nebulae (Harrington, 1968; Rubin, 1968; Tarter & Salpeter, 1969).

Then, several improvements in atomic processes, for instance in charge exchange and "low-temperature" dielectronic recombination (Pequignot, Stasińska & Aldrovandi, 1978; Butler, Heil & Dalgarno, 1980; Storey, 1981), as well as new prescriptions for higher densities, photon energies and optical depths (Davidson & Netzer, 1979; Kwan, 1984) have been progressively implemented, leading to more and more sophisticated photoionization codes. As examples, we can cite Mappings (Sutherland & Dopita, 1993), Mocassin (Ercolano et al., 2003), Nebu (Péquignot et al., 2001) and XStar (Kallman, 1999).

Aside from continuous updates of atomic data, the main differences between photoionization codes reside in the treatment of the transfer of the ionizing photons in the cloud: some consider a single average direction and compute the inward- and outward-going diffuse radiation fields using iterative techniques, while others consider several directions but an "outward-only" approximation (where the locally produced diffuse radiation is added to the incident flux and carried into the cloud). This diffuse radiation transfer is solved using different numerical treatments, for instance with classical techniques (e.g., Rubin, 1968; Harrington, 1968) or by means of Monte-Carlo techniques (e.g., Och, Lucy & Rosa, 1998). Photoionization codes also differ in the assumed geometry: most consider plane-parallel or spherical geometry, but some also incorporate a 3D approach (Gruenwald, Viegas & Broguière, 1997; Och, Lucy & Rosa, 1998; Morisset, 2006). Moreover, some codes allow one to investigate time-dependent in addition to static cases (e.g., Tylenda, 1979; Marten & Szczerba, 1997), which is particularly important if the timescale of stellar evolution is comparable to that of recombination processes. Finally, we can cite a few codes, which also account for hydrodynamical effects simultaneously to microphysical processes (e.g., Schmidt-Voigt & Koeppen, 1987; Schmidt-Voigt & Koppen, 1987; Marten & Schoenberner, 1991; Frank & Mellema, 1994a; Rodriguez-Gaspar & Tenorio-Tagle, 1998; Frank & Mellema, 1994b; Mellema & Frank, 1995; Mellema, 1995)

2.2.2 In this work (cloudy)

In this thesis, I adopt the latest version of the photoionization code CLOUDY (c13.03; described in Ferland et al. 2013)[2] to compute the nebular emission from gas ionized by young stars in galaxies. CLOUDY is an open-source plasma simulation code, which models physical conditions within clouds, over full density and temperature ranges. The goal is to simulate the ionization, level populations, molecular state, and thermal state of material exposed to an external radiation field or some other source of heating. To compute the synthetic spectrum of the ionized cloud, one has to specify the shape of the incident ionizing continuum – in my case, the spectral energy distribution computed using the GALAXEV stellar population synthesis code described in Section 2.1.5 – as well as the parameters of the diffuse gas. Overall, the main input parameters that have to be specified to compute the radiation emerging from gas ionized by young stars in this approach with CLOUDY are:

- the nature of the external incident radiation striking the cloud: I will consider ionizing star clusters at the center of H II regions, corresponding to simple stellar populations computed using the GALAXEV stellar population synthesis code (Section 2.1.5).
- the chemical composition and dust-grain content of the gas: CLOUDY handles in detail the lightest 30 elements at all stages of ionization, and I describe in Section 3.2.3 the

---

[2] Available from `http://www.nublado.org`, including the full source code and atomic and molecular data.

individual abundances and factors of depletion onto dust grains I adopt in this thesis.

- the geometry of the gas (see Fig. 2.4): I use a closed geometry to compute the nebular emission from H II regions, which means that the gas is assumed to be spherically distributed around the ionizing star clusters; instead, in Chapter 4, we use an open geometry to investigate the nebular emission from narrow-line emitting regions of AGN.
- the total hydrogen density of the gas: as detailed in Section 3.3.1, I investigate 4 hydrogen densities of the ionized gas, $n_{\rm H} = 10$, 10^2, 10^3 and $10^4\,{\rm cm}^{-3}$, spanning most of the range of observed electronic densities in extragalactic H II regions (e.g., Hunt & Hirashita, 2009).

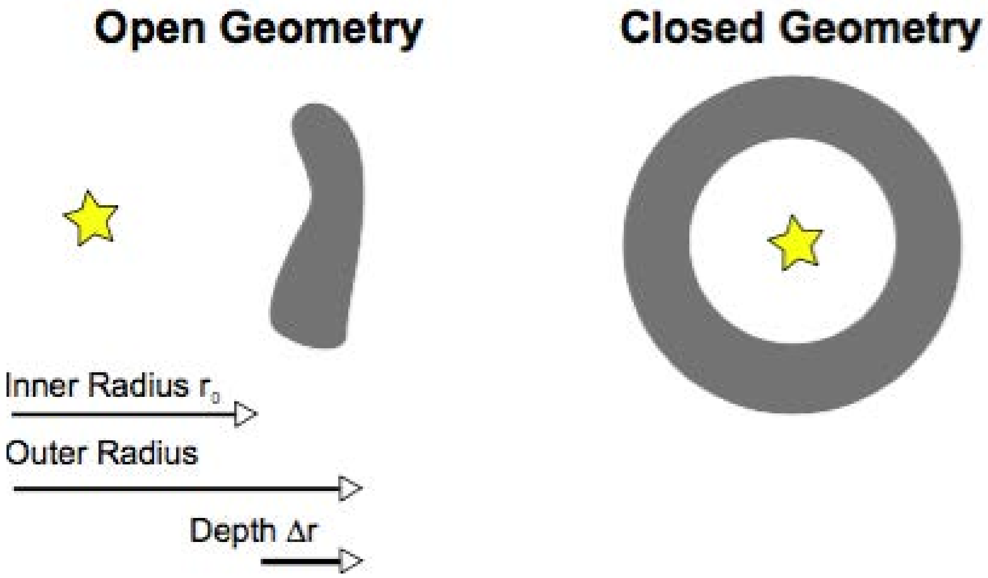

Figure 2.4: Open and closed geometry in CLOUDY. The closed geometry is appropriate to model an H II region surrounding an ionizing star cluster (Credit: Hazy/CLOUDY).

Once the incident radiation and initial conditions are defined, the code computes the thermal, ionization and chemical structure of the ionized cloud and the emergent spectrum (including nebular absorption and emission). This is achieved by simultaneously solving the equations of statistical and thermal equilibrium, the equations that balance ionization-neutralisation processes, and the heating-cooling processes: CLOUDY is a microphysics code. The resulting spectrum computed by CLOUDY is the sum of several components: the transmitted radiation attenuated by extinction through the gas, the diffuse radiation emitted by the gas, the reflected radiation[3] emitted from the illuminated face of the cloud towards the central source, and the emission lines. This is summarized in Fig. 2.5.

---

[3] We note that the reflected component is only computed for an open geometry in CLOUDY.

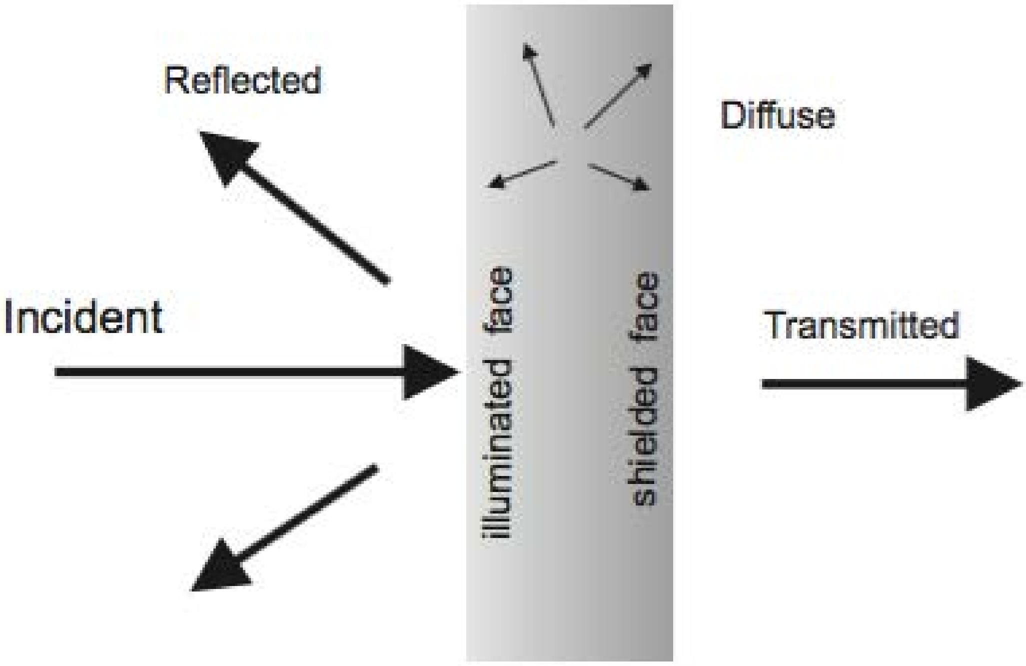

Figure 2.5: Radiation fields computed in the calculation of CLOUDY (Credit: Hazy/CLOUDY).

In this thesis, I am particularly interested in the intensities predicted by CLOUDY for a large number of optical and ultraviolet spectral lines (see Sections 3.3 and 3.4). In practice, I treat CLOUDY as a subroutine of another code (written in C++ computer language for the sake of compatibility with CLOUDY), in which I specify in a fully self-consistent and versatile way the properties of the incident radiation and gas parameters.

As an illustration of the effect of the gas on stellar radiation, Fig. 2.6 shows an example of H II spectrum computed using the combination of the GALAXEV and CLOUDY codes. The black spectrum is the incident stellar component predicted by the GALAXEV stellar population synthesis code, while the red spectrum is that output by the CLOUDY photoionization code.

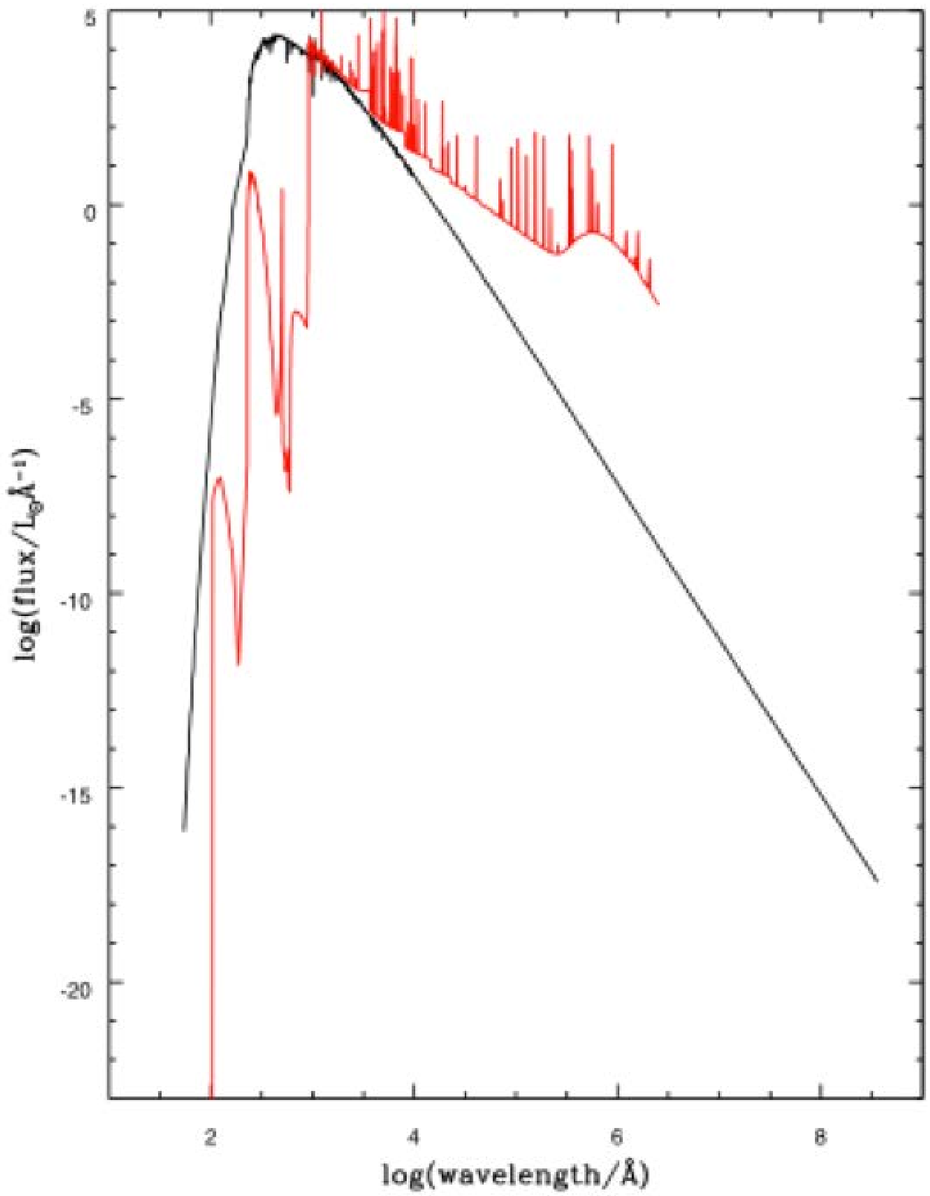

Figure 2.6: Example of H II spectrum computed using the combination of the GALAXEV and CLOUDY codes: the black spectrum is the incident stellar component predicted by the GALAXEV stellar population synthesis code (i.e. the pure stellar spectrum), while the red spectrum is that output by the CLOUDY photoionization code (i.e. when accounting for the stellar radiation throughout interstellar gas).

As a further illustration, I also show in Fig. 2.7 the evolution in time of the rate of ionizing photons, Q, emitted by an SSP. This drops considerably after an age of about 10 Myr, since after the most massive stars have died, most of the emission from a stellar population is produced at longer wavelengths (Fig. 2.8). The only remaining sources of ionizing photons at old ages are the central stars of planetary nebulae, which are very faint.

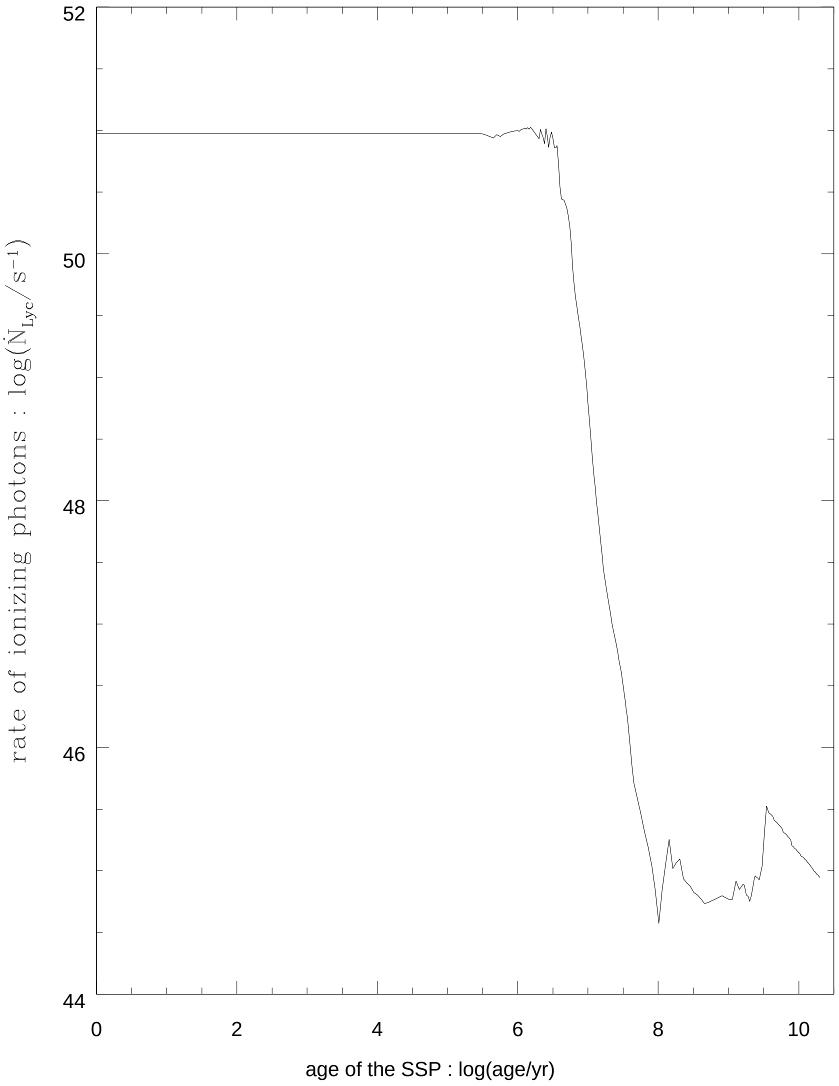

Figure 2.7: Rate of ionizing photons in a single H II region in function of the time

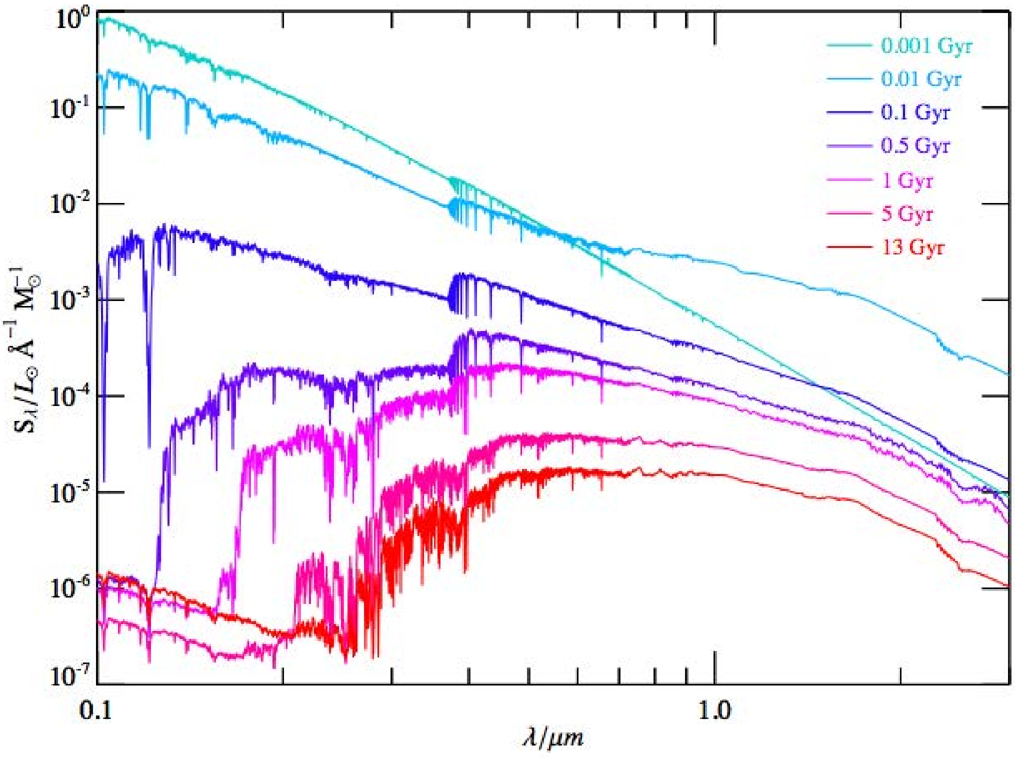

Figure 2.8: Spectra of an SSP at solar metallicity $Z_\odot$ computed at different ages with the updated Bruzual & Charlot (2003) stellar population synthesis code.

2.3 Conclusion

My aim in this thesis is to compute whole spectral energy distributions – including lines and continuum emission – of star-forming galaxies with arbitrary star formation histories. To achieve this, I start by computing the emission from single H II regions ionized by individual star clusters using a combination of the GALAXEV and CLOUDY codes, as described above (Sections 2.1.5 and 2.2.2), for wide ranges of input parameters. Then, I convolve this with a star formation history to compute the emission from an entire star-forming galaxy and exploit the results in line-ratio diagnostic diagrams, as we shall see in the next chapters.

CHAPTER 3

Modelling the nebular emission from star-forming galaxies

Contents

In this chapter, I present a new model of the nebular emission from star-forming galaxies in a wide range of chemical compositions, appropriate to interpret observations of galaxies at all cosmic epochs. The model relies on the combination of state-of-the-art stellar population synthesis and photoionization codes to describe the ensemble of H II regions and the diffuse gas ionized by young stars in a galaxy. I detail the main features of this model, in particular the self-consistent yet versatile treatment of element abundances and depletion onto dust grains, which allows one to relate the observed nebular emission from a galaxy to both gas-phase and dust-phase metal enrichment. I show that this model can account for the rest-frame ultraviolet and optical emission-line properties of galaxies at different redshifts and find that ultraviolet emission lines are more sensitive than optical ones to

parameters such as C/O abundance ratio, hydrogen gas density, dust-to-metal mass ratio and upper cutoff of the stellar initial mass function. I also find that, for gas-phase metallicities around solar to slightly sub-solar, widely used formulae to constrain oxygen ionic fractions and the C/O ratio from ultraviolet and optical emission-line luminosities are reasonable faithful. However, the recipes break down at non-solar metallicities, making them inappropriate to study chemically young galaxies. In such cases, a fully self-consistent model of the kind I have developed during my thesis is required to interpret the observed nebular emission.

We note that this chapter is extracted from the paper *Modelling the nebular emission from primeval to present-day star-forming galaxies* by Julia Gutkin, Stéphane Charlot and Gustavo Bruzual, published in the Monthly Notices of the Royal Astronomical Society.

3.1 Introduction

The emission from interstellar gas heated by young stars in galaxies contains valuable clues about both the nature of these stars and the physical conditions in the interstellar medium. In particular, prominent optical emission lines produced by H II regions, diffuse ionized gas and a potential active galactic nucleus in a galaxy are routinely used as global diagnostics of gas metallicity and excitation, dust content, star formation rate and nuclear activity (e.g., Izotov & Thuan, 1999; Kobulnicky, Kennicutt & Pizagno, 1999; Kauffmann et al., 2003; Nagao, Maiolino & Marconi, 2006; Kewley & Ellison, 2008), as we have seen in Chapter 1. Near-infrared spectroscopy enables such studies in the optical rest frame of galaxies out to redshifts $z \sim 1$–3 (e.g., Pettini & Pagel, 2004; Hainline et al., 2009; Richard et al., 2011a; Guaita et al., 2013; Steidel et al., 2014; Shapley et al., 2015). While the future *James Webb Space Telescope* will enable rest-frame optical emission-line studies out to the epoch of cosmic reionization, rapid progress is being accomplished in the observation of fainter emission lines in the rest-frame ultraviolet spectra of galaxies in this redshift range (e.g., Shapley et al., 2003; Erb et al., 2010; Stark et al., 2014, 2015a,b, 2016; Sobral et al., 2015). The interpretation of these new observations requires the development of models optimised for studies of the ultraviolet – in addition to optical – nebular properties of chemically young galaxies, in which heavy-element abundances (for example, the C/O ratio; Erb et al., 2010; Cooke et al., 2011) are expected to differ substantially from those in star-forming galaxies at lower redshifts. The development of such a sophisticated code is a primary motivation of my thesis work.

Several models have been proposed to compute the nebular emission of star-forming galaxies through the combination of a stellar population synthesis code with a photoionization code (e.g., Garcia-Vargas, Bressan & Diaz 1995; Stasińska & Leitherer 1996; Charlot & Longhetti 2001, hereafter CL01; Zackrisson et al. 2001; Kewley & Dopita 2002; Panuzzo et al. 2003; Dopita et al. 2013; see also Anders & Fritze-v. Alvensleben 2003; Schaerer & de Barros 2009). These models have proved valuable in exploiting observations of optical emission lines to constrain the young stellar content and ISM properties of star-forming galaxies (e.g., Brinchmann et al., 2004; Blanc et al., 2015). A limitation of current models of nebular emission is that these were generally calibrated using observations of H II regions and galaxies in the nearby Universe, which increasingly appear as inappropriate to study the star formation and ISM conditions of chemically young galaxies (e.g., Erb et al. 2010; Steidel et al. 2014, 2016; Shapley et al. 2015; see also Brinchmann, Pettini & Charlot 2008; Shirazi, Brinchmann & Rahmati 2014). I note that this limitation extends to chemical abundance estimates based on not only the so-called 'strong-line' method, but also the 'direct' (via the electronic temperature T_e) method, since both methods rely on the predictions of photoionization models (see Section 3.5). Another notable limitation of current popular models of the nebular emission from star-forming galaxies is that these do not incorporate important advances achieved over the past decade in the theories of stellar interiors (e.g., Eldridge, Izzard & Tout, 2008; Bressan et al., 2012; Ekström et al., 2012; Georgy et al., 2013; Chen et al., 2015) and atmospheres (e.g., Hauschildt & Baron, 1999; Hillier & Miller, 1999; Pauldrach, Hoffmann & Lennon, 2001; Lanz & Hubeny, 2003, 2007; Hamann & Gräfener, 2004; Martins et al., 2005; Puls et al., 2005; Rodríguez-Merino et al., 2005; Leitherer et al., 2010).

In the following sections, I present a new model of the ultraviolet and optical nebular emission from galaxies in a wide range of chemical compositions, appropriate to model and interpret observations of star-forming galaxies at all cosmic epochs. This model is based on the combination of the latest version of the Bruzual & Charlot (2003) stellar population synthesis code (Charlot & Bruzual, in preparation; which incorporates the stellar evolutionary tracks of Bressan et al. 2012; Chen et al. 2015 and the ultraviolet spectral libraries of Lanz & Hubeny 2003, 2007; Hamann & Gräfener 2004; Rodríguez-Merino et al. 2005; Leitherer et al. 2010) with the latest version of the photoionization code CLOUDY (c13.03; described in Ferland et al. 2013). I follow CL01 and use effective (i.e. galaxy-wide) parameters to describe the ensemble of H II regions and the diffuse gas ionized by successive stellar generations in a galaxy. As we will see, I take special care in parametrizing the abundances of heavy elements and their depletion onto dust grains in the ISM, which allows us to model in a self-consistent way the influence of 'gas-phase' and 'interstellar' (i.e. gas+dust-phase) abundances on emission-line properties.

I present an exhaustive grid of photoionization calculations I have computed with this model, exploring wide ranges of interstellar parameters, which is able to account well for observations of star-forming galaxies in several line-ratio diagrams at optical and ultraviolet wavelengths.

3.2 Modelling

I present here the model I have developed, in which the nebular emission of a star-forming galaxy is parametrized in terms of stellar population, gas and dust parameters.

To model the stellar and nebular emission from a star-forming galaxy, I adopt the isochrone synthesis technique introduced by Charlot & Bruzual (1991) and express the luminosity per unit wavelength λ emitted at time t as

$$L_\lambda(t) = \int_0^t dt'\, \psi(t-t')\, S_\lambda[t', Z(t-t')]\, T_\lambda(t,t')\,, \tag{3.1}$$

where $\psi(t-t')$ is the star formation rate at time $t-t'$, $S_\lambda[t', Z(t-t')]$ the luminosity produced per unit wavelength per unit mass by a single stellar generation of age t' and metallicity $Z(t-t')$ and $T_\lambda(t,t')$ the transmission function of the ISM, defined as the fraction of the radiation produced at wavelength λ at time t by a generation of stars of age t' that is transferred by the ISM. I describe below the prescriptions I adopt for the functions S_λ and T_λ in equation (3.1). I do not consider in this chapter the potential contributions to $L_\lambda(t)$ by shocks nor an AGN component. These will be addressed in Chapter 4.

3.2.1 Stellar emission

As explained in Section 2.1, I compute the spectral evolution of a single stellar generation $S_\lambda[t', Z(t-t')]$ in equation (3.1) above using the latest version of the Bruzual & Charlot (2003) stellar population synthesis model (Charlot & Bruzual, in preparation; see also Wofford et al. 2016). This incorporates stellar evolutionary tracks computed with the recent code of Bressan et al. (2012) for stars with initial masses up to 350 $\mathrm{M}_\odot$ (Chen et al., 2015) and metallicities in the range $0.0001 \leq Z \leq 0.040$ (the present-day solar metallicity corresponding to $Z_\odot = 0.01524$; Caffau et al. 2010; see also Section 3.2.3 below). These tracks include the evolution of the most massive stars losing their hydrogen envelope through the classical Wolf-Rayet phase (i.e., stars more massive than about 25 $\mathrm{M}_\odot$ at $Z = Z_\odot$, this threshold increasing as metallicity decreases).

To compute the spectral energy distributions of stellar populations, the above evolutionary tracks are combined with different stellar spectral libraries covering different effective-temperature, luminosity-class and wavelength ranges (Pauldrach, Hoffmann & Lennon, 2001; Rauch, 2002; Lanz & Hubeny, 2003; Hamann & Gräfener, 2004; Martins et al., 2005; Rodríguez-Merino et al., 2005; Sánchez-Blázquez et al., 2006; Lanz & Hubeny, 2007; Leitherer et al., 2010). Of major interest for the present study are the prescriptions for the ionizing spectra of hot stars. For O stars hotter than 27,500 K and B stars hotter than 15,000 K, the ionizing spectra come from the library of metal line-blanketed, non-local thermodynamic equilibrium (non-LTE), plane-parallel, hydrostatic models of Lanz & Hubeny (2003, 2007), which reach effective temperatures of up to 55,000 K and cover a wide range of metallicities (from zero to twice solar). The ionizing spectra of cooler stars come from the library of line-blanketed, LTE, plane-parallel, hydrostatic models of Rodríguez-Merino et al. (2005). For O stars hotter than 55,000 K, the ionizing spectra are taken from the library of line-blanketed, non-LTE, plane-parallel, hydrostatic models of Rauch (2002, which are also used to describe the radiation from faint, hot post-asymptotic-giant-branch stars). These are available for two metallicities, $Z_\odot$ and $0.1Z_\odot$, and interpolated in between. The lowest-metallicity spectra are used down to $Z = 0.0005$, below which pure blackbody spectra are adopted. Details are provided in Table 3.1. Finally, for Wolf-Rayet stars, the spectra come from the library of line-blanketed, non-LTE, spherically expanding models of Hamann & Gräfener (2004)[1] (see also Gräfener, Koesterke & Hamann 2002; Hamann & Gräfener 2003; Hamann, Gräfener & Liermann 2006; Sander, Hamann & Todt 2012; Hainich et al. 2014, 2015; Todt et al. 2015) available at four metallicities, $0.07Z_\odot$, $0.2Z_\odot$, $0.5Z_\odot$ and $Z_\odot$. The closest of these metallicities is selected to describe the emission from Wolf-Rayet stars at any metallicity in the stellar population synthesis model.

---

[1] Available from `http://www.astro.physik.uni-potsdam.de/~PoWR`

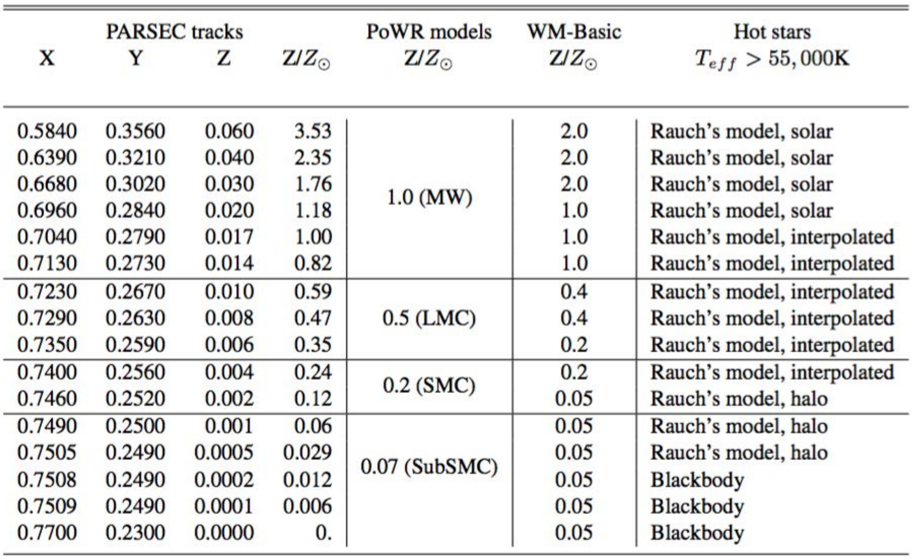

PARSEC tracks X	Y	Z	$Z/Z_\odot$	PoWR models $Z/Z_\odot$	WM-Basic $Z/Z_\odot$	Hot stars $T_{eff} > 55,000$K
0.5840	0.3560	0.060	3.53	1.0 (MW)	2.0	Rauch's model, solar
0.6390	0.3210	0.040	2.35		2.0	Rauch's model, solar
0.6680	0.3020	0.030	1.76		2.0	Rauch's model, solar
0.6960	0.2840	0.020	1.18		1.0	Rauch's model, solar
0.7040	0.2790	0.017	1.00		1.0	Rauch's model, interpolated
0.7130	0.2730	0.014	0.82		1.0	Rauch's model, interpolated
0.7230	0.2670	0.010	0.59	0.5 (LMC)	0.4	Rauch's model, interpolated
0.7290	0.2630	0.008	0.47		0.4	Rauch's model, interpolated
0.7350	0.2590	0.006	0.35		0.2	Rauch's model, interpolated
0.7400	0.2560	0.004	0.24	0.2 (SMC)	0.2	Rauch's model, interpolated
0.7460	0.2520	0.002	0.12		0.05	Rauch's model, halo
0.7490	0.2500	0.001	0.06	0.07 (SubSMC)	0.05	Rauch's model, halo
0.7505	0.2490	0.0005	0.029		0.05	Rauch's model, halo
0.7508	0.2490	0.0002	0.012		0.05	Blackbody
0.7509	0.2490	0.0001	0.006		0.05	Blackbody
0.7700	0.2300	0.0000	0.		0.05	Blackbody

Table 3.1: Detailed values adopted at each metallicity to reproduce spectra of O stars hotter than 55,000 K: PARSEC tracks (Bressan et al., 2012; Chen et al., 2015) are combined with the library of line-blanketed, non-LTE, plane-parallel, hydrostatic models of Rauch (2002).

3.2.2 Transmission function of the ISM

To compute the transmission function $T_\lambda(t,t')$ of the ISM in equation (3.1), I follow CL01 (see also Pacifici et al. 2012) and write this as the product of the transmission functions of the ionized gas, $T^+_\lambda(t,t')$, and the neutral ISM, $T^0_\lambda(t,t')$, i.e.

$$T_\lambda(t,t') = T^+_\lambda(t,t')\, T^0_\lambda(t,t')\,. \tag{3.2}$$

If the ionized regions are bounded by neutral material, $T^+_\lambda(t,t')$ will be close to zero at wavelengths blueward of the H-Lyman limit but greater than unity at the wavelengths corresponding to emission lines. In this work, I focus on the nebular emission from star-forming galaxies, which is controlled primarily by the function T^+_λ. I assume for simplicity that this depends only on the age t' of the stars that produce the ionizing photons. Since 99.9 per cent of the H-ionizing photons are produced at ages less than 10 Myr by a single stellar generation (e.g. Charlot & Fall, 1993; Binette et al., 1994), as in CL01, I write

$$T^+_\lambda(t,t') = \begin{cases} T^+_\lambda(t') & \text{for} \quad t' \leqslant 10\,\text{Myr}\,, \\ 1 & \text{for} \quad t' > 10\,\text{Myr}\,. \end{cases} \tag{3.3}$$

I do not consider in this chapter the attenuation by dust in the neutral ISM, which is controlled by the function T^0_λ, but it is possible to include it in my models as explained in Section 3.2.4.

I use the approach proposed by CL01 to compute the transmission function of the ionized gas in equation (3.3). This consists in describing the ensemble of H II regions and the diffuse gas ionized by a single stellar generation in a galaxy with a set of effective parameters (which can be regarded as those of an effective H II region ionized by a typical star cluster) and appealing to a standard photoionization code to compute $T^+_\lambda(t')$ at ages $t' \leqslant 10\,$Myr for this stellar generation. By construction, the contributions by individual H II regions and diffuse ionized gas to the total nebular emission are not distinguished in this prescription. This is justified by the fact that diffuse ionized gas, which appears to contribute around 20–50 per cent of the total H-Balmer-line emission in nearby spiral and irregular galaxies, is observed to be spatially correlated with H II regions and believed to also be ionized by massive stars (e.g., Haffner et al., 2009, and references therein; see also Hunter & Gallagher 1990; Martin 1997; Oey & Kennicutt 1997; Wang, Heckman & Lehnert 1997; Ascasibar et al. 2016). The effective parameters describing a typical H II region in this approach therefore reflect the global (i.e. galaxy-wide) properties of the gas ionized by a stellar generation throughout the galaxy. Fig. 3.1 illustrates the expansion in this way of a galaxy in a series of H II regions through the convolution of the evolution of individual star clusters with a star formation history.

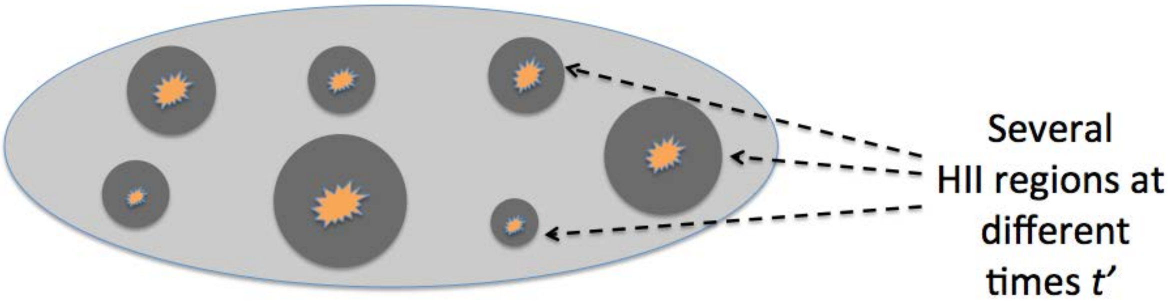

Figure 3.1: To model the nebular emission from an entire galaxy, I consider that each galaxy is expandable in series of SSPs.

As detailed in Section 2.2.2, to compute $T^{+}_{\lambda}(t')$ in this context, I appeal to the latest version of the photoionization code CLOUDY. I link this code to the spectral evolution of a single stellar generation, $S_\lambda[t', Z(t-t')]$, as achieved by CL01, to whom I refer for details. In brief, I compute the time-dependent rate of ionizing photons produced by a star cluster with effective mass M_* as

$$Q(t') = \frac{M_*}{hc}\int_0^{\lambda_{\rm L}} d\lambda\, \lambda S_\lambda(t')\,, \tag{3.4}$$

where h and c are the Planck constant and the speed of light, $\lambda_{\rm L} = 912$ is the wavelength at the Lyman limit and, for the sake of clarity, I have dropped the dependence of S_λ on stellar metallicity Z. In the CLOUDY code, the gas is described as spherical concentric layers centred on the ionizing source (assumed to be pointlike). From the expression of $Q(t')$ in equation (3.4), I compute the time-dependent ionization parameter – defined as the dimensionless ratio of the number density of H-ionizing photons to that of hydrogen – at the distance r from the ionizing source,

$$U(t', r) = Q(t')/(4\pi r^2 n_{\rm H} c)\,, \tag{3.5}$$

where I have assumed for simplicity that the effective density $n_{\rm H}$ does not depend on the age t' of the ionizing stars. The dependence of U on t' in the above expression implies that a galaxy containing several stellar generations is modelled as a mix of gas components characterized by different effective ionization parameters. As in CL01, I assume for simplicity in this chapter that galaxies are ionization-bounded.

It is useful to characterize a photoionization model in terms of the ionization parameter at the Strömgren radius, defined by

$$R_S^3(t') = 3Q(t')/(4\pi n_H^2 \epsilon \alpha_B)\,, \tag{3.6}$$

where ϵ is the volume-filling factor of the gas (i.e., the ratio of the volume-averaged hydrogen density to n_H), assumed not to depend on t', and α_B is the case-B hydrogen recombination coefficient corresponding to transitions to excited levels (for information, $\alpha_B \simeq 2.6\,10^{-13}$ for $T_e = 10{,}000\,K$; Aller 1984; Osterbrock & Ferland 2006). The geometry of the model is set by the difference between R_S and the inner radius of the gaseous nebula, r_{in}. For $r_{in} \ll R_S$, the thickness of the ionized shell is of the order of R_S, implying spherical geometry, while for $r_{in} \gtrsim R_S$, the geometry is plane-parallel. I adopt here models with spherical geometry, in which case the ionization parameter at the Strömgren radius, given by (equations 3.5 and 3.6)

$$U_S(t') = \frac{\alpha_B^{2/3}}{3c}\left[\frac{3Q(t')\epsilon^2 n_H}{4\pi}\right]^{1/3}, \tag{3.7}$$

is nearly proportional to the volume-averaged ionization parameter,

$$U_S(t') \approx \langle U\rangle(t')/3\,. \tag{3.8}$$

The above expression is valid for $r_{in} \ll R_S$ and neglects the weak dependence of α_B on r through the electron temperature.

Following CL01, I parametrize models for $T_\lambda^+(t')$ in terms of the zero-age ionization parameter at the Strömgren radius,[2]

$$U_S \equiv U_S(0). \tag{3.9}$$

As noted by CL01, the effective star-cluster mass M_* in equation (3.4) has no influence on the results other than that of imposing a maximum U_S at fixed n_H (equation 3.5). In practice, I adopt values of M_* in the range from 10^4 to $10^7 M_\odot$ for models with ionization parameters in the range from $\log U_S = -4.0$ to -1.0. The exact choice of the inner radius r_{in} also has a negligible influence on the predictions of models parametrized in terms of U_S, for $r_{in} \ll R_S$. As CL01, I set $r_{in} \lesssim 0.01\,$pc to ensure spherical geometry for all models. To evaluate $T_\lambda^+(t')$, I stop the photoionization calculations when the electron density falls below 1 per cent of n_H or if the temperature falls below 100 K.

3.2.3 Interstellar abundances and depletion factors

The chemical composition of the ISM has a primary influence on the transmission function $T_\lambda^+(t')$ of equation (3.3). In this work, I adopt the same metallicity for the ISM, noted Z_{ISM}, as for the ionizing stars, i.e., I set $Z_{ISM}=Z$. A main feature of my model is that I take special care in rigorously parametrizing the abundances of metals and their depletion onto dust grains in the ISM, to be able to model in a self-consistent way the influence of 'gas-phase' and 'interstellar' (i.e., total gas+dust-phase) abundances on the emission-line properties of a star-forming galaxy.

---

[2] In reality, CL01 parametrized their models in terms of the zero-age, volume-averaged ionization parameter $\langle U\rangle(0) \approx 3U_S(0)$.

Interstellar abundances

The interstellar metallicity is the mass fraction of all elements heavier than helium, i.e.

$$Z_{\mathrm{ISM}} = \left(\sum_{Z_i \geq 3} n_i A_i \right) \Bigg/ \left(\sum_{Z_i \geq 1} n_i A_i \right), \tag{3.10}$$

where Z_i, n_i and A_i are, respectively, the atomic number, number density and atomic mass of element i (with $n_1 = n_\mathrm{H}$). For all but a few species, I adopt the solar abundances of chemical elements compiled by Bressan et al. (2012) from the work of Grevesse & Sauval (1998), with updates from Caffau et al. (2010, see table 1 of Bressan et al. 2012). This corresponds to a present-day solar (photospheric) metallicity $Z_\odot = 0.01524$, and a protosolar (i.e. before the effects of diffusion) metallicity $Z_\odot^0 = 0.01774$. After some experimentation, I found that a minimal fine-tuning of the solar abundances of oxygen and nitrogen within the $\sim 1\sigma$ uncertainties quoted by Caffau et al. (2010) provides a slightly better ability for the model to reproduce the observed properties of SDSS galaxies in several optical line-ratio diagrams (defined by the [O II]$\lambda\lambda 3726, 3729$, H$\beta$, [O III]$\lambda 5007$, H$\alpha$, [N II]$\lambda 6584$ and [S II]$\lambda\lambda 6717, 6731$ emission lines; Section 3.3.2). Specifically, I adopt a solar nitrogen abundance 0.15 dex smaller and an oxygen abundance 0.10 dex larger than the mean values quoted in table 5 of Caffau et al. (2010, see also Nieva & Przybilla 2012). For consistency with my assumption $Z_{\mathrm{ISM}} = Z$, I slightly rescale the abundances of all elements heavier than helium (by about -0.04 dex, as inferred using equation 3.10) to keep the same total present-day solar metallicity, $Z_\odot = 0.01524$. Table 3.2 lists the solar abundances adopted in this work for the elements lighter than zinc. For reference, the solar N/O ratio in my model is $(\mathrm{N/O})_\odot = 0.07$.

I also wish to explore the nebular emission from star-forming galaxies with non-solar abundances. For $Z_{\mathrm{ISM}} = Z \neq Z_\odot$, I take the abundances of primary nucleosynthetic products to scale linearly with Z_{ISM} (modulo a small rescaling factor; see below). I adopt special prescriptions for nitrogen and carbon, which are among the most abundant species:[3]

Nitrogen: abundance studies in Galactic and extragalactic H II regions suggest that N has primary and secondary nucleosynthetic components (e.g., Garnett et al., 1995a; Henry, Edmunds & Köppen, 2000; Garnett, 2003). Both components are thought to be synthesised primarily through the conversion of carbon and oxygen during CNO cycles in stars with masses in the range from about 4 to 8 $\mathrm{M}_\odot$. While the production of primary N (in CNO cycles of H burning) does not depend on the initial metallicity of the star, that of secondary N (from CO products of previous stellar generations) is expected to increase with stellar metallicity (essentially CO; see footnote 3). Based on the analysis of several abundance datasets compiled from emission-line studies of individual H II regions in the giant spiral galaxy M101 (Kennicutt, Bresolin & Garnett, 2003) and different types of starburst galaxies (H II, starburst-nucleus and ultraviolet-selected; see the compilation by Mouhcine & Contini, 2002), Groves, Dopita & Sutherland (2004b) find that the abundance of combined primary+secondary nitrogen can be related to

---

[3] Carbon and nitrogen represent ~26 and ~6 per cent, respectively, of all metals by number at solar metallicity. The most abundant element is oxygen (~48 per cent by number), often used as a global metallicity indicator.

that of oxygen through an expression of the type[4]

$$\mathrm{N/H} \approx 0.41\,\mathrm{O/H}\left[10^{-1.6} + 10^{(2.33+\log \mathrm{O/H})}\right], \tag{3.11}$$

where H, N and O correspond to n_1, n_7 and n_8, respectively, in the notation of equation (3.10). I implement the above prescription in my models, after which I rescale the abundances of all elements heavier than He to preserve the same Z_{ISM} (using equation 3.10). It is important to note that equation (3.11), which includes my fine tuning of the solar O and N abundances, provides excellent agreement with the observational constraints on the gas-phase abundances of O and N in nearby H II regions and galaxies originally used by Groves, Dopita & Sutherland (2004b, see references above). I show this in Section 3.2.3 below (Fig. 3.2).

Carbon: The production of C is thought to arise primarily from the triple-α reaction of helium in stars more massive than about $8\,\mathrm{M}_\odot$ (e.g., Maeder, 1992; Prantzos, Vangioni-Flam & Chauveau, 1994; Gustafsson et al., 1999; Henry, Edmunds & Köppen, 2000), although less massive stars also produce and expel carbon (e.g., van den Hoek & Groenewegen, 1997; Marigo, Bressan & Chiosi, 1996, 1998; Henry, Kwitter & Bates, 2000; Marigo, 2002). Observations indicate that the C/O ratio correlates with the O/H ratio in Galactic and extragalactic H II regions as well as Milky-Way stars, presumably because of the dependence of the carbon yields of massive stars on metallicity (e.g., Garnett et al., 1995a, 1999; Gustafsson et al., 1999; Henry, Edmunds & Köppen, 2000). Intriguingly, this trend appears to turn over at the lowest metallicities, where the C/O ratio increases again (e.g., Akerman et al., 2004). The difficulty of characterizing the dependence of carbon production on metallicity has resulted in the secondary component to be either ignored (e.g., CL01, Kewley & Dopita 2002) or assigned a specific dependence on the O/H ratio (e.g., Dopita et al., 2013) in previous models of nebular emission from H II regions and galaxies. In my model, I prefer to account for the uncertainties in this component by keeping the C/O ratio (i.e., n_6/n_8 in the notation of equation 3.10) as an adjustable parameter at fixed interstellar metallicity Z_{ISM} (see Section 3.3.1 for details). Once a C/O ratio is adopted (in practice, by adjusting n_6 at fixed n_8), I rescale the abundances of all elements heavier than He to preserve the same Z_{ISM} (using equation 3.10). For reference, the solar C/O ratio in my model is $(\mathrm{C/O})_\odot = 0.44$.

To complete the parametrization of interstellar abundances, I must also specify that of helium. I follow Bressan et al. (2012) and write the He abundance by mass ($\propto n_2 A_2$; equation 3.10) as

$$Y = Y_{\mathrm{P}} + (Y^0_\odot - Y_{\mathrm{P}})\,Z_{\text{ISM}}/Z^0_\odot = 0.2485 + 1.7756\,Z_{\text{ISM}}, \tag{3.12}$$

where $Y_{\mathrm{P}} = 0.2485$ is the primordial He abundance and $Y^0_\odot = 0.28$ the protosolar one. This formula enables us to compute the helium mass fraction Y at any given metallicity Z_{ISM}. The hydrogen mass fraction is then simply $X = 1 - Y - Z_{\text{ISM}}$.

---

[4] I have introduced in equation (3.11) a scaling factor of 0.41 to account for the difference in solar abundances adopted here and in Groves, Dopita & Sutherland (2004b).

Z_i[a]	Element	$\log(n_i/n_\mathrm{H})$[b]	$(1 - f^i_\mathrm{dpl})$[c]
2	He	−1.01	1
3	Li	−10.99	0.16
4	Be	−10.63	0.6
5	B	−9.47	0.13
6	C	−3.53	0.5
7	N	−4.32	1
8	O	−3.17	0.7
9	F	−7.47	0.3
10	Ne	−4.01	1
11	Na	−5.70	0.25
12	Mg	−4.45	0.2
13	Al	−5.56	0.02
14	Si	−4.48	0.1
15	P	−6.57	0.25
16	S	−4.87	1
17	Cl	−6.53	0.5
18	Ar	−5.63	1
19	K	−6.92	0.3
20	Ca	−5.67	0.003
21	Sc	−8.86	0.005
22	Ti	−7.01	0.008
23	V	−8.03	0.006
24	Cr	−6.36	0.006
25	Mn	−6.64	0.05
26	Fe	−4.51	0.01
27	Co	−7.11	0.01
28	Ni	−5.78	0.04
29	Cu	−7.82	0.1
30	Zn	−7.43	0.25

[a] Atomic number

[b] Abundance by number relative to hydrogen

[c] f^i_dpl is the fraction of element i depleted onto dust grains (the non-refractory elements He, N, Ne, S and Ar have $f^i_\mathrm{dpl} = 0$)

Table 3.2: Interstellar abundances and depletion factors of the 30 lightest chemical elements for $Z_\mathrm{ISM} = Z_\odot = 0.01524$ and $\xi_\mathrm{d} = \xi_{\mathrm{d}\odot} = 0.36$ (see text for details).

Depletion factors

In my model, I account for the depletion of refractory metals onto dust grains. Observational determinations of depletion factors in Galactic interstellar clouds show a large dispersion depending on local conditions (e.g., Savage & Sembach, 1996). For simplicity, I adopt the default ISM depletion factors of CLOUDY for most elements, with updates from Groves, Dopita & Sutherland (2004b, see their Table 1) for C, Na, Al, Si, Cl, Ca and Ni. By analogy with my fine-tuning of the N and O abundances in Section 3.2.3, I slightly adjust the fraction of oxygen depleted from the gas phase (from 40 to 30 per cent for $\xi_\mathrm{d} = \xi_{\mathrm{d}\odot}$) to improve the model agreement with observed properties of SDSS galaxies in several optical line-ratio diagrams (Section 3.3.1). The depletion factors adopted in this work are listed in Table 3.2 for the elements lighter than zinc.

The elements depleted from the gas phase make up the grains, for which in CLOUDY I adopt a standard Mathis, Rumpl & Nordsieck (1977) size distribution and optical properties from Martin & Rouleau (1991). These grains influence radiative transfer via absorption and scattering of the incident radiation, radiation pressure, collisional cooling and photoelectric heating of the gas (see, e.g., Shields & Kennicutt, 1995; Dopita et al., 2002; Groves, Dopita & Sutherland, 2004a, for a description of the influence of these effects on nebular emission). In addition, the depletion of important coolants from the gas phase reduces the efficiency of gas cooling through infrared fine-structure transitions, which causes the electron temperature to rise, thereby increasing cooling through the more energetic optical transitions.

Following CL01, I explore the influence of metal depletion on the nebular emission from star-forming galaxies by means of the dust-to-metal mass ratio parameter, noted ξ_d. For $Z_\mathrm{ISM} = Z_\odot$, the values in Table 3.2 imply that 36 per cent by mass of all metals are in the solid phase, i.e., $\xi_{\mathrm{d}\odot} = 0.36$. To compute the depletion factor f_dpl^i of a given refractory element i for other dust-to-metal mass ratios in the range $0 \leq \xi_\mathrm{d} \leq 1$, I note that this must satisfy $f_\mathrm{dpl}^i = 0$ and 1 for $\xi_\mathrm{d} = 0$ and 1, respectively. I use these boundary conditions and the data in Table 3.2 to interpolate linearly f_dpl^i as a function of ξ_d for $\xi_\mathrm{d} \neq \xi_{\mathrm{d}\odot}$.

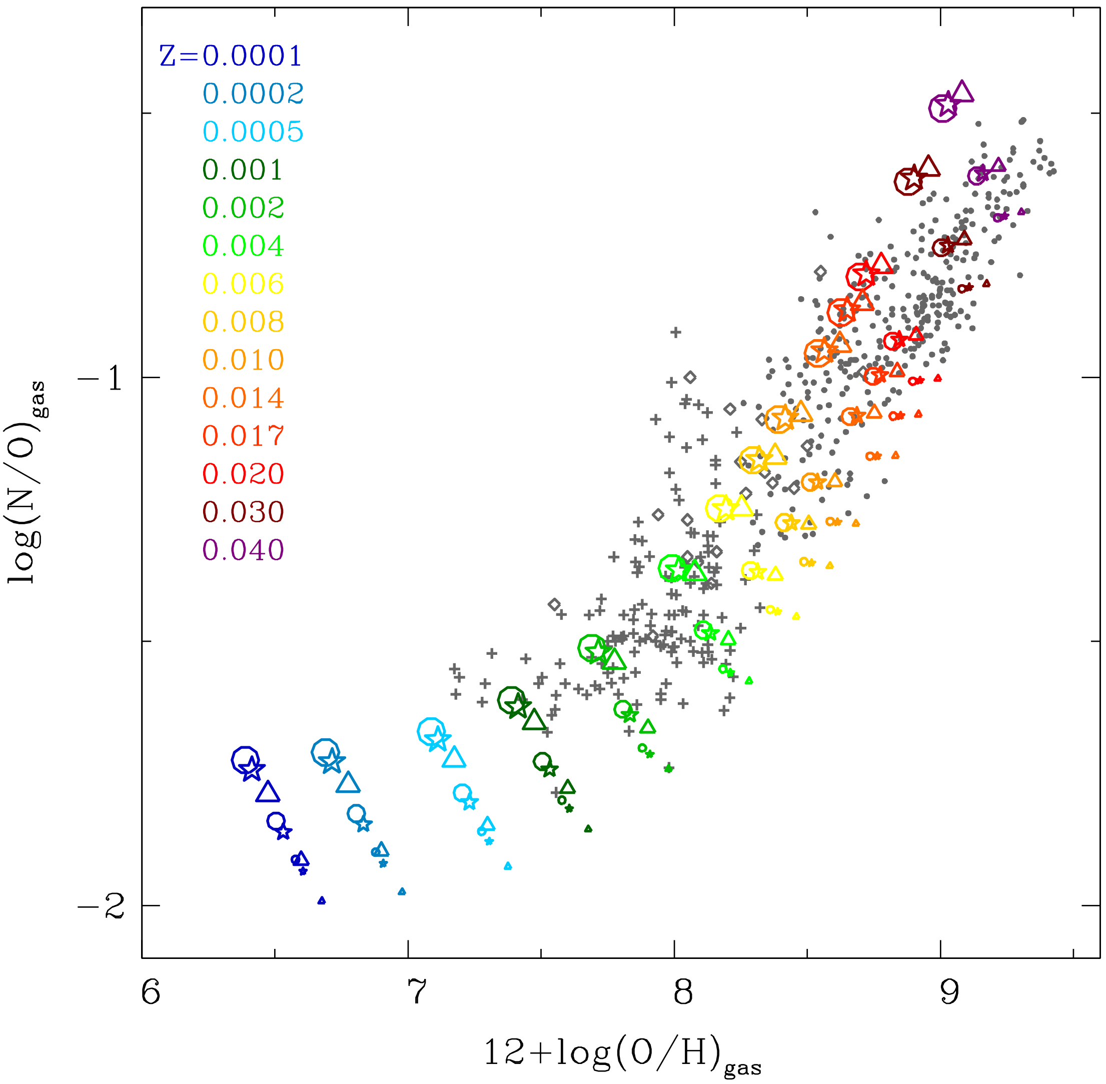

Figure 3.2: log $(\mathrm{N/O})_{\mathrm{gas}}$ as a function of 12 + log $(\mathrm{O/H})_{\mathrm{gas}}$, for models with interstellar metallicity Z_{ISM} = 0.0001, 0.0002, 0.0005, 0.001, 0.002, 0.004, 0.006, 0.008, 0.010, 0.014, 0.017, 0.020, 0.030 and 0.040 (colour-coded as indicated), carbon-to-oxygen abundance ratio C/O = 0.1 (triangle), 1.0 (star) and 1.4 (circle) times $(\mathrm{C/O})_{\odot}$, and dust-to-metal mass ratio ξ_{d} = 0.1, 0.3 and 0.5 (in order of increasing symbol size). The data (identical to those in fig. 2 of Groves, Dopita & Sutherland 2004b) are abundance datasets compiled from emission-line studies of individual H II regions in the giant spiral galaxy M101 (Kennicutt, Bresolin & Garnett, 2003, open diamonds) and different types of starburst galaxies (H II [crosses] and starburst-nucleus [dots]; see also Mouhcine & Contini 2002).

It is instructive to examine the differences in gas-phase oxygen abundance, $(\mathrm{O/H})_{\mathrm{gas}}$, corresponding to different plausible values of ξ_{d} at fixed interstellar metallicity Z_{ISM} in this context. Table 3.3 lists $(\mathrm{O/H})_{\mathrm{gas}}$ for the 14 metallicities at which stellar population models are available in the range $0.0001 \leq Z \leq 0.040$ (and for the present-day solar metallicity $Z_{\odot}$=0.01524; Section 3.2.1), for 3 dust-to-metal mass ratios, $\xi_{\mathrm{d}} = 0.1$, 0.3 and 0.5, and fixed $(\mathrm{C/O})_{\odot}$ ratio. The gas-phase oxygen abundance can change by typically 0.2 dex depending on the adopted ξ_{d}, the difference with the interstellar (gas+dust-phase) abundance, O/H, reaching up to 0.25 dex for $Z_{\mathrm{ISM}} = Z_{\odot}$, for example. Fig. 3.2 shows $(\mathrm{N/O})_{\mathrm{gas}}$ as a function $(\mathrm{O/H})_{\mathrm{gas}}$ for the 14 metallicities and 3 dust-to-metal mass ratios in Table 3.3, and for 3 values of the C/O ratio, 0.1, 1.0 and 1.4 times $(\mathrm{C/O})_{\odot}$. The models compare well with observational constraints on these quantities in nearby H II regions and star-forming galaxies, also shown on the figure (the data in Fig. 3.2 are the same as those in fig. 2 of Groves, Dopita & Sutherland 2004b). For reference, for solar values of the metallicity, $Z_{\odot}$, dust-to-metal mass ratio, $\xi_{\mathrm{d}\odot}$, and C/O ratio, $(\mathrm{C/O})_{\odot}$, the gas-phase abundances are $12 + \log(\mathrm{O/H})_{\odot,\mathrm{gas}} = 8.68$, $(\mathrm{N/O})_{\odot,\mathrm{gas}} = 0.10$ and $(\mathrm{C/O})_{\odot,\mathrm{gas}} = 0.31$. The large spread in $(\mathrm{N/O})_{\mathrm{gas}}$ and $(\mathrm{O/H})_{\mathrm{gas}}$ for models with different ξ_{d} and C/O at fixed metallicity in Fig. 3.2 emphasizes the importance of distinguishing gas-phase from interstellar metallicity when studying the metal content of star-forming galaxies.

Z_{ISM}	$12 + \log \mathrm{O/H}$	$12 + \log(\mathrm{O/H})_{\mathrm{gas}}$		
		ξ_{d}=0.1	ξ_{d}=0.3	ξ_{d}=0.5
0.0001	6.64	6.61	6.53	6.41
0.0002	6.94	6.91	6.83	6.71
0.0005	7.34	7.30	7.23	7.11
0.001	7.64	7.61	7.53	7.41
0.002	7.94	7.91	7.83	7.71
0.004	8.24	8.21	8.14	8.02
0.006	8.42	8.39	8.31	8.19
0.008	8.55	8.52	8.44	8.32
0.010	8.65	8.61	8.54	8.42
0.014	8.80	8.76	8.69	8.56
0.01524 ($Z_{\odot}$)	8.83	8.80	8.71	8.58
0.017	8.88	8.85	8.77	8.65
0.020	8.96	8.92	8.85	8.72
0.030	9.14	9.11	9.03	8.90
0.040	9.28	9.24	9.16	9.03

Table 3.3: Oxygen abundances for interstellar metallicities Z_{ISM} corresponding to the 14 metallicities at which stellar population models are available in the range $0.0001 \leq Z \leq 0.040$ (and for the present-day solar metallicity $Z_{\odot}$=0.01524), assuming $\mathrm{C/O} = (\mathrm{C/O})_{\odot}$. The second column lists the total interstellar (i.e. gas+dust-phase) oxygen abundance, $12 + \log \mathrm{O/H}$, while the three rightmost columns indicate the gas-phase oxygen abundances, $12 + \log(\mathrm{O/H})_{\mathrm{gas}}$, corresponding to three choices of the dust-to-metal mass ratio, $\xi_{\mathrm{d}} = 0.1$, 0.3 and 0.5.

3.2.4 Dust in ISM

In addition to the presence of dust grains in H II regions – taken into account by applying the depletion factors described above in Section 3.2.3 – I also include the absorption by dust in the ISM, more precisely in birth clouds around H II regions and in the diffuse ISM within the galaxy. Dust in the diffuse ISM contributes to the absorption of starlight emanating from ionized regions in a galaxy through the transmission function $T^0_\lambda(t,t')$ in equation (3.1). In practice, I use the 'quasi-universal' prescription by Chevallard et al. (2013, see also section 2.5 of Chevallard & Charlot 2016) to express the transmission function as a function of stellar age t' and galaxy inclination θ, while accounting for the fact that young stars in their birth clouds are typically more attenuated than older stars in galaxies (e.g. Silva et al., 1998; Charlot & Fall, 2000).

More precisely, I assume for simplicity that the dust attenuation optical depth of a galaxy depends only on the stellar age t' of the SSP,

$$T^0_\lambda(t,t') = T^0_\lambda(t')\,. \tag{3.13}$$

To compute this transmission function of the neutral gas $T^0_\lambda(t')$, I appeal to the two-component angle-averaged model of Charlot & Fall (2000). This model takes into account the fact that radiation from young stars is more attenuated than that from older stars. Indeed, as stars are born in giant molecular clouds, which dissipate on a timescale of about ~ 10Myr, stars younger than this limit are attenuated by dust both in stellar birth clouds and in the diffuse ISM, while older stars are attenuated only by dust in the diffuse ISM, as illustrated by Fig. 3.3.

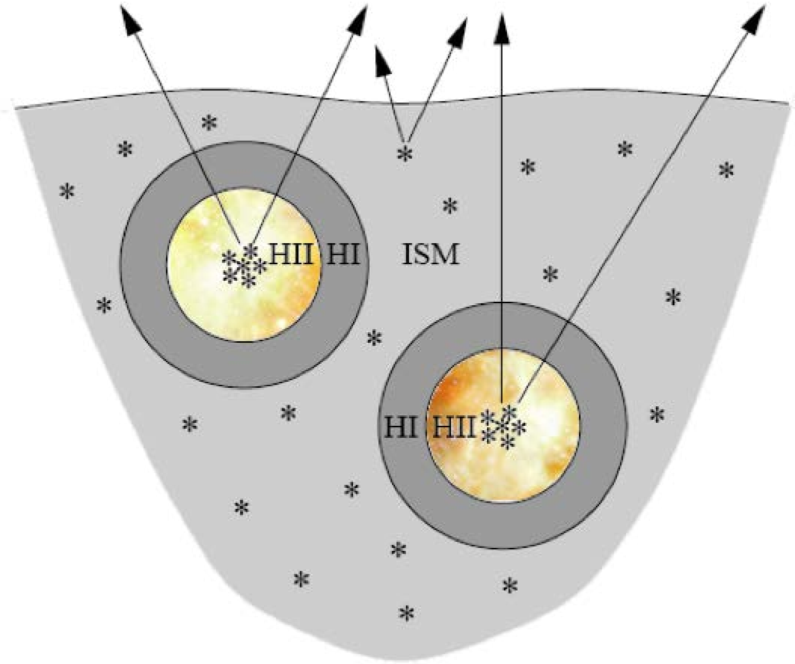

Figure 3.3: Schematic representation of attenuation by dust in the neutral ISM: newly born stars suffer extra attenuation in their birth clouds (Charlot & Fall, 2000).

We thus distinguish:

$$T_\lambda^0(t') = \begin{cases} \exp\,[-(\hat{\tau}_\lambda^{\mathrm{BC}} + \hat{\tau}_\lambda^{\mathrm{ISM}})] & \text{for} \quad t' \leqslant 10\,\mathrm{Myr}, \\ \exp\,[-\hat{\tau}_\lambda^{\mathrm{ISM}}] & \text{for} \quad t' > 10\,\mathrm{Myr}, \end{cases} \tag{3.14}$$

where $\hat{\tau}_\lambda(\mathrm{t}')$ is the "effective absorption" optical depth (BC for birth clouds and ISM for the ambient medium) affecting a stellar generation of age t'. This is the average attenuation affecting photons emitted in all directions by stars in all locations throughout the galaxy, which includes the effect of scattering on the path lengths of photons. This simple model for the absorption of photons relies on two main parameters: the total V-band attenuation optical depth of the dust $\hat{\tau}_V$, which includes contributions by the birth clouds and the diffuse ISM, $\hat{\tau}_V = \hat{\tau}_V^{\mathrm{ISM}} + \hat{\tau}_V^{\mathrm{BC}} = \hat{\tau}_V^{\mathrm{ISM}} + \hat{\tau}_V^{\mathrm{HI}} + \hat{\tau}_V^{\mathrm{HII}}$; and the fraction of the total attenuation optical depth contributed by dust in diffuse ISM, $\mu = \hat{\tau}_V^{\mathrm{ISM}}/\hat{\tau}_V$. For the wavelength dependence of $\hat{\tau}_\lambda^{\mathrm{BC}}(t')$ and $\hat{\tau}_\lambda^{\mathrm{ISM}}(t')$, I follow the prescription of Chevallard et al. (2013),

$$\hat{\tau}_\lambda^{\mathrm{BC}} = (1-\mu)\hat{\tau}_V\,(\lambda/5500\,)^{-1.3}\,, \tag{3.15}$$

$$\hat{\tau}_\lambda^{\mathrm{ISM}} = \mu\hat{\tau}_V\,(\lambda/5500\,)^{-n_\lambda}\,. \tag{3.16}$$

where the exponent n_λ is a linear function of wavelength and total V-band attenuation optical depth of the dust $\hat{\tau}_V$.

I do not present models attenuated by dust in the neutral ISM in this chapter, in which I focus on emission-line ratios at optical and ultraviolet wavelengths. However, it will be particularly important to include this component when computing line equivalent widths and the combined emission from stars and gas, which is the reason why my modelling incorporates this possibility. We shall see in Chapter 5 that we have already used the prescription outlined above in published analyses of the combined line and continuum emission of distant galaxies (Stark et al., 2014, 2015a,b, 2016).

3.3 Optical emission-line properties

I have built a comprehensive grid of models spanning wide ranges of interstellar parameters, for stellar populations with a Chabrier (2003) stellar IMF with upper mass cutoffs 100 and 300 $\mathrm{M}_\odot$. I show that these models can reproduce available observations of star-forming galaxies in several line-ratio diagrams at optical ([O II]$\lambda\lambda$3726, 3729, Hβ, [O III]λ5007, Hα, [N II]λ6584, [S II]$\lambda\lambda$6717, 6731) and ultraviolet (N V λ1240, C IV $\lambda\lambda$1548, 1551, He II λ1640, O III]λ1666, [C III]λ1907+C III]λ1909, [Si III]λ1883+Si III]λ1892) wavelengths.

3.3.1 Grid of photoionization models

My motivation is to build a grid of photoionization models that should be adequate for the purpose of investigating the emission-line properties of star-forming galaxies at all cosmic epochs. To this end, I adopt the following sampling of the main adjustable model parameters described in Section 3.2. I emphasize that these must be regarded as effective parameters describing the ensemble of H II regions and the diffused gas ionized by young stars in a galaxy:

Interstellar metallicity, Z_{ISM}: I consider 14 values of Z_{ISM} between 0.6 per cent of and 2.6 times solar, corresponding to metallicities at which stellar population models are available (Section 3.2.1). These are Z_{ISM} = 0.0001, 0.0002, 0.0005, 0.001, 0.002, 0.004, 0.006, 0.008, 0.010, 0.014, 0.017, 0.020, 0.030 and 0.040.

Zero-age ionization parameter at the Strömgren radius, U_S: I compute models for 7 values of U_S logarithmically spaced in the range $-4 \leq \log U_S \leq -1$, in bins of 0.5 dex.

Dust-to-metal mass ratio, ξ_d: I adopt 3 choices for the dust-to-metal mass ratio, $\xi_d = 0.1$, 0.3 and 0.5 ($\xi_{d\odot}$=0.36).

Carbon-to-oxygen abundance ratio, C/O: I consider 9 logarithmically spaced values of the interstellar C/O ratio, corresponding to factors of 0.10, 0.14, 0.20, 0.27, 0.38, 0.52, 0.72, 1.00 and 1.40 times the solar value, $(\mathrm{C/O})_\odot$=0.44.

Hydrogen gas density, n_H: I compute models for 4 hydrogen densities of the ionized gas, $n_H = 10$, 10^2, 10^3 and $10^4\mathrm{cm}^{-3}$. These span most of the range of observed electronic densities in extragalactic H II regions (e.g., Hunt & Hirashita, 2009).

Upper mass cutoff of the IMF, m_{up}: I adopt the Galactic-disc IMF of Chabrier (2003), for which I fix the lower mass cutoff at $m_L = 0.1\,\mathrm{M}_\odot$ and consider 2 values of the upper mass cutoff, $m_{up} = 100$ and $300\,\mathrm{M}_\odot$.

Parameter	Sampled values
$Z_{\rm ISM}$	0.0001, 0.0002, 0.0005, 0.001, 0.002, 0.004, 0.006, 0.008, 0.010, 0.014, 0.017, 0.020, 0.030, 0.040
$\log U_S$	−1.0, −1.5, −2.0, −2.5, −3.0, −3.5, −4.0
ξ_d	0.1, 0.3, 0.5
$\log(n_H/\mathrm{cm}^{-3})$	1, 2, 3, 4
$(\mathrm{C/O})/(\mathrm{C/O})_\odot$	0.10, 0.14, 0.20, 0.27, 0.38, 0.52, 0.72, 1.00, 1.40
$m_{up}/\mathrm{M}_\odot$	100, 300

Table 3.4: Grid sampling of the main adjustable parameters of the photoionization model of star-forming galaxies described in Section 3.2 (see Section 3.3.1 for details).

Table 3.4 summarizes the above sampling of the main adjustable model parameters, which leads to a total of 21,168 photoionization models, each computed at 90 stellar population ages t' between 0 and 10 Myr (equation 3.3). The photoionization models are available electronically from `http://www.iap.fr/neogal/models.html`; I provide details on the content of these files in Appendix A. In the remainder of this chapter, I compute all predictions of nebular emission from star-forming galaxies assuming star formation at a constant rate, $\psi(t-t') = 1\,\mathrm{M}_\odot\mathrm{yr}^{-1}$ (equation 3.1), for 100 Myr. Since most ionizing photons are released during the first 10 Myr of evolution of a single stellar generation (Section 3.2.2), assuming a constant star formation rate for 100 Myr ensures that a steady population of H II regions is established in the model galaxy. In this context, the age of 100 Myr should be interpreted as the effective age of the most recent episode of star formation in the galaxy. Finally, I assume for simplicity that all stars in a given galaxy have the same metallicity, i.e., I write

$$S_\lambda[t', Z(t-t')] \equiv S_\lambda(t', Z) \tag{3.17}$$

in equation (3.1).

3.3.2 Comparison with observations

In Fig. 3.4, I compare the predictions of a subset of the grid of photoionization models described in Section 3.3.1 with high-quality observations of emission-line ratios in the spectra of 28,075 low-redshift ($0.04 \leq z \leq 0.2$) star-forming galaxies from the Sloan Digital Sky Survey Data Release 7 (SDSS DR7 Abazajian & Survey, 2008). The models span full ranges of metallicity, $Z_{\rm ISM}$, ionization parameter, $U_{\rm S}$, and dust-to-metal mass ratio, $\xi_{\rm d}$, for fixed gas density, $n_{\rm H} = 100\,{\rm cm}^{-3}$, carbon-to-oxygen ratio, $({\rm C/O})_\odot = 0.44$, and IMF upper mass cutoff, $m_{\rm up} = 100\,{\rm M}_\odot$. The observational sample was assembled by Pacifici et al. (2012), who selected SDSS-DR7 galaxies with signal-to-noise ratio greater than 10 in all optical emission lines used to construct the data plotted in Fig. 3.4, i.e., [O II]$\lambda\lambda$3726, 3729 (hereafter [O II]λ3727), Hβ, [O III]λ5007, Hα, [N II]λ6584 and [S II]$\lambda\lambda$6717, 6731. In doing so, Pacifici et al. (2012) excluded galaxies for which nebular emission could be contaminated by an AGN, according to the conservative criterion of Kauffmann et al. 2003 in the standard line-diagnostic diagram of Baldwin, Phillips & Terlevich (1981, see also Veilleux & Osterbrock 1987) defined by the [O III]λ5007/Hβ and [N II]λ6584/Hα ratios (Fig. 3.4a).

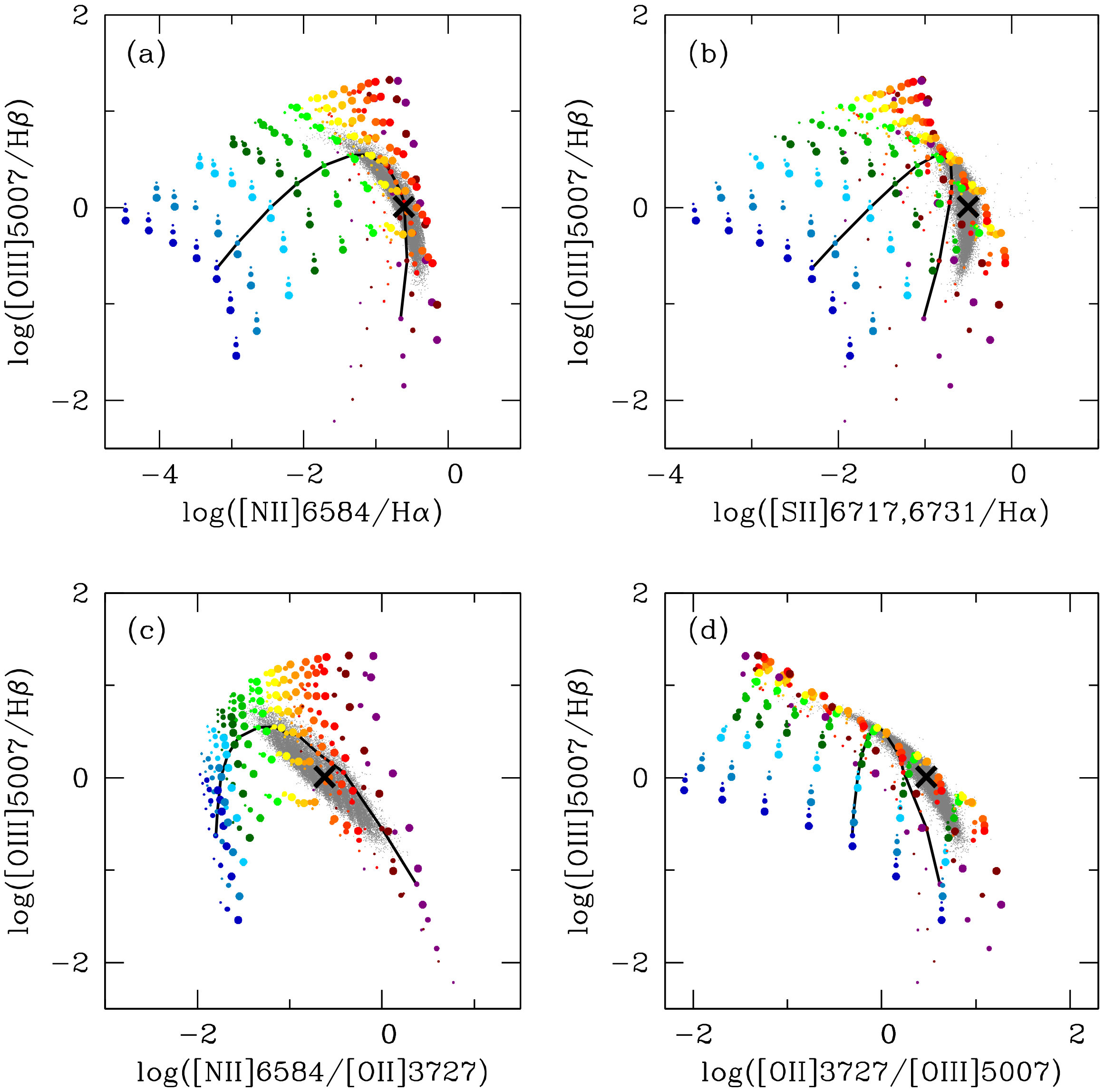

Figure 3.4: Luminosity ratios of prominent optical emission lines predicted by the photoionization models described in Section 3.2: (a) [O III]λ5007/Hβ against [N II]/Hα; (b) [O III]λ5007/Hβ against [S II]$\lambda\lambda$6717, 6731/Hα; (c) [O III]λ5007/Hβ against [N II]λ6584/[O II]λ3727; and (d) [O III]λ5007/Hβ against [O II]λ3727/[O III]λ5007. The models assume constant star formation over the past 100 Myr and fixed hydrogen density, $n_{\rm H}$ = 100 cm^{-3}, carbon-to-oxygen ratio, (C/O)$_\odot$=0.44, and IMF upper mass cutoff, $m_{\rm up}$ = 100 M$_\odot$. They are shown for 14 interstellar metallicities in the range $0.0001 \le Z_{\rm ISM} \le 0.040$ (colour-coded as in Fig. 3.2; see Table 3.3), 7 zero-age ionization parameters in the range $-4 \le \log U_{\rm S} \le -1$, in bins of 0.5 dex (in order of increasing [O III]/Hβ ratio at fixed metallicity), and 3 dust-to-metal mass ratios $\xi_{\rm d}$ = 0.1, 0.3 and 0.5 (in order of increasing symbol size). In each panel, a line links models with $\log U_{\rm S} = -3.0$ at all metallicities, while the black cross shows the 'standard' model defined in Section 3.3.2. The grey dots show high-quality observations of star-forming galaxies from the SDSS DR7, corrected for attenuation by dust as described in Brinchmann et al. (2004).

Fig. 3.4 shows that the model grid considered here succeeds in accounting for the observed properties of SDSS star-forming galaxies. Specifically, the emission-line properties of these galaxies are well reproduced by models with metallicities $Z_{\rm ISM} \gtrsim 0.004$, consistent with the results from previous studies (e.g., Brinchmann et al., 2004; Tremonti et al., 2004; Pacifici et al., 2012). Lower-metallicity galaxies are rare in the SDSS, but models with $0.0001 \lesssim Z_{\rm ISM} \lesssim 0.004$ will be crucial to interpret emission-line observations of chemically young galaxies at high redshifts, as already shown by Stark et al. (2014, 2015a, see also Section 3.4 below). Fig. 3.4 also confirms the usual finding that, observationally, nebular emission in metal-poor (metal-rich) galaxies seems to be associated with high (low) ionization parameter Brinchmann et al. (e.g., CL01; 2004).

It is important to stress that a same model can account simultaneously for the properties of a given galaxy in all panels of Fig. 3.4. I illustrate this by considering a 'standard' model accounting roughly for the typical (i.e. median) properties of the observational sample in all panels (black cross in Fig. 3.4). This standard model has the following parameters:

- $Z_{\rm ISM} = 0.014$
- $\xi_{\rm d} = 0.28$
- $\log U_{\rm S} = -3.4$
- $n_{\rm H} = 10^2\,{\rm cm}^{-3}$
- $\mathrm{C/O} = (\mathrm{C/O})_\odot = 0.44$
- $m_{\rm up} = 100\,{\rm M}_\odot$.

I note that the metallicity $Z_{\rm ISM} = 0.014$ is that closest to the present-day solar metallicity ($Z_\odot = 0.01524$) in Table 3.4. For reference, the standard model has a gas-phase oxygen abundance $12 + \log\,(\mathrm{O/H})_{\rm gas} = 8.70$, while the interstellar oxygen abundance is that corresponding to the metallicity $Z_{\rm ISM} = 0.014$ in Table 3.3, i.e., $12 + \log \mathrm{O/H} = 8.80$.

3.3.3 Influence of model parameters on optical emission-line properties

I now briefly describe the influence of the main adjustable parameters of my model on the predicted optical emission-line properties of star-forming galaxies (see also CL01). In this description, I explore the effect of varying a single parameter at a time, keeping the other main adjustable parameters fixed:

Interstellar metallicity. Fig. 3.4 (solid line) shows that increasing $Z_{\rm ISM}$ at fixed other parameters makes the [O III]/Hβ ratio rise to a maximum (around $Z_{\rm ISM} \approx 0.006$) and then decrease again. This is because gas cooling through collisionally excited optical transitions first increases as the abundance of metal coolants rises, until the electronic temperature drops low enough for cooling to become dominated by infrared fine-structure transitions (e.g., Spitzer, 1978). Efficient fine-structure cooling by doubly-ionized species in the inner parts of H II regions also makes the [O II]/[O III] ratio rise in Fig. 3.4d (Stasińska, 1980). The [S II]/Hα ratio behaves in a similar way to the [O III]/Hβ ratio (Fig. 3.4b). In contrast, my inclusion of secondary nitrogen production causes the [N II]/Hα and [N II]/[O II] to rise steadily with metallicity (Figs 3.4a and 3.4c). I note that, because of my adoption of the same metallicity for the stars and the ISM, lowering

$Z_{\rm ISM}$ also leads to a harder ionizing spectrum (since metal-poor stars evolve at higher effective temperatures than metal-rich ones; e.g., fig. 15 of Bressan et al. 2012). This has little influence on the results of Fig. 3.4, which are largely dominated by the other effects described above.

Zero-age ionization parameter at the Strömgren radius. Fig. 3.4 shows that increasing $U_{\rm S}$ at fixed other parameters makes the [O III]/Hβ ratio rise and the [O II]/[O III], [N II]/Hα and [S II]/Hα ratios drop. This is because increasing $U_{\rm S}$ at fixed density $n_{\rm H}$ and ionizing photon rate $Q(0)$ in my model amounts to increasing the effective gas filling factor ϵ (equation 3.7 of Section 3.2.2), causing the H II regions to be more compact and concentrated close to the ionizing star clusters. This strengthens the high-ionization [O III]λ5007 line relative to the lower-ionization [O II]λ3727, [N II]λ6584 and [S II]$\lambda\lambda$6717, 6731 lines.

Dust-to-metal mass ratio. The effects of changes in $\xi_{\rm d}$ at fixed other parameters are shown in Fig. 3.5. For clarity, I plot models for only a subset of 4 interstellar metallicities and 3 associated zero-age ionization parameters (using the dependence of $U_{\rm S}$ on $Z_{\rm ISM}$ identified by Carton et al., in preparation; see equation 4.2 of Chevallard & Charlot 2016). Increasing $\xi_{\rm d}$ depletes metal coolants from the gas phase. The electronic temperature increases, as does cooling through collisionally excited optical transitions (e.g. Shields & Kennicutt, 1995). The implied rise in [N II]/Hα and [S II]/Hα ratios is significantly stronger than that in [O III]/Hβ ratio (Figs 3.5a and 3.5b), because oxygen is a refractory element strongly depleted from the gas-phase (making the [O III]/Hβ ratio drop as $\xi_{\rm d}$ increases), while S and N are both non-refractory elements (Table 3.2). Fig. 3.5 further shows that, not surprisingly, the effect changing $\xi_{\rm d}$ is more pronounced at high than at low $Z_{\rm ISM}$.

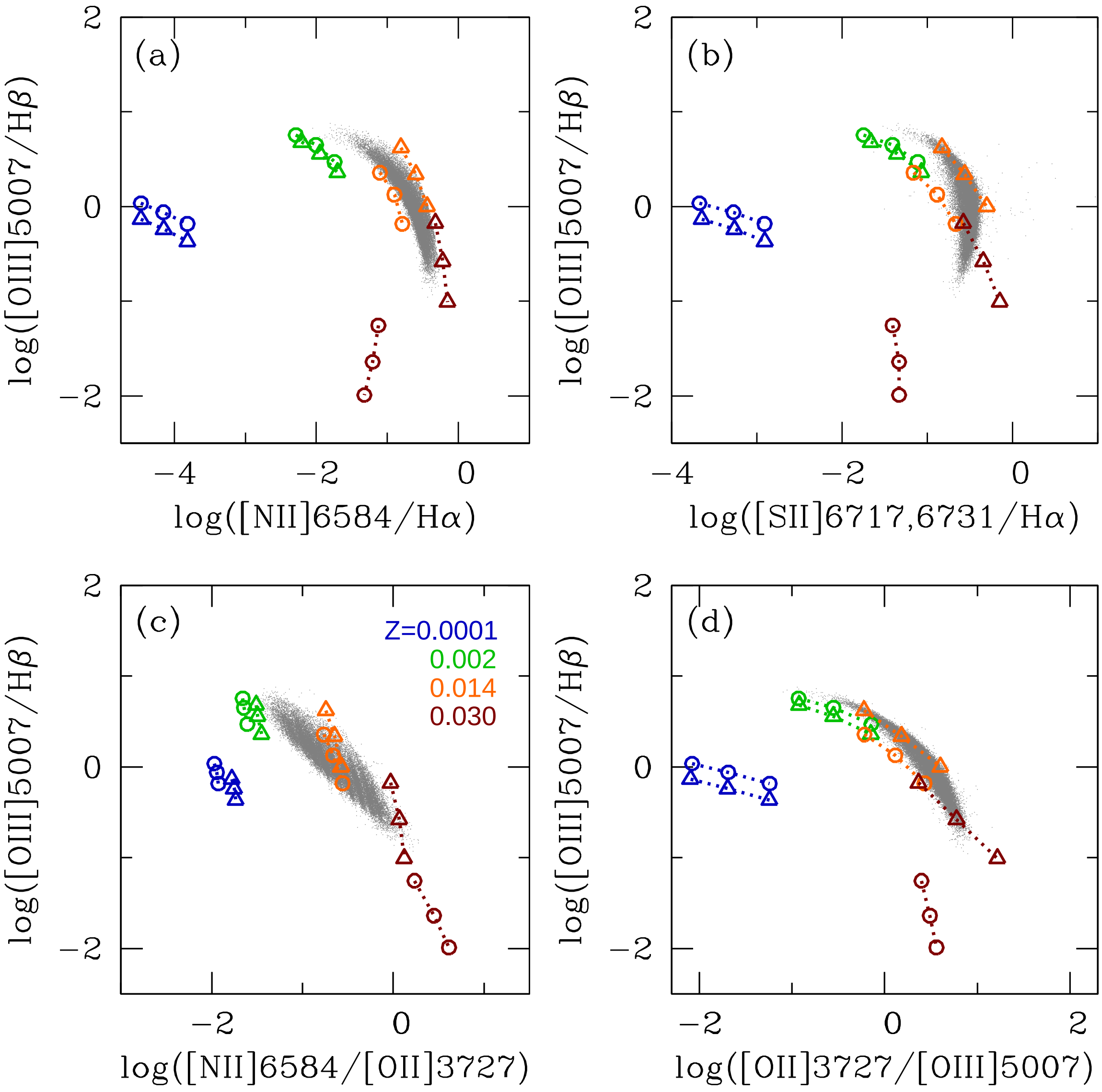

Figure 3.5: Same as Fig. 3.4, but for a subset of interstellar metallicities (colour-coded as indicated) and associated zero-age ionization parameters (using the dependence of U_{S} on Z_{ISM} identified by Carton et al., in preparation; see equation 4.2 of Chevallard & Charlot 2016): $Z_{\mathrm{ISM}} = 0.0001$ (blue) for $\log U_{\mathrm{S}} = -1.0$, -1.5 and -2.0 (in order of increasing [O III]/Hβ ratio and connected by a line); $Z_{\mathrm{ISM}} = 0.002$ (green) for $\log U_{\mathrm{S}} = -2.0$, -2.5 and -3.0; $Z_{\mathrm{ISM}} = 0.014$ (orange) for $\log U_{\mathrm{S}} = -2.5$, -3.0 and -3.5; and $Z_{\mathrm{ISM}} = 0.030$ (maroon) for $\log U_{\mathrm{S}} = -3.0$, -3.5 and -4.0. In each panel, models are shown for two different dust-to-metal mass ratios, $\xi_{\mathrm{d}} = 0.1$ (circles) and 0.5 (triangles).

Carbon-to-oxygen abundance ratio. In my model, increasing the C/O ratio at fixed other parameters amounts to increasing the abundance of carbon and decreasing the abundances of all other heavy elements to maintain the same $Z_{\rm ISM}$ (Section 3.2.3). As Fig. 3.6 shows, therefore, the effect of raising the C/O ratio on emission-line ratios involving N, O and S transitions is similar to that of lowering the interstellar metallicity $Z_{\rm ISM}$ (shown by the solid line in Fig. 3.4).

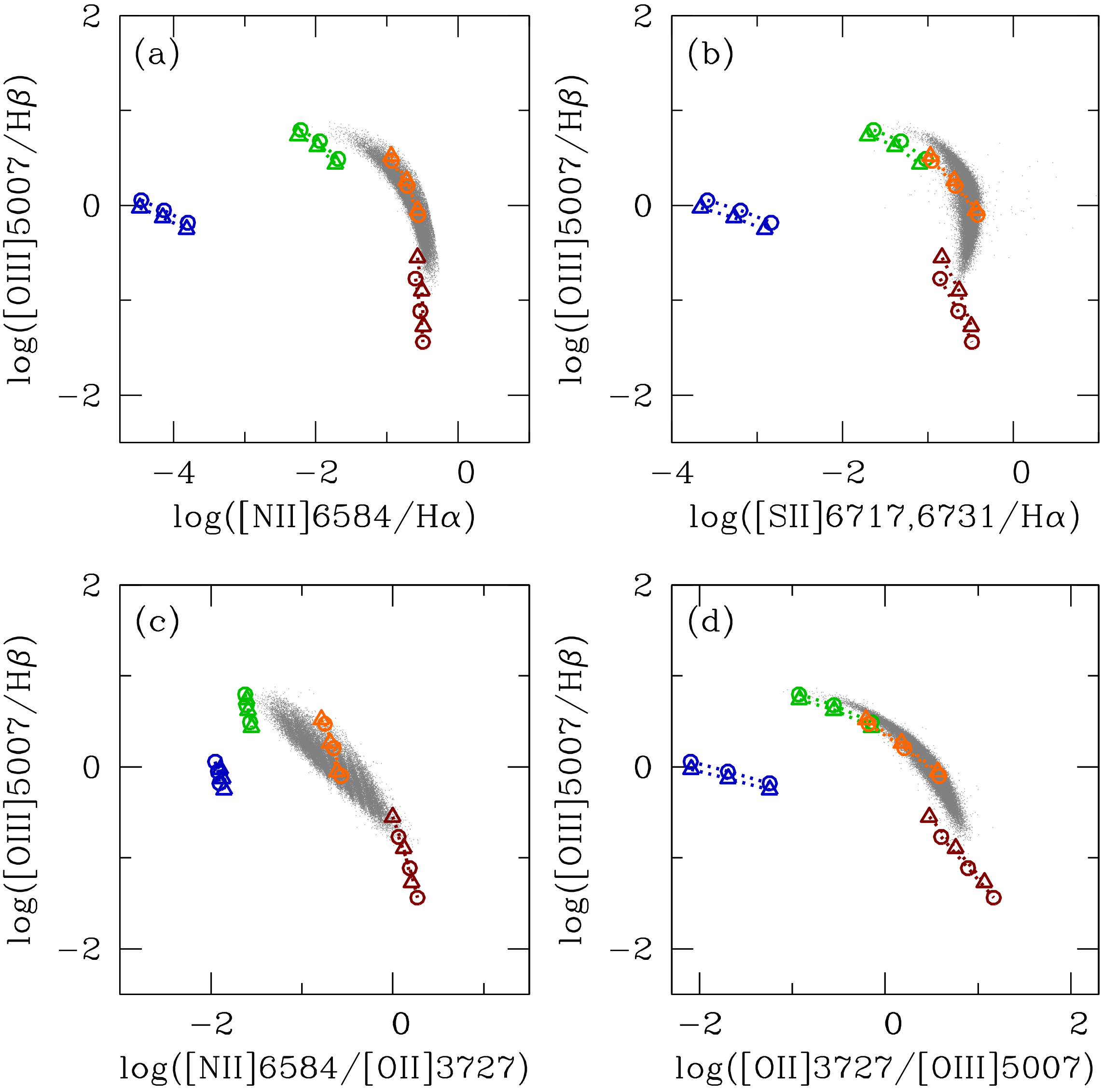

Figure 3.6: Same as Fig. 3.5, but for models with two different carbon-to-oxygen ratios, C/O = 0.1 (circles) and 1.4 (triangles) times $(\mathrm{C/O})_\odot$.

Hydrogen gas density. A rise in n_H increases the probability of an excited atom to be de-excited collisionally rather than radiatively. Since the critical density for collisional de-excitation is lower for infrared fine-structure transitions than for optical transitions, the net effect of raising n_H at fixed other parameters is to reduce the cooling efficiency through infrared transitions and increase that through optical transitions. Fig. 3.7 shows that the implied rise in the [O III]/Hβ, [N II]/Hα and [S II]/Hα ratios is small at low metallicity, but much stronger at high metallicity, where infrared fine-structure transitions dominate the cooling (e.g., Oey & Kennicutt, 1993, see also the discussion of Fig. 3.4 above).

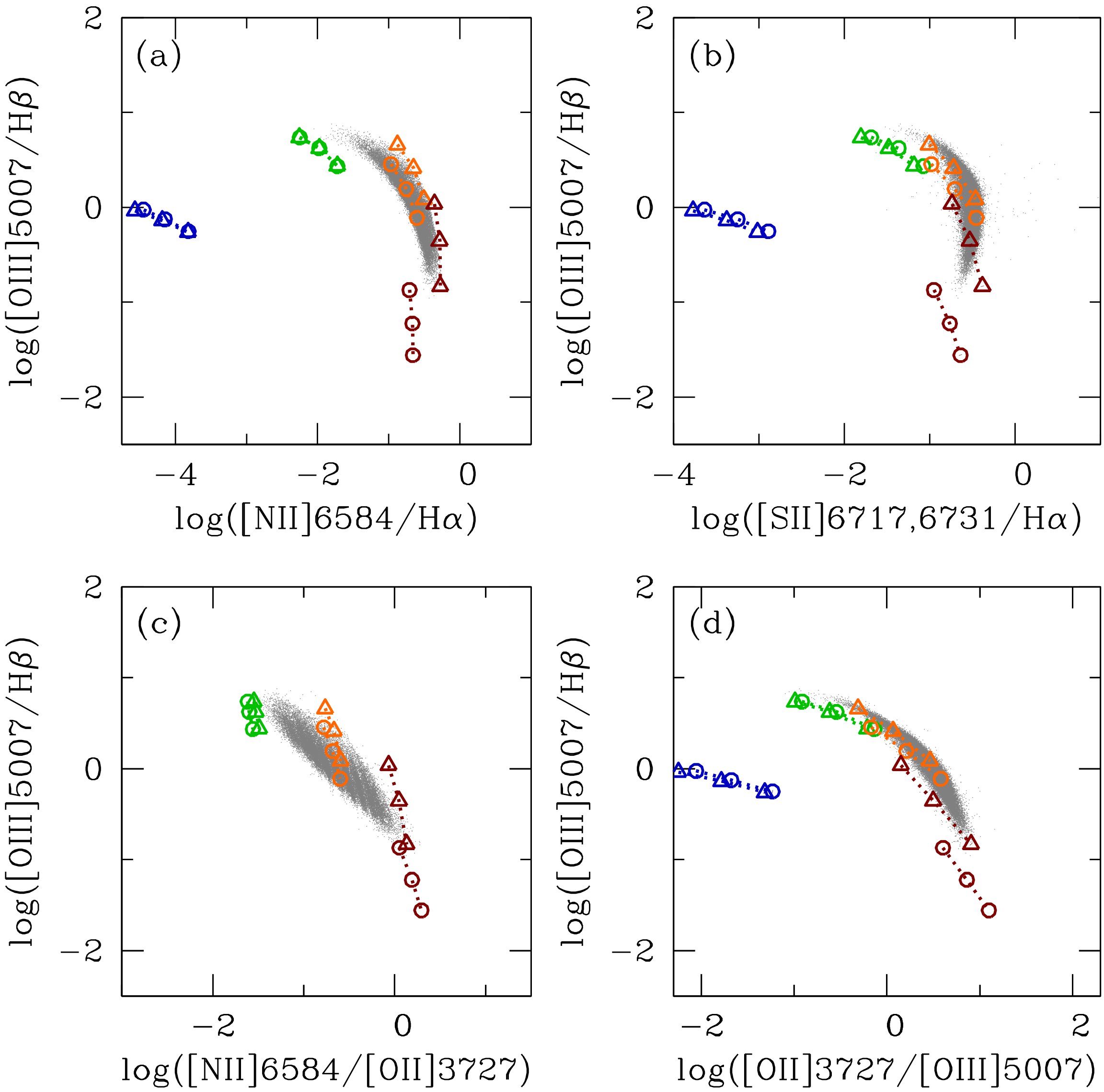

Figure 3.7: Same as Fig. 3.5, but for models with two different hydrogen densities, $n_H = 10\,\mathrm{cm}^{-3}$ (circles) and $10^3\,\mathrm{cm}^{-3}$ (triangles).

Upper mass cutoff of the IMF. Increasing $m_{\rm up}$ from 100 to 300 $\mathrm{M}_\odot$ makes the ionizing spectrum of the stellar population harder, since stars with initial masses greater than 100 $\mathrm{M}_\odot$ evolve at higher effective temperatures than lower-mass stars. As Fig. 3.8 shows, this makes the high-ionization lines stronger, causing a rise of the [O III]/Hβ ratio – and to a lesser extent, the [N II]/Hα and [S II]/Hα ratios – and a drop of the [O II]/[O III] ratio.

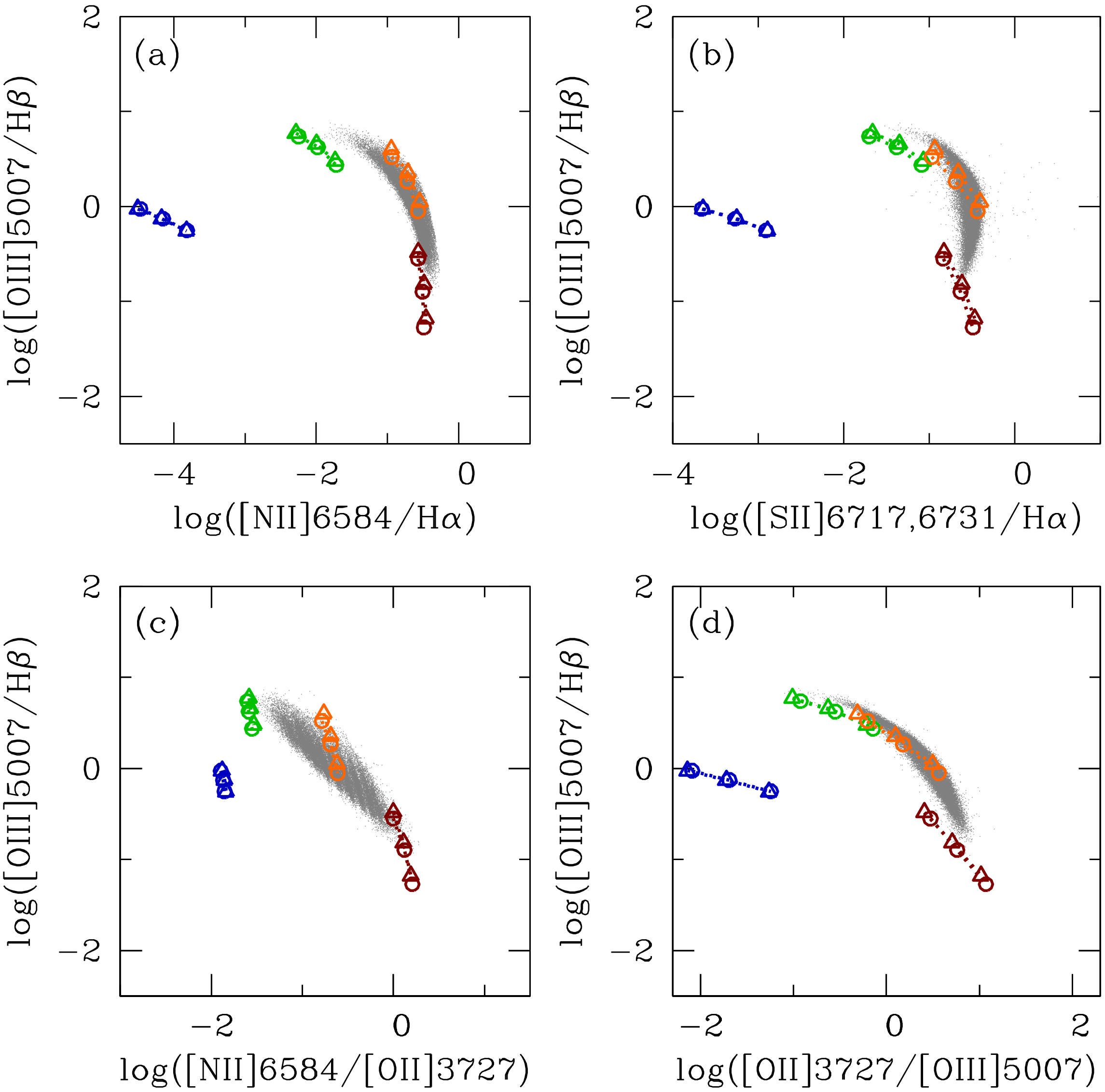

Figure 3.8: Same as Fig. 3.5, but for models with two different IMF upper mass cutoffs, $m_{\rm up} = 100\mathrm{M}_\odot$ (circles) and $300\mathrm{M}_\odot$ (triangles).

Hence, the various adjustable parameters of the model of nebular emission described in Section 3.2 influence, each in its own way, the optical emission-line spectra of star-forming galaxies. These specific signatures enable one to constrain simultaneously, in return, the star-formation and interstellar-gas parameters of observed galaxies with measured optical emission-line intensities (see, e.g., CL01; Brinchmann et al., 2004; Pacifici et al., 2012). As mentioned previously, a main originality (other than the use of updated stellar population and photoionization prescriptions) of the models presented in Figs 3.4–3.8 above relative to previous models of the optical nebular emission from star-forming galaxies lies in the versatile, yet self-consistent, accounting of gas-phase versus interstellar element abundances, which allows investigations of chemically young galaxies with non-scaled solar element abundance ratios.

3.4 Ultraviolet emission-line properties

I now investigate the ultraviolet properties of these models and compare them with observations of star-forming galaxies at various cosmic epochs.

One of my primary motivations in this work is to build a library of photoionization models useful to interpret observations of the rest-frame ultraviolet emission from young star-forming galaxies at high redshifts. In this section, I investigate the ultraviolet properties of the grid of models presented in the previous sections and compare these predictions with available observations of a small, heterogeneous sample of local and distant star-forming galaxies. For illustration purposes, I have selected – by means of a systematic investigation by eye of ratios involving the strongest ultraviolet emission lines – a set of emission-line ratios most sensitive to changes in the adjustable parameters of my model. These ratios involve six emission lines (or multiplets) commonly detected in the spectra of star-forming galaxies: N v $\lambda\lambda$1238, 1242 (hereafter N v λ1240); C iv $\lambda\lambda$1548, 1551 (hereafter C iv λ1550); He ii λ1640; O iii]λ1666; [Si iii]λ1883+Si iii]λ1892 (hereafter Si iii]λ1888); and [C iii]λ1907+C iii]λ1909 (hereafter C iii]λ1908). I note that, while the luminosities of O iii]λ1666, Si iii]λ1888 and C iii]λ1908 can usually be measured in a straightforward way when these lines are detectable, measurements of nebular He ii λ1640 may be challenged by the presence of a broad component arising from Wolf-Rayet stars, especially at metallicities $Z_{\rm ISM} \gtrsim 0.006$ (because of both a drop in photons capable of producing nebular He ii λ1640 and a rise in stellar He ii λ1640 emission as metallicity increases; e.g. Schaerer & Vacca 1998). At such metallicities, measurements of nebular N v λ1240 and C iv λ1550 are even more challenging, because of the contamination by strong P-Cygni absorption features from O-star winds (Walborn & Panek, 1984) coupled with interstellar absorption (see Vidal-García et al., in preparation, for a detailed modelling of these competing effects).

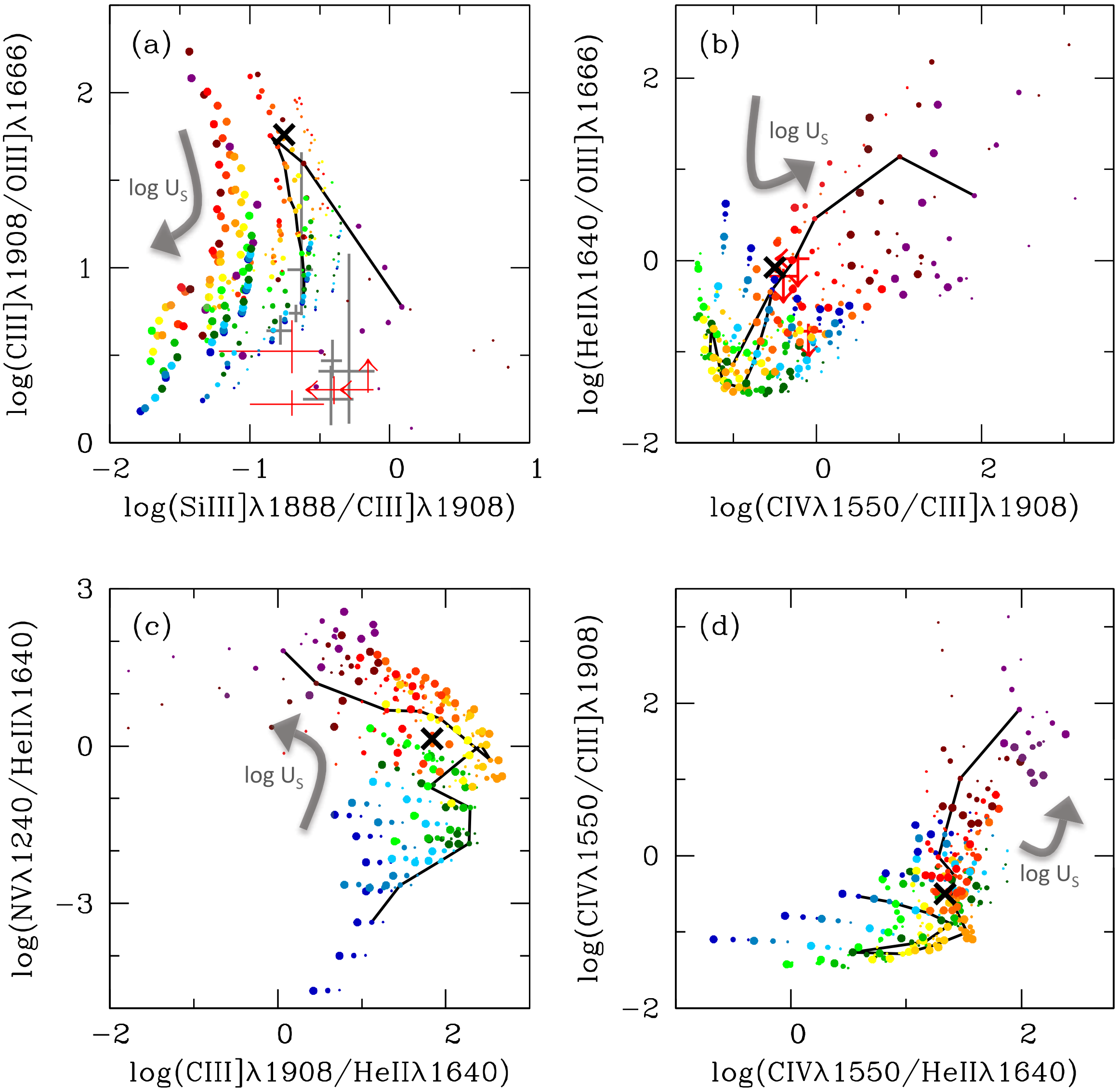

Figure 3.9: Luminosity ratios of prominent ultraviolet emission lines predicted by the photoionization models described in Section 3.2: (a) C III]λ1908/O III]λ1666 against Si III]λ1888/C III]λ1908; (b) He II λ1640/O III]λ1666 against C IV λ1550/C III]λ1908; (c) N V λ1240/He II λ1640 against C III]λ1908/He II λ1640; and (d) C IV λ1550/C III]λ1908 against C IV λ1550/He II λ1640. In each panel, the models and solid line are the same as in Fig. 3.4. In panel (a), the grey and red crosses refer to observations (including error bars and upper limits) of, respectively, six giant extragalactic H II regions in nearby low-luminosity, metal-poor, dwarf irregular galaxies observed with *HST*/FOS by Garnett et al. (1995a) and four low-mass, gravitationally-lensed dwarf galaxies at redshift in the range $2 \lesssim z \lesssim 3$ observed with Keck/LRIS and VLT/FORS2 by Stark et al. (2014, also reported in panel b).

Fig. 3.9 shows the ultraviolet properties of the same set of photoionization models (extracted from the grid of Table 3.4) as that for which I showed the optical properties in Fig. 3.4. Also shown in grey in the top-left panel of Fig. 3.9 are measurements of the C III]/O III] and Si III]/C III] ratios in the spectra of six giant extragalactic H II regions in nearby low-luminosity, metal-poor, dwarf irregular galaxies observed with the *Hubble Space Telescope*/Faint Object Spectrograph (*HST*/FOS; from Garnett et al. 1995a). In the top two panels, the red data points show measurements of (and limits on) the C III]/O III], Si III]/C III], He II/O III] and C IV/C III] ratios in the spectra of four low-mass, gravitationally-lensed dwarf galaxies at redshift in the range $2 \lesssim z \lesssim 3$ observed with the Keck low-resolution imaging spectrometer (LRIS) and Very Large Telescope Focal Reducer and Low Dispersion Spectrograph (VLT FORS2; from Stark et al. 2014). The model grid encompasses the few observational measurements in Fig. 3.9. In fact, the models presented here have already been used successfully to interpret rest-frame ultraviolet observations of the nebular emission from young star-forming galaxies at high redshifts (Stark et al., 2014, 2015a,b, 2016).

I now explore the influence of the main adjustable parameters of my model on the predicted emission-line properties of star-forming galaxies in these four ultraviolet diagnostics diagrams. As in Section 3.3.3 above, I describe the effect of varying a single parameter at a time, keeping the other main adjustable parameters fixed:

Interstellar metallicity. Globally, the effect of increasing $Z_{\rm ISM}$ at fixed other parameters, shown by the solid line in Fig. 3.9, can be understood in terms of the balance pointed out in Section 3.3.3 (Fig. 3.4) between the implied rise in the abundance of coolants, associated drop in electronic temperature and cooling through infrared fine-structure transitions. As a result, ratios of metal-line to He II $\lambda1640$ luminosities tend to rise, stagnate and eventually drop again when metallicity increases in Fig. 3.9, while the inclusion of secondary nitrogen production causes the N V/He II ratio to rise steadily with $Z_{\rm ISM}$ (Fig. 3.9c).

Zero-age ionization parameter at the Strömgren radius. In my model, increasing $U_{\rm S}$ at fixed other adjustable parameters causes the H II regions to be more compact and concentrated close to the ionizing star clusters (Section 3.3.3). Overall, this makes the luminosity ratios of lines with highest ionization potential to lines with lower ionization potential (such as the inverse of the C III]/O III] ratio plotted in Fig. 3.9a and the C IV/C III] ratio) and the He II $\lambda1640$ line (such as the C IV/He II and N V/He II ratios) rise in Fig. 3.9 (see fig. 1 of Feltre, Charlot & Gutkin 2016 for a graphical summary of the ionization potentials of the different species considered in Fig. 3.9).

Dust-to-metal mass ratio. Fig. 3.10 illustrates the influence of $\xi_{\rm d}$ on the predicted ultraviolet emission-line ratios, showing for clarity only models for the same subset of $Z_{\rm ISM}$ and $U_{\rm S}$ combinations as used in Fig. 3.5 above. As for optical transitions (Section 3.3.3), the response of ultraviolet transitions to a rise in $\xi_{\rm d}$ results from a balance between the implied depletion of coolants from the gas phase, the associated rise in electronic temperature and the relative depletions of different species (Table 3.2). For example, the C III]/He II and C IV/He II ratios drop at low $Z_{\rm ISM}$ as $\xi_{\rm d}$ rises, because of the disappearance of C from the gas phase, but the trend is opposite at high $Z_{\rm ISM}$, because the rise in electronic temperature induced by the depletion of heavy elements is more significant (Figs 3.10c and 3.10d). In Fig. 3.10a, the Si III]/C III] drops at all metallicities when $\xi_{\rm d}$ rises, because Si is far more depleted than C from the gas phase. In contrast, since N is not depleted, the N V/He II ratio shows only a mild increase as ξ_d rises in Figs 3.10c, because of the rise in electronic temperature. I note that, at high metallicity especially, the increase in dust optical depth ($\tau_\mathrm{d} \propto \xi_\mathrm{d} Z_\mathrm{ISM} n_\mathrm{H} \epsilon$) induced by a rise in ξ_d makes the electronic temperature drop through the enhanced absorption of energetic photons, causing the C IV/C III] and C IV/He II ratios to drop and the C III]/O III] ratio to rise.

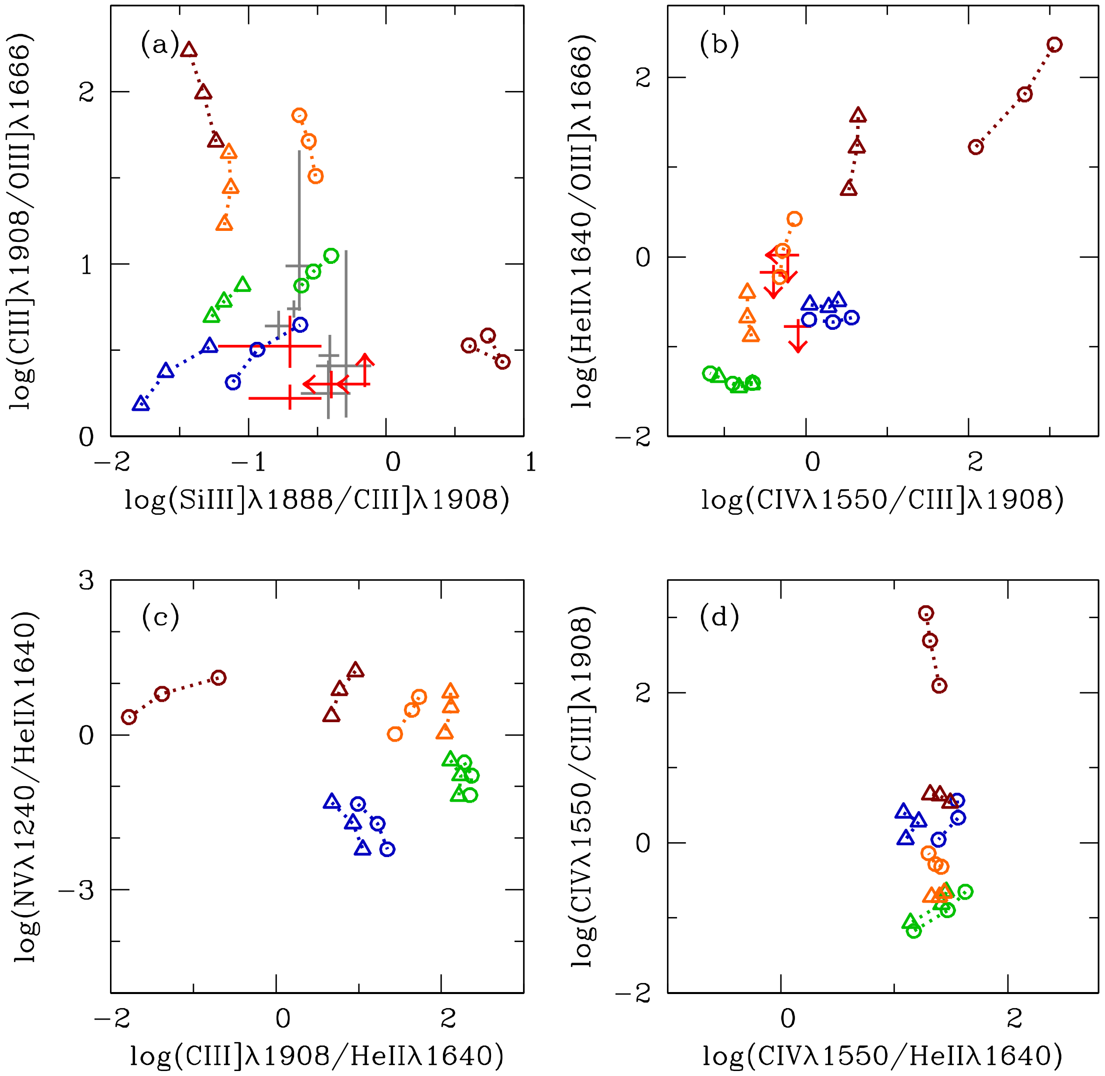

Figure 3.10: Same as Fig. 3.9, but for the same subset of interstellar metallicities and associated zero-age ionization parameters as in Fig. 3.5. In each panel, models are shown for two different dust-to-metal mass ratios, $\xi_\mathrm{d} = 0.1$ (circles) and 0.5 (triangles).

***Carbon-to-oxygen abundance ratio*.** Increasing the C/O ratio at fixed other parameters consists in increasing the abundance of C while decreasing those of all other heavy elements (Section 3.3.3). Fig. 3.11 shows that, as a result, raising the C/O ratio makes the C III]/O III], C III]/He II and C IV/He II ratios markedly larger and the Si III]/C III] ratio markedly smaller. Another important conclusion I can draw from this figure is that the presence of the C III] λ1908, C IV λ1550 and O III] $\lambda\lambda$1661, 1666 emission lines at ultraviolet wavelengths makes ultraviolet-line ratios more direct tracers of the C/O ratio of young star-forming galaxies than the standard optical emission lines investigated in Fig. 3.6.

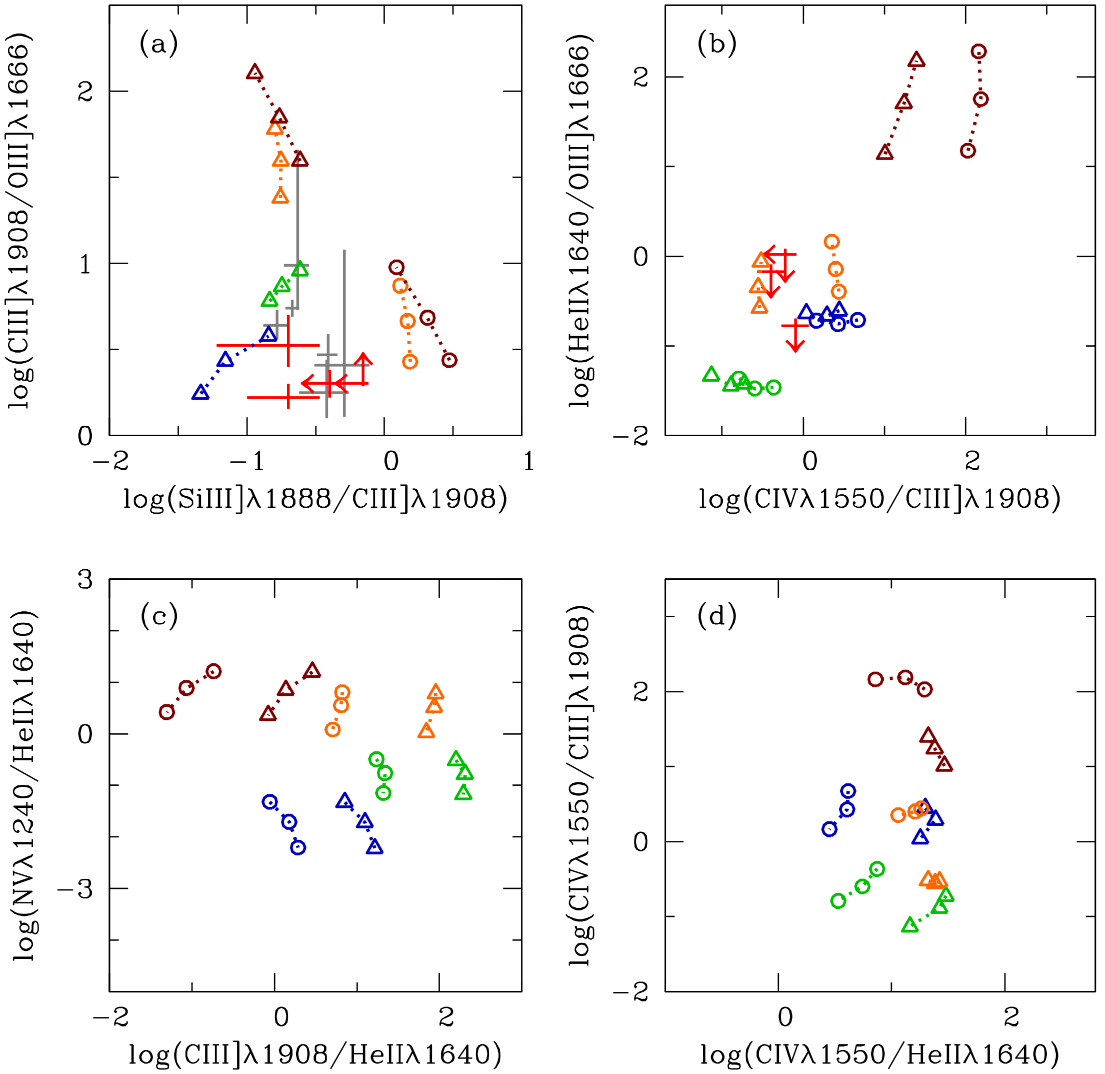

Figure 3.11: Same as Fig. 3.10, but for models with two different carbon-to-oxygen ratios, C/O = 0.1 (circles) and 1.4 (triangles) times $(\mathrm{C/O})_\odot$.

Hydrogen gas density. The effect of raising $n_{\rm H}$ at fixed other parameters is to increase radiative cooling through ultraviolet and optical transitions relative to infrared ones (Section 3.3.3). As Fig. 3.12 shows, this makes the C III]/He II and C IV/He II ratios rise and the He II/O III] ratio drop. Also, in my model, increasing $n_{\rm H}$ at fixed other parameters implies lowering the volume-filling factor as $\epsilon \propto 1/\sqrt{n_{\rm H}}$ (equation 3.7). As a result, the dust optical depth ($\tau_{\rm d} \propto \xi_{\rm d} Z_{\rm ISM} n_{\rm H} \epsilon$) rises as $\sqrt{n_{\rm H}}$, increasing the absorption of energetic photons (see also Feltre, Charlot & Gutkin, 2016), and hence, the C IV/C III] ratio drops (Figs 3.12b and 3.12d). Similarly to what was noted about optical transitions (Fig. 3.7), the influence of $n_{\rm H}$ on ultraviolet emission-line ratios in Fig. 3.12 is weaker at low than at high metallicity, where infrared fine-structure transitions usually dominate the cooling.

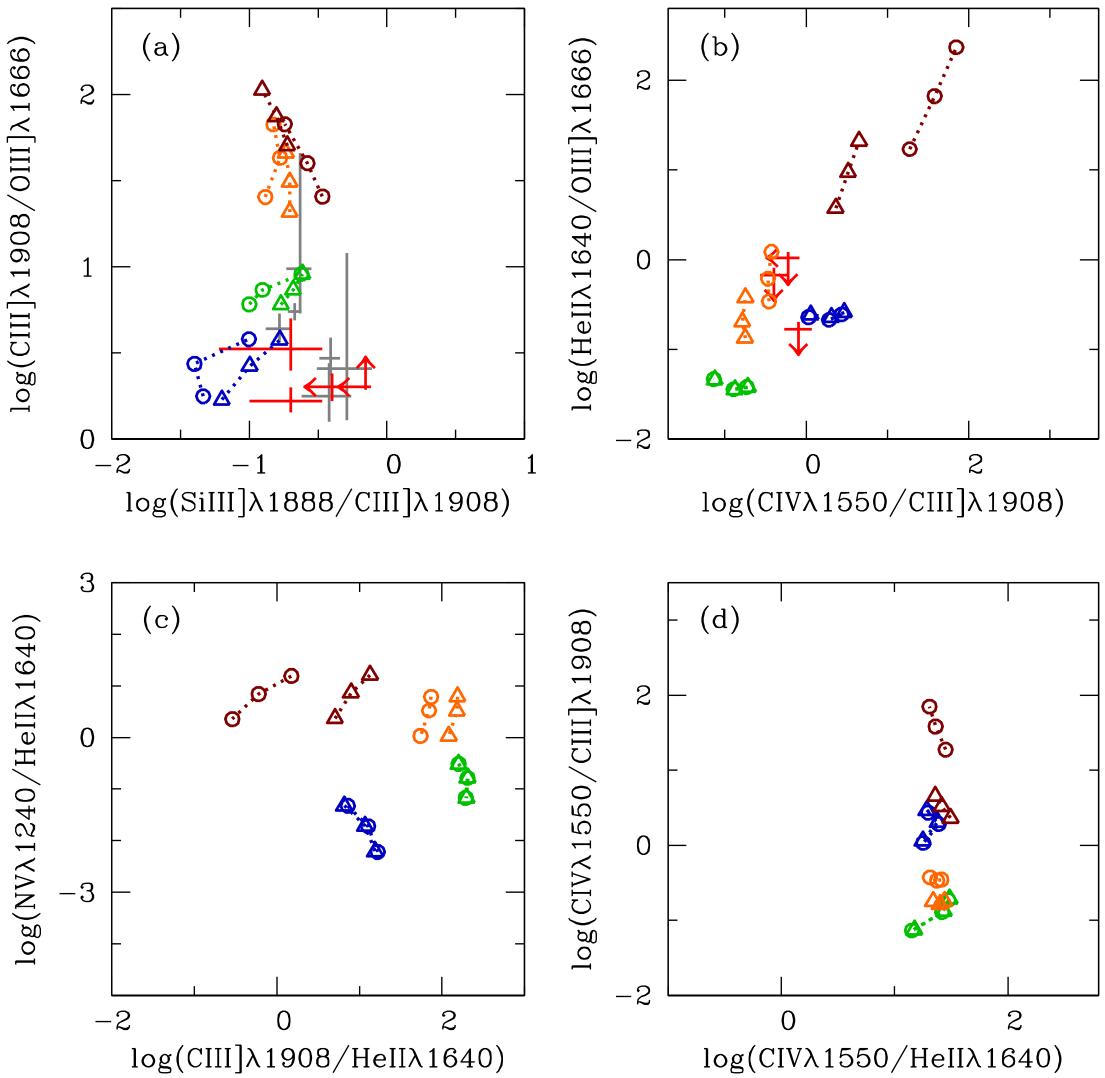

Figure 3.12: Same as Fig. 3.10, but for models with two different hydrogen densities, $n_{\rm H} = 10\,{\rm cm}^{-3}$ (circles) and $10^3\,{\rm cm}^{-3}$ (triangles).

Upper mass cutoff of the IMF. A rise in $m_{\rm up}$ from 100 to 300 $\rm M_\odot$ makes the ionizing spectrum harder (Section 3.3.3), the signature of which is much stronger at ultraviolet than at optical wavelengths. Fig. 3.13 (to be compared with Fig. 3.8) shows that a dominant effect at far-ultraviolet wavelengths is to boost the luminosity of the He II λ1640 recombination line, making the He II/O III] ratio rise and the C III]/He II, C IV/He II and N V/He II ratios drop significantly. Collisionally excited metal transitions are also affected, in the sense that high-ionization lines become more prominent. This is the reason for the slight drop in Si III]/C III] and C III]/O III] ratios and rise in the C IV/C III] ratio.

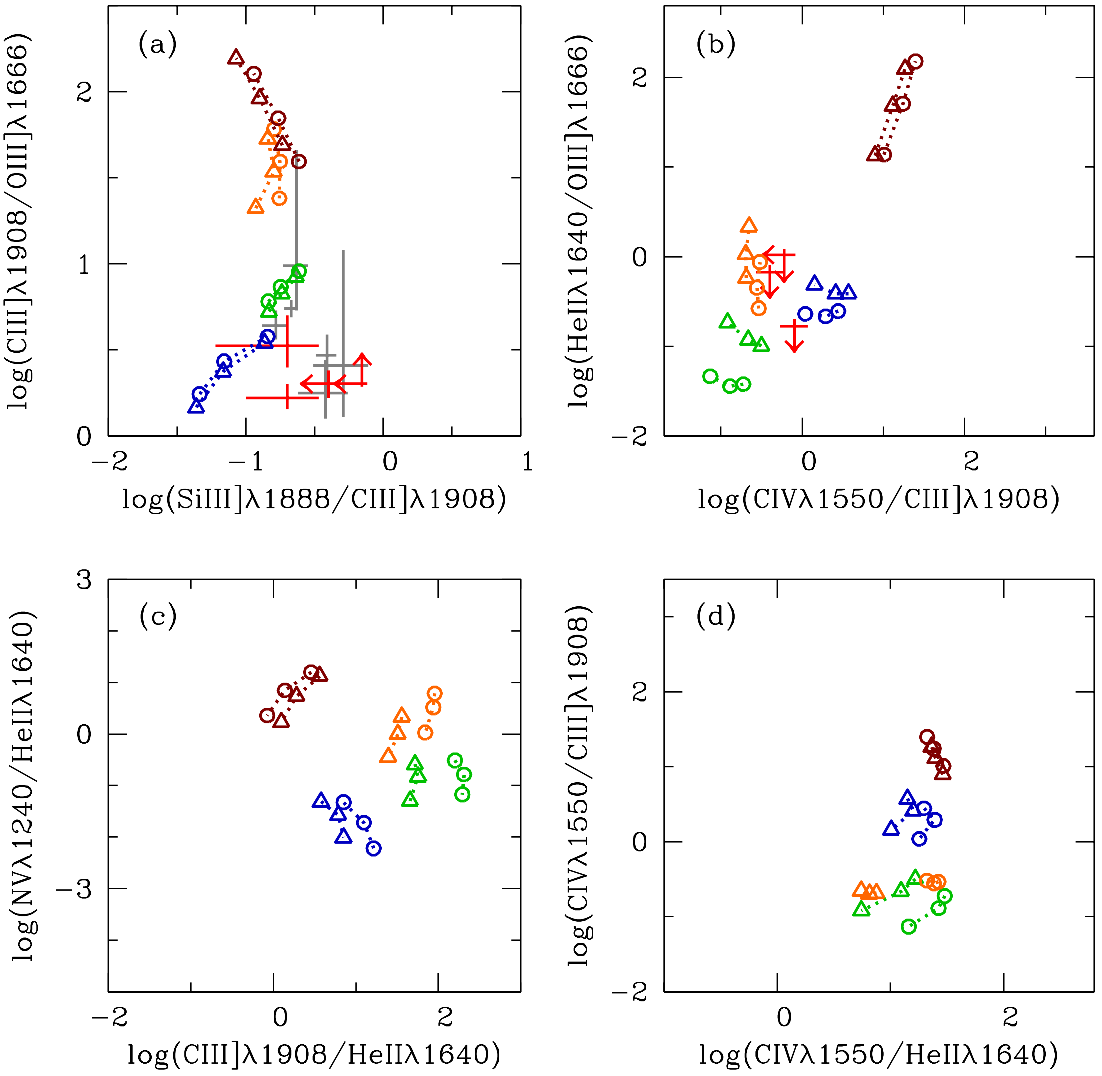

Figure 3.13: Same as Fig. 3.10, but for models with two different IMF upper mass cutoffs, $m_{\rm up}$ = 100$\rm M_\odot$ (circles) and 300$\rm M_\odot$ (triangles).

In summary, by comparing Figs 3.4–3.8 with Figs 3.9–3.13, I may conclude from my investigation in this section and the previous one that ultraviolet emission-line ratios are significantly more sensitive than optical ones to some parameters of young star-forming galaxies, such as the carbon-to-oxygen abundance ratio, hydrogen gas density, upper mass cutoff of the IMF and even dust-to-metal mass ratio. This makes ultraviolet emission lines ideal tracers of the early chemical evolution of galaxies, provided that these lines, which are typically much fainter than their optical counterparts, can be detected. I stress that my ability to draw such conclusions relies largely on the incorporation in my model of a versatile and self-consistent treatment of gas-phase versus interstellar element abundances.

3.5 Limitations of standard methods of abundance measurements

In Sections 3.3.3 and 3.4 above, I have described the dependence of the ultraviolet and optical nebular emission of a galaxy on physical properties. The specific dependence of each feature on different physical parameters enables one to extract valuable constraints on star-formation and chemical-enrichment properties from observed emission-line fluxes. This can be achieved by combining the photoionization models of star-forming galaxies described in Section 3.2 with a sophisticated spectral interpretation tool, as proposed for example in the framework of the BEAGLE tool by Chevallard & Charlot (2016, see their section 2.3). As a complement to such studies, in the present section, I explore how the photoionization model of Section 3.2 can also help identify potential limitations of abundance measurements involving the more approximate, although widely used, 'direct-T_e' method presented in Section 1.3.1. More precisely, I further exploit my model grid to investigate and quantify the limitations affecting standard recipes based on the direct-T_e method to measure element abundances from emission-line luminosities, focusing on the C/O ratio as a case study.

3.5.1 The 'direct-T_e' method

In the absence of sophisticated modelling, the best measurements of chemical abundances from nebular emission lines are generally considered to be those combining an estimate of the electron temperature (T_e) from ratios of auroral to nebular forbidden-line intensities (such as [O III]$\lambda4363/\lambda5007$ or [N II]$\lambda5755/\lambda6584$) with an estimate of the electron density ($n_e \sim n_H$ in the ionized gas) from ratios of nebular forbidden-line intensities (such as [O II]$\lambda3729/\lambda3726$ or [S II]$\lambda6717/\lambda6731$; see, e.g., Aller & Liller 1959; Peimbert 1967; Peimbert & Costero 1969; Aller 1984).[5] I note that a usually neglected uncertainty in this approach is that the ions used to derive T_e and n_e often trace different ionized zones (e.g., O^{2+} versus O^+; see Keenan et al., 2000). Once T_e is estimated for some ionic species (e.g. O^{2+}, see equation 1.2), the total gas-phase abundance of the corresponding element (in this case, O) can be inferred by adding the contributions by the other stages of ionization (here mainly O^+ and O^0). This is generally achieved by using the observed luminosities of corresponding emission lines (e.g., [O II]$\lambda3727$, [O I]$\lambda6300$) and by appealing to photoionization models to estimate the associated electronic temperatures, based on the one measured in the first ionization zone (e.g., equation 6 of Pagel et al., 1992; Kobulnicky & Skillman, 1996). Photoionization models must also be invoked to compute the gas-phase abundances of other metals (e.g., C, N, S), which requires estimates of

---

[5] I use the standard nomenclature and refer to forbidden transitions from the first-excited to ground levels as 'nebular lines', and to those from the second- to first-excited levels as 'auroral lines'.

the electron temperatures pertaining to the zones populated by the corresponding ions (e.g., Garnett, 1992; Izotov & Thuan, 1999; Stasińska, 2005; Izotov et al., 2006).

Hence, in the end, the 'direct-T_e' method of abundance measurements relies indirectly on photoionization calculations. This implies that element abundances derived using this method are tied to the physical parameters of the specific models adopted (abundances, depletion, ionizing radiation, gas density, etc.). As a result, standard calibrations of the direct-T_e method, based on observations of nearby H II regions and galaxies, may not be fully appropriate to investigate the abundances of, for example, chemically young galaxies in the early Universe (Section 1.1). Moreover, inferences made using the direct-T_e method generally do not provide any insight into interstellar (as opposed to gas-phase) element abundances in the ionized gas (Section 3.2.3). The models presented in Sections 3.2–3.4 above offer a unique means of investigating the impact of these limitations on abundance measurements in chemically young star-forming galaxies. In the remainder of this section, I focus on measurements of the C/O ratio, which appears to be a particularly sensitive probe of cosmic chemical evolution (e.g., Erb et al. 2010; Cooke et al. 2011; see also Garnett et al. 1999).

3.5.2 A case study: the C/O ratio

The C/O ratio of star-forming galaxies is often estimated through measurements of C^{2+} and O^{2+} emission lines, using the direct-T_e method and an ionization correction factor, as outlined in Section 3.5.1 above (e.g., Garnett, 1992; Garnett et al., 1995b; Izotov & Thuan, 1999; Erb et al., 2010). This is traditionally expressed as

$$\left(\frac{\mathrm{C}}{\mathrm{O}}\right)_\mathrm{gas} = \frac{\mathrm{C}^{+2}}{\mathrm{O}^{+2}} \times \left[\frac{X(\mathrm{C}^{+2})}{X(\mathrm{O}^{+2})}\right]^{-1} = \frac{\mathrm{C}^{+2}}{\mathrm{O}^{+2}} \times \mathrm{ICF}, \tag{3.18}$$

where $X(\mathrm{C}^{+2}) \equiv \mathrm{C}^{+2}/\mathrm{C}_\mathrm{gas}$ and $X(\mathrm{O}^{+2}) \equiv \mathrm{O}^{+2}/\mathrm{O}_\mathrm{gas}$ are the volume-averaged fractions of doubly-ionized C and O in the gas phase. Here, I have made explicit use of a subscript 'gas' to emphasize the fact that equation (3.18) is generally used to investigate the gas-phase C/O ratio. I now use my model of nebular emission from star-forming galaxies to investigate the uncertainties affecting both factors in the right-hand side of this expression: the conversion of emission-line luminosities into a $\mathrm{C}^{2+}/\mathrm{O}^{2+}$ ratio; and the dependence of the ICF on photoionization conditions. I also explore below the relation between the $\mathrm{C}^{+2}/\mathrm{O}^{+2}$ ratio and the interstellar (i.e. gas+dust-phase) C/O ratio in my model.

Several formulae have been proposed to convert measurements of ultraviolet and optical C^{2+} and O^{2+} emission-line luminosities into a ratio of (volume-averaged) densities of C^{2+} to O^{2+}, based on theoretical computations of the associated collision strengths and emission-rate coefficients, combined with the direct-T_e method (e.g., chapter 5 of Aller, 1984). These include the prescription of Garnett et al. (1995b),[6]

$$\left(\frac{\mathrm{C}^{+2}}{\mathrm{O}^{+2}}\right)_\mathrm{Garnett} = 0.089\ e^{-1.09/t_\mathrm{e}}\ \frac{L(\mathrm{C\,III]}\lambda1908)}{L(\mathrm{O\,III]}\lambda1666)}, \tag{3.19}$$

that of Izotov & Thuan (1999, see also Aller 1984),

$$\left(\frac{\mathrm{C}^{+2}}{\mathrm{O}^{+2}}\right)_\mathrm{Izotov} = 0.093\ e^{4.656/t_\mathrm{e}}\ \frac{L(\mathrm{C\,III]}\lambda1908)}{L([\mathrm{O\,III]}\lambda\lambda4959,5007)}, \tag{3.20}$$

---

[6] The flux labelled $I(\lambda1909)$ in equation (2) of Garnett et al. (1995b) refers to the C III]λ1908 doublet, not resolved in the *HST*/FOS observations.

and that of Erb et al. (2010, see also Shapley et al. 2003),

$$\left(\frac{\mathrm{C}^{+2}}{\mathrm{O}^{+2}}\right)_{\mathrm{Erb}} = 0.15\, e^{-1.1054/t_{\mathrm{e}}}\, \frac{L(\mathrm{C\,III]}\lambda1908)}{L(\mathrm{O\,III]}\lambda\lambda1661,1666)}\,, \tag{3.21}$$

where $t_{\mathrm{e}} = T_{\mathrm{e}}/10^4\,\mathrm{K}$ and L is the line luminosity. The electronic temperature in these expressions is usually taken to be that of the O^{+2} zone. This can be estimated from the $[\mathrm{O\,III}]\lambda\lambda4959,5007/[\mathrm{O\,III}]\lambda4363$ luminosity ratio using the calibration of Aller (1984),

$$t_{\mathrm{e}} = \frac{1.432}{\log[L([\mathrm{O\,III}]\lambda\lambda4959,5007)/L([\mathrm{O\,III}]\lambda4363)] - \log C_T}, \tag{3.22}$$

where

$$C_T = \left(8.44 - 1.09\,t_{\mathrm{e}} + 0.5\,{t_{\mathrm{e}}}^2 - 0.08\,{t_{\mathrm{e}}}^3\right)\frac{1+0.0004\,x}{1+0.044\,x} \tag{3.23}$$

and $x = 10^{-4}\,(n_{\mathrm{e}}/\mathrm{cm}^{-3}){t_{\mathrm{e}}}^{-1/2}$. If the $[\mathrm{O\,III}]\lambda4363$ line is not available (as in Erb et al. 2010), t_{e} can be estimated instead from the $\mathrm{O\,III}]\lambda\lambda1661,1666/[\mathrm{O\,III}]\lambda5007$ luminosity ratio, using the calibration of Villar-Martín, Cerviño & González Delgado (2004, their fig. 1).

In Figs 3.14a–3.14c, I compare the $\mathrm{C}^{+2}/\mathrm{O}^{+2}$ ratios estimated using equations (3.19)–(3.21) from the emission-line properties of the same subset of photoionization models as in Figs 3.4 and 3.9 above (extracted from the grid of Table 3.4) with the true $\mathrm{C}^{+2}/\mathrm{O}^{+2}$ ratios of these models (as provided by the CLOUDY code). In practice, I solve for t_{e} in equation (3.22) by setting n_{e} equal to the hydrogen density $n_{\mathrm{H}} = 100\,\mathrm{cm}^{-3}$ of these models when evaluating x in equation (3.23). The resulting electronic temperatures are shown as a function of gas-phase oxygen abundance, $12 + \log(\mathrm{O/H})_{\mathrm{gas}}$, in Fig. 3.14d. As expected, at fixed other model parameters, T_{e} drops markedly as the abundance of coolants rises (Sections 3.3.3 and 3.4).

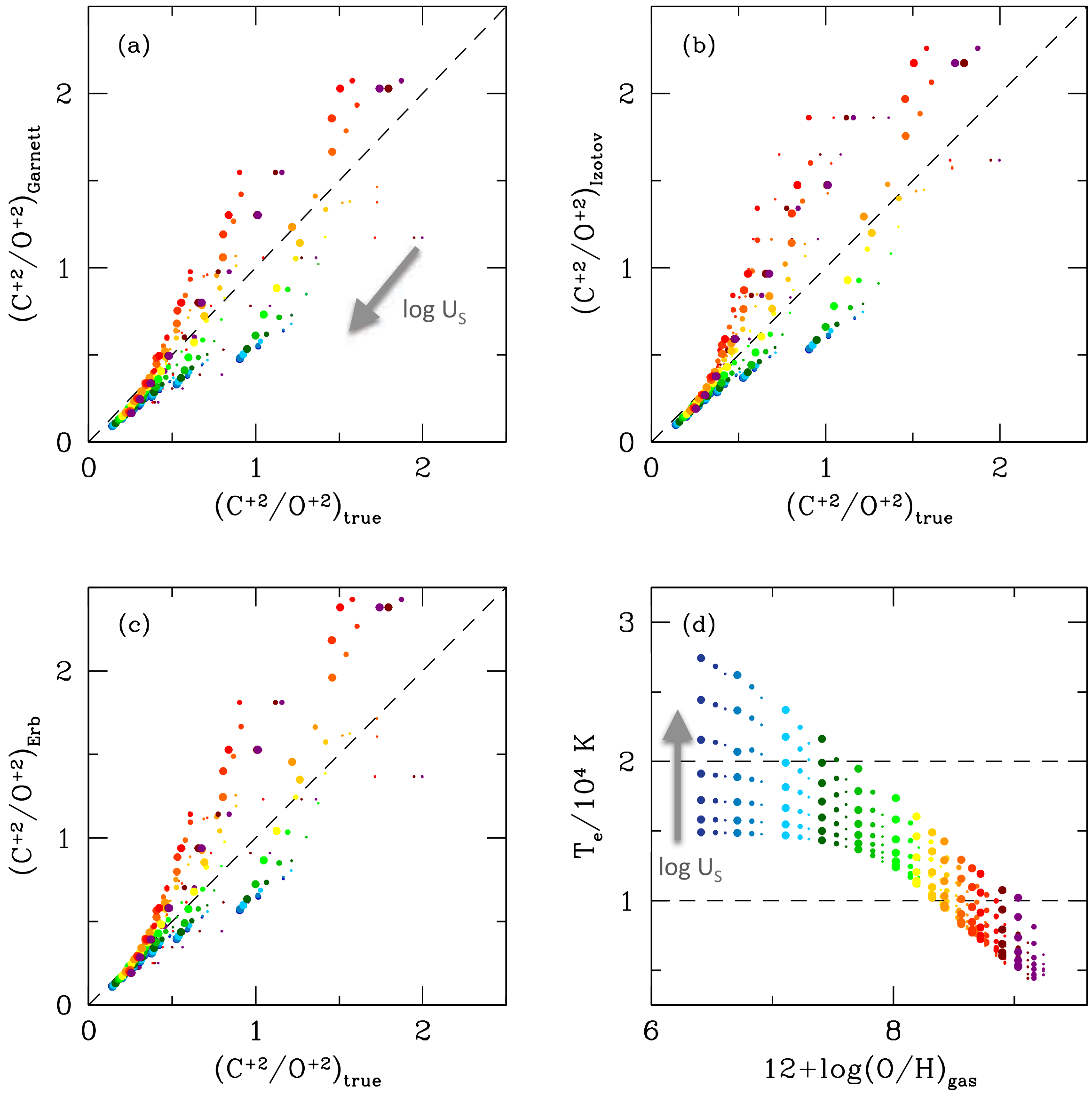

Figure 3.14: C^{+2}/O^{+2} ionic abundance ratio estimated from emission-line luminosities via standard formulae involving the direct-T_e method plotted against true C^{+2}/O^{+2} ratio, for the same models as in Fig. 3.4: (a) according the prescription of Garnett et al. (1995b, equation 3.19 of Section 3.5.2); (b) according the prescription of Izotov & Thuan (1999, equation 3.20); (c) according the prescription of Erb et al. (2010, equation 3.18). (d) Model electronic temperature in the O^{+2} plotted against gas-phase oxygen abundance for the same models as in panels (a)–(c). Dashed horizontal lines brackett the approximate T_e range over which equations (3.19)–(3.21) were calibrated (see text for details).

Figs 3.14a–3.14c show that the C^{+2}/O^{+2} ratio estimated using the standard formulae of equations (3.19)–(3.21) can differ substantially from the true one, by an amount ranging from a factor of ∼2 underestimate at low metallicity (blue points) to a factor of ∼2 overestimate at high metallicity (red points). The difference shrinks around solar metallicity (orange points). The most likely reason for the discrepancy at non-solar metallicities is that the formulae in equations (3.19)–(3.21) were derived using C^{+2} (^1S–^3P) and O^{+2} (^3P–$^5S_2$) collision strengths computed for a restricted range of electronic temperatures typical of H II regions with solar-to-slightly sub-solar metallicity, i.e. $10,000 \lesssim T_e/\mathrm{K} \lesssim 20,000$ (Aller, 1984; Garnett et al., 1995a). As Fig. 3.14d shows, H II regions at low and high metallicities can reach temperatures outside this range. Hence, I conclude from Fig. 3.14 that the ability to estimate the C^{+2}/O^{+2} ratio from emission-line luminosities using simple standard recipes breaks down at non-solar metallicities.

I now turn to the other main potential source of uncertainty affecting estimates of the $(C/O)_{gas}$ ratio via emission-line luminosities, i.e., the correction factor (ICF) to convert C^{+2}/O^{+2} into $(C/O)_{gas}$ in equation (3.18). Fig. 3.15a shows the ICF as a function of volume-averaged fraction of doubly-ionized oxygen, $X(O^{+2})$, for the same models of star-forming galaxies as in Fig. 3.14. The quantity $X(O^{+2})$ and the ICF depend sensitively on the ionization parameter and, at fixed U_S, the metallicity Z_{ISM}, which influences both the electronic temperature and the hardness of the ionizing radiation (since $Z = Z_{ISM}$; see Sections 3.3.3 and 3.4). Specifically, a rise in U_S and a drop in Z_{ISM} both make the fraction of doubly-ionized oxygen larger. At the same time, the lower ionization potential of C^{+2} (47.9 eV) relative to O^{+2} (54.9 eV) implies that $X(C^{+2})$ starts to drop before $X(O^{+2})$, because of the ionization of C to C^{+3}, causing the ICF to also increase. Also shown for comparison in Fig. 3.15a are the pioneer, dust-free calculations of the ICF by Garnett et al. (1995a) for OB stellar associations at ages $t' = 0$ and 2 Myr (in the notation of Section 3.2.2), based on early prescriptions by Mihalas (1972) and Panagia (1973). These calculations for large $X(O^{+2})$ are in reasonable agreement with my more sophisticated models of H II-region populations in star-forming galaxies.

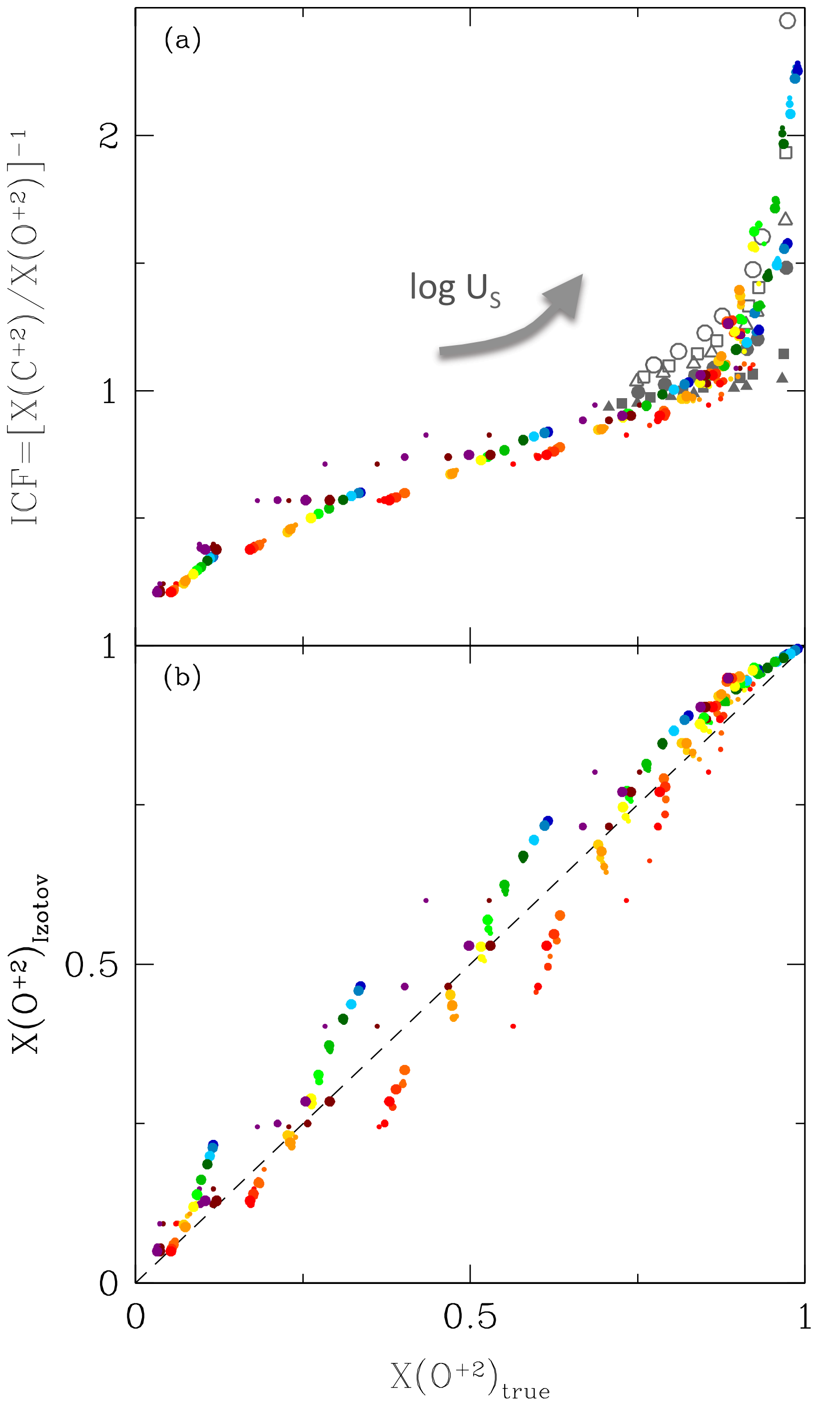

Figure 3.15: (a) Ionization correction factor entering equation (3.18), $[X(\mathrm{C}^{+2})/\mathrm{X}(\mathrm{O}^{+2})]^{-1}$, plotted against volume-averaged fraction of doubly-ionized oxygen, $X(\mathrm{O}^{+2})$, for the same models as in Fig. 3.4. The circles, squares and triangles show the results of early calculations by Garnett et al. (1995a) for OB stellar associations of metallicity 0.001, 0.004 and 0.008, respectively, and ages 0 Myr (filled symbols) and 2 Myr (open symbols; see text for details). (b) $X(\mathrm{O}^{+2})$ estimated from emission-line luminosities via standard formulae involving the direct-T_e method (equations 3.24–3.26) plotted against true $X(\mathrm{O}^{+2})$, for the same models as in (a).

It is important to note that, although the scatter in the ICF predicted at fixed $X(\mathrm{O}^{+2})$ by my models is moderate in Fig. 3.15a, the influence of this scatter on estimates of the $(\mathrm{C/O})_{\mathrm{gas}}$ ratio via equation (3.18) is amplified by the uncertainties affecting observational estimates of $X(\mathrm{O}^{+2})$ from ratios of oxygen emission lines through the direct-T_e method (Section 3.5.1). To show this, I make the standard approximation that the fraction of doubly-ionized oxygen can be estimated as

$$X(\mathrm{O}^{+2}) \approx \frac{\mathrm{O}^{+2}/\mathrm{H}^+}{\mathrm{O}^+/\mathrm{H}^+ + \mathrm{O}^{+2}/\mathrm{H}^+}\,, \tag{3.24}$$

i.e., I neglect the contributions by O^0 and O^{3+} to the total oxygen abundance. These contributions are expected to be significant only in the cases of, respectively, very low and very high ionization parameter (e.g. Kobulnicky, Kennicutt & Pizagno, 1999; Izotov et al., 2006). I adopt the prescription of Izotov et al. (2006, their equations 3 and 5) to compute the abundances of O^+ and O^{+2} in equation (3.24) from observed emission-line luminosities, i.e.,

$$\begin{aligned}\log \mathrm{O}^+/\mathrm{H}^+ = {} & \log \frac{L([\mathrm{O\,II}]\lambda3727)}{L(\mathrm{H}\beta)} - 6.039 + \frac{1.676}{t_\mathrm{e}} - 0.40 \log t_\mathrm{e} \\ & - 0.034 t_\mathrm{e} + \log(1 + 1.35x)\end{aligned} \tag{3.25}$$

and

$$\begin{aligned}\log \mathrm{O}^{+2}/\mathrm{H}^+ = {} & \log \frac{L([\mathrm{O\,III}]\lambda\lambda4959,5007)}{L(\mathrm{H}\beta)} - 5.800 + \frac{1.251}{t_\mathrm{e}} \\ & - 0.55 \log t_\mathrm{e} - 0.014 t_\mathrm{e}\,,\end{aligned} \tag{3.26}$$

where t_e and x have the same meaning as before. Fig. 3.15b shows the fraction of doubly-ionized oxygen estimated in this way, $X(\mathrm{O}^{+2})_{\mathrm{Izotov}}$, as a function of the true $X(\mathrm{O}^{+2})$, for the same models as in Fig. 3.15a. Again, as in Fig. 3.14 above, there is a large metallicity-dependent bias in the ionic abundance estimated using standard formulae and the direct-T_e method relative to the true one, except at solar-to-slightly sub-solar metallicity.

Overall, therefore, Figs 3.14 and 3.15 indicate that estimates of the $(\mathrm{C/O})_{\mathrm{gas}}$ ratio via standard recipes involving the direct-T_e method are subject to strong biases and uncertainties affecting the derivation of both the $\mathrm{C}^{+2}/\mathrm{O}^{+2}$ ratio and the ICF in equation (3.18), especially at non-solar metallicities. A full model of the type presented in this thesis is required for more reliable abundance estimates at all metallicities. Interestingly, such a model offers the possibility to also explore in a physically consistent way the dependence of the ICF on the properties of the photoionized gas and the ionizing stellar populations.

To this end, I show in Fig. 3.16 the dependence of the ICF on ionization parameter for models in a full range of interstellar metallicities, $0.0001 \leq Z_{\mathrm{ISM}} \leq 0.040$, and fixed dust-to-metal mass ratio, $\xi_\mathrm{d} = 0.3$, carbon-to-oxygen ratio, $\mathrm{C/O} = (\mathrm{C/O})_\odot$, hydrogen density, $n_\mathrm{H} = 100\,\mathrm{cm}^{-3}$, and IMF upper mass cutoff, $m_{\mathrm{up}} = 100\,\mathrm{M}_\odot$. The trend of increasing ICF at increasing $\log U_\mathrm{S}$ and decreasing Z_{ISM} is the same as that described in the context of Fig. 3.15 above. The added interest of Fig. 3.16 is to explicit the strong dependence of the ICF on metallicity (see also fig. 11 of Erb et al., 2010). In contrast, as Fig. 3.17 shows, the other main adjustable parameter of the model have only a weak influence on the ICF, at fixed metallicity $Z_{\mathrm{ISM}} = 0.014$. In particular, increasing ξ_d makes the gas-phase metallicity lower at fixed Z_{ISM}, which leads to a slightly higher ICF, especially at large $\log U_\mathrm{S}$ (see above; Fig. 3.17a). Also, since C is more depleted onto dust grains than O (Table 3.2), a drop in C/O ratio at fixed Z_{ISM} and ξ_d causes the gas-phase metallicity to decrease a little, and hence, the ICF to rise

(Fig. 3.17b). Changes in the hydrogen gas density have a negligible influence on the ICF (Fig. 3.17b). In contrast, raising the upper mass limit of the IMF from 100 to 300 $\mathrm{M}_{\odot}$ makes the ionizing spectrum harder (Section 3.3.3), causing more ionization of C to C^{+3} and hence a greater ICF (Fig. 3.17d).

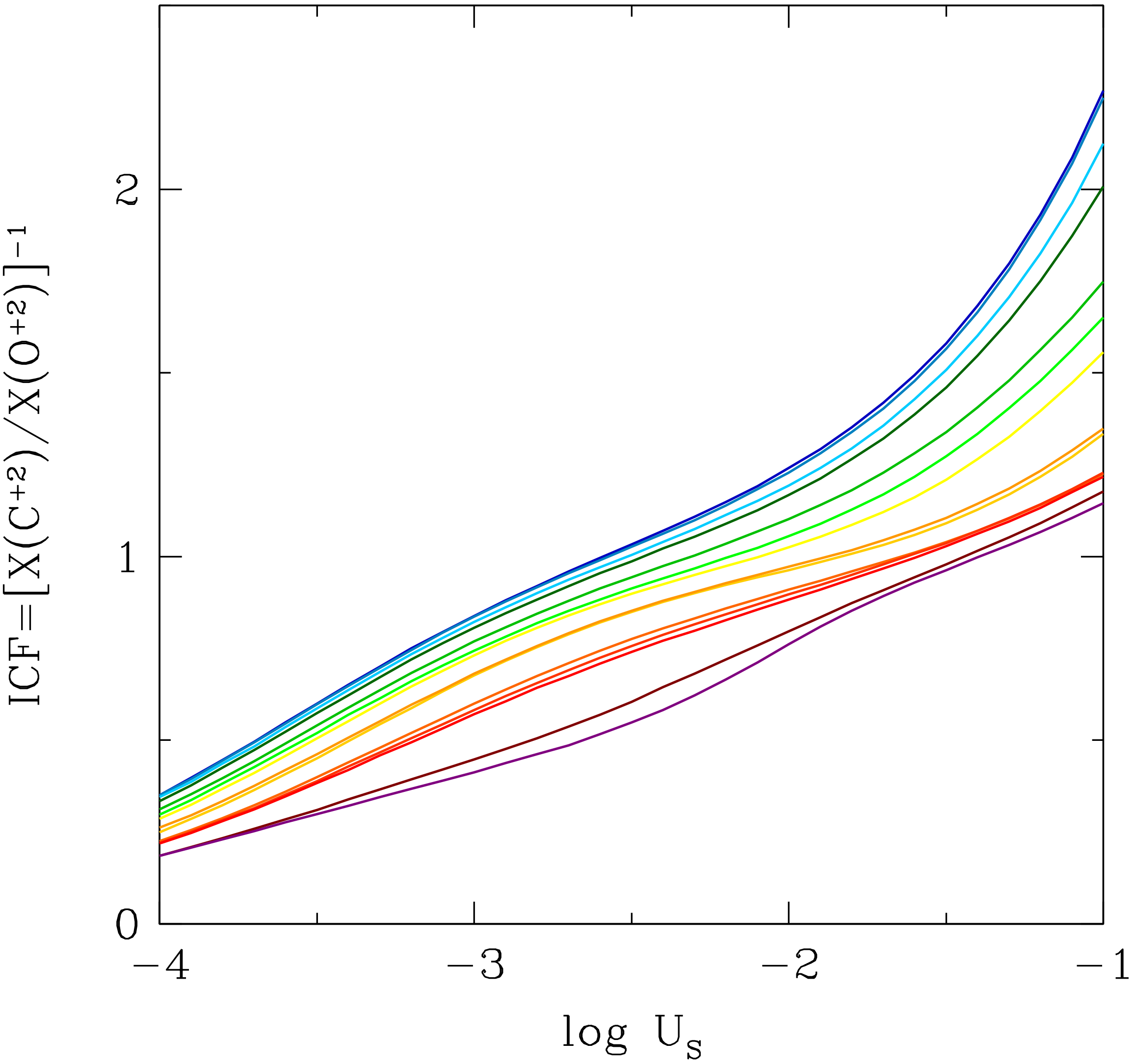

Figure 3.16: Dependence of the ionization correction factor entering equation (3.18), $[X(\mathrm{C}^{+2})/\mathrm{X}(\mathrm{O}^{+2})]^{-1}$, on ionization parameter, $\log U_{\mathrm{S}}$, for the full range of interstellar metallicities in Table 3.4, $0.0001 \leq Z_{\mathrm{ISM}} \leq 0.040$ (colour-coded as in Fig. 3.2), and for fixed dust-to-metal mass ratio, $\xi_{\mathrm{d}} = 0.3$, hydrogen density, $n_{\mathrm{H}} = 100\,\mathrm{cm}^{-3}$, carbon-to-oxygen ratio, $(\mathrm{C/O})_{\odot} = 0.44$, and IMF upper mass cutoff, $m_{\mathrm{up}} = 100\,\mathrm{M}_{\odot}$.

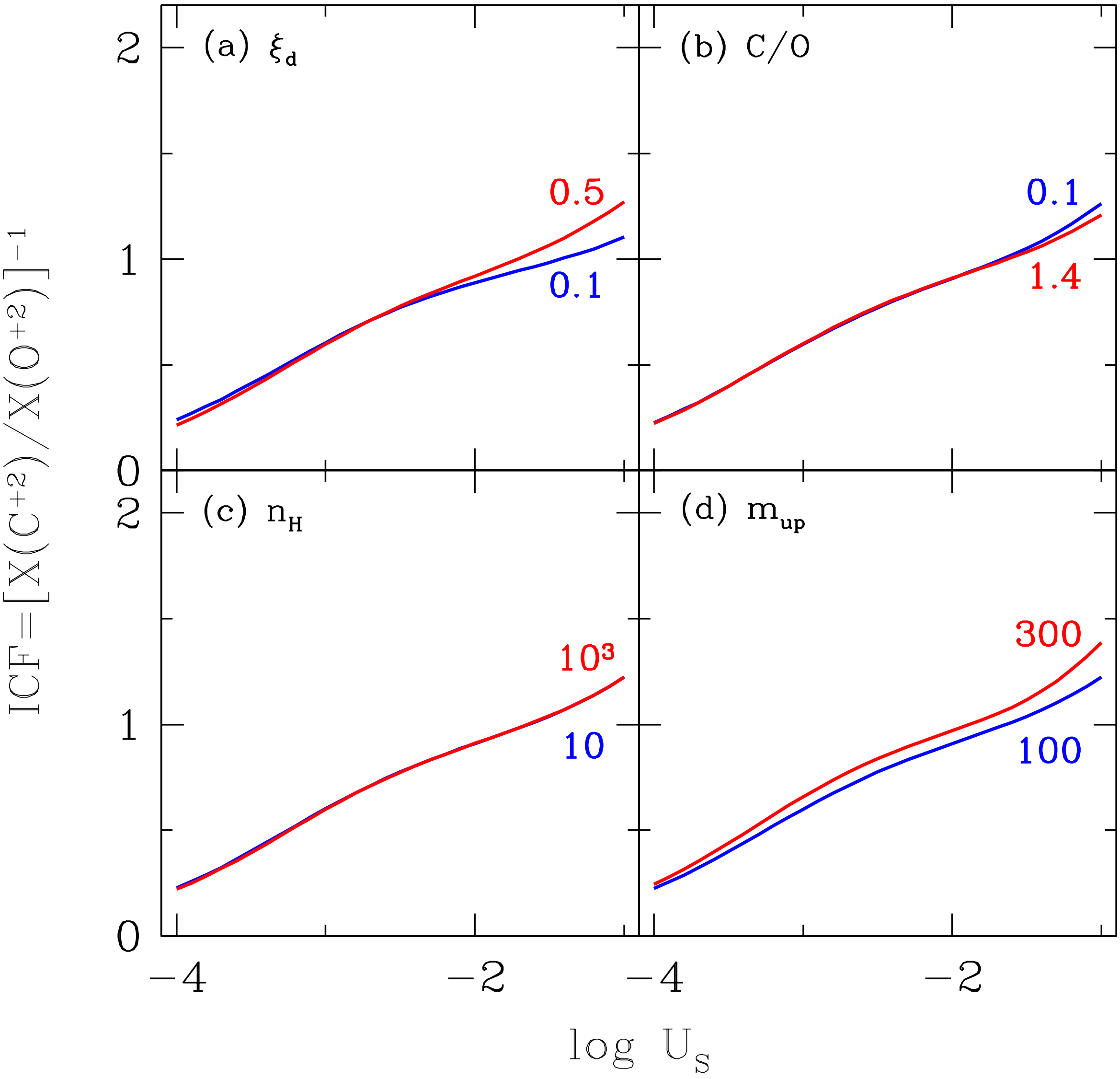

Figure 3.17: Dependence of the ionization correction factor entering equation (3.18), $[X(C^{+2})/X(O^{+2})]^{-1}$, on ionization parameter, $\log U_S$, for the interstellar metallicity $Z_{\rm ISM}$ = 0.014 and for: (a) n_H = $100\,\mathrm{cm}^{-3}$, $(C/O)_\odot$ = 0.44, m_{up} = $100\,M_\odot$ and two different dust-to-metal mass ratios, ξ_d = 0.1 and 0.5; (b) ξ_d = 0.3, n_H = $100\,\mathrm{cm}^{-3}$, m_{up} = $100\,M_\odot$ and two different carbon-to-oxygen ratios, C/O = 0.1 and 1.4 times $(C/O)_\odot$; (c) ξ_d = 0.3, $(C/O)_\odot$ = 0.44, m_{up} = $100\,M_\odot$ and two different hydrogen densities, n_H = 10 and $10^3\,\mathrm{cm}^{-3}$; (d) ξ_d = 0.3, n_H = $100\,\mathrm{cm}^{-3}$, $(C/O)_\odot$ = 0.44, and two different IMF upper mass cutoffs, m_{up} = 100 and $300\,M_\odot$

.

Finally, I stress that one of the unique features of the models presented in this thesis regarding abundance estimates in star-forming galaxies is the possibility to relate emission-line measurements to not only gas-phase, but also interstellar (i.e. gas+dust-phase) element abundances. This is enabled by the careful parametrization of abundances and depletion factors described in Section 3.2.3 (Table 3.2). In the case of the C/O ratio, for example, since carbon is more depleted onto dust grains than oxygen, I find from the model library in Table 3.4 that the interstellar C/O ratio is 1.06, 1.24 and 1.40 times larger than the gas-phase one, $(\mathrm{C/O})_{\mathrm{gas}}$, for dust-to-metal mass ratios $\xi_{\mathrm{d}} = 0.1$, 0.3 and 0.5, respectively, and for $Z_{\mathrm{ISM}} = 0.014$ and $\mathrm{C/O} = (\mathrm{C/O})_{\odot}$. These numbers change by only about 1 per cent across the whole metallicity range ($0.0001 \leq Z_{\mathrm{ISM}} \leq 0.040$; because of my inclusion of secondary nitrogen production) and for interstellar C/O ratios across the full range considered (between 0.1 and 1.4 times solar).

3.6 Conclusions

I have presented a new model of the ultraviolet and optical nebular emission from star-forming galaxies, based on a combination of state-of-the-art stellar population synthesis and photoionization codes to describe the H II regions and the diffuse gas ionized by successive stellar generations (following the approach of CL01). A main feature of this model is the self-consistent yet versatile treatment of element abundances and depletion onto dust grains, which allows one to relate the observed nebular emission from a galaxy to both gas-phase and dust-phase metal enrichment, over a wide range of chemical compositions. This feature should be particularly useful to investigate the early chemical evolution of galaxies with non-solar carbon-to-oxygen abundance ratios (e.g., Erb et al. 2010; Cooke et al. 2011; see also Garnett et al. 1999). In my model, the main adjustable parameters pertaining to the stellar ionizing radiation are the stellar metallicity, Z, the IMF (the upper mass cutoff can reach $m_{\mathrm{up}} = 300\,\mathrm{M}_{\odot}$) and the star formation history. The main adjustable parameters pertaining to the ISM are the interstellar metallicity, Z_{ISM} (taken to be the same as that of the ionizing stars), the zero-age ionization parameter of a newly born H II region, U_{S}, the dust-to-metal mass ratio, ξ_{d}, the carbon-to-oxygen abundance ratio, C/O, and the hydrogen gas density, n_{H}. These should be regarded as 'effective' parameters describing the global conditions of the gas ionized by young stars throughout the galaxy.

I have built a comprehensive grid of photoionization models of star-forming galaxies spanning a wide range of physical parameters (Table 3.4). These models reproduce well the optical (e.g. [O II]$\lambda\lambda3726,3729$, Hβ, [O III]$\lambda5007$, Hα, [N II]$\lambda6584$, [S II]$\lambda\lambda6717,6731$) and ultraviolet (e.g. N V $\lambda1240$, C IV $\lambda\lambda1548,1551$, He II $\lambda1640$, O III]$\lambda1666$, [C III]$\lambda1907$+C III]$\lambda1909$, [Si III]$\lambda1883$+Si III]$\lambda1892$) emission-line properties of observed galaxies at various cosmic epochs. I find that ultraviolet emission lines are more sensitive than optical ones to parameters such as the C/O ratio, the hydrogen gas density, the upper IMF cutoff and even the dust-to-metal mass ratio, ξ_{d}. This implies that spectroscopic studies of the redshifted rest-frame ultraviolet emission of galaxies out to the reionization epoch should provide valuable clues about the nature of the ionizing radiation and early chemical enrichment of the ISM. In fact, my modelling has already been combined with a model of the nebular emission from narrow-line emitting regions of active galaxies to identify ultraviolet line-ratio diagnostics of photoionization by an AGN versus star formation (Feltre, Charlot & Gutkin, 2016), which is the heart of the next Chapter 4. It has also been used successfully to constrain the ionizing radiation and ISM parameters of galaxies at redshifts $2 \lesssim z \lesssim 9$, based on observed ultraviolet emission-line properties (Stark et al., 2014, 2015a,b, 2016).

It is worth mentioning that the stellar population synthesis code I use to generate the ionizing radiation in this thesis (Section 3.2.1) does not incorporate binary stars, while models including binary stars (e.g., Eldridge, Izzard & Tout, 2008; Eldridge & Stanway, 2012) have been preferred over existing 'single-star' models to account for the observed rest-frame far-ultraviolet and optical composite spectra of a sample of 30 star-forming galaxies at redshift around $z = 2.40$ (Steidel et al., 2016). I find that my new model can account remarkably well for the observed ultraviolet and optical emission-line properties of the composite Steidel et al. (2016) spectrum, with best-fitting metallicity $Z_{\rm ISM} = 0.006$ (i.e. $0.4Z_\odot$), ionization parameter $\log U_{\rm S} = -3.0$ and carbon-to-oxygen ratio $\rm C/O = 0.52(C/O)_\odot$. Specifically, the predicted emission-line ratios of the best-fitting model are [O III]$\lambda5007$/H$\beta = 4.14$ (to be compared with the observed 4.25 ± 0.09), [N II]$\lambda6584$/H$\alpha = 0.09$ (0.10 ± 0.01), [S II]$\lambda\lambda6717,6731$/H$\alpha = 0.18$ (0.18 ± 0.01), [O II]$\lambda3727$/[O III]$\lambda5007 = 0.68$ (0.66 ± 0.01), Si III]$\lambda1888$/C III]$\lambda1908 = 0.16$ (0.33 ± 0.07), C III]$\lambda1908$/O III]$\lambda1663 = 4.05$ (4.22 ± 0.53) and O III]$\lambda1663$/He II $\lambda1640 = 6.84$ (4.47 ± 2.69). I further find that the predictions of my model for the He II $\lambda1640$ emission luminosity in low-metallicity star-forming galaxies are comparable to those of Schaerer (2003). For example, for a Chabrier (2003) IMF truncated at 1 and 100 $\rm M_\odot$ (very similar to the Salpeter 1955 IMF with same lower and upper cutoffs used by Schaerer 2003) and for the metallicity $Z = 0.001$, I find line luminosities between $2.7\times10^{38}\,\rm erg\,s^{-1}$ and $4.04\times10^{39}\,\rm erg\,s^{-1}$ per unit star formation rate (depending on $U_{\rm S}$ and $\xi_{\rm d}$), consistent with the value $8.39\times10^{38}\,\rm erg\,s^{-1}$ in table 4 of Schaerer (2003, his IMF 'A'). The calculations of Schaerer (2003) extend all the way down to zero metallicity. For the smallest metallicity I investigate in my study, $Z = 0.0001$, the model I have developed spans a range of He II $\lambda1640$ luminosities between $1.03 \times 10^{39}\,\rm erg\,s^{-1}$ and $9.70 \times 10^{39}\,\rm erg\,s^{-1}$, which can be compared to the values 2.91×10^{37}, 1.40×10^{39} and $1.74 \times 10^{40}\,\rm erg\,s^{-1}$ at $Z = 10^{-5}$, 10^{-7} and 0. in table 4 of Schaerer (2003).

My fully self-consistent modelling of the nebular emission and chemical composition of the ISM in star-forming galaxies provides a unique way to test the reliability of standard recipes based on the direct-$T_{\rm e}$ method to measure element abundances from emission-line luminosities (e.g., Aller, 1984; Garnett et al., 1995b; Izotov & Thuan, 1999; Izotov et al., 2006; Shapley et al., 2003; Erb et al., 2010). I find that, for gas-phase metallicities around solar to slightly sub-solar, widely used formulae to constrain oxygen ionic fractions and the C/O ratio from ultraviolet and optical emission-line luminosities are reasonably faithful. However, the recipes break down at non-solar metallicities (both low and high; see Section 3.5.2), making their application inappropriate to studies of chemically young galaxies. In such cases, a fully self-consistent model of the kind I have developed in this thesis is required to interpret the observed nebular emission. This can be achieved in an optimal way by appealing to a dedicated spectral analysis tool, such as the BEAGLE tool of Chevallard & Charlot (2016), which already incorporates my model. Finally, I note that, while all the calculations presented in this chapter pertain to ionization-bounded galaxies, my model provides a unique means of investigating the spectral signatures of the escape of ionizing photons from density-bounded galaxies. This will be the subject of a forthcoming study.

I remind that my model grid is available electronically from `http://www.iap.fr/neogal/models.html`.

CHAPTER 4

Comparison between star-forming galaxies and AGN

Contents

Another very interesting application is to use my models of the nebular emission from star-forming galaxies (hereafter 'SF models') to compare with models of active galactic nuclei (hereafter 'AGN models'), and then identify new line-ratio diagnostics to discriminate between gas photoionization by AGN and star formation.

In this section, we confirm the appropriateness of widely used optical spectral diagnostics of nuclear activity versus star formation and explore new diagnostics at ultraviolet wavelengths. We find that combinations of a collisionally excited metal line or line multiplet, such as C IV $\lambda\lambda1548, 1551$, O III]$\lambda\lambda1661, 1666$, N III]$\lambda1750$, [Si III]$\lambda1883$+Si III]$\lambda1892$ and [C III]$\lambda1907$+C III]$\lambda1909$, with the He II $\lambda1640$ recombination line are individually good discriminants of the nature of the ionizing source. Diagrams involving at least 3 of these lines allow an even more stringent distinction between active and inactive galaxies, as well as valuable constraints on interstellar gas parameters and the shape of the ionizing radiation. Several line ratios involving Ne-based emission lines, such as [Ne IV]$\lambda2424$, [Ne III]$\lambda3343$ and [Ne V]$\lambda3426$, are also good diagnostics of nuclear activity. Our results provide a comprehensive framework to identify the sources of photoionization and physical conditions of the ionized gas from the ultraviolet and optical nebular emission from galaxies. Again, this will be particularly useful to interpret observations of high-redshift galaxies with future facilities, such as the *JWST* and extremely large ground-based telescopes.

We note that this section is extracted from the paper *Nuclear activity versus star formation: emission-line diagnostics at ultraviolet and optical wavelengths* by Anna Feltre, Stéphane Charlot and Julia Gutkin, published in the Monthly Notices of the Royal Astronomical Society.

4.1 Introduction

Studies of the nebular emission from H II regions and AGN often rely on the predictions of standard photoionization codes, such as MAPPINGS (Sutherland & Dopita, 1993; Allen et al., 2008; Dopita et al., 2013) and CLOUDY (Ferland, 1993; Ferland et al., 1998, 2013), which have both undergone regular updates over the past decades. These studies have shown that important constraints on the density, ionization and metallicity of the photoionized gas can be derived from the relative intensities of ultraviolet and (mainly) optical emission lines. This has led to the identification of standard optical line-ratio diagnostic diagrams to separate nebular emission from active and inactive galaxies, such as the Baldwin, Phillips & Terlevich (1981, BPT) and Veilleux & Osterbrock (1987) diagrams based on the Hα, Hβ, [O II]$\lambda3727$, [O III]$\lambda5007$, [O I]$\lambda6300$, [N II]$\lambda6584$ and [S II]$\lambda\lambda6717, 6731$ emission lines, of the type presented in the previous chapter. In addition, ultraviolet emission lines have proven to be useful to distinguish between photoionization by AGN and shocks (e.g. Villar-Martin, Tadhunter & Clark, 1997; Allen, Dopita & Tsvetanov, 1998), while they have not been systematically investigated yet to discriminate between nuclear activity and star formation.

We now compute a large grid of photoionization models of AGN narrow-line regions, which we combine with predictions of the nebular emission from star-forming galaxies presented in Chapter 3, to explore new line-ratio diagnostics of photoionization by nuclear activity and star formation in galaxies. To perform a meaningful analysis, we compute photoionization models of AGN narrow-line regions using the same code as I have developed to compute models of nebular emission from star-forming galaxies, and adopt the same parametrization of the metal and dust content in the ionized gas. We establish the suitability of these models by showing that they confirm previous widely used observational criteria to separate active from inactive galaxies in optical line-ratio diagrams (BPT; Veilleux & Osterbrock, 1987). On these grounds, we investigate the extent to which the relative intensities of ultraviolet lines commonly detected in galaxy spectra can allow one to discriminate between photoionization by an AGN and star formation. This leads us to propose new ultraviolet spectral diagnostics of the nature of ionizing radiation, which should be particularly useful to prepare the exploration of galaxies near the reionization epoch with future facilities, such as *JWST* and ground-based ELT.

4.2 Photoionization models from AGN

As we have seen in Section 3.2, in the computation of nebular emission from star-forming galaxies, the rate of ionizing photons produced by a star cluster evolves as the stellar population ages, and the nebular emission from an entire galaxy is computed by convolving that of individual star clusters with the star formation history.

In the case of photoionization by an AGN power source (i.e. the accretion disc surrounding a central black hole; see Section 4.2.1), we may assume that the ionizing source does not evolve in time. In this case, the analog of equation (3.4) for the effective rate of ionizing photons seen by gas irradiated by an accretion disc of luminosity L_{AGN} is

$$Q = L_{\mathrm{AGN}} \int_{\nu_{\mathrm{L}}}^{\infty} d\nu \frac{S_\nu}{h\nu} , \tag{4.1}$$

where h is the Planck constant and ν_{L} is the frequency at the Lyman limit, $h\nu_{\mathrm{L}} = 13.6\,\mathrm{eV}$. In this expression, the quantity S_ν is the luminosity per unit frequency of the accretion disc (equation 4.5 below).

We then have the same definitions of the ionization parameter at the distance r from the ionizing source, $U(r)$, the Strömgren radius, R_{S}, and the ionization parameter at the Strömgren radius, U_{S}, as adopted in equations (3.5) (3.6) (3.7) respectively, but not depending anymore on time, i.e.

$$U(r) = Q/(4\pi r^2 n_{\mathrm{H}} c) , \tag{4.2}$$

where Q is the rate of the ionizing photons (in s^{-1}) now defined by equation (4.1), and

$$R_{\mathrm{S}}^3 = 3Q/(4\pi n_{\mathrm{H}}^2 \epsilon \alpha_{\mathrm{B}}) , \tag{4.3}$$

$$U_{\mathrm{S}} = \frac{\alpha_{\mathrm{B}}^{2/3}}{3c} \left(\frac{3Q\epsilon^2 n_{\mathrm{H}}}{4\pi} \right)^{1/3} \approx \langle U \rangle / 3 . \tag{4.4}$$

All calculations presented in this chapter account for the depletion of metals onto dust grains in the photoionized gas and the associated absorption and scattering of incident radiation, radiation pressure, collisional cooling and photoelectric heating of the gas (see, e.g., Ferland 1996, but also Shields & Kennicutt 1995, Dopita et al. 2002 and Groves, Dopita & Sutherland 2004a for a description of these effects on the emergent nebular emission). One of the most notable effects of the depletion of metals from the gas phase is the less efficient cooling through infrared fine-structure transitions, which increases the electron temperature, and hence, cooling through the more energetic optical transitions. Exactly as done until now, we adopt the default dust properties of CLOUDY, consisting of a mixture of graphite and silicates with a standard Mathis, Rumpl & Nordsieck (1977) grain size distribution and optical properties from Martin & Rouleau (1991). We now describe in more detail the parametrization of our photoionization models of AGN.

4.2.1 Narrow-line regions of AGN

At least 3 approaches have been adopted in the past to parametrize the gas distribution in photoionization models of AGN narrow-line regions: (i) a combination of matter- and ionization-bounded clouds (Binette, Wilson & Storchi-Bergmann, 1996); (ii) the 'locally emitting clouds' model (Ferguson et al., 1997), which combines clouds of different densities at different distances from the ionizing source; and, more recently, (iii) clouds of a single type, but including dust and dominated by radiation pressure (Dopita et al., 2002; Groves, Dopita & Sutherland, 2004a). This third kind of approach has been shown to provide good agreement with observations over a wide range of ionization parameters (most recently by, e.g., Richardson et al. 2014). It is therefore the one we adopt in the present work.

Contrary to the 'closed geometry' used in the previous chapter to compute SF models with CLOUDY, as appropriate for spherical H II regions, we adopt here the so-called 'open geometry', appropriate for gas with small covering factor (typically less than 10 per cent for AGN narrow-line regions; Maiolino, Marconi & Oliva, 2001; Baskin & Laor, 2005), and describe the physical conditions of the photoionized gas in terms of the following main adjustable parameters, also listed in Table 4.1.

Luminosity per unit frequency S_ν of the accretion disc. The emission from the accretion disc in an AGN is usually approximated by a broken power law, for which we adopt here the form

$$S_\nu \propto \begin{cases} \nu^{\alpha} & \text{at wavelengths} \quad 0.001 \le \lambda/\mu m \le 0.25\,, \\ \nu^{-0.5} & \text{at wavelengths} \quad 0.25 < \lambda/\mu m \le 10.0\,, \\ \nu^{2} & \text{at wavelengths} \quad \lambda/\mu m > 10.0\,. \end{cases} \tag{4.5}$$

Hence, we keep the power-law index α at ultraviolet and optical wavelengths as an adjustable parameter. We explore values of this parameter in the range $-2.0 \le \alpha \le -1.2$, encompassing values often adopted in the literature (e.g., Groves, Dopita & Sutherland, 2004a) and consistent with observational constraints. For example, Zheng et al. (1997) find $\alpha \approx -1.8$ in the composite spectrum of 41 radio-quiet quasars at redshifts $0.3 \lesssim z \lesssim 1.5$ observed with the *HST* Faint Object Spectrograph, while Lusso et al. (2015) find the stacked ultraviolet spectrum of 53 quasars at $z \sim 2.4$ observed with the *HST* Wide Field Camera 3 to have a slope of $\alpha \approx -1.7$ blueward of Lyα. The power-law indices at longer wavelengths in expression (4.5) are taken from Feltre et al. (2012). We adopt a fixed accretion-disc luminosity $L_{\rm AGN} = 10^{45}$ erg s^{-1} cm^{-2} and an inner radius of the narrow-line region $r_{\rm in} \approx 300$ pc, corresponding to an incident flux of $L_{\rm AGN}/4\pi r_{\rm in}^2 \approx 10^2$ erg s^{-1} cm^{-2} (Netzer, 2013).

Ionization parameter $U_{\rm S}$ at the Strömgren radius. This is related to the gas density, $n_{\rm H}$, the volume-filling factor of the gas, ϵ, and the rate of ionizing photons, Q, via equation (4.4). As adopted until now, we consider below values of this parameter in the range $-4.0 \le \log U_{\rm S} \le -1.0$. We note that other authors sometimes use the ionization parameter at the inner edge $r_{\rm in}$ of the narrow-line region, noted U_0, as an adjustable parameter (e.g. Groves, Dopita & Sutherland, 2004b; Nagao, Maiolino & Marconi, 2006). According to equation (4.2), U_0 will be larger than U_S for $r_{in} \ll R_S$ and more similar to U_S for $r_{in} \gtrsim R_S$.

Hydrogen number density n_H. We consider values of this parameter in the range $10^2 \leq n_H/\mathrm{cm}^3 \leq 10^4$ (in addition to the values explored in the SF models, we also run test models with densities up to $n_H = 10^6$ cm^{-3}).

Gas metallicity Z. We adopt the same relative abundances of heavy elements as described in Section 3.2.3, taken from Bressan et al. (2012, largely based on Caffau et al. 2010) for solar metallicity. As explained in Section 3.2.3, all heavy elements except nitrogen are assumed to scale linearly with oxygen abundance. Secondary production of nitrogen is accounted for following the prescription of Groves, Dopita & Sutherland (2004a), and the nitrogen abundance is properly rescaled to account for the difference in solar abundance between Bressan et al. (2012) and Groves, Dopita & Sutherland (2004a), as expressed in equation (3.11). The helium abundance is again given by equation (3.12) (Bressan et al., 2012). The present-age solar metallicity adopted in this work is $Z_\odot = 0.01524$ (Bressan et al., 2012), and we compute AGN models for 15 values of the metallicity across the range $0.0001 \leq Z \leq 0.070$ (this includes higher metallicities than considered for the SF models).

Dust-to-heavy element mass ratio ξ_d. This accounts for the depletion of metals onto dust grains in the ionized gas. To explore the impact of the presence of dust on the emission line properties and diagnostics, as for the SF models, we consider values of the dust-to-metal mass ratio in the range $0.1 \leq \xi_d \leq 0.5$.

Parameter	AGN narrow-line regions	Star-forming galaxies
Ionizing spectrum	$\alpha = -1.2, -1.4, -1.7, -2.0$	constant star formation rate, age = 10^8 yr
$\log U_S$	$-1.0, -2.0, -3.0, -4.0$	$-1.0, -1.5, -2.0, -2.5, -3.0, -3.5, -4.0$
$\log(n_H/\mathrm{cm}^{-3})$	2.0, 3.0, 4.0	1.0, 2.0, 3.0, 4.0
Z	0.0001, 0.0002, 0.0005, 0.001, 0.002, 0.004, 0.006, 0.008, 0.014, 0.01774, 0.030, 0.040, 0.050, 0.060, 0.070	0.0001, 0.0002, 0.0005, 0.001, 0.002, 0.004, 0.006, 0.008, 0.010, 0.014, 0.017, 0.020, 0.030, 0.040
ξ_d	0.1, 0.3, 0.5	0.1, 0.3, 0.5

Table 4.1: Adjustable parameters of the AGN narrow-line region (second column) and SF (third column) photoionization models. See Section 4.2 for details.

4.2.2 Differences between AGN and SF models

The main motivation of the present work is to identify emission-line diagnostics of active versus inactive galaxies. To this end, we compare the AGN photoionization models described in the previous subsection with the models of the nebular emission from star-forming galaxies described in Chapter 3. As a reminder, these calculations combine the latest version of the Bruzual & Charlot (2003) stellar population synthesis model (Charlot & Bruzual, in preparation) with the photoionization code CLOUDY, by convolving the spectral evolution of single, ionization bounded H II regions with a star formation history to compute the nebular emission of a whole galaxy. In this context, the parameters of the photoionization model should be interpreted as effective (i.e. galaxy-wide) ones, describing the ensemble of H II regions and the diffuse gas ionized by stars throughout the galaxy.

In Chapter 3, I have ran a large grid of SF models encompassing models with both solar and non-solar C/O abundance ratio and different stellar IMFs and star formation histories (Section 3.2). In this chapter, we consider only the models for a standard, solar C/O abundance ratio of 0.44, a standard Chabrier (2003) IMF truncated at 0.1 and 100 $M_\odot$ and constant star formation rate, at an age of 100 Myr. I remind that the star formation history and age have a negligible influence on the predicted emission-line ratios, so long as star formation has been constant for at least 10 Myr, corresponding to the age over which 99.9 per cent of the ionizing photons are released by a single stellar generation (e.g. CL01). In the rightmost column of Table 4.1, we remind for comparison the ranges in ionization parameter, $-4.0 \leq \log U_\mathrm{S} \leq -1.0$, gas density, $10 \leq n_\mathrm{H}/\mathrm{cm}^3 \leq 10^4$, metallicity, $0.0001 \leq Z \leq 0.030$, and dust-to-metal mass ratio, $0.1 \leq \xi_\mathrm{d} \leq 0.5$, covered by the grid of SF models considered here. In these calculations, the metallicity of the ionizing stars is again always taken to be the same as that of the photoionized gas.

The main feature differentiating models of active versus inactive galaxies in Table 4.1 is the spectral energy distribution of the incident ionizing radiation. In this respect, a comparison between the input ionizing spectra associated with AGN and SF models is instructive to understand the differences in the predictions of these models outlined in Sections 4.3 and 4.4. In Fig. 4.1 (inspired from fig. 19 of Steidel et al. 2014 and fig. 4 of Stark et al. 2015b), we compare the spectral energy distributions of AGN models with various spectral indices (grey shaded area) to that of SF models with two metallicities, $Z = 0.001$ (blue line) and 0.030 (orange line). The two stellar population spectra start to differ significantly at photon energies greater than 20 eV, the lowest-metallicity one being the hardest, as low-metallicity stars evolve at higher temperatures and luminosities than high-metallicity ones (e.g., Chen et al., 2015). We also note that up to energies of ~ 30 eV, the spectra of AGN accretion discs and star-forming galaxies are relatively similar, while above ~ 50 eV, the stellar population spectra drop abruptly. Thus, emission lines associated with ion species requiring ionization energies greater than 50 eV should be the most promising indicators of the presence of an AGN, as we shall see in the following sections (see also Steidel et al., 2014; Stark et al., 2015b).

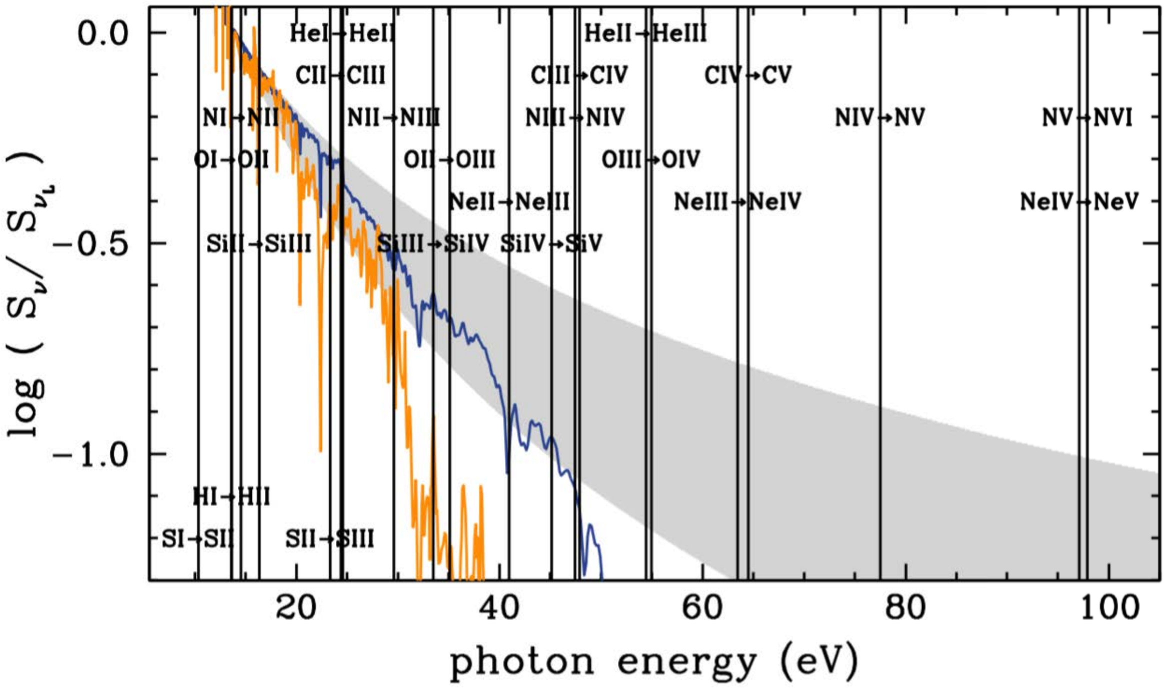

Figure 4.1: Examples of spectral energy distributions (in units of the luminosity per unit frequency at the Lyman limit) of the incident ionizing radiation in the AGN and SF models of Table 4.1. The grey shaded area indicates the location of AGN ionizing spectra with power-law indices between $\alpha = -2.0$ (bottom edge) and -1.2 (top edge). The blue and orange lines show the ionizing spectra of stellar populations of metallicities $Z = 0.001$ and 0.030, respectively. Vertical lines indicate the ionizing energies of ions of different species.

4.3 Optical emission lines and standard AGN/star-formation diagnostics

The luminosity ratios of strong optical emission lines are standard diagnostics of the source of the ionizing radiation in external galaxies, as they allow one to discriminate between the spectra of H II regions (i.e. star-forming galaxy) and those of type-2 AGN (i.e. narrow-line regions; e.g. BPT; Veilleux & Osterbrock, 1987). As a result, diagnostic diagrams defined by optical lines ratios, such as [O III]λ5007/Hβ, [N II]λ6584/Hα, [S II]λ6724/Hα and [O I]λ6300/Hα, are widely used in the literature to interpret observations of the nebular emission from active and inactive galaxies (e.g. Dopita et al., 2002; Kauffmann et al., 2003; Groves, Dopita & Sutherland, 2004b; Kewley et al., 2001, 2006, 2013b,a). In this section, we show that the models presented in Section 4.2 reproduce well observations of nearby galaxies powered by either star formation or an AGN in different standard optical line-ratio diagrams.

We also investigate the dependence of these line ratios on the adjustable parameters of the models.

4.3.1 SDSS observational sample

To establish the usefulness of our AGN and SF models to interpret observations of the nebular emission from galaxies, we appeal to high-quality observations of nearby galaxies from the Sloan Digital Sky Survey Data Release 7 (SDSS DR7; Abazajian & Survey, 2008).[1] By analogy with Juneau et al. (2014, see also Kewley et al. 2006; Yuan, Kewley & Sanders 2010), we select all primary targets (SCIENCEPRIMARY = 1) in the redshift range $0.04 \leq z \leq 0.2$. The lower redshift cut limits the influence of strong aperture effects, while the upper one allows the detection of galaxies with intrinsically weak emission lines while increasing the statistics on Seyfert 2 galaxies (Juneau et al., 2014). We consider only those galaxies with measurements available simultaneously for all six optical emission lines entering the definitions of the diagnostics mentioned above, i.e., Hβ, [O III]λ5007, [O I]λ6300, Hα, [N II]λ6584 and [S II]λ6724. Following Juneau et al. (2014), we further select galaxies according to signal-to-noise ratio (S/N) in line-ratio rather than individual-line measurements, which allows the sampling of a wider range of intrinsic emission-line properties (we use the factors in table 4 of Juneau et al. 2014 to scale up the formal errors in flux-ratio uncertainties in the MPA-JHU catalogs, as inferred from the results of duplicate observations of the same galaxies). We adopt the same criterion as these authors and require $\mathrm{S/N} > 2.12$ $(= 3/\sqrt{2})$ in the emission-line ratios of interest to us, i.e., [O III]λ5007/Hβ, [N II]λ6584/Hα, [S II]λ6724/Hα and [O I]λ6300/Hα. This leaves us with a final sample of 202,083 galaxies with high-quality line-ratio measurements. We correct the emission-line ratios for attenuation by dust, based on the departure of the observed Balmer decrement from the dust-free case-B recombination value and using the standard reddening curve of Cardelli, Clayton & Mathis (1989).

4.3.2 [O III]λ5007 Hβ versus [N II]λ6584 Hα diagram

We start by considering the standard [O III]λ5007/Hβ versus [N II]λ6584/Hα diagram originally proposed by BPT to discriminate between AGN and star-forming galaxies. Fig. 4.2 shows several versions of this diagram, in which we plot AGN and SF models with different input parameters over the SDSS observations described in Section 4.3.1. Each panel corresponds to different assumptions about the gas density, n_{H} (increasing from left to right), and metallicity, Z (increasing from top to bottom), as indicated. Also indicated in parenthesis is the interstellar oxygen abundance, which includes the components in the gas and dust phases. In each panel, we show AGN models corresponding to wide ranges in power-law index, α, and ionization parameter, U_{S}, and SF models corresponding to the same range in U_{S}. The long-dashed and dot-dashed black lines indicate, respectively, the popular criteria of Kewley et al. (2001) and Kauffmann et al. (2003) to distinguish AGN from star-forming galaxies.

---

[1] We use the emission-line measurements made available online by the Max-Planck-Institute for Astrophysics (Garching) and Johns Hopkins University (MPA-JHU) collaboration in the file `SepcObjAll.fits` at http://home.strw.leidenuniv.nl/~jarle/SDSS/.

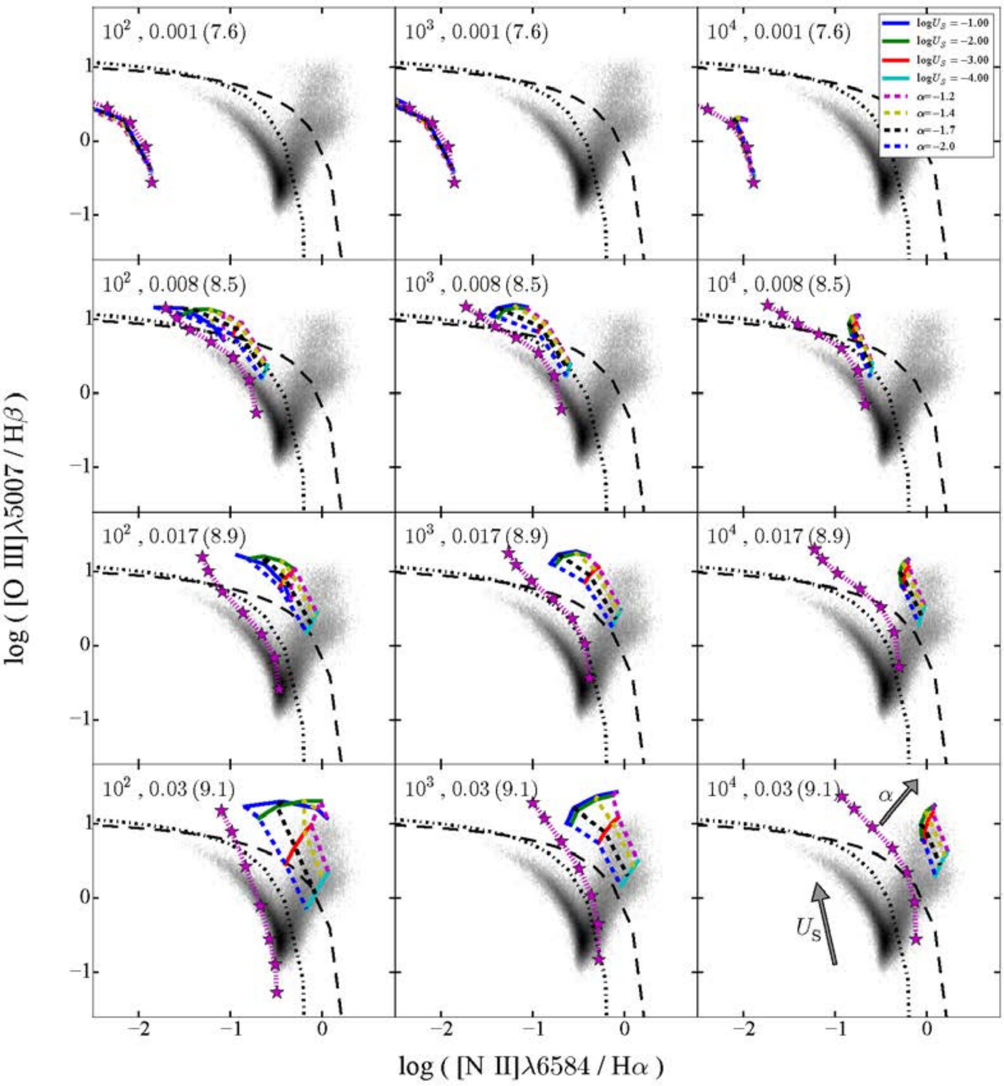

Figure 4.2: Predictions of the AGN and SF models described in Section 4.2 in the standard [O III]λ5007/Hβ versus [N II]λ6584/Hα BPT diagnostic diagram, for different assumptions about the gas density ($n_{\rm H} = 10^2$, 10^3 and 10^4 cm^{-3} from left to right) and metallicity (Z = 0.0001, 0.001, 0.01774, and 0.030 from top to bottom). Also indicated in parenthesis in each panel is the interstellar oxygen abundance, 12 + log (O/H), which includes the components in the gas and dust phases. In each panel, we show AGN models corresponding to wide ranges in power-law index, $-2.0 \le \alpha \le -1.2$, and ionization parameter, $-4.0 \le \log U_{\rm S} \le -1.0$ (both increasing from bottom to top as indicated in the lower-right panel, and colour-coded as indicated in the top-right panel), and SF models (magenta stars) corresponding to the same range in $U_{\rm S}$. In each panel, the data are the SDSS observations described in Section 4.3.1, while the long-dashed and dot-dashed black lines indicate, respectively, the criteria of Kewley et al. (2001) and Kauffmann et al. (2003) to distinguish AGN from star-forming galaxies.

It is important to note that the parameter ranges considered in Fig. 4.2 encompass wider combinations of $n_{\rm H}$, Z and $U_{\rm S}$ than typically observed in the nearby Universe. For example, low-metallicity AGN are extremely rare in local surveys such as the SDSS (Groves, Heckman & Kauffmann, 2006), while in star-forming galaxies, there appears to be an anticorrelation between ionization parameter and metallicity, in the sense that metal-rich galaxies are generally found to have only modest ionization parameters (e.g., Brinchmann et al., 2004), as noted in Section 3.3.2. Also, gas densities estimated from optical line-doublet analyses are typically around $n_{\rm H} \sim 10^3$ cm^{-3} for AGN narrow-line regions and $n_{\rm H} \sim 10^2$ cm^{-3} for SF models (e.g., sections 5.6 and 13.4 of Osterbrock & Ferland, 2006). This should be kept in mind when examining the location of models relative to SDSS data in Fig. 4.2.

Fig. 4.2 (top panels) shows that, at low metallicity ($Z \lesssim 0.008$), AGN and SF models predict similar [O III]λ5007/Hβ and [N II]λ6584/Hα optical line ratios, on the side of the BPT diagram corresponding to star-forming galaxies. This is expected from the similarity of the spectra of accretion discs and low-metallicity stellar populations at the ionizing energies of these ions (Fig. 4.1). As metallicity increases (from top to bottom in Fig. 4.2), AGN and SF models start occupying distinct regions of the BPT diagram, on either side of the Kewley et al. 2001 and Kauffmann et al. (2003) criteria (SF models falling in the AGN part of the diagram are those combining high $U_{\rm S}$ and high Z). This is consistent with the results from previous studies that gas in local AGN is generally found to be metal-rich, with $9.0 < \log({\rm O/H}) + 12 < 9.3$ (e.g. Kewley & Dopita, 2002; Groves, Dopita & Sutherland, 2004a). The rise in [O III]λ5007/Hβ and [N II]λ6584/Hα for both AGN and SF models as metallicity increases in Fig. 4.2 follows from the increase in the abundance of coolants. The effect is more pronounced for [N II]λ6584/Hα than for [O III]λ5007/Hβ because of secondary nitrogen production at $Z \gtrsim 0.1{\rm Z}_\odot$ (Groves, Dopita & Sutherland, 2004b, Section 4.2.1 above). At the highest metallicity, [O III]λ5007/Hβ and [N II]λ6584/Hα start to decline again, because the high efficiency of cooling makes the electronic temperature (and hence collisional excitation) drop. We also note in Fig. 4.2 that, as expected from Fig. 4.1, flattening the ionizing spectrum by increasing the power-law index α makes both [O III]λ5007/Hβ and [N II]λ6584/Hα larger for AGN models, the effect being more pronounced at high than at low metallicity and ionization parameter. The SDSS observations are compatible with the entire explored range of spectral slopes.

Fig. 4.2 further confirms that, as noted by Groves, Dopita & Sutherland (2004b), the [O III]λ5007/Hβ and [N II]λ6584/Hα optical emission-line ratios tend to be less sensitive to changes in density, over the range from 10^2 to 10^4 cm^{-3}, than to changes in metallicity and ionization parameter. When $n_{\rm H}$ exceeds the critical density for which the efficiency of collisional de-excitation reaches that of radiative cooling for infrared fine-structure transitions (typically a few times 10^3 cm^{-3}), the electronic temperature rises (Stasińska, 1990). Radiative cooling through optical transitions, which have higher critical densities (about 10^5 cm^{-3} for [N II]λ6584 and 10^6 cm^{-3} for [O III]λ5007), increases, causing O III]λ1663/Hβ and especially [N II]λ6584/Hα to increase. The effect is more pronounced at high than at low metallicity, and for SF than for AGN models (O III]λ1663/Hβ even slightly drops for $n_{\rm H} \gtrsim 10^4$ cm^{-3} in AGN models with the highest $U_{\rm S}$). We note that, at metallicities $Z \gtrsim 0.017$ and gas densities $n_{\rm H} \gtrsim 10^3$ cm^{-3}, AGN models with ionization parameters across the full explored range ($-4 \leq \log U_{\rm S} \leq -1$) are compatible with SDSS data in Fig. 4.2. At lower $n_{\rm H}$, only ionization parameters $\log U_{\rm S} \lesssim -3$ are favored. For completeness, we also computed AGN models gas densities $n_{\rm H} = 10^5$ and 10^6 cm^{-3} (not shown). While models with $n_{\rm H} = 10^5$ cm^{-3} are still marginally consistent with SDSS data in Fig. 4.2, at least for metallicities in the range

$0.017 \lesssim Z \lesssim 0.030$, this is not the case for those with $n_{\rm H} = 10^6$ cm^{-3}. The inappropriateness of models with extreme $n_{\rm H}$ to reproduce observations is consistent with the conclusion reached by Nagao, Maiolino & Marconi (2006) from the analysis of ultraviolet emission lines in narrow-line regions in high-redshift AGN (using a similar, but simplified model).

It is worth pointing out that, unlike Dopita et al. (2002) and Groves, Dopita & Sutherland (2004b), who show that dusty, radiation-pressure dominated models are able to reproduce in a natural way observed ultraviolet and optical emission-line properties of AGN across a wide range of ionization parameters, Nagao, Maiolino & Marconi (2006) reach a different conclusion in claiming that high-ionization AGN are best reproduced by dust-free models. Fig. 4.3 illustrates the effect of metal depletion onto dust grains in our AGN models in the [O III]λ5007/Hβ versus [N II]λ6584/Hα BPT diagram. We show models corresponding to $n_{\rm H} = 10^3$ cm^{-3}, $Z = 0.030$ and dust-to-metal mass ratios $\xi_{\rm d} = 0.1$, 0.3 and 0.5, from left to right. As $\xi_{\rm d}$ rises, the removal of coolants from the gas phase reduces the cooling efficiency through infrared-fine structure transitions. This makes the electronic temperature rise, and hence cooling through the optical transitions larger (Shields & Kennicutt, 1995; Charlot & Longhetti, 2001). For important refractory coolants, such as oxygen, the effect of depletion is compensated by the rise in electronic temperature, in such a way that [O III]λ5007/Hβ increases only slightly in Fig. 4.3 as $\xi_{\rm d}$ increases. The emission-lines strengths of non-refractory elements, such as nitrogen and sulfur, increase more significantly, as illustrated by the implied significant rise in [N II]λ6584/Hα.

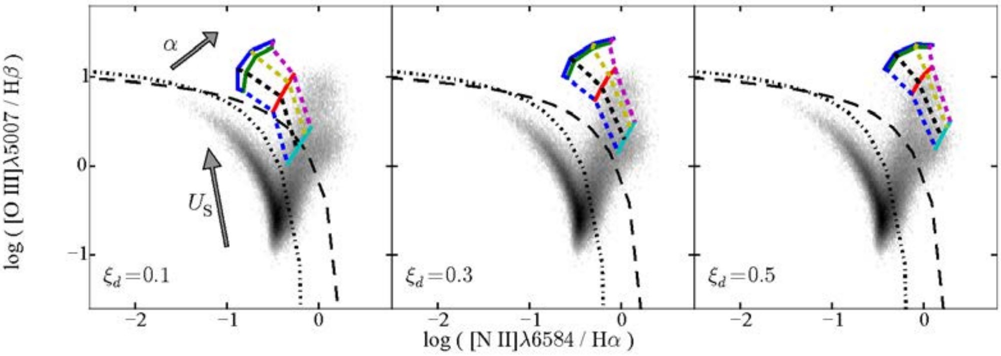

Figure 4.3: Predictions of the AGN models described in Section 4.2 in the [O III]λ5007/Hβ versus [N II]λ6584/Hα BPT diagram, for a gas density $n_{\rm H} = 10^3$ cm^{-3}, a metallicity $Z = 0.030$ and dust-to-metal mass ratios $\xi_{\rm d} = 0.1$, 0.3 and 0.5, from left to right. In each panel, we show AGN models corresponding to wide ranges in power-law index, $-2.0 \leq \alpha \leq -1.2$, and ionization parameter, $-4.0 \leq \log U_{\rm S} \leq -1.0$. The data and colour coding of the models are the same as in Fig. 4.2. The long-dashed and dot-dashed black lines indicate, respectively, the criteria of Kewley et al. (2001) and Kauffmann et al. (2003) to distinguish AGN from star-forming galaxies.

4.3.3 Other AGN/star-formation diagnostic diagrams

Other optical line-ratio diagrams have been proposed to discriminate between AGN and star-forming galaxies, such as the [O III]λ5007/Hβ versus [S II]λ6724/Hα and [O III]λ5007/Hβ versus [O I]λ6300/Hα diagrams (Veilleux & Osterbrock, 1987). We show in Fig. 4.4 how our AGN and SF models behave in these diagrams, for two values of the metallicity, $Z = 0.008$ and 0.030, a dust-to-metal mass ratio in the middle of the explored range, $\xi_\mathrm{d} = 0.3$, and the same ranges in power-law index, α, and ionization parameter, U_S, as in Fig. 4.2. For simplicity, we adopt a single choice of gas density, which differs for the AGN models, $n_\mathrm{H} = 10^3\ \mathrm{cm}^{-3}$, and the SF models, $n_\mathrm{H} = 10^2\ \mathrm{cm}^{-3}$. As mentioned above, these values are those typically estimated from optical line-doublet analyses in nearby active and inactive galaxies (e.g., sections 5.6 and 13.4 of Osterbrock & Ferland, 2006).

The results of Fig. 4.4 are qualitatively similar to those obtained for the standard [O III]λ5007/Hβ versus [N II]λ6584/Hα BPT diagram in Fig. 4.2, confirming the success of our AGN and SF models to account for the observed optical emission-line properties of active and inactive galaxies, on either side of the Kewley et al. (2001) separation criterion (long-dashed line in Fig. 4.4). In fact, by exploring models (not shown) across the full ranges in n_H, Z and ξ_d considered in Figs 4.2 and 4.4, we find that the dependence of [S II]λ6724/Hα and [O I]λ6300/Hα on these parameters is similar to that of [O III]λ5007/Hβ and [N II]λ6584/Hα described in Section 4.3.2. We conclude that the photoionization models presented in Section 4.2 reproduce well the observed optical properties of AGN narrow-line regions and star-forming galaxies in the nearby Universe. These models therefore provide a solid foundation to explore the emission-line properties of active and inactive galaxies at ultraviolet wavelengths.

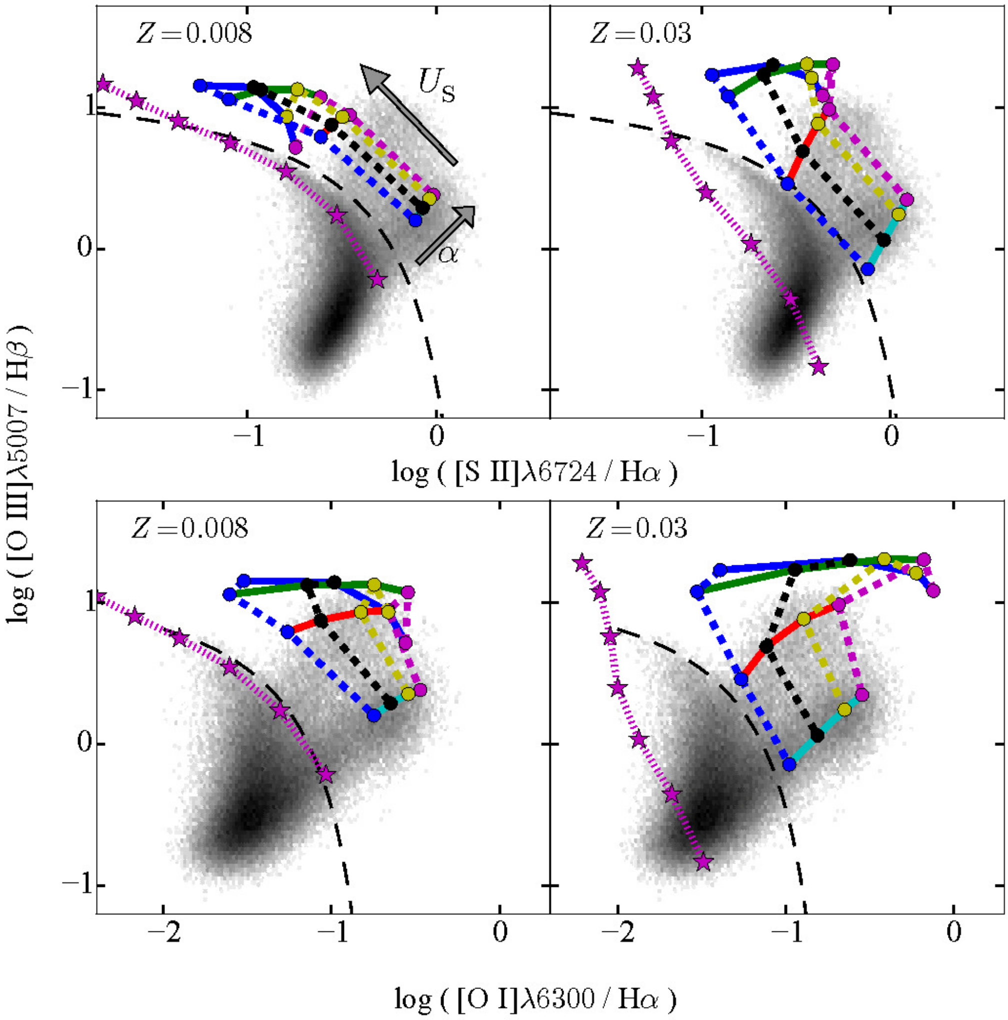

Figure 4.4: Predictions of the AGN and SF models described in Section 4.2 in the [O III]λ5007/Hβ versus [S II]λ6724/Hα (top) and [O III]λ5007/Hβ versus [O I]λ6300/Hα (bottom) diagrams of Veilleux & Osterbrock (1987), for two values of the metallicity, Z = 0.008 (left) and 0.030 (right), and a dust-to-metal mass ratio ξ_d = 0.3. In each panel, we show AGN models corresponding to wide ranges in power-law index, $-2.0 \leq \alpha \leq -1.2$, and ionization parameter, $-4.0 \leq \log U_S \leq -1.0$ (both increasing from bottom to top as indicated in the upper-left panel, and colour-coded as in Fig. 4.2), and SF models corresponding to the same range in U_S. AGN and SF models have gas densities n_H = 10^3 and 10^2 cm^{-3}, respectively. The long-dashed black line indicates the criterion of Kewley et al. (2001) to distinguish AGN from star-forming galaxies.

4.4 Ultraviolet emission lines and new AGN/star-formation diagnostics

In this section, we examine the ultraviolet properties of the photoionization models of AGN narrow-line regions and star-forming galaxies presented in Section 4.2, which we showed in Section 4.3 to reproduce well the optical emission-line properties of nearby active and inactive galaxies. We consider primarily, but not exclusively, far- and near-ultraviolet emission lines commonly detected in the spectra of high-redshift galaxies, with the goal to identify the best spectral diagnostics to discriminate between AGN and star-forming galaxies. Specifically, we consider the lines N V λ1240 (multiplet), O I λ1304 (triplet), S IV λ1397+O IV]λ1402 (hereafter simply S IV+O IV]λ1400), [N IV]λ1483+N IV]λ1487 (hereafter simply N IV]λ1485), C IV λ1550, He II λ1640, O III]$\lambda\lambda$1661, 1666 (hereafter simply O III]λ1663), N III]λ1750 (multiplet), Si II λ1814 (multiplet), Si III]λ1888, C III]λ1908, [O III]λ2321, [Ne IV]λ2424, [Ne III]λ3343, [Ne V]λ3426 and [O II]λ3727. We focus on luminosity ratios between emission lines relatively close in wavelength to minimize sensitivity of diagnostics to attenuation by dust (Veilleux, 2002), but we also consider particularly promising diagnostics involving lines separated by several hundred angström. We exclude the H-Lyα line from our analysis, because of complications linked to the absorption of this resonant line by dust and, at high redshift, circumgalactic neutral hydrogen (e.g., Charlot & Fall, 1993; Hainline et al., 2011; Schenker et al., 2014).

4.4.1 Ultraviolet observational samples

To compare the predictions of our models with observations of ultraviolet emission lines in active and inactive galaxies, we appeal to two main samples: (i) a sample of 22 type-2 AGN assembled by Dors et al. (2014, and references therein), consisting of 12 Seyfert-2 galaxies in the local Universe, with spectra from the *International Ultraviolet Explorer*, and 10 X-ray selected type-2 quasars at redshift $1.5 \lesssim z \lesssim 4.0$, with VLT/FORS spectra; and (ii) a sample of 5 gravitationally lensed, low-mass star-forming galaxies at redshifts $1.5 \lesssim z \lesssim 3.0$, with Keck/LRIS and VLT/FORS2 spectra from Stark et al. (2014). Line-flux measurements for all these objects are available for N V λ1240, C IV λ1550, He II λ1640 and C III]λ1908. For star-forming galaxies, measurements are also available for N III]λ1750 and Si III]λ1888. We note that line-flux measurements of AGN narrow-line regions can potentially be contaminated by star formation in the host galaxy (e.g. Bonzini et al., 2013; Antonucci et al., 2015).

It is important to point out that the above line measurements were not corrected for attenuation by dust. This is not important for the sample of low-mass star-forming galaxies, which have been shown to be extremely dust-poor Stark et al. (table 7 of 2014). For the AGN sample, we prefer not to correct the observed flux by adopting an arbitrary attenuation curve, as the dispersion between different standard curves is large at ultraviolet wavelengths (e.g., Fig. 9 of Charlot & Fall, 2000). Instead, when comparing AGN models with these data, we compute the attenuation that would be inferred using the Calzetti et al. (2000) curve for a V-band attenuation of one magnitude ($A_{\mathrm{V}} = 1$) and mention when this would have a non-negligible effect on our analysis.

4.4.2 Diagnostics based on the C IV λ1550, He II λ1640 and C III] λ1908 emission lines

Together with the He II λ1640 Balmer recombination line, the C IV λ1550 and C III] λ1908 collisionally excited line doublets are among the most commonly detected ultraviolet emission lines in galaxy spectra. Diagnostics involving the relative intensities of these 3 lines, originally investigated by Villar-Martin, Tadhunter & Clark (1997), are commonly invoked to distinguish between photoionization by AGN and shocks in galaxies. This is because, while AGN and shocks produce similar optical-line ratios, the C IV λ1550/He II λ1640 and C III] λ1908/He II λ1640 ultraviolet-line ratios produced by shocks are predicted to be much larger than those produced by AGN (Allen, Dopita & Tsvetanov, 1998; Groves, Dopita & Sutherland, 2004b, and references therein). These ultraviolet-line ratios have also been used to investigate the metallicity of narrow-line regions of AGN (e.g., Nagao, Maiolino & Marconi, 2006). Indeed, combining either C IV λ1550/He II λ1640 or C III] λ1908/He II λ1640, which are sensitive to metallicity, with C III] λ1908/C IV λ1550, which depends primarily on ionization parameter, provides good diagnostics of the metallicity in these environments (e.g. Groves, Dopita & Sutherland, 2004b). In the following paragraphs, we use the AGN and SF photoionization models presented in Section 4.2 to examine whether C IV λ1550/He II λ1640, C III] λ1908/He II λ1640 and C III] λ1908/C IV λ1550 can help discriminate between active and inactive galaxies.

Figs 4.5 and 4.6 show a collection of AGN and SF models in, respectively, the C III] λ1908/C IV λ1550 versus C IV λ1550/He II λ1640 and C III] λ1908/He II λ1640 versus C IV λ1550/He II λ1640 diagrams. Each panel in these figures corresponds to different assumptions about the gas density, n_H (increasing from left to right), and dust-to-metal ratio, ξ_d (increasing from top to bottom), as indicated. In each panel, we show AGN models corresponding to wide ranges in power-law index, α, and ionization parameter, U_S, and SF models (stars connect by dotted lines) corresponding to the same range in U_S, for different metallicities Z (colour-coded as indicated in the top-right panel). Also shown in Figs 4.5 and 4.6 are the observations of AGN (crosses with error bars) and star-forming galaxies (large diamonds with upper and lower limits) described in Section 4.4.1.

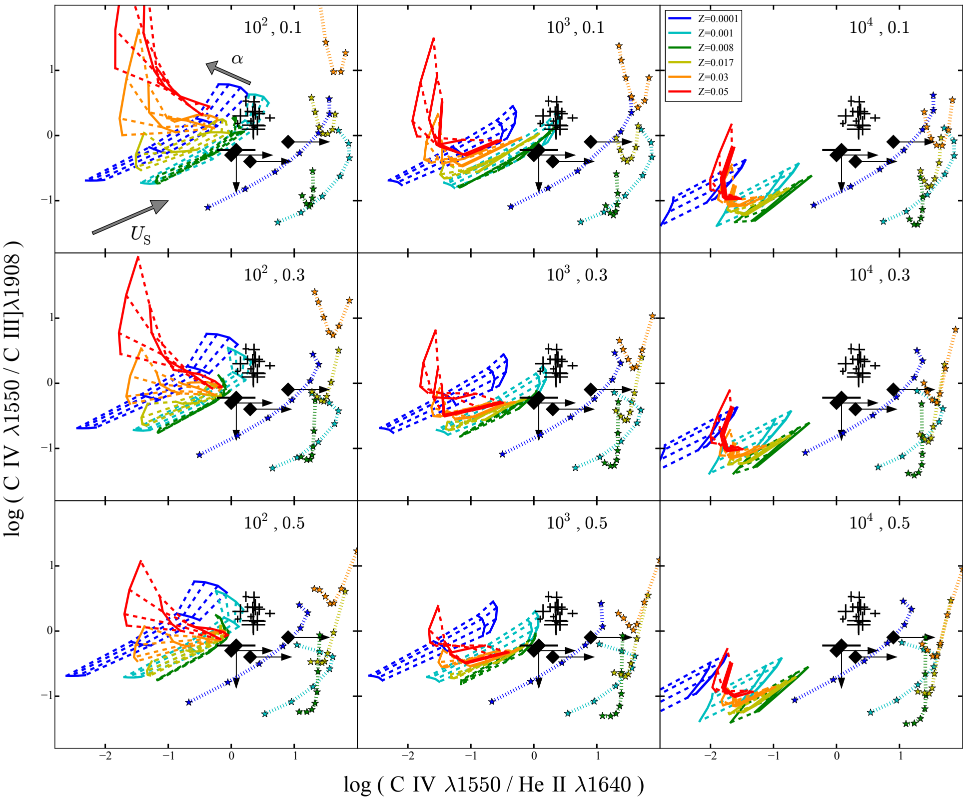

Figure 4.5: Predictions of the AGN and SF models described in Section 4.2 in the C IV $\lambda1550$/C III]$\lambda1908$ versus C IV $\lambda1550$/He II $\lambda1640$ diagnostic diagram, for different assumptions about the gas density ($n_\mathrm{H} = 10^2$, 10^3 and $10^4\ \mathrm{cm}^{-3}$ from left to right) and dust-to-metal mass ratio ($\xi_\mathrm{d} = 0.1$, 0.3 and 0.5 from top to bottom). In each panel, we show AGN models corresponding to wide ranges in power-law index, $-2.0 \leq \alpha \leq -1.2$ (connected by solid lines), and ionization parameter, $-4.0 \leq \log U_\mathrm{S} \leq -1.0$ (connected by dashed lines; α and U_S increasing as indicated in the upper-left panel), and SF models (stars connect by dotted lines) corresponding to the same range in U_S, for different metallicities Z (colour-coded as indicated in the top-right panel). Also shown in each panel are the observations of AGN (crosses with error bars) and star-forming galaxies (large diamonds with upper and lower limits) described in Section 4.4.1.

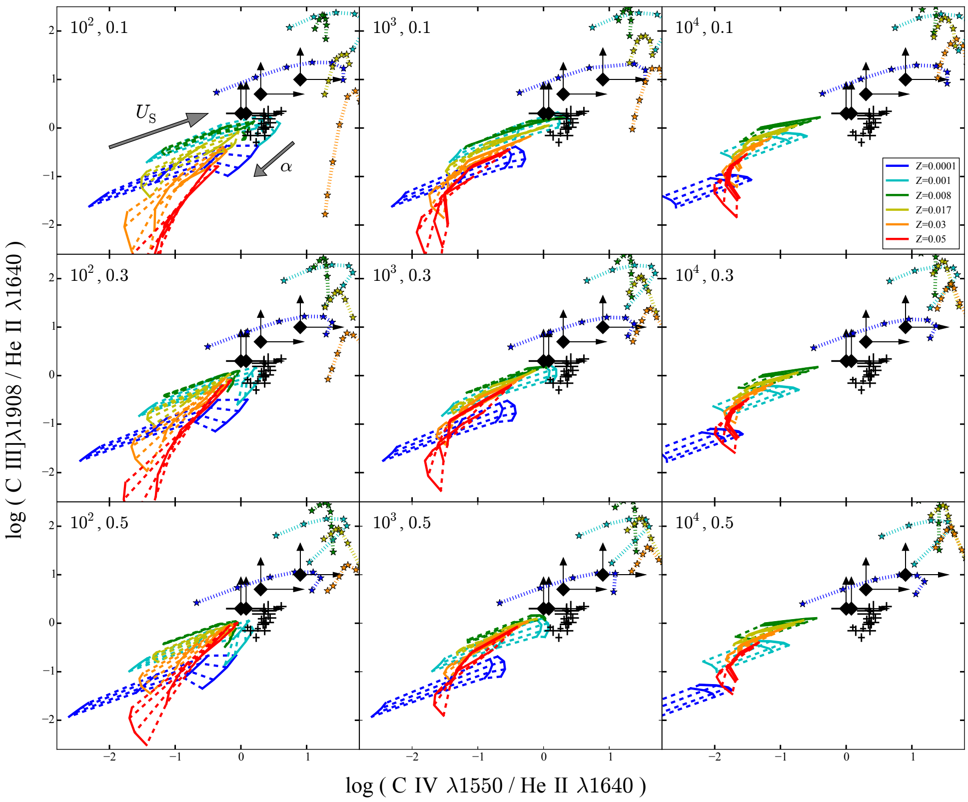

Figure 4.6: Same as Fig. 4.5, but for the C III]λ1908/He II λ1640 versus C IV λ1550/He II λ1640 diagnostic diagram.

The first impression when looking at Figs 4.5 and 4.6 is that models of active and inactive galaxies populate different areas of the C IV λ1550/C III]λ1908 versus C IV λ1550/He II λ1640 and C IV λ1550/He II λ1640 versus C III]λ1908/He II λ1640 diagrams. Furthermore, observations of active galaxies tend to overlap with AGN models (at least for some combinations of parameter), while the upper limits derived from observations of star-forming galaxies point towards SF models. Interestingly, the ultraviolet observations of active galaxies in Figs 4.5 and 4.6 tend to favor AGN models with high ionization parameter, $\log U_S \sim -1$, while the optical observations of SDSS galaxies in Figs 4.2–4.4 were compatible with a much larger range in U_S Groves, Dopita & Sutherland (a similar result was already noted by 2004b). This finding should be modulated by the fact that the SDSS AGN sample is much larger than that with available ultraviolet data in Figs 4.5 and 4.6. Moreover, the high U_S favored by AGN data in these figures could also result, at least in part, from the contamination of line-flux measurements by star formation (Section 4.4.1). This is compatible with the position of the SF models relative to the AGN models in Figs 4.5 and 4.6.

As a complement to the detailed description of the ultraviolet properties of SF models in Section 3.4, it is useful to examine here how the ultraviolet emission-line properties of AGN models vary as a function of the different adjustable parameters, such as gas density, metallicity, spectral power-law index, ionization parameter and dust-to-metal mass ratio. According to Figs 4.5 and 4.6, and modulo the above remark about potential contamination by circumnuclear star formation, the models in best agreement with AGN data are those with $n_{\mathrm{H}} \lesssim 10^3$ cm^{-3} (see also Nagao, Maiolino & Marconi, 2006). At fixed other parameters, increasing n_{H} means lowering the volume-filling factor, ϵ (equation 4.4). Since ϵ scales as $1/\sqrt{n_{\mathrm{H}}}$, the dust optical depth $\tau_{\mathrm{d}} \propto \xi_{\mathrm{d}} Z n_{\mathrm{H}} \epsilon$ (Brinchmann et al., 2013) rises as $\sqrt{n_{\mathrm{H}}}$. The implied extra absorption of energetic photons causes the electronic temperature, and hence, C IV λ1550/C III]λ1908 and C IV λ1550/He II λ1640, to drop (Fig. 4.5). This is also globally the case for C III]λ1908/He II λ1640 in Fig. 4.6, except in models with very low ionization parameter ($\log U_{\mathrm{S}} \lesssim -3$) and high metallicity ($Z \gtrsim 0.017$). We note that, as metallicity increases, the luminosity ratios of both C IV λ1550 and C III]λ1908 to He II λ1640 also increase in Figs 4.5 and 4.6 but then stagnate beyond $Z \sim 0.008$. As for the optical metal-line transitions discussed in Section 4.3.2 (Fig. 4.2), this is caused by a regulation between the rise in the abundance of coolants and the associated drop in electronic temperature, when metallicity increases.

The power-law index of the ionizing spectrum, α, controls the relative proportions of photons capable of ionizing different elements. As shown by Fig. 4.1, the ionization potential rises from C III, to He II, to C IV. Thus, at fixed other parameters, we expect C III]λ1908/He II λ1640 to drop and both C IV λ1550/C III]λ1908 and C IV λ1550/He II λ1640 to rise, when α increases from -2.0 (steepest AGN spectrum in Fig. 4.1) to -1.2 (flattest spectrum). This is globally what Figs 4.5 and 4.6 show, except for some combinations of parameters. For example, a rise in α appears to trigger a drop in C IV λ1550/C III]λ1908 at high metallicity ($Z \gtrsim 0.017$; Fig. 4.5) and a drop in C IV λ1550/He II λ1640 at low gas density ($n_{\mathrm{H}} = 10^2$ cm^{-3}; Figs 4.5 and 4.6). Also, increasing the ionization parameter U_{S}, which corresponds here to increasing the filling factor ϵ at fixed α and gas density n_{H} (equation 4.4), causes the ionized nebula to be more compact and concentrated close to the ionizing source (equation 4.3). This makes C IV λ1550/C III]λ1908, C IV λ1550/He II λ1640 and C III]λ1908/He II λ1640 increase with the ionization parameter, U_{S}, except for the drop in C IV λ1550/C III]λ1908 in the most metal-rich models (Fig. 4.5). Fig. 4.6 further shows that C IV λ1550/He II λ1640 and C III]λ1908/He II λ1640 never exceed ~ 0.6 dex in AGN models, in agreement with results of Groves, Dopita & Sutherland (2004b).

Changes in the dust-to-metal mass ratio have a complex effect on C IV λ1550/C III]λ1908, C IV λ1550/He II λ1640 and C III]λ1908/He II λ1640 in the AGN models in Figs 4.5 and 4.6, which results from the combination of several factors. An increase in ξ_{d} causes the electronic temperature to rise because of the depletion of coolants from the gas phase, which should increase C IV λ1550/He II λ1640 and C III]λ1908/He II λ1640 (for reference, about 60 per cent of carbon is depleted onto dust grains for $\xi_{\mathrm{d}} = 0.5$). At the same time, fewer C ions can be collisionally excited in the gas phase, which should lower C IV λ1550/He II λ1640 and C III]λ1908/He II λ1640. Moreover, increasing ξ_{d} raises the dust optical depth in the ionized gas, which scales as $\tau_{\mathrm{d}} \propto \xi_{\mathrm{d}} Z n_{\mathrm{H}} \epsilon$ (Brinchmann et al., 2013). The effect is accentuated at high ionization parameter, since the filling factor scales as $\epsilon \propto U_{\mathrm{S}}^{3/2}$ at fixed other parameters (equation 4.4). The predictions in Figs 4.5 and 4.6 therefore require a careful self-consistent treatment of metal abundances and depletion, such as that described in Section 3.2.3.

The position of AGN models (and observations) versus SF ones in Figs 4.5 and 4.6 provides valuable information about the potential of C IV λ1550/C III]λ1908, C IV λ1550/He II λ1640 and C III]λ1908/He II λ1640 to discriminate between active and inactive galaxies. For example, the similar ranges in C IV λ1550/C III]λ1908 spanned by AGN and SF models in Fig. 4.5 indicate that knowledge of this line ratio alone is not enough to distinguish between the 2 types of photoionization. In contrast, as Fig. 4.6 shows, C IV λ1550/He II λ1640 and C III]λ1908/He II λ1640 can help separate, each on their own, between nuclear activity and star formation, except in a few extreme cases: in the most metal-rich SF models with $n_\mathrm{H} = 10^2$ cm^{-3} and $\xi_\mathrm{d} \lesssim 0.3$, C III]$\lambda$1908/He II λ1640 can resemble that of AGN models, as can C IV λ1550/He II λ1640 in the most metal-poor SF models with $\log U_\mathrm{S} \lesssim -3$. In this context, combined information about C IV λ1550/He II λ1640 and C III]λ1908/He II λ1640 provides more unequivocal constraints on the nature of the ionizing source, while additional information on C IV λ1550/C III]λ1908 will provide further clues on the metal and dust abundance, ionization parameter and spectral power-law index (Fig. 4.5).

In the next subsections, we investigate emission-line ratio based on other ion species. For this purpose, it is useful to define a reference set of model parameters. As in Section 4.3.3 above, we adopt for simplicity a single choice of gas density, which differs for the AGN models, $n_\mathrm{H} = 10^3$ cm^{-3}, and the SF models, $n_\mathrm{H} = 10^2$ cm^{-3}. Also, except when otherwise indicated, we adopt a single dust-to-metal mass ratio, $\xi_\mathrm{d} = 0.3$, in the middle of the explored range. Finally, in all line-ratio diagrams in the remainder of this section, we adopt C III]λ1908/He II λ1640 as the ordinate. It is because this ratio has been shown above to be a good discriminant between photoionization by an AGN and star formation, and hence, it will allow a straightforward identification of other line ratios sensitive to the nature of the ionizing source. We favour C III]λ1908/He II λ1640 over C IV λ1550/He II λ1640 in this exercise, because observations of C IV λ1550 can be contaminated by the P-Cygni profile of photospheric stellar emission in young galaxies, while strong C III]λ1908 emission is now commonly detected in high-redshift galaxies (e.g., Stark et al., 2015a; Zitrin et al., 2015).

4.4.3 N V λ1240-based diagnostics

Ultraviolet emission-line ratios involving the N V λ1240 multiplet, such as N V λ1240/C IV λ1550 and N V λ1240/He II λ1640, have been exploited to interpret observations of active galaxies using AGN photoionization models, in particular as metallicity diagnostics (Groves, Dopita & Sutherland, 2004b; Nagao, Maiolino & Marconi, 2006, and references therein). Here, we investigate the extent to which N V λ1240-based emission-line ratios can be used as diagnostics of the nature of the photoionization source in a galaxy.

In Fig. 4.7, we show C III]λ1908/He II λ1640 as a function of N V λ1240/He II λ1640, N V λ1240/C IV λ1550 and N V λ1240/N III]λ1750 (from left to right) for a collection of AGN and SF models with reference values of the gas density n_H and dust-to-metal mass ratio ξ_d (Section 4.4.2). In each panel, we show AGN and SF models corresponding to same ranges in power-law index, α, ionization parameter, U_S, and metallicity, Z, as in Fig. 4.5. Also shown in Fig. 4.7 are the observations of AGN (crosses) and star-forming galaxies (large diamonds) described in Section 4.4.1, when available. We draw the dust attenuation vector in these figures, which, unlike in Figs 4.5 and 4.6, is not negligible because of the wide wavelength range spanned by N V λ1240-based line-ratio diagnostics (we recall that AGN data are not corrected for attenuation; see Section 4.4.1).

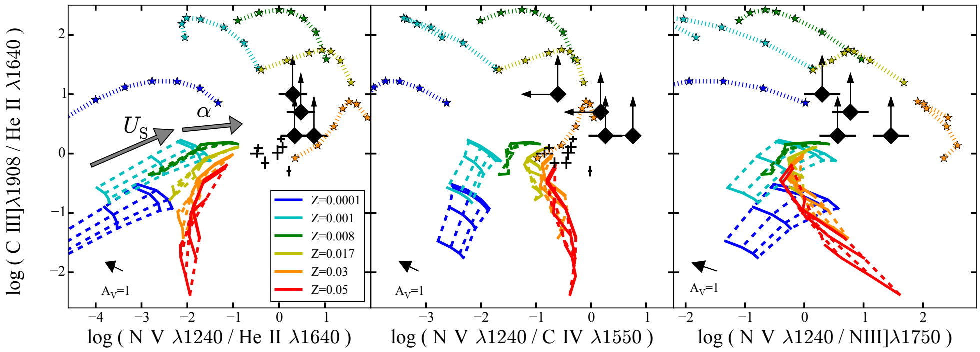

Figure 4.7: Predictions of the AGN and SF models described in Section 4.2 in the C III]λ1908/He II λ1640 versus N V λ1240/He II λ1640, N V λ1240/C IV λ1550 and N V λ1240/N III]λ1750 diagnostic diagrams (from left to right), for a dust-to-metal mass ratio $\xi_d = 0.3$ (our reference value in Section 4.4.2). AGN and SF models have gas densities $n_H = 10^3$ and 10^2 cm^{-3}, respectively. In each panel, we show AGN models corresponding to wide ranges in power-law index, $-2.0 \leq \alpha \leq -1.2$ (connected by solid lines), and ionization parameter, $-4.0 \leq \log U_S \leq -1.0$ (connected by dashed lines; α and U_S increasing as indicated in the left panel), and SF models (stars connect by dotted lines) corresponding to the same range in U_S, for different metallicities Z (colour-coded as indicated in the left panel). Also shown in each panel are the observations of AGN (crosses with error bars) and star-forming galaxies (large diamonds) described in Section 4.4.1, when available. In each panel, black arrows indicate the effect of attenuation by dust for $A_V = 1$ mag and a Calzetti et al. (2000) attenuation curve (AGN data are not corrected for attenuation).

Fig. 4.7 shows that AGN and SF models populate distinct areas of the C III]λ1908/He II λ1640 versus N V λ1240/He II λ1640, N V λ1240/C IV λ1550 and N V λ1240/N III]λ1750 diagrams, exhibiting the same trends as the observations of active and inactive galaxies. We note that AGN models around solar metallicity have traditionally been found to predict lower N V λ1240 line luminosity than observed in broad- and narrow-line regions of AGN (e.g., Osmer & Smith, 1976; Kraemer, Ruiz & Crenshaw, 1998). In fact, some authors appeal to very high metallicities (up to $Z \sim 10 Z_\odot$) to reproduce observations (Netzer, 2013). We show in Fig. 4.8 that by choosing slightly different values of the dust-to-metal ratio, $\xi_d = 0.5$, and gas density in narrow-line regions, $n_H = 10^2$ cm^{-3}, our AGN models are in better agreement with available observations of active galaxies. In this context, we should also keep in mind the possible contamination of these nuclear line-flux measurements by star formation in Figs 4.7 and 4.8 (Section 4.4.1).

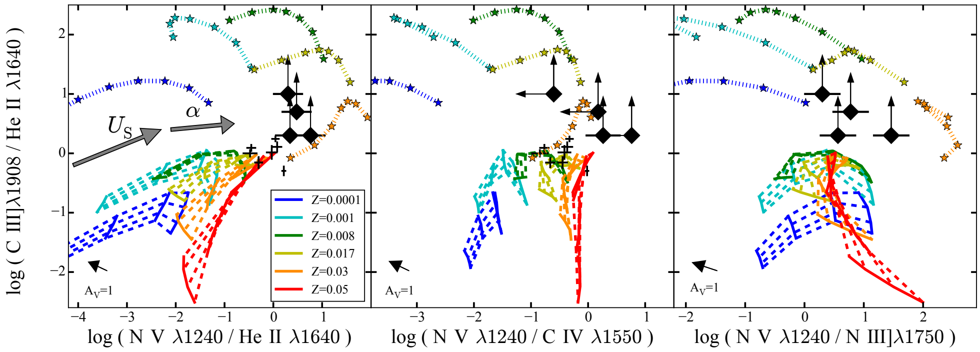

Figure 4.8: Same as Fig. 4.7, but for a dust-to-metal mass ratio $\xi_{\rm d} = 0.5$ and an AGN model gas density $n_{\rm H} = 10^2$ cm^{-3}.

The behaviour of models with different $n_{\rm H}$, α, $U_{\rm S}$ and $\xi_{\rm d}$ in Figs 4.7 and 4.8 can be largely understood from that described for the diagrams defined by the C iv λ1550, He ii λ1640 and C iii]λ1908 emission lines in Figs 4.5 and 4.6. For example, increasing the gas density raises the dust optical depth, which lowers the electronic temperature, and hence, N v λ1240/He ii λ1640, N v λ1240/C iv λ1550 and N v λ1240/N iii]λ1750. Also, a steepening of the ionizing spectrum (from $\alpha = -1.2$ to -2.0) reduces the amount of highly energetic photons, which should make N v λ1240/He ii λ1640, N v λ1240/C iv λ1550 and N v λ1240/N iii]λ1750 drop according to the ionization potentials of these ions (Fig. 4.1). At high Z and high $\xi_{\rm d}$, the effect in Fig. 4.8 is modulated by the increased amount of dust and the different depletion levels of carbon and nitrogen. As noted previously (Section 4.4.2), raising the ionization parameter $U_{\rm S}$ at fixed α and $n_{\rm H}$ makes the ionized nebula more concentrated close to the ionizing source. This causes N v λ1240/He ii λ1640, N v λ1240/C iv λ1550 and N v λ1240/N iii]λ1750 to globally increase together with C iii]λ1908/He ii λ1640 in Figs 4.7 and 4.8, although the changes are more complex at the highest metallicities for N v λ1240/C iv λ1550 and N v λ1240/N iii]λ1750. An increase in $\xi_{\rm d}$ causes a depletion of coolants from the gas phase, a rise in the electronic temperature, and hence, since nitrogen is a non-refractory element, a rise in N v λ1240/He ii λ1640.

Figs 4.7 and 4.8 indicate that N v λ1240/He ii λ1640 N v λ1240/C iv λ1550 and N v λ1240/N iii]λ1750 cannot be used individually to discriminate between photoionization by an AGN and star formation in a galaxy, even though positive values of log(N v λ1240/He ii λ1640) appear to be achievable only with metal-rich stellar ionizing spectra. This is consistent with the fact that such spectra differ most markedly from AGN spectra (Fig. 4.1). Combined with information about C iii]λ1908/He ii λ1640, N v λ1240-based line ratios can provide interesting clues about the nature of the ionizing source, and even about metallicity and the ionization parameter in galaxies powered by star formation. Yet, N v λ1240-based diagnostics are not optimal because of their strong dependence on the details of secondary nitrogen enhancement. Also, as indicated by the large dynamic range spanned by the abscissae in Figs 4.7 and 4.8, N v λ1240 emission is very weak and hence difficult to detect at low metallicity (Nagao, Maiolino & Marconi, 2006).

4.4.4 He II λ1640-based diagnostics

The He II λ1640 recombination line depends less strongly on metallicity and ionization parameter than collisionally excited metal lines. For this reason, He II λ1640 can be used as a standard reference line at ultraviolet wavelengths, similarly to Hβ at optical wavelengths. In this section, we propose 3 He II λ1640-based emission-line ratio diagnostics to distinguish between photoionization by an active nucleus and star formation. Specifically, we show in Fig. 4.9 the C III]λ1908/He II λ1640 versus O III]λ1663/He II λ1640, N III]λ1750/He II λ1640 and Si III]λ1888/He II λ1640 diagrams (from left to right) for the same collection of AGN and SF models as in Fig. 4.7.

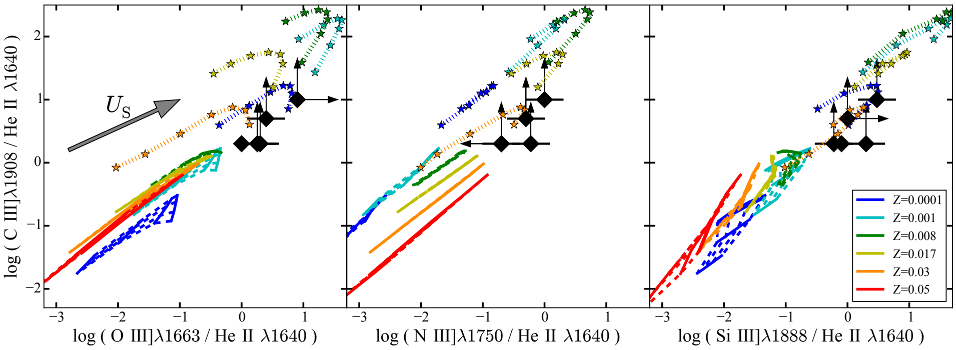

Figure 4.9: Predictions of the AGN and SF models described in Section 4.2 in the C III]λ1908/He II λ1640 versus O III]λ1663/He II λ1640, N III]λ1750/He II λ1640 and Si III]λ1888/He II λ1640 diagnostic diagrams (from left to right), for a dust-to-metal mass ratio $\xi_d = 0.3$ and gas densities $n_H = 10^3$ and 10^2 cm^{-3} for AGN and SF models, respectively (our reference values in Section 4.4.2). In each panel, the models and observations (when available) are the same as in Fig. 4.7.

AGN and SF models occupy distinct areas of the 3 diagrams in Fig. 4.9, the observations of low-mass star-forming galaxies being consistent with the predictions of SF models. Thus, O III]λ1663/He II λ1640, N III]λ1750/He II λ1640 and Si III]λ1888/He II λ1640 could be used individually to constrain the dominant source of ionizing photons in a galaxy. We note that, although the most metal-rich SF models ($Z = 0.030$) can reach values of O III]λ1663/He II λ1640, N III]λ1750/He II λ1640 and Si III]λ1888/He II λ1640 similar to those in some AGN models, this should not weaken the value of these diagnostic line ratios to interpret observations of only moderately enriched galaxies at high redshifts. Fig. 4.9 further shows that, while AGN models with different metallicities separate well in the C III]λ1908/He II λ1640 versus N III]λ1750/He II λ1640 diagram, this is not the case for the C III]λ1908/He II λ1640 versus O III]/He II λ1640 and Si III]λ1888/He II λ1640 diagrams. Also, none of the diagrams in this figure can help constrain the power-law index α of the ionizing radiation. It is worth pointing out that, as shown in Section 4.5, the predictions in the left panel of Fig. 4.9 are similar to those that would be obtained using only one component (at either $\lambda = 1661$ or 1666 Å) of the O III] doublet.

4.4.5 O-based diagnostics in the far and near ultraviolet

In the previous section, we have introduced O III]λ1663/He II λ1640 as an ultraviolet emission-line diagnostic of nuclear activity versus star formation in galaxies. Other oxygen transitions, such as O I λ1304, [O III]λ2321 and [O II]λ3727 can also potentially help discriminate between photoionization by an AGN and star formation when combined with He II λ1640.

Fig. 4.10 shows C III]λ1908/He II λ1640 as a function of O I λ1304/He II λ1640, [O III]λ2321/He II λ1640 and [O II]λ3727/He II λ1640 (from left to right) for the same collection of AGN and SF models as in Fig. 4.7, with reference values of the gas density $n_{\rm H}$ and dust-to-metal mass ratio (Section 4.4.2), in wide ranges of power-law index α and ionization parameter $U_{\rm S}$. AGN and SF models occupy distinct regions of these diagrams, in agreement with available observations of star-forming galaxies. This makes different combinations of the line ratios in Fig. 4.10 good diagnostics of nuclear activity versus star formation. We note the similarity of O III]/He II λ1640 in AGN models and the most metal-rich SF models (middle panel) and of [O II]λ3727/He II λ1640 in AGN models and the most metal-poor SF models (right panel).

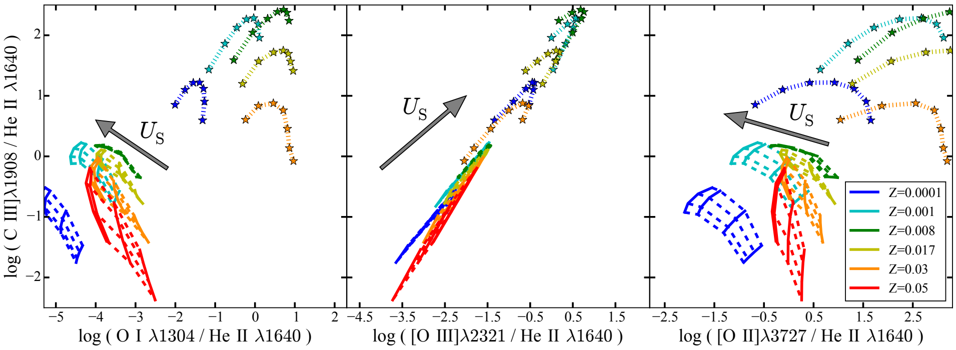

Figure 4.10: Predictions of the AGN and SF models described in Section 4.2 in the C III]λ1908/He II λ1640 versus O I λ1304/He II λ1640, [O III]λ2321/He II λ1640 and [O II]λ3727/He II λ1640 diagnostic diagrams (from left to right), for a dust-to-metal mass ratio $\xi_{\rm d} = 0.3$ and gas densities $n_{\rm H} = 10^3$ and 10^2 cm^{-3} for AGN and SF models, respectively (our reference values in Section 4.4.2). In each panel, the models are the same as in Fig. 4.7.

It is also worth noting that, given the wide predicted dynamic range in O I λ1304/He II λ1640 and [O III]λ2321/He II λ1640 in Fig. 4.10, simple lower and upper limit on these emission-line ratios can already provide valuable clues about the nature of the ionizing source in a galaxy. For example, upper limits such as log(O I λ1304/He II λ1640) $\lesssim -2.5$ and log([O III]λ2321/He II λ1640) $\lesssim -2.5$ could be enough to identify the presence of an AGN. We further note that attenuation by dust should have a negligible effect on the capacity to discriminate between nuclear activity and star formation using the diagrams in Fig. 4.10. For example, adopting the Calzetti et al. (2000) curve, an attenuation of $A_V = 1$ would affect O-based line ratios by between 0.1 and 0.4 dex and C III]λ1908/He II λ1640 by only 0.07 dex. A potentially more serious complication is that, in AGN spectra, the O I λ1304 emission-line triplet is expected to be blended with the S II $\lambda\lambda$1304, 1309 doublet (e.g. Matsuoka et al., 2007), although Rodríguez-Ardila et al. (2002) manage to robustly de-blend these components in high-S/N *HST* spectroscopic observations of a Seyfert 1 galaxy.

4.4.6 Ne-based diagnostics in the near ultraviolet

The high ionization potential of NeV (~ 97 eV) requires a hard ionizing spectrum for significant [Ne V]λ3426 emission to be produced, which is unlikely to arise from stellar populations (see Fig. 4.1). For this reason, a detection of [Ne V]λ3426 has been claimed to be a powerful diagnostic of the presence of an AGN (Mignoli et al., 2013, and references therein). We now explore several Ne-based line-ratio diagnostics involving the [Ne III]λ3343, [Ne IV]λ2424 and [Ne V]λ3426 emission lines (given the faintness of [NeV] emission, we consider here only [Ne V]λ3426 and not the ~ 3 times weaker [Ne V]λ3346 line; Vanden Berk et al. 2001).

Fig. 4.11 shows C III]λ1908/He II λ1640 as a function of [Ne IV]λ2424/He II λ1640, [Ne III]λ3343/He II λ1640 and [Ne V]λ3426/He II λ1640 (from left to right) for the same collection of AGN and SF models as in Fig. 4.7. As expected from Fig. 4.1, AGN models reach the highest [Ne IV]λ2424/He II λ1640 and especially [Ne V]λ3426/He II λ1640 values, but they overlap with SF models for lower values of these line ratios. Interestingly, AGN and SF models separate more markedly in the C III]λ1908/He II λ1640 versus [Ne III]λ3343/He II λ1640 diagram (middle panel of Fig. 4.11).

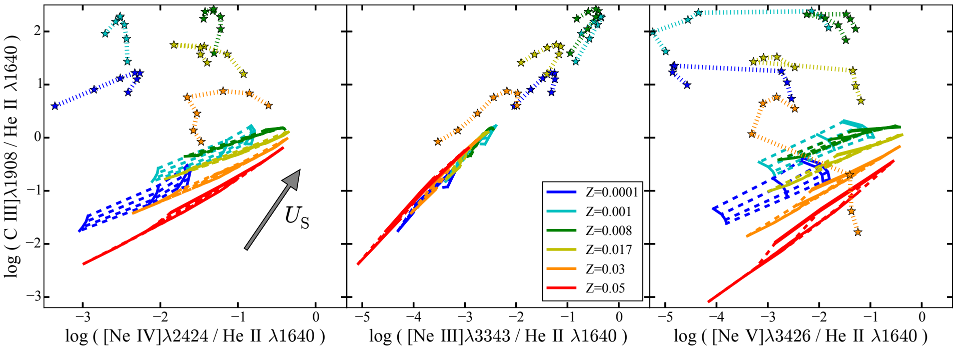

Figure 4.11: Predictions of the AGN and SF models described in Section 4.2 in the C III]λ1908/He II λ1640 versus [Ne IV]λ2424/He II λ1640, [Ne III]λ3343/He II λ1640 and [Ne V]λ3426/He II λ1640 diagnostic diagrams (from left to right), for a dust-to-metal mass ratio $\xi_d = 0.3$ and gas densities $n_H = 10^3$ and 10^2 cm^{-3} for AGN and SF models, respectively (our reference values in Section 4.4.2). In each panel, the models are the same as in Fig. 4.7.

To further explore the usefulness of [Ne IV]λ2424 and [Ne V]λ3426 to discriminate between nuclear activity and star formation, we compute luminosity ratios between these emission lines and several lines from other ions. In Figs 4.12 and 4.13, we show C III]λ1908/He II λ1640 as a function of the luminosity ratios defined by [Ne IV]λ2424 and [Ne V]λ3426, respectively, and each of the following 9 emission lines: C IV λ1550, C III]λ1908, O III]λ1663, N V λ1240, N IV]λ1485, N III]λ1750, S IV+O IV]λ1400, Si II λ1814 and Si III]λ1888. The clear separation between active and inactive galaxies in these diagrams is remarkable. It indicates that combinations of C III]λ1908/He II λ1640 with any of the explored Ne-based line ratios can help discriminate between nuclear activity and star formation. Moreover, several Ne-based emission-line ratios investigated in Figs 4.12 and 4.13 are, on their own, good diagnostics of photoionization by an AGN versus star formation. This is the case for [Ne IV]λ2424/C IV λ1550, [Ne V]λ3426/C IV λ1550, [Ne IV]λ2424/C III]λ1908, [Ne IV]λ2424/N V λ1240, [Ne V]λ3426/N V λ1240, [Ne IV]λ2424/N III]λ1750, [Ne IV]λ2424/S IV+O IV]λ1400, [Ne V]λ3426/S IV+O IV]λ1400, [Ne IV]λ2424/Si II λ1814, [Ne V]λ3426/Si II λ1814 and [Ne IV]λ2424/Si III]λ1888. The other Ne-based emission-line ratios in Figs 4.12 and 4.13 tend to reach, in the most metal-rich SF models, values similar to those of AGN models, requiring C III]λ1908/He II λ1640 information for a more secure identification of the ionizing source.

We note that, although the diagnostics diagrams in Figs 4.12 and 4.13 were constructed using dust-free models, the dynamic range in Ne-based line-ratio strength is so large that attenuation by dust should not affect significantly the above results. For example, adopting the Calzetti et al. (2000) curve, an attenuation of $A_V = 1$ would affect Ne-based line ratios by between 0.1 and 0.5 dex (from the smallest to the largest wavelength leverage) and C III]λ1908/He II λ1640 by only 0.07 dex. More problematic could be the challenge of measuring some of these lines. For example, [Ne III]λ3343 can potentially be blended with the [Ne V]λ3347 line (Schirmer et al., 2013), while Si II λ1814 has been found to be very weak in high-redshift quasars (Negrete et al., 2014).

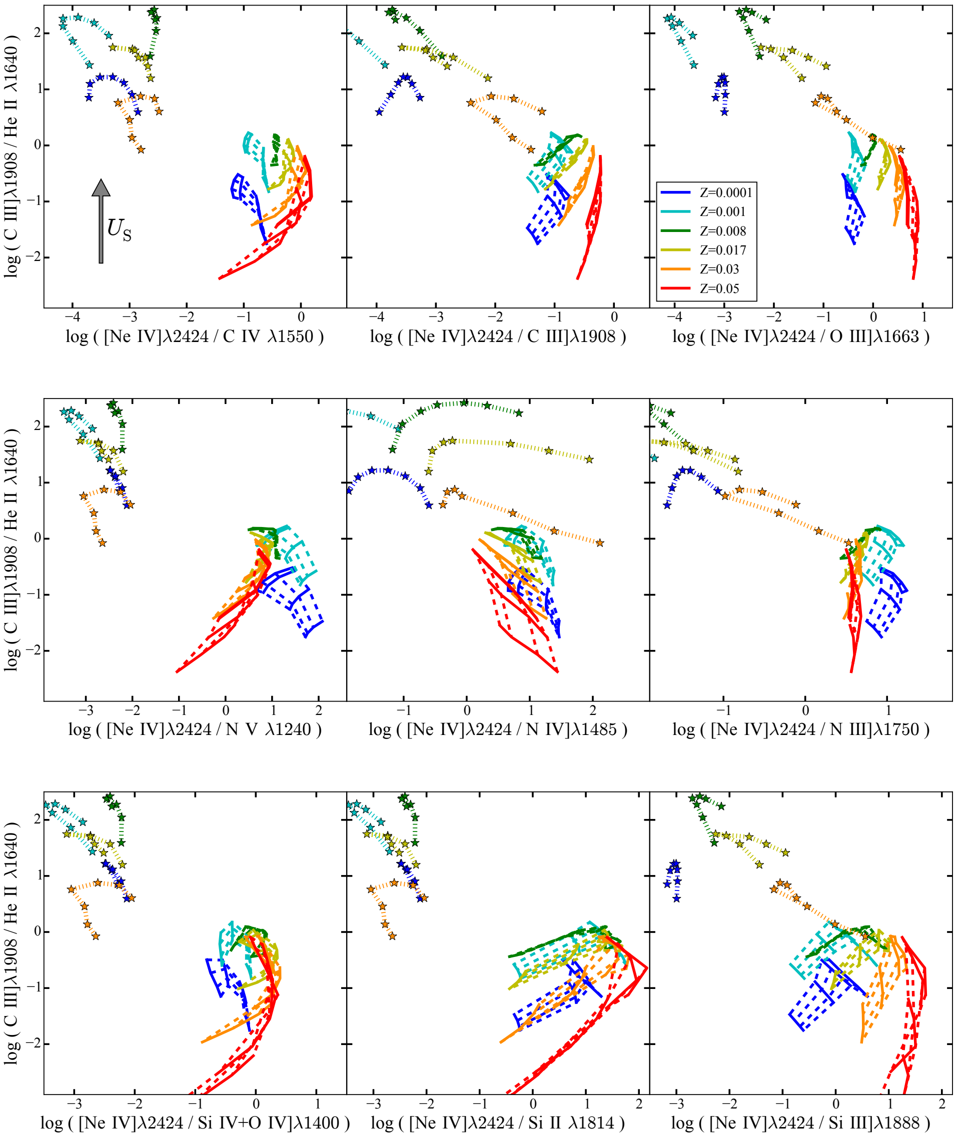

Figure 4.12: Predictions of the AGN and SF models described in Section 4.2 in several diagnostic diagrams defined by C III]λ1908/He II λ1640 against various [Ne IV]λ2424-based line ratios, for a dust-to-metal mass ratio ξ_d = 0.3 and gas densities n_H = 10^3 and 10^2 cm^{-3} for AGN and SF models, respectively (our reference values in Section 4.4.2). In each panel, the models are the same as in Fig. 4.7.

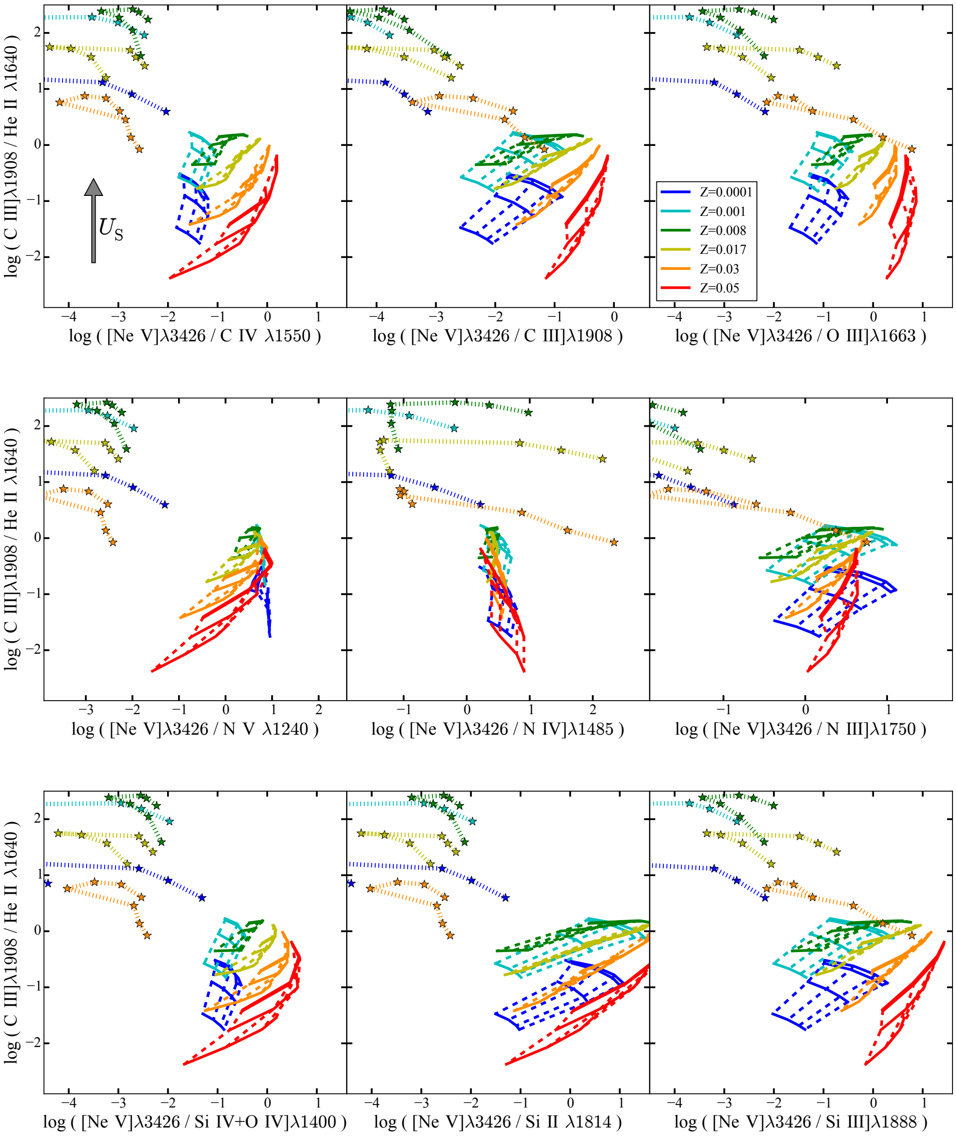

Figure 4.13: Same as Fig. 4.12, but for [Ne V]λ3426-based instead of [Ne IV]λ2424-based line ratios.

4.4.7 Distinguishing active from inactive galaxies in emission line-ratio diagrams

The main outcome of the previous subsections is that models of nebular emission from active and inactive galaxies populate different areas of diagrams defined by the luminosity ratios of several ultraviolet emission lines. So far, we have compared in a same diagram AGN and SF models in reduced ranges of gas density n_{H} and dust-to-metal ratio ξ_{d}, for grids of ionization parameter U_{S}, metallicity Z and spectral power-law index α. To fully assess how different emission-line ratios can help discriminate between nuclear activity and star formation, we must plot in a same diagram models spanning full ranges in all the adjustable parameters listed in Table 4.1.

As an example, we show in Fig. 4.14 the full grids of AGN (gray dots) and SF (turquoise stars) models in the optical BPT (top) and ultraviolet C III]λ1908/He II λ1640 versus C IV λ1550/He II λ1640 (bottom) diagnostic diagrams. AGN and SF models can occupy similar regions of the BPT diagram. This similarity was already noted before for low-metallicity AGN and SF models (Fig. 4.2 of Section 4.3.2). SF models lying above the Kewley et al. (2001) separation criteria in Fig. 4.14 (top) are those combining high ionization parameter ($\log U_{\mathrm{S}} \gtrsim -2$) and metallicity ($Z \gtrsim 0.008$), a combination not commonly observed in the local Universe (e.g., Brinchmann et al., 2004). In contrast, Fig. 4.14 (bottom) shows that the separation between AGN and SF models is far more distinct in the C III]λ1908/He II λ1640 versus C IV λ1550/He II λ1640 diagram. Galaxies with observed line ratios falling in the region of the diagram populated by AGN models will therefore be likely to be powered by nuclear activity.

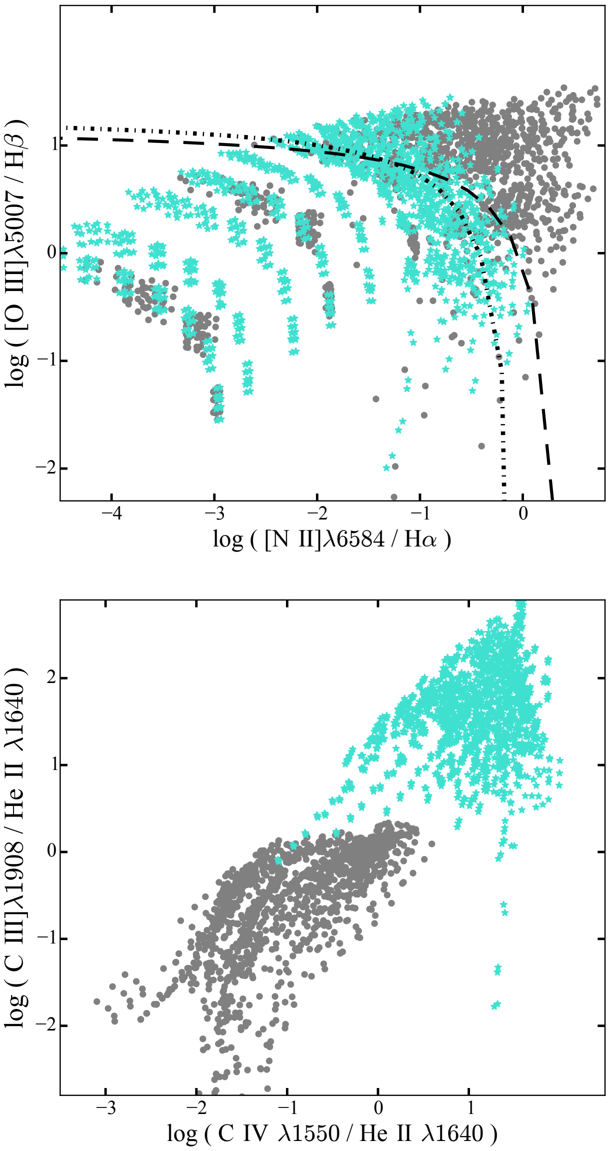

Figure 4.14: Distribution of AGN (gray dots) and SF (turquoise stars) models spanning full ranges in all the adjustable parameters listed in Table 4.1 in the optical [O III]λ5007/Hβ versus [N II]λ6584/Hα (BTP; top panel) and ultraviolet C III]λ1908/He II λ1640 versus C IV λ1550/He II λ1640 (bottom panel) diagnostic diagrams. In the top panel, the long-dashed and dot-dashed black lines indicate, respectively, the criteria of Kewley et al. (2001) and Kauffmann et al. (2003) to distinguish AGN from star-forming galaxies.

In Section 4.5, we show the analogs of Fig. 4.14 for the different ultraviolet emission-line ratios proposed to discriminate between active and inactive galaxies in Sections 4.4.2–4.4.6, and which involve emission lines currently detected in observations of high-redshift galaxies (Erb et al., 2010; Stark et al., 2014), i.e., N V λ1240, C IV λ1550, He II λ1640, O III]λ1663 (and the corresponding individual doublet components), N III]λ1750, Si III]λ1888 (and the corresponding individual doublet components) and C III]λ1908. Figs 4.15, 4.16 and 4.17 show such diagnostic diagrams with C III]λ1908/He II λ1640, C IV λ1550/He II λ1640 and C IV λ1550/C III]λ1908, respectively, on the ordinate axis. As seen previously, in some of these diagrams, SF models with highest metallicity ($Z \gtrsim 0.030$), lowest density ($n_\mathrm{H} = 10^2$ cm^{-3}) and lowest ionization parameter ($\log U_\mathrm{S} \lesssim -3$) can have line luminosity ratios similar to those of AGN models. This is the case for the C III]λ1908/He II λ1640 versus N V λ1240/C IV λ1550, [O III]λ5007/He II λ1640, N III]λ1750/He II λ1640 and Si III]λ1888/He II λ1640 diagnostic diagrams (Fig. 4.15). Also, SF models with lowest metallicity ($Z = 0.0001$) can overlap with AGN models in the C IV λ1550/He II λ1640 versus N V λ1240/He II λ1640, N V λ1240/C IV λ1550, N V λ1240/N III]λ1750, N III]λ1750/He II λ1640 and Si III]λ1888/He II λ1640 diagrams (Fig. 4.16). Despite these limitations, over most of the parameter space, the diagrams in Figs 4.15 and 4.16 remain good diagnostics of photoionization by nuclear activity versus star formation in galaxies. The overlap between AGN and SF models is larger in C IV λ1550/C III]λ1908 versus N V λ1240-based diagrams (top panels of Fig. 4.17), making these the least reliable diagnostics of active versus inactive galaxies investigated here.

4.5 Ultraviolet line-ratio diagnostic diagrams of active and inactive galaxies

Fig. 4.15, 4.16 and 4.17 show diagnostic diagrams defined by the luminosity ratios of several ultraviolet emission lines currently detected in observations of high-redshift galaxies (Erb et al., 2010; Stark et al., 2014), i.e., N V λ1240, C IV λ1550, He II λ1640, O III]λ1663 (and the corresponding individual doublet components), N III]λ1750, Si III]λ1888 (and the corresponding individual doublet components) and C III]λ1908. In each panel of each figure, we show AGN (gray dots) and SF (turquoise stars) models spanning full ranges in all the adjustable parameters listed in Table 4.1. Figs 4.15, 4.16 and 4.17 show diagnostic diagrams with C III]λ1908/He II λ1640, C IV λ1550/He II λ1640 and C IV λ1550/C III]λ1908, respectively, on the ordinate axis. We refer to the previous Section 4.4.7 for more details about the usefulness of these diagrams to discriminate between nuclear activity and star formation in galaxies.

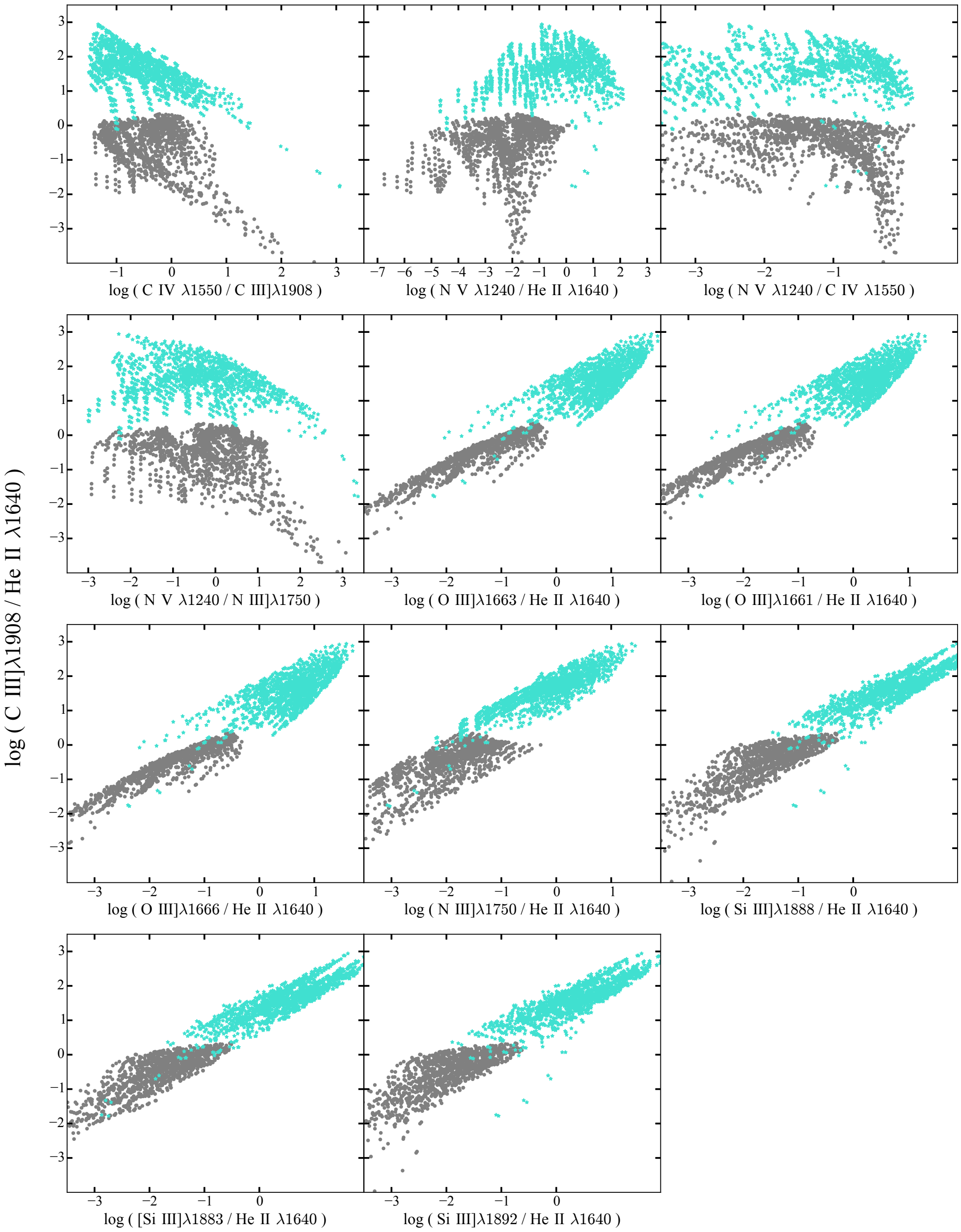

Figure 4.15: Distribution of AGN (gray dots) and SF (turquoise stars) models spanning full ranges in all the adjustable parameters listed in Table 4.1 in ultraviolet line-ratio diagrams defined by C III]λ1908/He II λ1640 as a function of C IV λ1550/C III]λ1908, N V λ1240/He II λ1640, N V λ1240/C IV λ1550, N V λ1240/N III]λ1750, O III]λ1663/He II λ1640, O III]λ1661/He II λ1640, O III]λ1666/He II λ1640, N III]λ1750/He II λ1640, Si III]λ1888/He II λ1640, [Si III]λ1883/He II λ1640 and Si III]λ1892/He II λ1640.

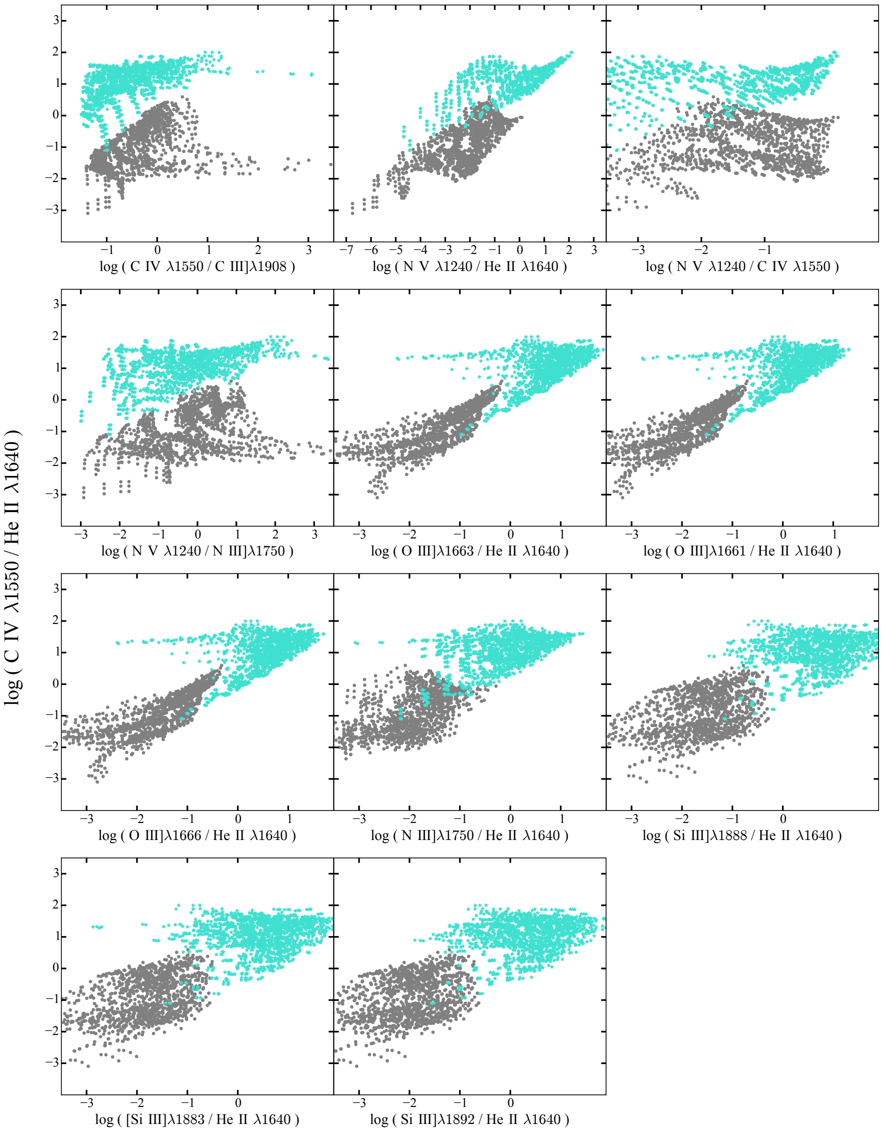

Figure 4.16: Distribution of AGN (gray dots) and SF (turquoise stars) models spanning full ranges in all the adjustable parameters listed in Table 4.1 in ultraviolet line-ratio diagrams defined by C IV λ1550/He II λ1640 as a function of C IV λ1550/C III]λ1908, N V λ1240/He II λ1640, N V λ1240/C IV λ1550, N V λ1240/N III]λ1750, O III]λ1663/He II λ1640, O III]λ1661/He II λ1640, O III]λ1666/He II λ1640, N III]λ1750/He II λ1640, Si III]λ1888/He II λ1640, [Si III]λ1883/He II λ1640 and Si III]λ1892/He II λ1640.

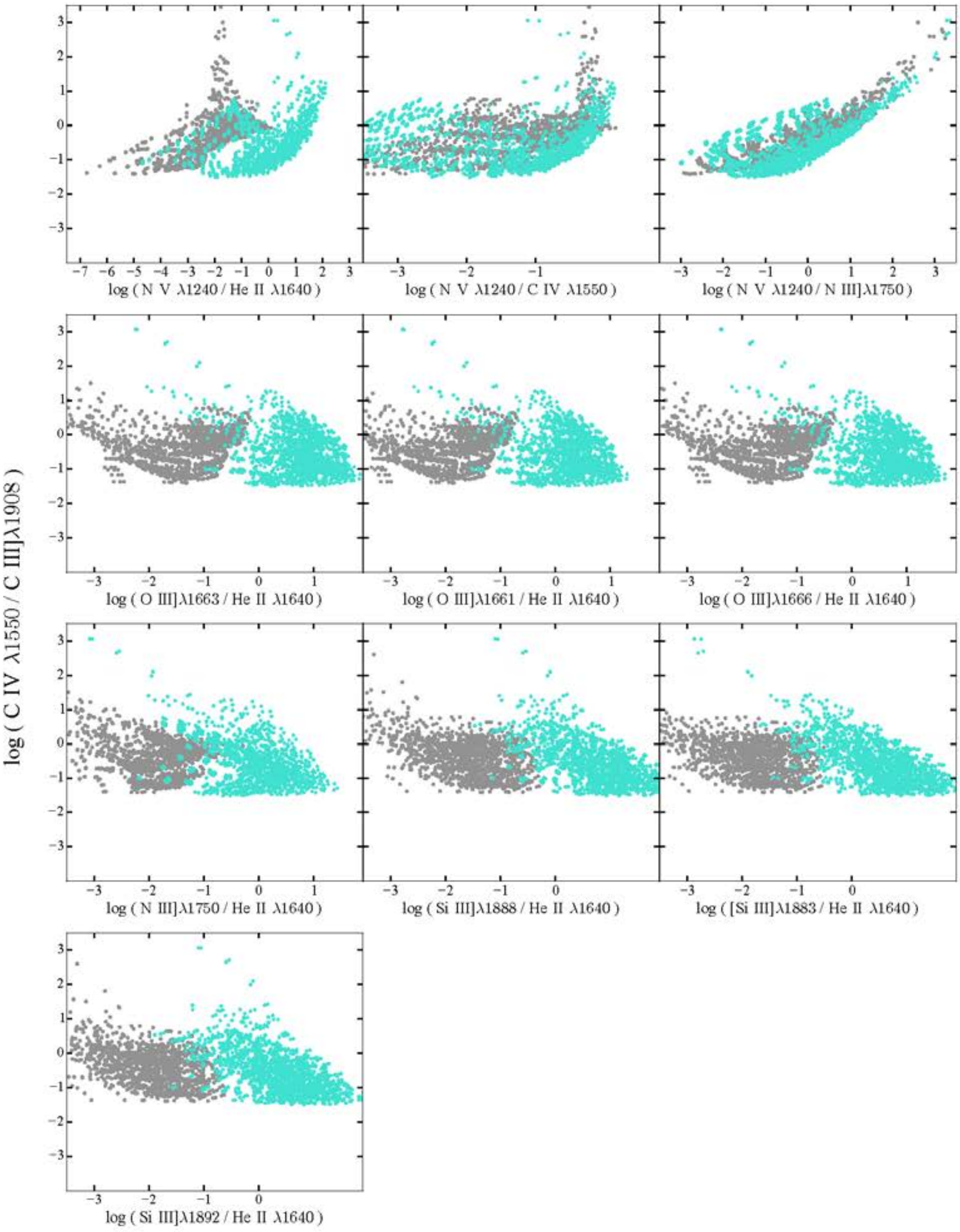

Figure 4.17: Distribution of AGN (gray dots) and SF (turquoise stars) models spanning full ranges in all the adjustable parameters listed in Table 4.1 in ultraviolet line-ratio diagrams defined by C IV λ1550/C III]λ1908 as a function of N V λ1240/He II λ1640, N V λ1240/C IV λ1550, N V λ1240/N III]λ1750, O III]λ1663/He II λ1640, O III]λ1661/He II λ1640, O III]λ1666/He II λ1640, N III]λ1750/He II λ1640, Si III]λ1888/He II λ1640, [Si III]λ1883/He II λ1640 and Si III]λ1892/He II λ1640.

4.6 Conclusions

We have developed a simple model to compute the nebular emission from narrow-line emitting regions of active galaxies in the presence of dust. These AGN models are parametrized in terms of the hydrogen density, ionization parameter, metallicity and dust-to-metal mass ratio of the ionized gas and the power-law index of the ionizing spectrum. We have shown that the models reproduce well the observed properties of active galaxies in standard diagrams defined by optical lines ratios, such as [O III]λ5007/Hβ, [N II]λ6584/Hα, [S II]λ6724/Hα and [O I]λ6300/Hα, used to discriminate between photoionization by nuclear activity and star formation in galaxies. In the same diagrams, the models of nebular emission from star-forming galaxies (SF models) I have developed and presented in the previous Chapter 3 reproduce well the observed properties of SDSS galaxies. Given these premises, our main goal in the present study has been to extend the comparison between the properties of AGN and SF models to ultraviolet wavelengths and identify new emission line-ratio diagnostics of nuclear activity versus star formation. Such diagnostics should be particularly useful to interpret the rest-frame ultraviolet emission from high-redshift galaxies.

We find that several combinations of the He II λ1640 recombination line with a collisionally excited metal line can serve, taken individually, as a good diagnostics of nuclear activity versus star formation in galaxies. This is the case for the luminosity ratios of C IV λ1550, O III]λ1663, N III]λ1750, Si III]λ1888 and C III]λ1908 to He II λ1640. The more numerous the available measurements of these different metal lines in addition to He II λ1640, the more stringent the constraints on the nature of the ionizing source. Other ultraviolet emission-line ratios, such as C IV λ1550/C III]λ1908, N V λ1240/He II λ1640 and N V λ1240/C IV λ1550, do not individually allow a clear discrimination between active and inactive galaxies. However, information on these ratios will be useful to further investigate the physical parameters of the ionized gas, such as ionization parameter and metallicity, when combined with the luminosity ratio of either C IV λ1550, O III]λ1663, N III]λ1750, Si III]λ1888 or C III]λ1908 to He II λ1640 (Figs 4.5 and 4.7). We note that, for some combinations of gas density and dust-to-metal mass ratio at either extremely low ($Z \sim 0.0001$) or high ($Z \gtrsim 0.030$, i.e. greater than about twice solar) metallicity, AGN and SF models can occupy similar regions in some of these line-ratio diagnostic diagrams (see Section 4.4 for detail).

It is also interesting to note that AGN and SF models separate particularly well in various ultraviolet diagnostic diagrams involving Ne-based emission lines, such as [Ne IV]λ2424, [Ne III]λ3343 and [Ne V]λ3426. In such diagrams, the luminosity ratios predicted by AGN and SF models can differ by up to 3 or 4 orders of magnitude. While this reflects the extreme faintness, and hence, unlikely observability, of some emission lines involved in the definition of these ratios, simple lower and upper limit on these emission-line ratios can already provide valuable clues about the nature of the ionizing source. For example, a detection of [Ne IV]λ2424 or [Ne V]λ3426 is likely to be associated to the presence of an active nucleus and, combined with other ultraviolet line, may also provide valuable information about the physical conditions in the ionized gas.

The AGN and SF models investigated in this thesis compare well with currently available observations of rest-frame ultraviolet emission lines of active and inactive galaxies. In particular, our AGN models can account for the N V λ1240, C IV λ1550, He II λ1640 and C III]λ1908 emission-line properties of active galaxies at various redshifts from the sample of Dors et al. (2014, and references therein). We find that the observed N-based emission-line ratios from this sample are best accounted for by models with slightly different parameters than those favored by other line ratios. This could be related to the traditional finding that AGN models around solar metallicity predict lower N v λ1240 line luminosity than observed in broad- and narrow-line regions of AGN (e.g., Osmer & Smith, 1976; Kraemer, Ruiz & Crenshaw, 1998). This could also arise from a possible contamination of the AGN line-flux measurements by star formation (Section 4.4.1). The SF models I have developed, for their part, are in remarkable agreement with available measurements of (or upper limits on) the N v λ1240, C iv λ1550, He ii λ1640, O iii]λ1663, N iii]λ1750, Si iii]λ1888 and C iii]λ1908 emission-line properties of gravitationally lensed, low-mass star-forming galaxies at redshifts $z \sim 2$ from Stark et al. (2014). These ultraviolet emission lines are now detected routinely in quasars and galaxies out to high redshifts, although the lack of published measurements prevented us from inserting them in the present study (e.g., Humphrey et al., 2007; Hainline et al., 2011; Pâris et al., 2012; Alexandroff et al., 2013; Pâris et al., 2014; Lusso et al., 2015). Soon, high-quality ultraviolet spectroscopic observations will also be collected for large samples of galaxies out to the reionization epoch with future facilities such as *JWST* and ground-based ELT. Our AGN and SF models will allow one to extract valuable information from these observations about the nature of the dominant ionizing sources in the early Universe.

In this work, we have not investigated the spectral signatures of photoionization by shocks, which can also contribute to the observed emission-line spectra of galaxies (Rich, Kewley & Dopita, 2011). The contribution by shocks to photoionization in the early Universe has been the subject of several studies. Dopita et al. (2011) argues that this could be substantial, while Miniati et al. (2004) and Wyithe, Mould & Loeb (2011) favor a negligible contribution. Unfortunately, existing shock models (e.g., Allen, Dopita & Tsvetanov, 1998; Allen et al., 2008) cannot be straightforwardly compared with the AGN and SF models considered here, because of the different ways in which the photoionized gas is parametrized. Allen, Dopita & Tsvetanov (1998); Allen et al. (2008) investigate ultraviolet emission-line diagnostics to discriminate between photoionization by shocks and nuclear activity. They propose the C ii]λ2326/C iii]λ1908 versus C iv λ1550/C iii]λ1908 diagram as one of the most suitable discriminant between AGN and shocks with velocities less than $400\,\mathrm{km\,s^{-1}}$, while higher-velocity shocks overlap with AGN models in this diagram. We have used the AGN and SF models described in Section 4.2 to investigate whether the C ii]λ2326/C iii]λ1908 versus C iv λ1550/C iii]λ1908 diagram could also be useful to distinguish AGN from star-forming galaxies. In reality, we find that the 2 types of models overlap significantly in this diagram. We plan to investigate in a self-consistent way the ultraviolet spectral signatures of shocks versus AGN and SF models in a future study.

The ultraviolet line-ratio diagrams presented in this thesis to discriminate between active and inactive galaxies are designed to help interpret current and future observations of the nebular emission from galaxies at all redshifts. These diagrams are also valuable to constrain the physical properties of photoionized gas, such as hydrogen density, ionization parameter, metallicity and dust-to-metal mass ratio. We note that, in this context, spatially resolved spectroscopy will be particularly useful to trace the different spatial scales of nuclear activity and star formation. To optimise the usefulness of the diagnostic diagrams presented in this work for the interpretation of observed emission-line properties of galaxies, we are exploring statistical machine learning techniques to build an automated classifier able to probabilistically separate active from inactive galaxies (Stenning et al., in preparation). The spectral features most influencing this classification will also reveal which emission-line ratios might be considered as the most reliable discriminants between nuclear activity and star formation. Finally, it is worth mentioning that the AGN and SF models of nebular emission analysed in this thesis are being incorporated in the Bayesian spectral interpretation tool BEAGLE (Chevallard & Charlot, 2016) to produce statistical constraints on the shape of the ionizing radiation and interstellar gas parameters.

CHAPTER 5

Linking my nebular emission modelling with observations

Contents

The model I have developed in this thesis has already been used successfully to interpret observations of high-redshift star-forming galaxies (Stark et al., 2014, 2015a,b, 2016). I present here these main applications and their conclusions.

Our understanding of galaxy growth in the first billion years of cosmic time has developed rapidly in the last five years following a series of deep imaging campaigns in particular with the infrared channel of the Wide Field Camera 3 (WFC3/IR) onboard the *Hubble Space Telescope* (HST). Deep WFC3/IR exposures have delivered more than ~ 1500 galaxies photometrically-selected to lie between $\simeq 0.5-1$ Gyr after the Big Bang (e.g. Bouwens et al. 2015b) and the first small samples of galaxies within the first 0.5 Gyr of cosmic time (e.g., Zheng et al. 2012; Ellis et al. 2013; Coe et al. 2013; Atek et al. 2015; Zitrin et al. 2015; Oesch et al. 2014).

These studies demonstrate that the $z \gtrsim 6$ galaxy population is different from well-studied samples at $z \simeq 2-3$. The UV luminosities, star formation rates, and stellar masses tend to be lower at $z \simeq 6$ (e.g. Smit et al. 2012; McLure et al. 2013; Schenker et al. 2013; Bouwens et al. 2014; Salmon et al. 2015; Duncan et al. 2014; Grazian et al. 2015), the sizes are smaller (e.g., Oesch et al. 2010; Ono et al. 2013; c.f., Curtis-Lake et al. 2016), and the UV continuum colors are bluer (e.g., Wilkins et al. 2011; Finkelstein et al. 2012; Rogers, McLure & Dunlop 2013; Bouwens et al. 2014). Specific star formation rates at $z \gtrsim 6$ are large, indicating a rapidly growing young stellar population (e.g., Stark et al. 2013; González et al. 2014; Salmon et al. 2015).

In this chapter, I present various spectral analyses – based on the models presented in Chapters 3 and 4 – of different samples of high-redshift galaxies, in which we detected prominent ultraviolet and optical emission lines. I focus on the derivation of stellar and gas parameters, and in particular compare emission features of galaxies at $z \simeq 2-3$ and $z \gtrsim 6$.

This chapter is extracted from the four papers I have co-authored with Daniel Stark: *Ultraviolet Emission Lines in Young Low Mass Galaxies at $z \simeq 2$: Physical Properties and Implications for Studies at $z > 7$*; *Spectroscopic detections of C III]λ1909 at $z \simeq 6-7$: A new probe of early star forming galaxies and cosmic reionisation*; *Spectroscopic detection of C IV λ1548 in a galaxy at $z = 7.045$: Implications for the ionizing spectra of reionization-era galaxies* and *Lyα and C III] Emission in $z = 7-9$ Galaxies: Accelerated Reionization Around Luminous Star Forming Systems?*, all published in the Monthly Notices of the Royal Astronomical Society.

5.1 Ultraviolet emission lines in young low-mass galaxies at $z \simeq 2$

5.1.1 Introduction

We present deep spectroscopy of 17 very low mass ($M^\star \simeq 2.0 \times 10^6$ $M_\odot$ to 1.4×10^9 $M_\odot$) and low luminosity ($M_{UV} \simeq -13.7$ to -19.9) gravitationally lensed galaxies in the redshift range $z \simeq 1.5-3.0$. Deep rest-frame ultraviolet spectra reveal large equivalent width emission from numerous emission lines (N IV], O III], C IV, Si III], C III]) which are rarely seen in individual spectra of more massive star-forming galaxies. C III] is detected in 16 of 17 low-mass star-forming systems with rest-frame equivalent widths as large as 13.5 Å. Nebular C IV emission is present in the most extreme C III] emitters, requiring an ionizing source capable of producing a substantial component of photons with energies in excess of 47.9 eV.

Using the photoionization models presented in Chapter 3, we will attempt to understand what these powerful UV emission lines tell us about the nature of low-mass galaxies at high redshift. Our ultimate goals are twofold. Firstly we seek to understand whether the spectra of low-mass galaxies are consistent with the picture of bursty star formation expected with strong stellar feedback. And secondly, motivated by the very low success rate in recovering Lyα at $z \gtrsim 6$, we aim to determine whether UV lines such as C III], C IV, and O III] might be detectable in $z \gtrsim 6$ galaxy spectra.

5.1.2 Observational sample

Here is a description of the Keck and VLT observations that have been performed to investigate what range of properties (metallicity, age, ionization parameter) are required to reproduce the UV emission-line spectra of this low-mass sample.

Keck/LRIS Optical spectra of lensed galaxies in the Abell 1689 field were obtained with the the Low Resolution Imaging Spectrometer (LRIS; Oke et al. 1995) on the Keck I telescope on 09 May 2010 and 24 February 2012. Both nights were clear and the seeing was 0.7 (May 2010) and 1.0 arcsec (Feb 2012). The blue and red side exposures were 1800 sec and 740 sec, respectively. Total integration times were 18 ksec (blue) and 12.6 ksec (red) for the May 2010 observations and 9.0 ksec (blue) and 5.9s ksec (red) for the Feb. 2012 observations. The individual exposures were rectified, cleaned of cosmic rays and stacked using the pipeline of Kelson (2003). The one dimensional spectra were optimally extracted using the Horne (1986) algorithm.

VLT/FORS2 The FORS2 spectrograph on the Very Large Telescope UT1 (Antu) was used to target lensed background galaxies in the field of three massive clusters:
MACSJ0451+0006 (hereafter MACS 0451), Abell 68, and Abell 1689. The observations were performed to cover the wavelength range 3800-9500 Å with a spectral resolution of 10.3 Å as measured from the FWHM of bright isolated sky lines. The FORS reduction pipeline was used to perform flat-fielding, wavelength calibration, sky subtraction, and object extraction. Flux calibration was performed using standard A0V stars.

We have targeted galaxies with and without spectroscopic redshifts. Systems with known redshifts were identified through earlier campaigns targeting multiply-imaged systems (e.g., Santos et al., 2004; Broadhurst et al., 2005; Richard et al., 2007; Frye et al., 2007; Richard et al., 2014). Redshift confirmation of the input spectroscopic sample was achieved through identification of Lyα emission or interstellar UV absorption lines.

We isolate a subset of these for analysis in this work using three basic selection criteria. First, to ensure emission line measurements are made at the correct rest-frame wavelengths, we only consider galaxies with robust spectroscopic redshifts. Most galaxies that fall in our 'robust' category have their redshift confirmed from two separate spectral features (i.e., Lyα emission and metal absorption or continuum break). For several systems, the spatial extent and asymmetry of Lyα prove sufficient for redshift confirmation. Any galaxies on the Keck and VLT masks lacking a confident redshift determination are excised from the sample. Second, we require that C III] falls in the spectral window covered by the Keck and VLT spectra. This criterion restricts the redshift range to $1.3 < z < 4.0$. Objects outside this redshift range are not included in our sample. We also excise objects with redshifts which place the primary emission lines of interest under strong atmospheric OH lines. As the sky lines are strongest in the red side of the optical, this primarily impacts galaxies at $z \gtrsim 2.5$. And finally, to ensure reliable emission line equivalent width measurements, we only consider galaxies with UV continuum detections in the spectra. Given the depth of the spectra, this requirement has the effect of limiting our sample to galaxies with apparent optical magnitudes brighter than $m \simeq 25-26$, placing a lower threshold on the UV flux of galaxies in our sample. While there are several fainter objects on our masks with confirmed redshifts (from Lyα), the faint continuum dictates that additional emission lines can only be detected if equivalent widths are very large (i.e., >50 Å rest-frame), well in excess of the equivalent widths expected for the UV metal lines. Examination of the spectra of the faint Lyα emitters that we excise from our sample confirms the absence of additional emission lines at the 50 Å level.

After removing galaxies that do not satisfy the three criteria listed above, we are left with a sample of 17 lensed galaxies. As we will discuss, the rest-ultraviolet spectra of 16 of the 17 galaxies reveal C III] emission. Colour images of the 16 C III] emitters are shown in Fig. 5.1. The redshifts range between $z = 1.599$ and $z = 2.976$. The sample is comprised of four galaxies from the MACS 0451 field, two galaxies from the Abell 68 field, and eleven galaxies from Abell 1689 field. While the MACS 0451 and Abell 68 observations are entirely based on VLT spectra, the spectroscopic sample toward Abell 1689 is made up of a mixture of Keck and VLT spectra. Nine galaxies have deep Keck spectra, and five have deep VLT spectra. For the three systems with both Keck and VLT observations, we examine both spectra, ensuring that the redshift identifications and emission line measurements are consistent.

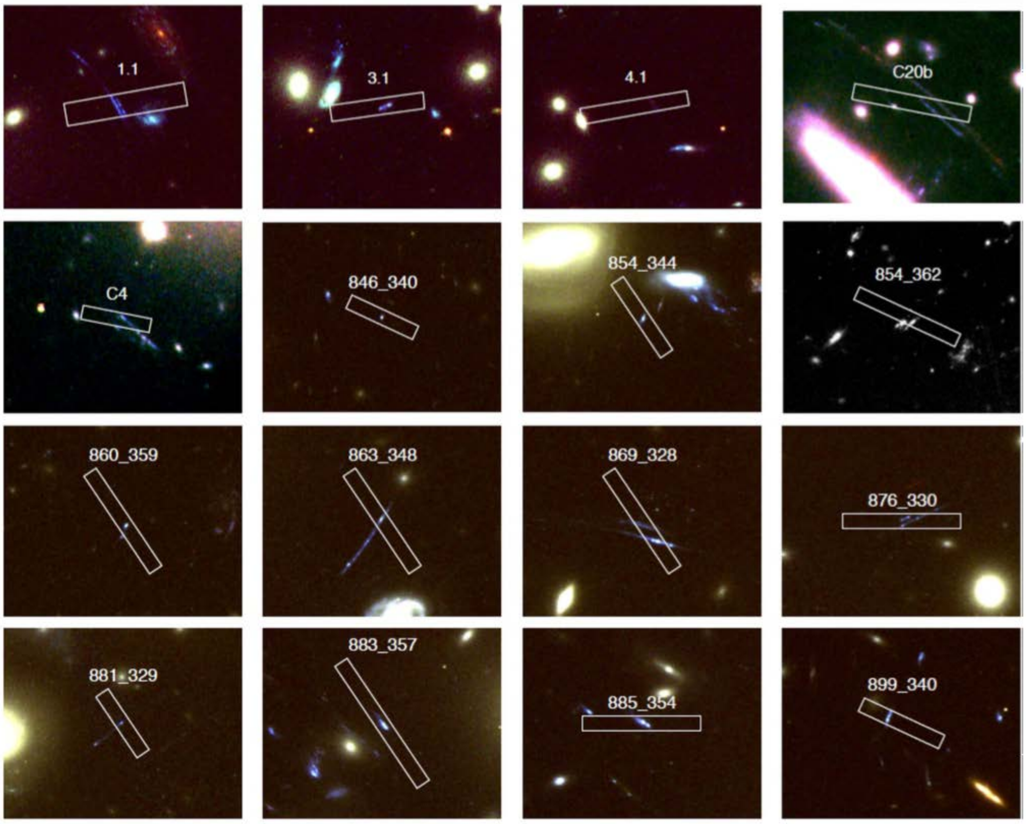

Figure 5.1: Colour images of the 16 dwarf star-forming galaxies at $1.6 \lesssim z \lesssim 3.0$. All of the galaxies have strong collisionally excited emission lines in the rest-frame ultraviolet. We overlay the position angle and slit positions of the Keck/LRIS and VLT/FORS spectra.

From now, we will focus our modelling efforts on the four dwarf star-forming galaxies with the highest quality spectra in the above sample: 876_330, 863_348, 860_359 and MACS 0451-1.1. In Table 5.1, we present the apparent optical magnitudes, lensing magnifications (μ), rest-frame absolute ultraviolet magnitudes, and Lyα and C III] equivalent widths of these galaxies.

Name	$z_{\rm spec}$	RA	DEC	$m_{\rm AB}$	μ	$M_{\rm UV}$	$W_{{\rm Ly}\alpha,0}$ (Å)	$W_{\rm CIII],0}$ (Å)	Redshift-ID
				MACS 0451					
1.1	2.060	04:51:53.399	+00:06:40.31	22.1	45.0 ± 2.5	-18.6 ± 0.1	...	6.7 ± 0.6	IS abs, Opt em
				Abell 1689					
860_359	1.702	13:11:26.426	-01:21:31.22	24.5	4.3 ± 0.3	-18.4 ± 0.1	163.8 ± 25.5	12.4 ± 1.5	Lyα em, Metal em
863_348	1.834	13:11:27.350	-01:20:54.82	24.1	35 ± 3.7	-16.6 ± 0.1	73.1 ± 8.6	13.5 ± 1.6	Lyα em, Metal em
876_330	1.834	13:11:30.320	-01:19:51.13	24.1	27 ± 3.1	-16.9 ± 0.2	>50.0	10.0 ± 2.7	Lyα em, Metal em

Table 5.1: Properties of spectroscopic sample of the four lensed galaxies presented in this study. Each galaxy has a deep Keck/LRIS or VLT/FORS2 spectrum. We report V_{606}-band magnitudes in MACS 0451. In Abell 1689, we report i_{775}-band magnitudes for all sources where available. The lensing flux magnification (μ) are derived from up-to-date cluster mass models. The rest-UV spectrum of 876_330 was presented in Christensen et al. (2012). The primary means of redshift identification is listed in the right-most column. 'IS abs' refers to UV metal absorption lines, 'Metal em' refers to UV emission from metallic species (i.e., O III]$\lambda\lambda1661, 1666$, C III]$\lambda1908$, and 'Opt em' denotes rest-optical emission lines (i.e., Hα, [O III]$\lambda5007$). We note that the two galaxies 863_348 and 876_330 are multiple images.

While C III] is typically the strongest emission line other than Lyα in the rest-UV spectra of low-luminosity galaxies at high redshift, the spectra of these four galaxies shown in Fig. 5.2 reveal additional emission features. By characterizing the flux ratios of the ultraviolet emission lines, we can gain additional insight into the ionized gas physical conditions and stellar populations of our sample of dwarf star-forming galaxies. In Table 5.2, we list the flux ratios relative to C III] for these four galaxies with high-quality spectra in our sample.

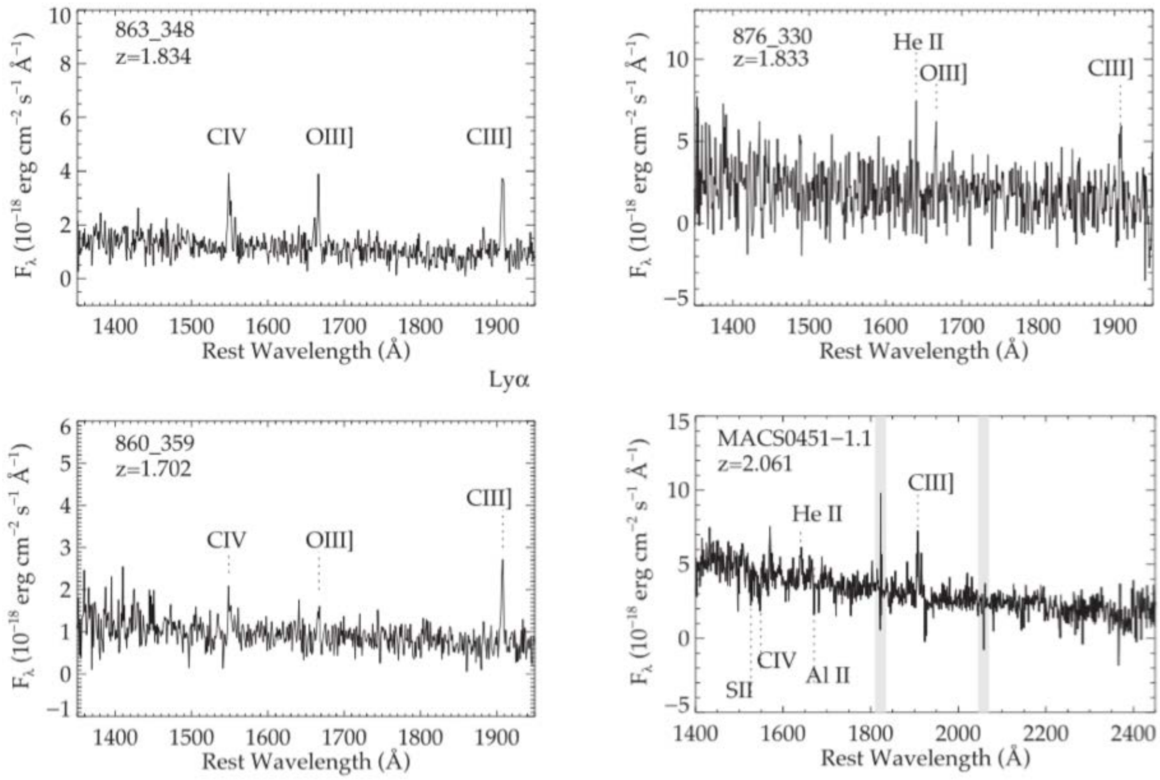

Figure 5.2: Prominent emission lines in rest-UV spectra of four intrinsically faint gravitationally-lensed galaxies: 876_330, 863_348, 860_359 and MACS 0451-1.1. The strongest line is typically the blended C III]λ1908 doublet, but we often note emission from the blended C IV λ1549 doublet, He II λ1640, O III]$\lambda\lambda$1661, 1666, and [Si III]$\lambda\lambda$1883, 1892. The fluxes are as observed, with no adjustment for lensing magnification. Vertical grey swaths in MACS 0451-1.1 correspond to wavelengths with strong sky residuals.

	A1689	A1689	A1689	M0451	A1689
$f_{\mathrm{line}}/f_{\mathrm{CIII]}}$	876_330	863_348	860_359	1.1	881_329
NVλ1240	$\lesssim 1.1$	$\lesssim 0.2$	$\lesssim 0.6$	...	$\lesssim 2.9$
NIV]λ1487	0.5±0.2	$\lesssim 0.1$	$\lesssim 0.1$	...	$\lesssim 0.7$
CIVλ1549	$\lesssim 0.6$	0.8±0.1	0.4±0.1	...	0.5±0.3
He IIλ1640	$\lesssim 0.5$	$\lesssim 0.1$	$\lesssim 0.2$	0.5±0.1	$\lesssim 0.5$
OIII]λ1661	$\lesssim 0.4$	0.2±0.1	$\lesssim 0.2$	0.2±0.1	$\lesssim 0.5$
OIII]λ1666	0.5±0.2	0.6±0.1	0.3±0.1	0.3±0.1	$\lesssim 0.5$
NIII]λ1750	$\lesssim 0.3$	$\lesssim 0.1$	$\lesssim 0.1$	$\lesssim 0.1$	$\lesssim 0.3$
[SiIII]λ1883	$\lesssim 0.3$	0.2±0.1	0.1±0.1	0.2±0.1	$\lesssim 0.5$
[SiIII]λ1892	$\lesssim 0.3$	$\lesssim 0.1$	0.1±0.1	0.2±0.1	$\lesssim 0.5$

Table 5.2: Rest-UV emission flux ratios (relative to the blended C III]λ1908 doublet). If line is not detected significantly, we list the 2σ upper flux ratio limit. No C IV λ1549 flux measurement is possible for MACS0451-1.1 owing to prominent interstellar absorption feature.

5.1.3 Photoionization modelling

We now explore whether photoionization models can reproduce the ultraviolet emission line ratios and equivalent widths of the dwarf galaxies. First, we investigate whether the emission lines can be explained entirely by a low gas-phase metallicity, or if variations in the age, stellar metallicity, and ionization parameter are also required. Second, we examine whether there is enough energetic radiation output by low-metallicity stellar populations to power the C IV emission seen in several dwarf systems.

Method

We appeal to the models described in Chapter 3 to compute the emission from the photoionized interstellar gas in the four star-forming galaxies in Table 5.1.

In practice, to interpret the nebular emission from these galaxies, we use the comprehensive grid of models I have assembled, which covers the wide range of input adjustable parameters detailed in Section 3.3.1: interstellar metallicity, Z_{ISM} ($= Z$), upper mass cutoff of the IMF, m_{up}, zero-age ionization parameter of a newly born H II region, U_{S}, dust-to-metal mass ratio, ξ_{d}, carbon-to-oxygen abundance ratio, C/O, and hydrogen gas density, n_{H}. In addition, for this study, unlike in previous chapters, we also include attenuation of line and continuum photons by dust in the neutral ISM, using the 2-component model of Charlot & Fall (2000), as implemented by da Cunha, Charlot & Elbaz (2008, their equations 1–4). As explained in Section 3.2.4, this is parameterized in terms of the total V-band attenuation optical depth of the dust, $\hat{\tau}_V$, and the fraction μ of this arising from dust in the diffuse ISM rather than in giant molecular clouds. We explore 10 attenuation optical depths $\hat{\tau}_V$ between 0 and 1, and for each $\hat{\tau}_V$, 10 values of μ between 0 and 1. Accounting for these two dust components is important to describe the attenuation of emission-line equivalent widths. We adopt a Bayesian approach similar to that of Brinchmann et al. (2004, their equation 1; see also equation 2.10 of Pacifici et al. 2012) to compute the likelihood of each model given the data.

Finally, in this study, as in previous chapters, we neglect the contribution by stars older than 10 Myr to nebular emission, and assume constant star formation rate and a standard Chabrier (2003) IMF.

Results

The C III] equivalent widths spanned by this subset range from fairly typical values for dwarf star-forming systems (6.7 Å in MACS 0451-1.1) to the most extreme values in our sample (13.5 Å in 863_348), as presented in Table 5.1. As our goal is to determine what is required to produce the ultraviolet spectra, we do not fit the continuum SEDs or optical spectral features. We instead find the range of models within our grid which provides the closest match to the equivalent width of C III] and the flux ratios of C IV, O III]λ1661, O III]λ1666, [Si III]λ1883, and Si III]λ1892 with respect to C III]. It is worth noting that we do not include the He II/C III] ratio in the fitting process, as He II includes a stellar wind component which is non-trivial to decompose from the nebular component at low S/N (see Erb et al., 2010).

The properties of the best fitting (i.e., median) models are listed in Table 5.3, revealing a very similar picture to that implied by the rest-optical spectra and broadband SEDs. The extreme UV emission line strengths of our low-mass galaxies strongly favour models with low oxygen abundances (0.04-0.13 $Z_\odot$), young ages (6-50 Myr) for an assumed constant star formation history, large ionization parameters ($\log U_S = -2.16$ to -1.84), and low C/O ratios ($\log$C/O $= -0.74$ to -0.58).

Property	876_330	863_348	860_359	MACS 0451-1.1
$\log U_S$	$-2.16^{+0.27}_{-0.32}$	$-1.84^{+0.15}_{-0.21}$	$-2.13^{+0.16}_{-0.16}$	$-1.97^{+0.28}_{-0.30}$
$12 + \log\,(\mathrm{O/H})$	$7.74^{+0.27}_{-0.56}$	$7.82^{+0.10}_{-0.53}$	$7.79^{+0.19}_{-0.46}$	$7.29^{+0.58}_{-0.22}$
$\log(\mathrm{C/O})$	$-0.68^{+0.14}_{-0.17}$	$-0.74^{+0.08}_{-0.08}$	$-0.58^{+0.07}_{-0.08}$	$-0.71^{+0.13}_{-0.09}$
$\log(\mathrm{age/yr})$	$7.55^{+0.79}_{-0.48}$	$6.75^{+0.52}_{-0.52}$	$7.30^{+0.56}_{-0.34}$	$7.71^{+0.74}_{-0.57}$
$\log\{W([\mathrm{OIII}]4959, 5007 + \mathrm{H}\beta)\}$	$2.84^{+0.25}_{-0.28}$	$3.18^{+0.09}_{-0.18}$	$3.00^{+0.18}_{-0.19}$	$2.78^{+0.24}_{-0.23}$
μ	$0.70^{+0.18}_{-0.39}$	$0.78^{+0.12}_{-0.35}$	$0.77^{+0.13}_{-0.38}$	$0.70^{+0.18}_{-0.39}$
$\hat{\tau}_V$	$0.20^{+0.40}_{-0.20}$	$0.01^{+0.22}_{-0.18}$	$0.14^{+0.42}_{-0.19}$	$0.19^{+0.38}_{-0.18}$
HeII/CIII]	0.006	0.005	0.004	0.002
CIV/CIII]	0.438	0.892	0.404	1.113
EW(CIII])	9.597	10.556	12.302	6.715

Table 5.3: Properties of best-fitting (i.e. median) models and the 68% confidence intervals for the low-mass galaxies in our sample with the best UV spectra. In the bottom three rows, we present a subset of the line flux ratios and equivalent widths of the median model.

The probability density functions of $\log U_S$ and 12+logO/H are shown in Fig. 5.3. We note that as with the modelling of the continuum SED, the ages are only valid for the assumed star formation history. More complicated star formation histories (i.e., those with a young and old component) would likely fit the data equally well as long as the recent star formation dominates the observed emission. Given the ease in fitting the emission lines with a single component constant star formation history (as this provides a satisfactory statistical fit to the continuum SEDs), we do not explore two component models. As can be seen in Table 5.3, the models which best fit the ultraviolet spectra have large equivalent width [O III]+Hβ emission lines (600-1500 Å rest-frame). Not only are these values consistent with the observations, but they provide further evidence for a close connection between the optical extreme emission line galaxy population and the strong UV line emitters in our sample.

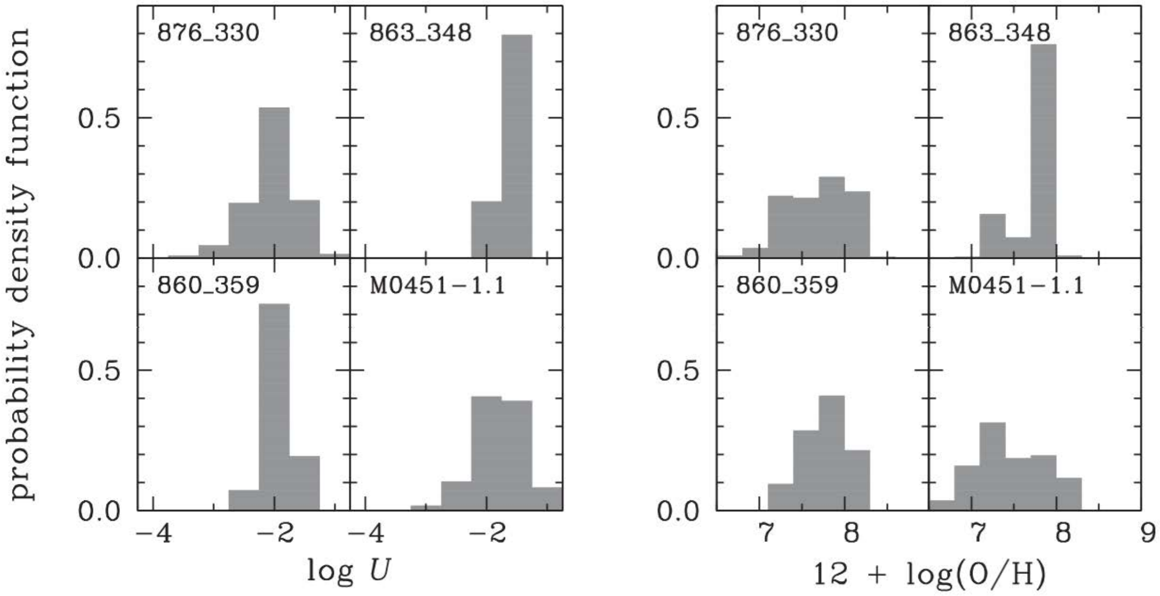

Figure 5.3: Results from photoionization modelling of C III] emitters. To reproduce the extreme ultraviolet equivalent widths, we require large ionization parameters (left panel) and low-metallicity gas and massive stars (right panel). The models also require young ages (best fits of 6-51 Myr) and sub-solar carbon to oxygen abundances. Details of the best fits are provided in Table 5.3.

The first question we posed at the outset of this study was whether the prominent UV emission lines could be explained simply by the larger electron temperature that follows inefficient cooling in low-metallicity gas. The best fitting parameters derived from my modelling indicate that this is not the case. Stellar population ages must be considerably lower and ionization parameters somewhat larger than are commonly inferred for more massive star-forming systems at high redshift (e.g., Hainline et al., 2009; Richard et al., 2011a; Reddy et al., 2012).

The second question we motivated was whether the large equivalent width C IV emission seen in our most extreme galaxies could be powered by normal stellar populations without resorting to other energetic sources. The C IV/C III] ratios of the best fitting models (Table 5.3) indicate that moderately low-metallicity models with large ionization parameters produce ample energetic radiation to drive the observed C IV emission. We note that these same models predict weak He II λ1640 emission, in agreement with the observations presented in Table 5.2. While further data are certainly required to determine if AGN, high-mass X-ray binaries, or fast radiative shocks help power the high ionization emission lines, the models suggest that they are not required to explain the C IV emission.

5.1.4 Conclusion

The C III]λ1908 doublet is typically the strongest line other than Lyα and is detected in 16 galaxies with rest-frame equivalent widths up to 14 Å. We have considered whether the UV emission lines can be reproduced by the photoionization models I have computed. We find that the extreme C III] emitting galaxies in our sample require models with large ionization parameters ($\log U_S = -2.16$ to -1.84), metal poor gas (0.04-0.13 $Z_\odot$), sub-solar C/O ratios (logC/O = -0.74 to -0.58), and a hard radiation field from moderately metal poor and young (6-50 Myr for constant star formation history) massive stars. In other words, we interpret such powerful metal line emission as arising from large ionization parameters and electron temperatures associated with metal-poor galaxies dominated by very young stellar populations.

Based on the photoionization models considered in Section 5.1.3, extreme rest-frame optical emission lines are almost always accompanied by large equivalent width C III] emission in the rest-frame ultraviolet. Detection of C III] in the reionization era need not wait for future facilities. For a bright (H_{160}=24.5) gravitationally-lensed galaxy at $z \simeq 6$, similar to many discovered recently (e.g., Richard et al., 2011b; Zitrin et al., 2012; Bradley & CLASH Team, 2013), a C III] emitter with rest-frame equivalent width between 7 and 13 Å would have a line flux (3-6$\times10^{-18}$ erg cm^{-2} s^{-1}) which is readily detectable with existing spectrographs. In the brightest known $z \gtrsim 6$ galaxies (J_{125}=24.0 in Zitrin et al. 2012), an extreme C III] emitter (similar to 863_348) could have line fluxes as bright as 1.4$\times10^{-17}$ erg cm^{-2} s^{-1}, requiring no more than an hour for detection.

If UV lines are detected, photoionization modelling of the line strengths (together with the broadband SED) will yield much improved constraints on the age and metallicity of the stellar populations, allowing us to put better constraints on the ionizing output of galaxies in the reionization era (e.g., Robertson et al., 2013). This is what we will investigate now.

5.2 Spectroscopic detections of CIII]λ1909 at $z \simeq 6-7$

5.2.1 Introduction

In this work, we demonstrate the validity of a new way forward via the detection of an alternative diagnostic line, C III] λ1909, seen in spectroscopic exposures of a star-forming galaxy at $z_{\mathrm{Ly}\alpha}$ = 6.029. We also report tentative detection of C III] λ1909 in a galaxy at $z_{\mathrm{Ly}\alpha}$ = 7.213. The former 3.3σ detection is based on a 3.5 hour X-shooter spectrum of a bright (J_{125} = 25.2) gravitationally-lensed galaxy behind the cluster Abell 383, while the latter 2.8σ detection is based on a 4.2 hour MOSFIRE spectra of one of the most distant spectroscopically confirmed galaxies, GN-108036, with J_{140} = 25.2. Both targets were chosen for their continuum brightness and previously-known redshift (based on Lyα), ensuring that any C III] emission would be located in a favorable portion of the near-infrared sky spectrum.

Since the availability of secure Lyα redshifts significantly narrows the wavelength range where C III] is sought, this increases confidence in these, otherwise, low S/N detections. We compare our C III] and Lyα equivalent widths in the context of those found at $z \simeq 2$ from earlier work and discuss the motivation for using lines other than Lyα to study galaxies in the reionization era.

5.2.2 Observational sample

Here we report VLT/X-Shooter and Keck/MOSFIRE spectroscopic observations of the C III]λ1908 doublet in two $z > 6$ galaxies.

VLT/XShooter The first system we discuss is a bright gravitationally-lensed system at $z = 6.03$. The galaxy, reported in Richard et al. (2011b) and Bradley & CLASH Team (2013), is multiply-imaged into a pair by the foreground cluster Abell 383. The two images, A383-5.1 and A383-5.2, are both bright (J_{125}=24.6 and 25.2) and highly-magnified (11.4× and 7.3×). Lyα emission was detected in each image by Richard et al. (2011b) and, at the redshift $z_{\mathrm{Ly}\alpha} = 6.029$, the C III] doublet falls within a relatively clean region of the J-band. We chose to pursue A383-5.2 (shown in Fig. 5.4) because A383-5.1 (the brighter of the two lensed images) is located closer to the cluster centre, where diffuse light from bright cluster galaxies contributes considerably to the background in the near-infrared. Observations were conducted on the nights of 2013 October 27 and 2013 December 15 for 3 and 2 observing blocks of 1 hour each, respectively. One observation block comprised three exposures of 955 sec. in the visible arm, covering the wavelength range 5630-10090 Å at a resolution of R~8800, and 3 exposures of 968 sec. in the near-infrared arm (with 4 sub-integrations of 242 sec.), covering the wavelengh range 10350-24780 Å at a resolution of R~5300. The total exposure time on source was 14325 sec in the visible arm and 14520 sec in the near-infrared arm. The sky conditions were clear and the seeing was very good in the first 3 observing blocks, with a range of 0.50-0.70 arcsec and a median seeing of 0.55 arcesec, but less good in the second set of 2 observation blocks, with a range of 0.60-0.90 arcsec. A spectroscopic standard star was observed on both nights for absolute flux calibration, and multiple telluric standard stars were observed to estimate telluric correction.

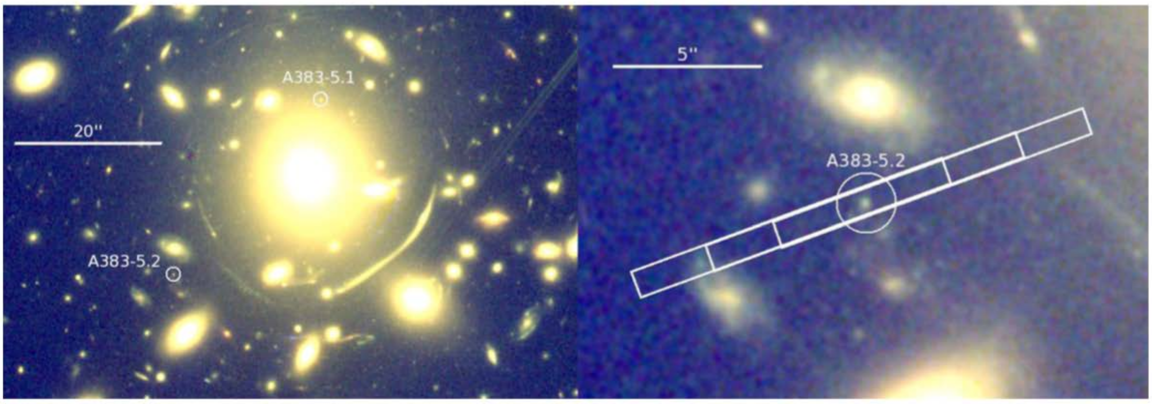

Figure 5.4: Overview of the VLT/XShooter observations of the $z_{\mathrm{Ly}\alpha} = 6.027$ galaxy A383-5.2 first reported in Richard et al. (2011b). (*Left:*) location of the targeted image A383-5.2 with respect to the cluster centre. (*Right:*) Position and orientation of the XShooter slit, showing the three dither positions.

The final combined 2D spectrum at wavelengths near Lyα and C III] are presented in Fig. 5.5, and the extracted 1D XShooter spectrum of this spectroscopically-confirmed z = 6.027 galaxy A383-5.2 is shown in Fig. 5.6.

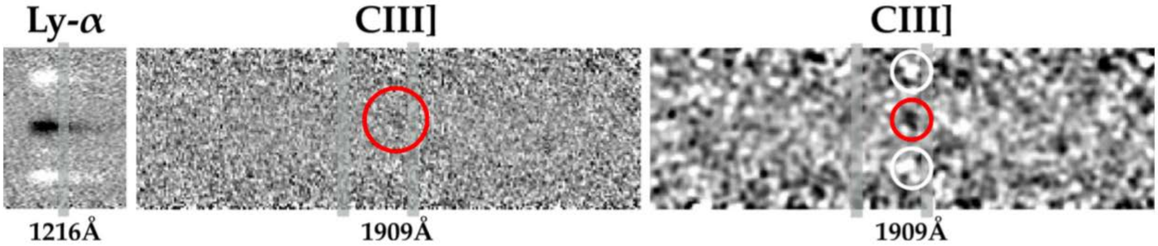

Figure 5.5: Shooter 2D spectrum of the $z_{\mathrm{Ly}\alpha} = 6.027$ galaxy A383-5.2. The leftmost panel is centred on Lyα emission which is detected with the visible arm at 0.8546 μm. The location of C III] λ1909 at 1.3412μm is shown in the middle (unsmoothed) and rightmost (smoothed) panels. The smoothing is performed via a Gaussian filter with radius of 3 pixels. The [C III] λ1907 emission line is under the OH sky line just blueward of C III] λ1909.

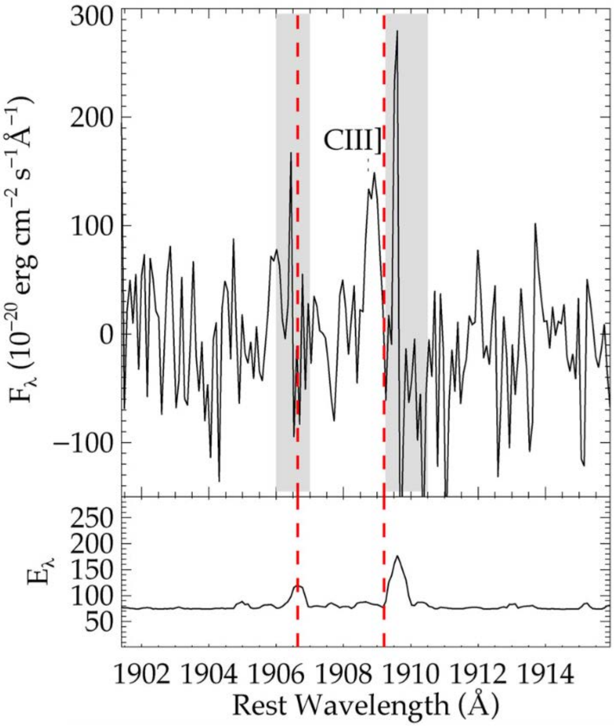

Figure 5.6: Extracted 1D XShooter spectrum of the spectroscopically-confirmed z = 6.027 galaxy A383-5.2. The likely C III] emission feature is noted with a dotted line in the top panel. Red dashed lines denote the narrow window over which C III] is expected based off of the Lyα redshift. The measured line flux of the 3.3σ detection is 3.7×10^{-18} erg cm^{-2} s^{-1}. Wavelengths of strong skylines are visible in the error spectrum shown in the bottom panel. Units of the error spectrum are identical to the object spectrum.

Keck/MOSFIRE The second system we discuss is the z = 7.2 galaxy GN-108036. We secured spectroscopic observations of GN-108036 with MOSFIRE (McLean et al., 2012) on the Keck I telescope on the nights of March 6 and April 11, 2014. GN-108036 is one of the most distant spectroscopically-confirmed galaxies at z=7.213, located in the GOODS North field, and first verified by (Ono et al., 2012) based on three separate exposures with the DEep Imaging Multi-Object Spectrograph (DEIMOS) on Keck 2; the rest-frame equivalent width of Lyα is reported as 33 Å. During the March run, we compiled a total of 3.1 hours of exposure in the H band with an 0.8 arcsec slit. Conditions were generally clear, but with slight cloud during the first half of the observations. The median FWHM of a reference star included on the mask was 0.6 arcsec. On the April night, we secured an additional 1.1 hours, with a median seeing FWHM of 0.5 arcsec and clear conditions. This galaxy was first identified as a bright (J_{140}=25.2) z-band dropout in Ouchi et al. (2009). At this redshift, the C III] doublet is located in a region free from atmospheric absorption within the H-band. The final combined 2D spectrum at a wavelength near C III] is presented in Fig. 5.7, and the 1D extraction is shown in Fig. 5.8.

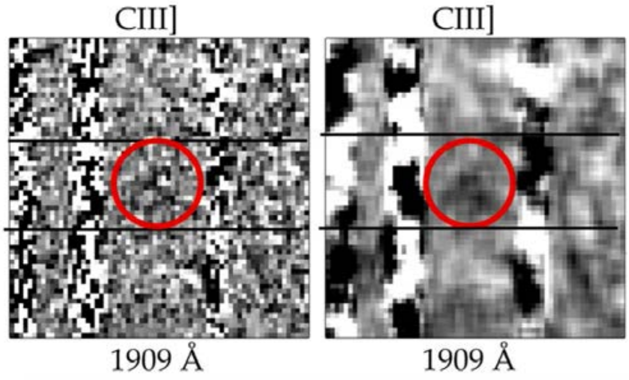

Figure 5.7: MOSFIRE 2D H-band spectrum of the $z = 7.213$ galaxy GN-108036 (unsmoothed in left panel, smoothed in right panel). The spectroscopic redshift from Ono et al. (2012) allows the spectrum to be converted to the rest-frame. Black horizontal lines define the location of the galaxy on the MOSFIRE slit. The red circle denotes the expected wavelength and spatial position of the C III] λ1909 emission line.

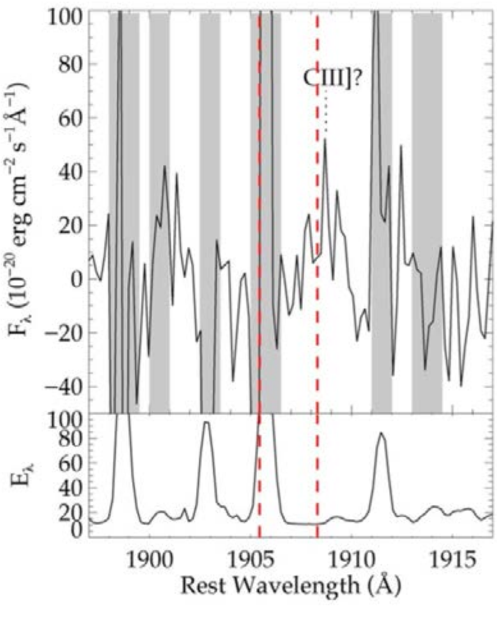

Figure 5.8: Extracted MOSFIRE 1D spectrum of GN-108036. The tentative 2.8σ C III] emission feature is marked by a dotted line. The error spectrum is shown in the bottom panel with the same units as the object spectrum in the top panel. Red dashed lines denote the narrow window over which the centroid C III] is expected based off of the Lyα redshift. Sky emission features are apparent in the error spectrum and are denoted in the top panel by vertical grey swath.

Given the lower significance of the C III] λ1909 detection in GN-108036, we will focus most of the remaining discussion on the more secure detection in A383-5.2.

5.2.3 Modelling the continuum and emission lines of A383-5.2

We now describe the modelling of the continuum and emission lines for A383-5.2.

The broadband SED of A383-5.2 on Fig. 5.9 exhibits a very strong break between the H_{160}-band and the [3.6] and [4.5] bands. Richard et al. (2011b) interpret this as a Balmer Break indicative of an evolved (800 Myr) stellar population. Alternatively the break could arise if nebular emission from [O III]+Hβ and Hα provide substantial contributions within the [3.6] and [4.5] filters, as might be expected if the SED is dominated by a very young stellar population. Distinguishing between these two very different interpretations of the SED is clearly important and can only proceed via direct measurements of the rest-frame optical emission lines. Here we consider whether adding a C III] line flux constraint, which is sensitive to star formation on shorter timescales than that based on the stellar continuum, can clarify the past star formation history of A383-5.2.

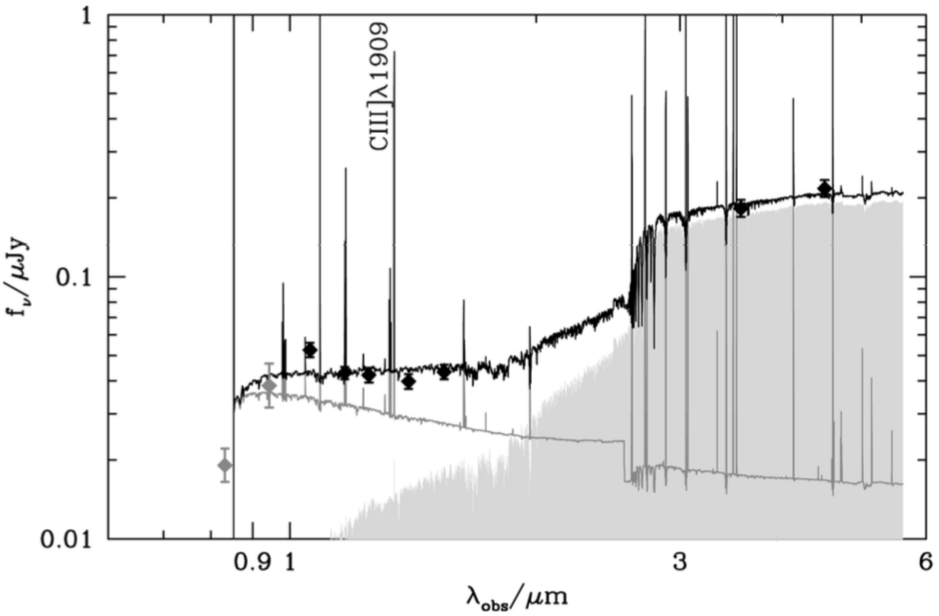

Figure 5.9: SED of A383-5.2 and population synthesis models which provide best fit to the continuum SED and C III] equivalent width. The observed SED is denoted by the diamond data points. The two grey data points at <1μm are not included in the fit because of the uncertainty associated with Lyα emission contamination and IGM absorption. The data are best fit by a model with a two component star formation history. The UV continuum and C III] equivalent width are powered by a recent star formation episode (grey curve), while the optical continuum is dominated by an older generation of stars (solid grey swath). The composite SED is shown in black.

Method

To interpret the combined stellar and nebular emission from A383-5.2, we fit the continuum spectral energy distribution and C III] equivalent width of A383-5.2 using an approach similar to that adopted in last Section 5.1.3 (see Stark et al. 2014 for further details). As we will describe in more detail in Section 5.2.3, the need to simultaneously fit the continuum spectral energy distribution and the C III] equivalent width motivates us to explore a wider range of star formation histories than in the previous study four low-mass galaxies with high-quality spectra at redshifts $z \simeq 1.5-3.0$ (see Section 5.2.3 and Stark et al. 2014 for further details). In particular, we now consider models with two-component star formation histories: a 'starburst' component (represented by a 10 Myr-old stellar population with constant SFR) and an 'old' component (represented by a stellar population with constant or exponentially declining SFR with age between 10 Myr and the age of the Universe at the galaxy redshift). The relative contribution of the burst component is a free parameter; in the limiting case where the burst provides a negligible contribution to the stellar mass fraction, the star formation history approaches the single component star formation histories which are commonly used in high-redshift SED fitting. Given the young ages at redshifts $z > 6$, this simple modelling of star formation and chemical enrichment adequately samples the allowed parameter space.

A383-5.2

Model fit to A383.5.2	
$\log U_{\mathrm{S}}$	$-1.79^{+0.36}_{-0.43}$
$\log\,(M_{*,\mathrm{young}}/M_{*,\mathrm{tot}})$	$-2.99^{+0.05}_{-0.03}$
$\log\,(Z/Z_{\odot})$	$-1.37^{+0.23}_{-0.16}$
$\log(\mathrm{C/O})$	$-0.57^{+0.06}_{-0.06}$
$\log(\mathrm{age/yr})$	$8.72^{+0.10}_{-0.10}$
$\log(M_{*,\mathrm{tot}}/M_{\odot})$	$9.50^{+0.10}_{-0.10}$
$\log(\mathrm{SFR}/M_{\odot}\mathrm{yr}^{-1})$	$0.30^{+0.07}_{-0.07}$
$\hat{\tau}_V$	$0.05^{+0.05}_{-0.05}$

Table 5.4: Results of fitting procedure for A383-5.2.

The acceptable parameter fits are shown in Table 5.4. Including the nebular line constraints in the modelling has provided several key advances. First the dependence of emission line equivalent widths on the ionized gas physical conditions allows new constraints on the metallicity, relative C/O abundance, and ionization parameter in star-forming galaxies at $z \simeq 6$. As can be seen in Table 5.4, the large equivalent width of C III] in A383-5.2 requires models with a very low metallicity ($\log(Z/Z_{\odot}) = -1.37^{+0.23}_{-0.16}$), large ionization parameter ($\log U_{\mathrm{S}} = -1.79^{+0.36}_{-0.43}$), and low C/O ratio ($\log \mathrm{C/O} = -0.57^{+0.06}_{-0.06}$), similar to the population of ultra-faint lensed galaxies at $z \simeq 2$ (Stark et al., 2014). These constraints are almost entirely lost when the C III] equivalent width is not included in the fitting procedure. The total stellar mass implied by the models is $3.2{\times}10^9$ $M_\odot$, in close agreement with that reported in Richard et al. (2011b). The current star formation rate is 2.0 $M_\odot$ yr^{-1}. This estimate is within 2× that inferred from the Lyα luminosity, 3.2 $(f_{esc,Ly\alpha})^{-1}$ $M_\odot$ yr^{-1} (see Section 3.1.1 in Stark et al. 2015a for details).

Given the systematic uncertainties in both quantities and the slightly different model assumptions, we consider this agreement satisfactory.

We find that single component star formation histories struggle to reproduce the continuum SED and C III] equivalent width. Very young ($\lesssim 10^7$ yr), dusty, and metal poor models can reproduce the apparent Balmer Break with strong [O III]+Hβ and Hα emission dominating the [3.6] and [4.5] fluxes. But with strong attenuation and substantial reddening, the young single component models underpredict the C III] equivalent width and overestimate the H_{160} flux. Similarly, while an old stellar population produced by a single component star formation history can account for the large break between the H_{160}-band and [3.6], it is unable to reproduce a large equivalent width C III] emission or a blue UV continuum slope supported by the available imaging and spectroscopy.

We thus find that the observational data indicate a two-component star formation history (Fig. 5.9). The nebular lines and far UV continuum are dominated by a recent burst, while the rest-optical light seen by the *Spitzer*/IRAC filters is powered by a somewhat older stellar population. Both populations contribute roughly equally to the emerging near-UV continuum. The young burst component contributes very little to the total stellar mass ($\sim 10^{-3}$) but provides enough ionizing output to match the observed C III] equivalent width.

A383-5.2 is certainly not unique in this respect at very high redshift: Rodríguez Espinosa et al. (2014) have recently argued that a two component star formation history is necessary to explain the combined emission line and continuum constraints on a pair of galaxies at $z = 5.07$. But whether multi-component star formation histories are typical among at $z \gtrsim 6$ sources is not yet clear. Very young stellar ages (<10 Myr for constant star formation) have been suggested based on the large equivalent width of optical nebular emission lines required to match the *Spitzer*/IRAC colours of $z \simeq 7-8$ galaxies (e.g. Finkelstein et al. 2013; Smit et al. 2014). But it is unlikely that such systems (located 650-800 Myr after the Big Bang) have only been forming stars for such a short period. Indeed the average stellar continuum of $z \simeq 8$ galaxies is indicative of older (100 Myr for constant star formation) stars (Dunlop et al., 2013; Labbé et al., 2013). Multi-component star formation histories with a recent upturn powering the nebular emission provide a natural explanation for this tension. As larger samples of galaxies with UV metal line and high S/N continuum constraints emerge, it will be possible to clarify the nature of early galaxy star formation histories in more detail.

5.2.4 Conclusion

We have demonstrated it may be feasible to detect the C III] 1908 Å doublet in the growing sample of bright ($H \simeq 25$) star-forming galaxies at $z > 6$. The two sources we discuss are very different and illustrate the challenges even with state-of-the-art near-infrared spectrographs on the largest ground-based telescopes. A363-5.2 is a gravitationally-lensed galaxy at a redshift $z_{Ly\alpha}$ =6.029. It is bright ($J_{125} = 25.2$), highly magnified (×7.4) and a likely 3.3σ C III] λ1909 detection has been secured in only a 3.5 hour exposure. The source is typical of the brightest sources that have been located in lensing surveys of foreground clusters (e.g. the CLASH program). GN-108036 is more typical of the bright sources found in deep blank field surveys. Although not fainter (J_{140} = 25.2), as it is unlensed, it is more luminous and even with a 4.2 hour exposure, the putative C III] feature is much fainter and only detected at 2.8σ. Clearly deeper data is highly desirable to confirm this detection.

The likely detection of C III] in A383-5.2 has enabled us to break degeneracies of interpretation in the SED of this $z > 6$ source. Specifically, including the strength of C III] in my model fits to the spectral energy distribution allows us to determine a low metallicity (log$Z$ = −1.37), a large ionization parameter (logU_S = −1.79) and a low C/O ratio.

5.3 Spectroscopic detection of CIVλ1548 in a galaxy at $z = 7.045$

5.3.1 Introduction

In the previous Section 5.2, we have reported tentative C III] detections in two galaxies with previously confirmed redshifts (z = 6.029 and z = 7.213) from Lyα. Here we build on this progress with an exploration of the strength of high-ionization emission features (C IV $\lambda\lambda$1548, 1551 and He II λ1640) in a small sample of $z \simeq 7$ UV-selected galaxies using the MOSFIRE (McLean et al., 2012) spectrograph on the Keck I telescope.

More precisely, we present Keck/MOSFIRE observations of UV metal emission lines in four bright (H=23.9-25.4) gravitationally-lensed $z \simeq 6-8$ galaxies behind the cluster Abell 1703, and we focus particularly on the spectrum of A1703-zd6, a highly-magnified star-forming galaxy with a Lyα redshift of $z = 7.045$.

At $z \simeq 2-3$, nebular C IV emission is observed in just 1% of UV-selected galaxies (Steidel et al., 2002; Hainline et al., 2011). The presence of strong C IV emission in one of the small sample of galaxies targeted in this work may indicate hard ionizing spectra are more common at $z \simeq 7$. We will see that the total estimated rest-frame equivalent width of the C IV doublet and C IV/Lyα flux ratio are comparable to measurements of narrow-lined AGNs. Photoionization models show that the nebular C IV line can also be reproduced by a young stellar population, with very hot metal poor stars dominating the photon flux responsible for triply ionizing carbon. Regardless of the origin of the C IV, we show that the ionizing spectrum of A1703-zd6 is different from that of typical galaxies at $z \simeq 2$, producing more H ionizing photons per unit 1500 Å luminosity (log($\xi_{\rm ion}$/erg^{-1} Hz)=25.68) and a larger flux density at 30-50 eV.

5.3.2 Observational sample

Near-infrared spectroscopic observations of Abell 1703 were carried out with MOSFIRE (McLean et al., 2012) on the Keck-I Telescope on April 11, 2014 UT. The spectroscopic observations were taken using the YJ grating with the J-band filter, which has a resolution of R=3318 and covers a wavelength range of λ=1.15-1.35μm. A mask was created for Abell 1703 with 1.0 arcsec width slits. Individual exposures were 120 seconds with two position dithers of 3.0 arsec having a total integration time of 2.6 hours. The average seeing throughout the observation was 0.80 arcsec (FWHM). The four $z \gtrsim 5$ galaxies on the mask are shown in Fig. 5.10.

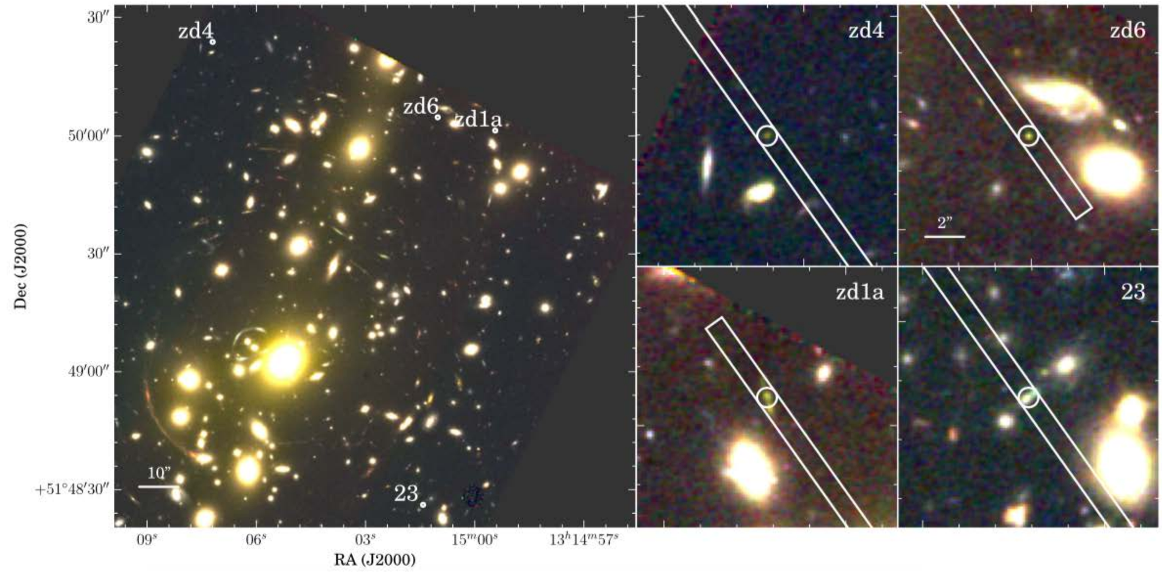

Figure 5.10: Overview of the Keck/MOSFIRE J-band observations of four gravitationally-lensed galaxies at $5.8 < z < 7.0$ in the field of Abell 1703. Positions of the galaxies are overlaid on the HST color image (z_{850}, J_{125}, H_{160}-bands) of the cluster. The right panel shows a zoomed in view.

In this study, we focus on the highly magnified star-forming galaxy A1703-zd6, as its spectrum reveals a confident detection of the nebular C IV λ1548 emission line, while UV metal emission lines are not detected in the three other galaxies.

A1703-zd6 is a bright (H=25.9) z-band dropout first identified in Bradley et al. (2012). A spectroscopic redshift ($z = 7.045$) was achieved via detection of Lyα at 9780 Å (Schenker et al., 2012). The absolute UV magnitude is found to be $M_{UV} = -19.3$ after correcting for the source magnification ($\mu = 5.2$).

The spectra were reduced using the publicly-available MOSFIRE Data Reduction Pipeline (DRP)[1]. The MOSFIRE DRP performs the standard NIR spectroscopic reduction; flat-fielding, wavelength calibration, sky-subtraction, and Cosmic Ray removal to produce 2D spectra. The instrumental response and telluric absorption across the J-band were corrected using longslit observations of a standard star. The absolute flux calibration was performed using a star placed in the mask of the science field with HST ACS (F850LP) and WFC3/IR (F125W, F160W) photometry. The C IV doublet is easily resolved by MOSFIRE at $z \simeq 7$. If C IV traces gas at the same redshift as Lyα ($z = 7.045 \pm 0.003$), we would expect C IV λ1548 to be located between 1.2450 and 1.2460μm and C IV λ1550 between 1.2471 and 1.2481μm. As can be seen in the 2D spectrum shown in Fig. 5.11, C IV λ1548 is confidently detected at 1.2458μm, which is within the window defined by the Schenker et al. (2012) Lyα detection. C IV λ1550 is also likely detected at 1.2474μm.

---

[1] https://keck-datareductionpipelines.github.io/MosfireDRP/

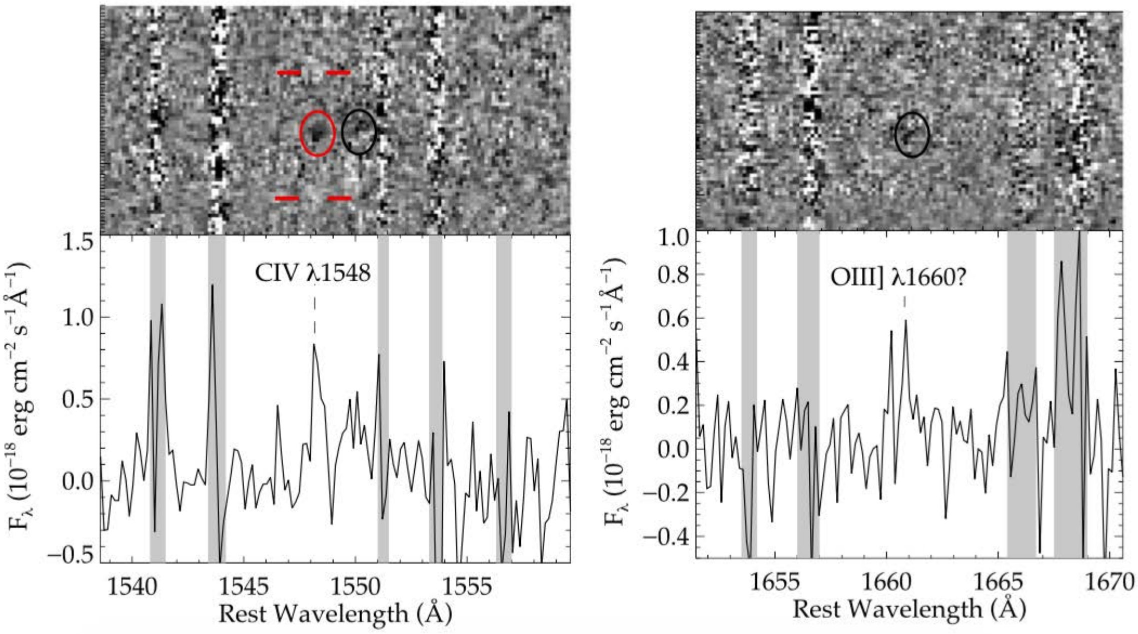

Figure 5.11: Keck/MOSFIRE J-band spectrum of the gravitationally-lensed $z_{\mathrm{Ly}\alpha} = 7.045$ galaxy A1703-zd6. The spectroscopic redshift was known prior to MOSFIRE observations from Lyα emission (Schenker et al., 2012). Top panels show the two-dimensional (unsmoothed) spectra with black showing positive emission. The red oval identifies the emission feature at the rest-frame wavelength expected for C IV λ1548. The characteristic negative emission from the dither pattern is demarcated by red horizontal lines. Black ovals highlight the expected location of C IV λ1550 (left panel) and O III]λ1661 (right panel). The one-dimensional extracted spectra are shown below. Vertical grey swaths indicate regions of elevated noise from OH sky lines.

At $z = 7.0433$, the O III]λ1666 is located on top of a strong skyline at 1.340μm (Fig. 5.11) and is not detected in the MOSFIRE spectrum. We also do not detect He II λ1640 or N IV]$\lambda\lambda$1483, 1487. Flux and rest-frame equivalent width limits (2σ) are provided in Table 5.5. Non-detection of He II and N IV] is consistent with the emission line spectra of $z \simeq 1.5 - 3$ metal poor dwarf galaxies (Christensen et al., 2012; Stark et al., 2014). In these systems, the FUV metal lines (C IV, C III], O III]) are typically much stronger than He II and N IV].

Line	λ_{rest} (Å)	λ_{obs} (Å)	Line Flux (10^{-18} erg cm^{-2} s^{-1})	W_0 (Å)
Ly$\alpha^{\dagger}$	1215.67	9780	28.4 ± 5.3	65 ± 12
NIV]	1483.3	...	<3.6	<15.7
...	1486.5	...	<4.3	<19.0
CIV	1548.19	12457.9	4.1 ± 0.6	19.9 ± 3.6
...	1550.77	12473.5	3.8 ± 0.9	18.1 ± 4.6
He II	1640.52	...	<2.1	<11.4
OIII]	1660.81	13358.3	1.8 ± 0.7	9.8 ± 3.9
...	1666.15	...	...	...

Table 5.5: Emission line properties of the $z_{\mathrm{Ly}\alpha} = 7.045$ galaxy A1703-zd6 (Bradley et al., 2012). An aperture correction of 1.20× must be applied to the emission line fluxes if computing line luminosities. The † next to Lyα notes that this flux measurement is from Schenker et al. (2012). Measurement of the line flux of the C IV λ1550 component is challenging. We place a lower limit on its flux and rest-frame equivalent width of 2.1×10^{-18} erg cm^{-2} s^{-1} and 9.8 Å, respectively. The O III]λ1666 emission line is obscured by a skyline. The equivalent widths include the aperture correction and are quoted in the rest-frame. The limits are 2σ.

5.3.3 A hard ionizing spectrum at $z = 7$

Here we use photoionization models to characterize the shape of the ionizing spectrum required to produce the observed spectral properties of A1703-zd6. We explore galaxy models with stellar input spectra and AGN models.

Stellar models We fit the observed C IV λ1548 emission equivalent width (the component of the doublet that is most robustly detected) and broadband F125W and F160W fluxes of the galaxy using again an approach similar to that adopted in the previous studies of this chapter, by comparing these observed values with the models of nebular emission I have developed.

As in Section 5.2, we consider models with 2-component star formation histories: a ‘starburst’ component (represented here by a 3 Myr-old stellar population with constant SFR) and an ‘old’ component (represented by a stellar population with constant or exponentially declining SFR with age between 10 Myr and the age of the Universe at the galaxy redshift, i.e. 0.75 Gyr). To interpret the combined stellar and nebular emission from the galaxy, we use the same Bayesian approach as done before (Stark et al., 2014, 2015a, following Brinchmann et al. 2004).

The values reported for each quantity in Table 5.6 are the median and 16%-84% percentile range of the probability density function obtained from this Bayesian analysis. The “best-fit” values correspond to the model producing the minimum χ^2.

A1703-zd6	
$\log U_\mathrm{S}$	$-1.35^{+0.24}_{-0.39}$
$12 + \log(\mathrm{O/H})$	$7.04^{+0.31}_{-0.25}$
$\log(\xi_\mathrm{ion}/\mathrm{Hz\,erg^{-1}})$	$25.68^{+0.27}_{-0.19}$
$\log[W(\mathrm{Ly}\alpha)/\mathrm{\AA}]$	$2.06^{+0.33}_{-0.23}$
$\log(\mathrm{NIV\,1486/CIV\,1548})$	$-1.93^{+0.32}_{-0.18}$
$\log(\mathrm{NV\,1240/CIV\,1548})$	$-2.44^{+0.42}_{-0.42}$
$\log(\mathrm{HeII\,1640/CIV\,1548})$	$-1.59^{+0.22}_{-0.20}$

Table 5.6: A1703-zd6 photoionization modelling results. We fit the C IV λ1548 equivalent width and J_{125} and H_{160} broadband flux densities.

In practice, we find that the requirement to reproduce the strong C IV λ1548 emission equivalent width implies that the best-fit models are entirely dominated by the young stellar component (for reference, the best-fit model rest-frame equivalent width for this line is 19.9 Å). Such models also provide excellent fits to the observed F125W and F160W fluxes (with a dust attenuation optical depth consistent with zero). Also, since nebular emission is constrained only by the equivalent width of a single component of the C IV doublet in our analysis, the resulting constraints on the gas density and C/O ratio are extremely weak.

The models demonstrate that the C IV emission line strength of A1703-zd6 can be reproduced by stellar input spectra. The range of acceptable model parameters is shown in Table 5.6. Models that fit the observed spectral properties have a large ionization parameter ($\log U_\mathrm{S}$ = -1.35) and very low metallicity (12 + logO/H = 7.04). The production rate of hydrogen ionizing photons per observed (i.e. attenuated) 1500 Å luminosity is very large ($\log(\xi_\mathrm{ion}/\mathrm{erg^{-1}Hz})$=25.68) in models that reproduce the data. We note that we do not attenuate the ionizing photon output in our calculation of ξ_{ion}, as a primary goal is to be able to predict how many hydrogen ionizing photons were produced based on the observed 1500 Å luminosity.

The ionizing spectrum of the best-fitting stellar model (Fig. 5.12) reveals a significant flux of energetic radiation at 40-50 eV capable of producing nebular C IV emission. The flux density drops off significantly above ~ 54 eV, resulting in much weaker emission from He II and N V. Stellar models predict N V λ1240 and He II λ1640 fluxes that are 30-250× weaker than the C IV λ1548 line strength (Table 5.6). These lines are unlikely to be detected if the C IV emission is powered by a stellar population.

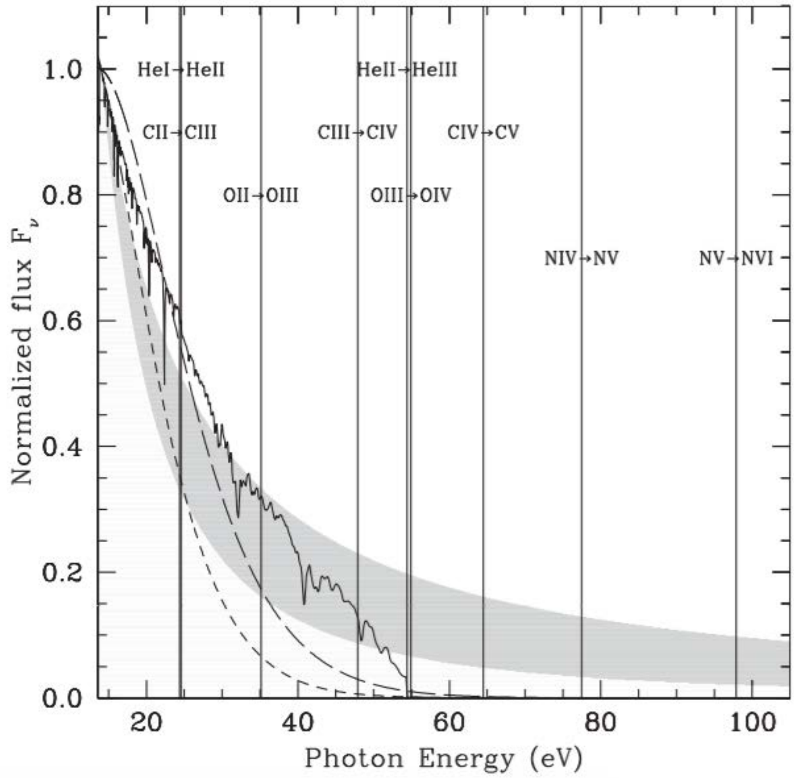

Figure 5.12: Ionizing spectra from different sources, plotted together with the ionizing potentials of different ions (vertical lines). The solid spectral energy distribution corresponds to the best-fit galaxy model reported in Section 5.3.3, while the shaded area shows the range in ionizing spectra produced by $F_\nu \propto \nu^\alpha$ AGN models with spectral indices between $\alpha = 1.2$ (upper ridge) and 2.0 (lower ridge). For comparison to the radiation field in typical galaxies at $z \simeq 2$ (Steidel et al., 2014), we also display blackbody spectra with temperatures of 45,000 (short dashed) and 55,000 K (long dashed), respectively. All spectra are normalized to unity at 13.6 eV.

AGN models We also explore a comparison of A1703-zd6 to AGN photoionization models, using the models presented in Chapter 4 of the narrow line emission regions of AGNs. In contrast to the stellar model fits, we do not include the constraints from the line equivalent widths and broadband photometry because of the arbitrary scaling of the AGN and host galaxy luminosities that would be required to model the underlying continuum. The AGN fit is instead focused on the two most robustly constrained flux ratios, namely O III]λ1661/C IV λ1548 and He II λ1640/C IV λ1548. Given the tentative nature of the O III]λ1661 detection, we adopt a 5σ upper limit ($<3.5\times10^{-18}$ erg cm^{-2} s^{-1}) to the line flux. We note that this limit is consistent with the observed faint flux level of the possible emission feature (1.8×10^{-18} erg cm^{-2} s^{-1}). The measurement of C IV λ1548 and upper limits on O III]λ1661 and He II thus translate into upper limits for the emission line ratios O III]λ1661/C IV λ1548 and He II λ1640/C IV λ1548 used in the fit.

The fitting procedure demonstrates that the existing observational constraints are also marginally consistent with photoionization by an AGN. The two flux ratio limits favour best-fit AGN models corresponding to metallicity and hydrogen density of Z=0.001 and 10^2cm^{-3}, respectively. The ionizing spectra of acceptable AGN models is shown in Fig. 5.12, where we overlay the $z \simeq 2$ galaxy ionizing spectrum on the AGN and stellar photoionization models which reproduce the spectral features of A1703-zd6. Both models predict that the $z = 7.045$ galaxy must have a larger output of 20-50 eV radiation than is commonly seen in $z \simeq 2-3$ galaxies.

The AGN power law spectrum has considerably greater flux than the galaxy models at energies in excess of 50 eV. As a result, AGN models predict stronger He II λ1640 than the galaxy models discussed just before, with a flux that is 40% that of the measured C IV λ1548 flux. Current limits suggest the He II flux is less than 50% that of C IV λ1548 at 2σ. Deeper J-band observations may thus be able to detect He II if A1703-zd6 is powered by an AGN.

Finally, in Fig. 5.12 we overlay the $z \simeq 2$ galaxy ionizing spectrum on the AGN and stellar photoionization models which reproduce the spectral features of A1703-zd6. Both models predict that the $z = 7.045$ galaxy must have a larger output of 20-50 eV radiation than is commonly seen in $z \simeq 2-3$ galaxies.

5.3.4 Conclusion

We have reported the detection of strong nebular C IV λ1548 emission in the spectrum of A1703-zd6, a spectroscopically confirmed galaxy at $z = 7.045$. The total C IV equivalent width is greater than in existing samples of $z \simeq 2$ metal poor star-forming galaxies (Christensen et al., 2012; Stark et al., 2014); the absence of strong C IV emission in typical galaxies at $z \simeq 2$ points to a negligible output of photons with energies greater than 47.9 eV – that is the ionizing potential of C IV, consistent with the radiation field expected from the blackbody models predicted for $z \simeq 2$ galaxies in Steidel et al. (2014). The C IV equivalent width of A1703-zd6 is more similar to that seen in narrow-lined AGNs (Hainline et al., 2011; Alexandroff et al., 2013), pointing to a hard radiation field in one of the most distant known galaxies.

Using the photoionization models presented in Chapters 3 and 4, we have shown that the extreme spectral properties of A1703-zd6 can be powered by an AGN or an intense population of young, very hot, metal-poor stars, and photoionization models point to an ionizing spectrum that is very different from that inferred for typical $z \simeq 2$ galaxies.

If such extreme radiation fields are typical in UV-selected systems at $z \gtrsim 7$, it would indicate that reionization-era galaxies are more efficient ionizing agents than previously thought. Alternatively, we suggest that the small sample of Lyα emitters at $z \gtrsim 7$ may trace a rare population with intense radiation fields capable of ionizing their surrounding hydrogen distribution. Additional constraints on high-ionization emission lines in galaxies with and without Lyα detections will help clarify whether hard ionizing spectra are common in the reionization era.

5.4 Lyα and CIII] emission in $z = 7 - 9$ galaxies

5.4.1 Introduction

A last application of the photoionization models I have developed regards new Keck/MOSFIRE spectroscopic observations of four luminous galaxies at $z \simeq 7-9$ selected to have intense rest-frame optical line emission by Roberts-Borsani et al. (2016). Previous spectroscopic follow-up has revealed Lyα emission in two of the four galaxies. Our new MOSFIRE observations confirm that Lyα is present in the entire sample. The ubiquity of Lyα emission in this unique photometric sample is puzzling given that the IGM is expected to be significantly neutral over $7 < z < 9$. To investigate this surprising result in more detail, we have initiated a campaign to target UV metal line emission in the four Lyα emitters as a probe of the ionizing radiation field at early times. Here we present the detection of very large equivalent width C III]$\lambda\lambda1907, 1909$ emission in EGS-zs8-1 ($W_{\mathrm{CIII]},0} = 22 \pm 2$ Å), a galaxy from this sample previously shown to have Lyα emission at $z = 7.73$. We will see that photoionization models indicate that an intense radiation field ($\log_{10}\, \xi^*_{ion}$ [erg^{-1} Hz] $\simeq 25.6$) and moderately low metallicity (0.11 $Z_\odot$) are required to reproduce the C III] line emission and intense optical line emission implied by the broadband SED.

5.4.2 Observational sample

We present new observations of three of the four galaxies identified in Roberts-Borsani et al. (2016), for which we have obtained new spectral constraints. Data were obtained over three separate observing runs using the near-infrared multi-object spectrograph MOSFIRE (McLean et al., 2012) on the Keck I telescope.

The first observing run was 12-15 April 2015. We observed EGS-zs8-2 in the Y-band, targeting the tentative Lyα detection reported in Roberts-Borsani et al. (2016). The seeing was between 0.5 arcsec and 0.8 arcsec and skies were clear in 4.0 hours of integration. The integration time of individual Y-band exposures was 180 seconds. Both EGS-zs8-1 and EGS-zs8-2 were then observed in the H-band to constrain the strength of the C III]$\lambda\lambda1907, 1909$ doublet. Conditions were mostly clear and seeing was 0.5 arcsec during the 2.5 hours of on-source integration. On 11 June 2015, we obtained an additional 1.0 hr of H-band observations on EGS-zs8-1 and EGS-zs8-2 in clear conditions with average seeing of 0.6 arcsec, bringing the total H-band integration time to 3.5 hrs. The individual H-band exposures are 120 seconds. Finally, on 30 November 2015, we obtained a Y-band spectrum of COS-zs7-1. Conditions were clear and the average seeing was 0.7 arcsec. We obtained 48 exposures of 180 seconds, totaling 2.4 hours of on-source Y-band integration on COS-zs7-1. Each mask contained 1-2 isolated stars for absolute flux calibration and numerous lower redshift galaxies.

The publicly-available MOSFIRE Data Reduction Pipeline was used to reduce the spectra. The DRP performs flat-fielding, wavelength calibration, sky-subtraction, and cosmic ray removal, outputting reduced two dimensional spectra. Using the output from the DRP, we calculated two-dimensional signal to noise maps for each object. One-dimensional spectra were then obtained using a boxcar extraction with apertures matched to the object profile, typically in the range 6-8 pixels (1.08 arcsec - 1.44 arcsec).

We now provide details about of the three galaxies, for which we have obtained new spectral constraints.

EGS-zs8-1 EGS-zs8-1 is a bright (H_{160}=25.0) galaxy with a red IRAC color ([3.6]-[4.5]=0.53± 0.09). As described in Roberts-Borsani et al. (2016), the 4.5μm flux excess suggests very large rest-frame equivalent width (911 ± 122Å) [O III]+Hβ emission. The optical line equivalent widths quoted here and below are inferred through computation of the line flux required to produce the measured IRAC flux excess, in the same manner as earlier studies (Shim et al., 2011; Stark et al., 2013; Smit et al., 2014; Roberts-Borsani et al., 2016). The spectroscopic redshift $z_{\rm Ly\alpha} = 7.733$ was confirmed by Oesch et al. (2015) through detection of a strong Lyα emission line using MOSFIRE (see Fig. 5.13a). The Lyα line flux (1.7×10^{-17} erg cm^{-2} s^{-1}) is one of the largest among $z > 7$ galaxies and suggests a rest-frame equivalent width of $W_{\rm Ly\alpha} = 21 \pm 4$ Å.

The MOSFIRE H-band spectrum of EGS-zs8-1 covers the wavelength range between 1.5154 μm and 1.8223 μm. In Fig. 5.13b, the narrow spectral window between 1.650 and 1.675μm is shown, revealing a clean detection of both components of the C III]$\lambda\lambda$1907, 1909 doublet. We measure line fluxes of $4.5\pm0.5\times10^{-18}$ erg cm^{-2} s^{-1} and $3.6\pm0.5\times10^{-18}$ erg cm^{-2} s^{-1} for the 1907 and 1909 Å components, respectively. The total flux in the resolved C III] doublet is close to 50% that of Lyα, nearly 10× greater than is seen in the most extreme C III] emitting galaxies at lower redshift (e.g., Erb et al. 2010; Christensen et al. 2012; Stark et al. 2014). Since the continuum is undetected in the spectrum, we calculate the rest-frame equivalent widths using continuum flux derived from the broadband SED. The measurements indicate a total C III]$\lambda\lambda$1907, 1909 rest-frame equivalent width of 22 ± 2 Å (12 ± 2 Å for [C III] λ1907 and 10 ± 1 Å for C III] λ1909), similar to the value recently derived in a gravitationally-lensed galaxy at $z = 6.024$ (Stark et al., 2015a).

The flux ratio of the C III]$\lambda\lambda$1907, 1909 doublet provides a measurement of the electron density of the ionized gas. The ratio of C III]λ1909/λ1907 varies from $\simeq 0.8$ for n_e=3×10^4 cm^{-3} to 1.5 for n_e=10^2 cm^{-3}. The measured C III]λ1909/λ1907 flux ratio of EGS-zs8-1 (1.25 ± 0.22) suggests that C III] traces reasonably high density gas. The electron density of the system is determined by using IRAF's NEBULAR package (Shaw & Dufour, 1995). Assuming an electron temperature of 15,000 K, consistent with metal poor C III] emitting galaxies at lower redshifts (e.g., Erb et al. 2010; Christensen et al. 2012, Mainali et al. 2016 in prep), we infer an electron density of 9100^{+12200}_{-7800} cm^{-3} for EGS-zs8-1. The error bars on the measurement are calculated by including 1σ error in the flux ratio as well as varying the electron temperature between 12,600 K and 20,000 K. While uncertainties are clearly still significant, the C III] density is noticeably larger than the average density (250 cm^{-3}) traced by [O II] or [S II] at $z \simeq 2.3$ (Sanders et al., 2016). The tendency for C III] to imply larger densities than [O II] and [S II] is well known (e.g., James et al. 2014, Mainali et al. 2016, in prep) and may indicate that the higher ionization line tends to be produced in denser regions within the galaxy. Larger samples with multiple density diagnostics are required at lower redshift to assess whether the C III] density offset is actually physical.

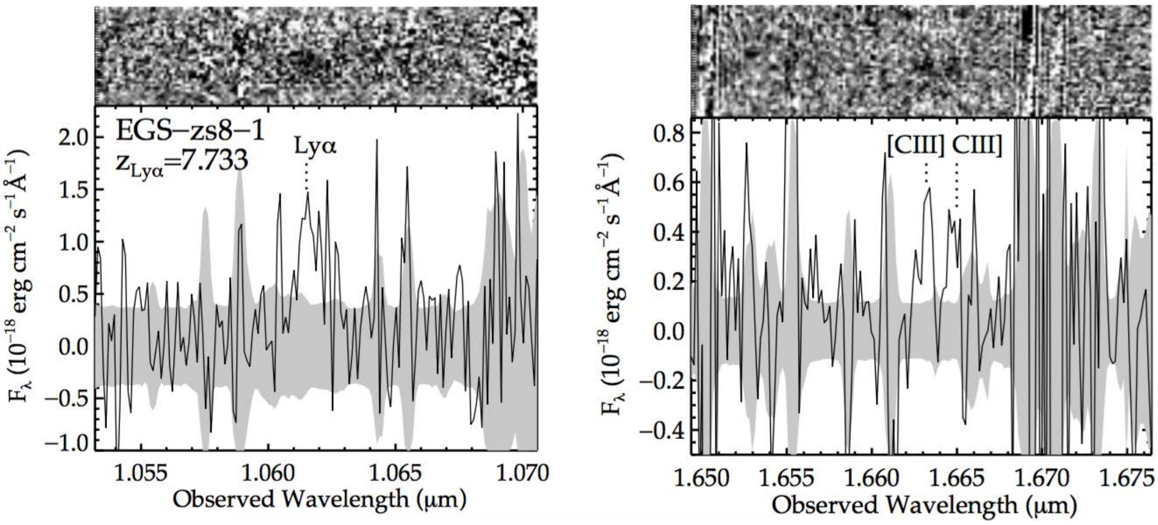

Figure 5.13: Keck/MOSFIRE spectra of EGS-zs8-1, a z = 7.733 galaxy that was originally spectroscopically confirmed in Oesch et al. (2015). (Left:) Two-dimensional and one-dimensional Y-band spectra centered on the Lyα emission line. Data are from Oesch et al. (2015). (Right:) H-band observations showing detection of the C III]$\lambda\lambda$1907, 1909 doublet. The top panels show the two dimensional SNR maps (black is positive), and the bottom panel shows the flux calibrated one-dimensional extractions. We note that the grey area is the 1σ error range of the spectra.

EGS-zs8-2 EGS-zs8-2 is another bright (H_{160}=25.1) galaxy identified in CANDELS imaging by Roberts-Borsani et al. (2016). The IRAC color of EGS-zs8-2 ([3.6]-[4.5]=0.96 ± 0.17) is redder than EGS-zs8-1, likely reflecting yet more extreme optical line emission. We estimate a rest-frame [O III]+Hβ equivalent width of 1610 ± 302 Å is required to reproduce the flux excess in the [4.5] filter. A 4.7σ emission feature was identified by Roberts-Borsani et al. (2016) at a wavelength of 1.031μm. Roberts-Borsani et al. (2016) tentatively interpret this feature as Lyα.

We obtained a Y-band spectrum of EGS-zs8-2 with the goal of verifying the putative Lyα detection. The spectrum we obtained shows a 7.4σ emission line at 1.0305 μm (Fig. 5.14a), confirming that EGS-zs8-2 is indeed a Lyα emitter at $z_{Ly\alpha}$ = 7.477. The measured line flux ($7.4 \pm 1.0 \times 10^{-18}$ erg cm^{-2} s^{-1}) is less than half that of EGS-zs8-1. We calculate the Lyα equivalent width using the broadband SED to estimate the underlying continuum flux. The resulting value ($W_{Ly\alpha}$=9.3±1.4 Å) is the smallest of the Roberts-Borsani et al. (2016) galaxies.

The MOSFIRE H-band spectrum covers 14587 to 17914 Å, corresponding to rest-frame wavelengths between 1720 and 2113 Å for EGS-zs8-2. In Fig. 5.14b, we show the spectral window centered on the C III]$\lambda\lambda$1907, 1909 doublet. No emission lines are visible. There are two weak sky lines in the wavelength range over which the doublet is situated. However the separation of the individual components of the doublet is such that at least one of the two lines must be located in a clean region of the spectrum. We estimate 3σ upper limits of

2.3×10^{-18} erg cm^{-2} s^{-1} for individual components. The non-detection suggests that the total flux in the C III] doublet must be less than 62% of the observed Lyα flux, fully consistent with the ratio observed in EGS-zs8-1 and in extreme C III] emitters at lower redshift. We place a 3σ upper limit on the doublet rest-frame equivalent width of <14 Å. Deeper data may yet detect C III] in EGS-zs8-2.

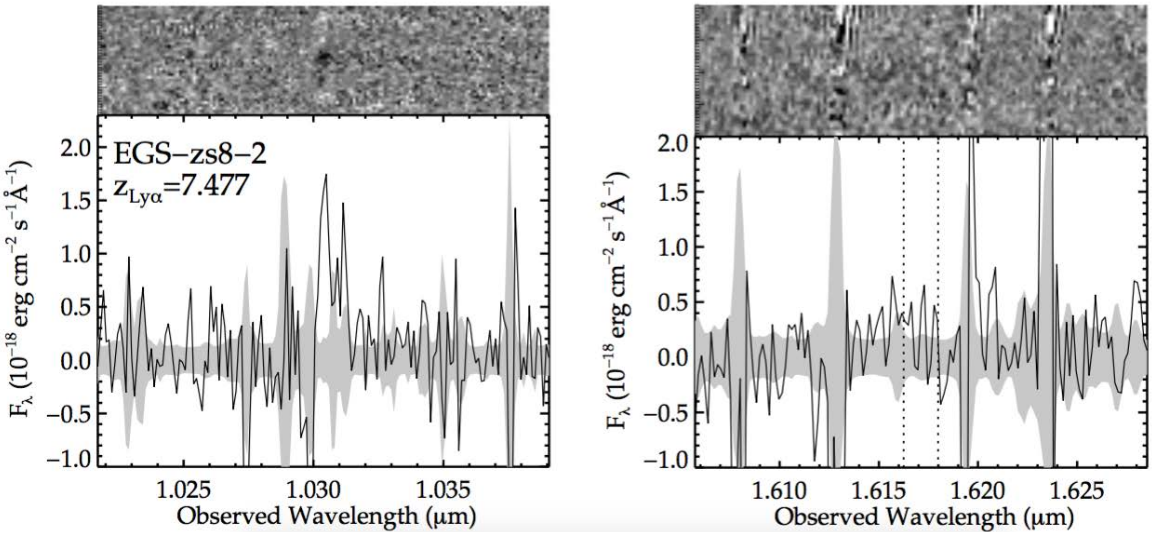

Figure 5.14: Keck/MOSFIRE spectra of EGS-zs8-2, a z = 7.477 galaxy presented in Roberts-Borsani et al. (2016). (Left:) Two-dimensional and one-dimensional Y-band spectra centered on the Lyα emission line, confirming the tentative redshift identification presented in Roberts-Borsani et al. (2016). (Right:) H-band observations showing non-detection of the C III]$\lambda\lambda$1907, 1909 doublet. The top panels show the two dimensional SNR maps (black is positive), and the bottom panel shows the flux calibrated one-dimensional extractions.

COS-zs7-1 Prior to this study, COS-zs7-1 was the only source from Roberts-Borsani et al. (2016) lacking a near-infrared spectrum. Similar to the other galaxies from Roberts-Borsani et al. (2016), COS-zs7-1 is bright in the near-infrared (H_{160}=25.1) and has IRAC color ([3.6]-[4.5]=1.03 ± 0.15) that indicates intense optical line emission. In addition to Roberts-Borsani et al. (2016), the galaxy has been reported elsehwere (e.g., Tilvi et al. 2013; Bowler et al. 2014). We estimate an [O III]+Hβ rest-frame equivalent width of 1854 ± 325 Å based on the [4.5] flux excess, making COS-zs7-1 the most extreme optical line emitter in the Roberts-Borsani et al. (2016) sample. Roberts-Borsani et al. (2016) derive a reasonably well-constrained photometric redshift (z_{phot}=$7.14^{+0.12}_{-0.12}$) that places Lyα in a narrow 290 Å window between 9750 and 10041 Å.

The Keck/MOSFIRE Y-band spectrum spans between 9750 Å and 11238 Å, covering the full range over which Lyα is predicted to lie. We identify a 6.25σ emission line at 9913 Å that is coincident with the expected spatial position of COS-zs7-1 (Fig. 5.15). The emission line is seen to have the standard negative - positive - negative pattern, indicating that it is present in both dither positions. If the feature is Lyα, it would correspond to $z_{\mathrm{Ly}\alpha} = 7.154$, in excellent agreement with the photometric redshift derived by Roberts-Borsani et al. (2016). No other emission lines are visible at the spatial position of COS-zs7-1 in the Y-band spectrum. We conclude that Lyα is the most likely interpretation of the line given the pronounced dropout in the z-band and the evidence for strong [O III]+Hβ emission in the [4.5] filter. The emission line is clearly distinct from sky lines with emission spanning 9905-9915 Å; however the red side of the line coincides with positive residuals from a weak OH line at 9917 Å, complicating the line flux measurement. Integrating the emission line blueward of the OH line, we find a total flux of $2.5 \pm 0.4 \times 10^{-17}$ erg cm^{-2} s^{-1} and a rest-frame Lyα equivalent width of 28 ± 4 Å.

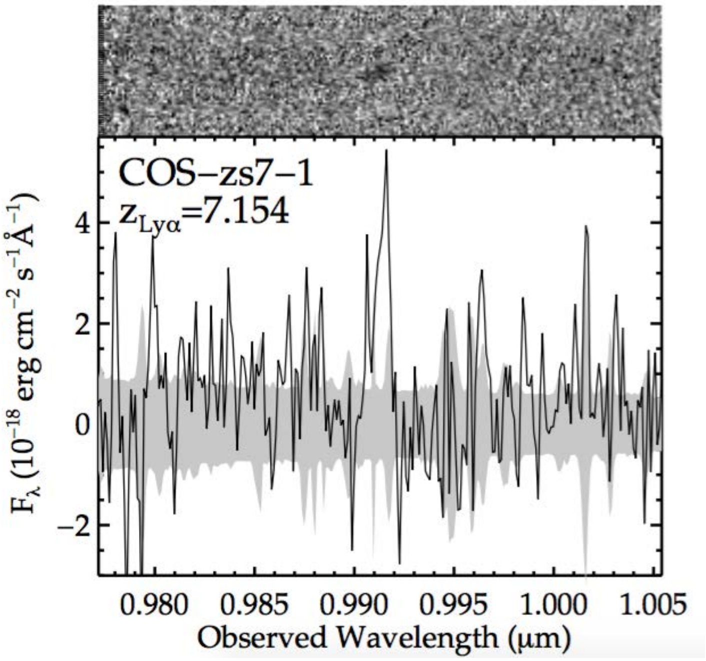

Figure 5.15: Keck/MOSFIRE Y-band spectrum of COS-zs7-1, a bright (H=25.1) dropout presented in Roberts-Borsani et al. (2016). We identify an emission feature at the spatial position of the dropout at 9913 Å which is likely to be Lyα at $z = 7.154$. The top panel shows the two dimensional SNR map (black is positive), clearly showing the characteristic negative-positive-negative signature expected from the subtraction of dithered data. The bottom panel shows the flux calibrated one-dimensional extraction.

Table 5.7 summarizes the various emission line measures and the related physical properties for all three sources in the context of earlier work, in particular for GN-108036 (Section 5.2) and A1703_zd6 (Section 5.3).

Source	$z_{Ly\alpha}$	Line	$\lambda_{\rm rest}$ (Å)	$\lambda_{\rm obs}$ (Å)	Line Flux (10^{-18} erg cm^{-2} s^{-1})	W$_0$ (Å)	H$_{160}$	W$_{\rm [OIII]+H\beta}$ (Å)	Ref
EGS-zs8-1	7.730	Lyα	1215.67	10616	17 ± 3	21 ± 4	25.0	911 ± 122	[1]
		[CIII]	1906.68	16630	4.5 ± 0.5	12 ± 2	...	...	This work
		CIII]	1908.73	16645	3.6 ± 0.5	10 ± 1	...	...	This work
EGS-zs8-2	7.477	Lyα	1215.67	10305	7.4 ± 1.0	9.3 ± 1.4	25.1	1610 ± 302	[2], This work
		[CIII]	1906.68	—	$<2.3(3\sigma)$	$<7.1(3\sigma)$	...	...	This work
		CIII]	1908.73	—	$<2.3\ (3\sigma)$	$<7.1(3\sigma)$	...	...	This work
COS-zs7-1	7.154	Lyα	1215.67	9913	25 ± 4	28 ± 4	25.1	1854 ± 325	This work
EGS8p7	8.683	Lyα	1215.67	11774	17	28	25.3	895 ± 112	[3]
z7_GSD_3811	7.664	Lyα	1215.67	10532	5.5 ± 0.9	$15.6^{+5.9}_{-3.6}$	25.9	—	[4]
z8_GND_5296	7.508	Lyα	1215.67	10343	2.6 ± 0.8	7.5 ± 1.5	25.6	1407 ± 196	[5]
...	7.508	Lyα	1215.67	10347	10.6 ± 1.2	46.9 ± 5.4	...	...	[6]
SXDF-NB1006-2	7.215	Lyα	1215.67	9988	$19^{+2.5}_{-0.9}$	>15.4	—	—	[7]
GN-108036	7.213	Lyα	1215.67	9980	25	33	25.2 (F140W)	455 ± 95	[8]
A1703_zd6	7.045	Lyα	1215.67	9780	28.4 ± 5.3	65 ± 12	25.9	—	[9]
		CIV	1548.19	12458	4.1 ± 0.6	19.9 ± 3.6	...	—	[10]
BDF-3299	7.109	Lyα	1215.67	9858	12.1 ± 1.4	50	26.2	—	[11]
BDF-521	7.008	Lyα	1215.67	9735	16.2 ± 1.6	64	25.9	—	[11]

Table 5.7: Rest-UV emission line properties of $z > 7$ spectroscopically confirmed galaxies. The top half of the table shows the targets observed in this work. In the bottom half of the table, we include measurements for other sources in the literature with spectroscopic redshifts above $z \simeq 7$. The equivalent widths include the aperture correction and are quoted in the rest-frame. The upper limits are 3σ. References: [1] Oesch et al. (2015); [2] Roberts-Borsani et al. (2016); [3] Zitrin et al. (2015); [4] Song et al. (2016); [5] Finkelstein et al. (2013); [6] Tilvi et al. (2014); [7] Shibuya et al. (2012); [8] Ono et al. (2012); [9] Schenker et al. (2012); [10] Stark et al. (2015b); [11] Vanzella et al. (2011).

5.4.3 Photoionization modelling

The broadband SEDs of the Roberts-Borsani et al. (2016) galaxies suggest the presence of extremely large equivalent width [O III]+Hβ emission. Here we investigate whether the available data require an intense radiation field that may favor the escape of Lyα. In the case of EGS-zs8-1 and EGS-zs8-2, we fold in the new constraints on C III]$\lambda\lambda 1907, 1909$ emission. We fit the available emission-line and broadband fluxes of the three galaxies detailed above in Section 5.4.2 using the Bayesian spectral interpretation tool BEAGLE (Chevallard & Charlot, 2016), which incorporates in a flexible and consistent way the production of radiation in galaxies and its transfer through the interstellar and intergalactic media. The version of BEAGLE used here relies on the model grid presented in Chapter 3 to describe the emission from stars and the interstellar gas. The main adjustable parameters are the same as adopted until now, and for this study we consider models with fixed hydrogen density, $n_{\rm H} = 100\,{\rm cm}^{-3}$, and two values of the C/O abundance ratio, equal to 1.0 and 0.52 times the standard value in nearby galaxies, $({\rm C/O})_\odot \approx 0.44$. Attenuation by dust is described using the 2-component model of Charlot & Fall (2000), combined with the Chevallard et al. (2013) 'quasi-universal' prescription to account for the effects linked to dust/star geometry (including ISM clumpiness) and galaxy inclination. Finally, we adopt the prescription of Inoue et al. (2014) to include absorption by the IGM.

We parametrize the star formation histories of model galaxies in BEAGLE as exponentially delayed functions $\psi(t) \propto t\,\exp(-t/\tau_{\rm SFR})$, for star formation timescale in the range

$7 \leq \log(\tau_{\mathrm{SFR}}/\mathrm{yr}) \leq 10.5$ and formation redshift in the range $z_{\mathrm{obs}} \leq z_{\mathrm{form}} \leq 50$ (where z_{obs} is the observed galaxy redshift). We adopt a standard Chabrier (2003) IMF. We superpose on this smooth exponential function a current burst with a fixed duration 10 Myr, whose strength is parametrized in terms of the specific star formation rate, in the range $-14 \leq \log(\psi_{\mathrm{S}}/\mathrm{yr}^{-1}) \leq -7$. We consider V-band dust attenuation optical depths in the range $-3 \leq \log \hat{\tau}_V \leq 0.7$ and fix the fraction of this arising from dust in the diffuse ISM rather than in giant molecular clouds to $\mu = 0.4$ (Wild et al., 2011).

With this parametrization, we use BEAGLE to fit the available constraints on the Lyα equivalent width (taken as a lower limit owing to resonant scattering), [C III]λ1907+C III]λ1909 equivalent width (for EGS-zs8-1 and EGS-zs8-2), and broadband F125W, F140W, F160W and IRAC 3.6 μm and 4.5 μm fluxes. We obtain as output the posterior probability distributions of the above free model parameters, as well as those of a large collection of derived parameters, such as for example the production rate of hydrogen ionizing photons per 1500 Å luminosity, ξ^*_{ion} (Table 5.8). The ξ^*_{ion} values correspond to the intrinsic UV emission from the stellar population model that reproduces the data, computed before reprocessing by gas and before attenuation by dust. Below we also present ξ_{ion}, which is computed considering the UV emission after it has been reprocessed by gas and attenuated by dust. This latter quantity provides the total Lyman continuum production rate given the observed far-UV emission.

ID	$\log_{10}$ [sSFR (yr^{-1})]	$\tau_{V,\mathrm{eff}}$	$\log U_{\mathrm{S}}$	Z	$\log_{10}\ \xi^*_{ion}$ [erg^{-1}Hz]	ξ_{d}	[C/O]
EGS-zs8-1	$-7.66^{+0.26}_{-0.33}$	$0.01^{+0.02}_{-0.01}$	$-1.61^{+0.37}_{-0.39}$	$1.7^{+0.8}_{-0.6} \times 10^{-3}$	$25.59^{+0.03}_{-0.04}$	$0.28^{+0.10}_{-0.10}$	0.52
EGS-zs8-2	$-7.61^{+0.28}_{-0.39}$	$0.02^{+0.04}_{-0.02}$	$-2.26^{+0.46}_{-0.46}$	$2.6^{+2.6}_{-1.5} \times 10^{-3}$	$25.58^{+0.04}_{-0.04}$	$0.23^{+0.12}_{-0.09}$	1.00
COS-zs7-1	$-8.14^{+0.39}_{-0.29}$	$0.01^{+0.03}_{-0.01}$	$-2.16^{+0.55}_{-0.48}$	$1.6^{+1.5}_{-0.7} \times 10^{-3}$	$25.58^{+0.04}_{-0.09}$	$0.27^{+0.14}_{-0.11}$	1.00

Table 5.8: Results from photoionization modelling using BEAGLE tool. The quoted uncertainties correspond to the 68% central credible interval.

The modelling procedure is able to successfully reproduce the broadband SEDs of the Roberts-Borsani et al. (2016) galaxies (i.e., Fig. 5.16). Matching the large flux excess in the IRAC [4.5] filter requires models with very large specific star formation rates (7-24 Gyr^{-1}), indicating a population undergoing rapid stellar mass growth. The implied interstellar metallicities are in the range Z=0.0016-0.0026, which is equivalent to 0.10-0.17 $Z_\odot$ using the solar metallicity value ($Z_\odot$=0.01524, see Section 3.2.3). The strong C III]$\lambda\lambda$1907, 1909 emission in EGS-zs8-1 forces the models to low metallicity (0.11 $Z_\odot$) and significantly reduces the allowable metallicity range. Because of the depletion of metals onto dust grains (parameterized by the ξ_{d} parameter, see Section 3.2.3) the gas-phase metallicity will be lower than the total interstellar metallicity that is fit by the models and reported in Table 5.8. After accounting for the derived ξ_{d} values using the method described in Section 3.2.3, the gas-phase oxygen abundance is found to range between 12+logO/H = 7.76, 7.77, 7.97 for COS-zs7-1, EGS-zs8-1, EGS-zs8-2, respectively. The detection of C III]$\lambda\lambda$1907, 1909 in the spectrum of EGS-zs8-1 allows us to consider variations in the C/O abundance ratio. We fit the broad-band fluxes and emission lines equivalent widths with the two different set of models corresponding to (C/O)$_\odot$, and 0.52 (C/O)$_\odot$. A visual analysis of the maximum-a-posteriori SED, and a comparison of the Bayesian evidence obtained with the two settings, indicates a slight preference of the model corresponding to 0.52 (C/O)$_\odot$, which exhibits a (marginally) larger sSFR, and a lower metallicity than the model with Solar-scaled C/O. The values reported in Table 5.8 thus correspond to the sub-Solar C/O models.

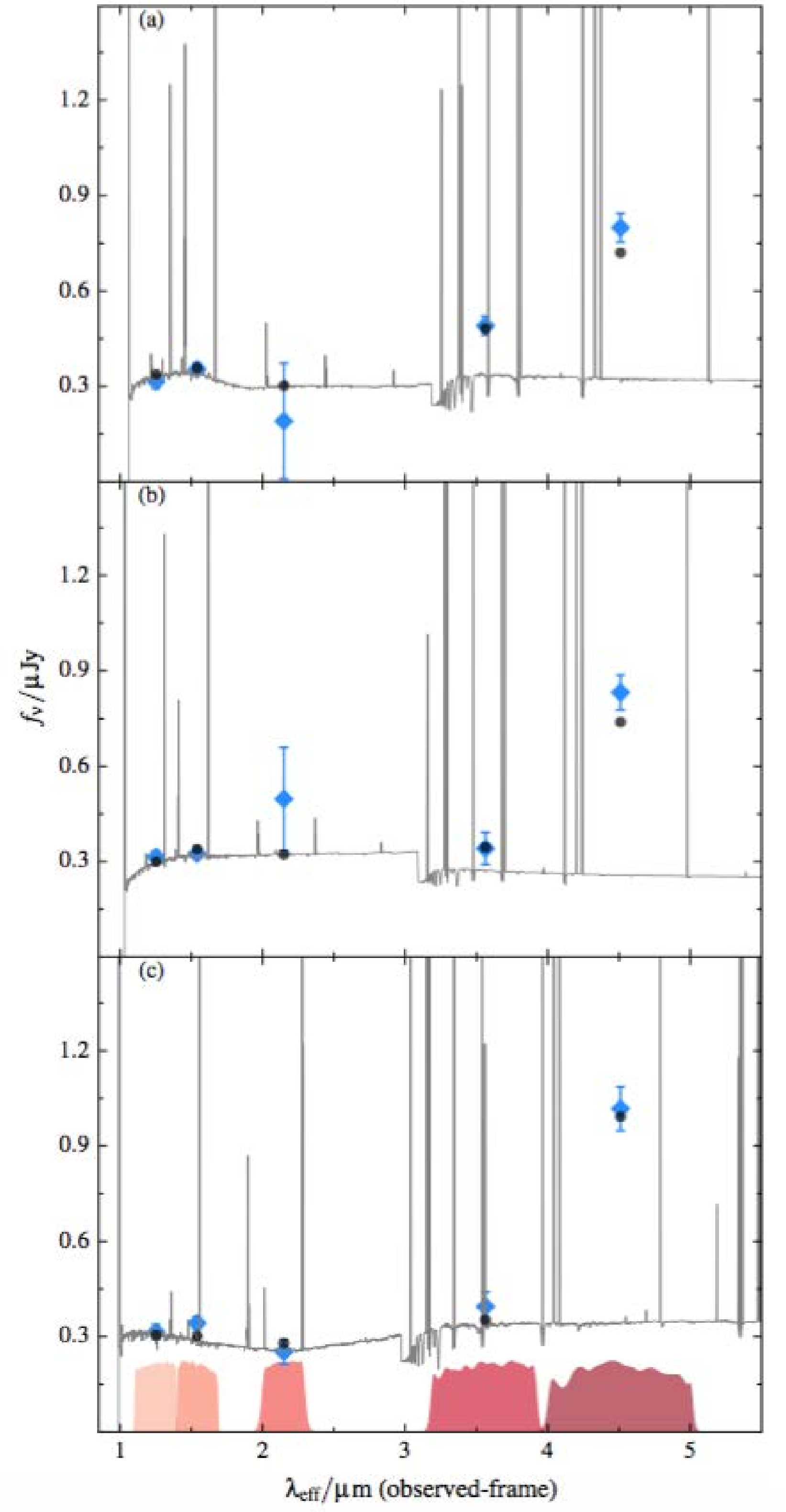

Figure 5.16: Spectral energy distributions of EGS-zs8-1 (panel a), EGS-zs8-2 (panel b), and COS-zs7-1 (panel c). The best-fitting BEAGLE SED models are overlaid. Blue diamonds show the observed photometry reported in Roberts-Borsani et al. (2016). The black circles show the synthetic photometry from BEAGLE.

As expected for galaxies dominated by such young and sub-solar stellar populations, the models suggest very large Lyman continuum photon production efficiencies, $\log_{10}\,\xi^{*}_{ion}$ [erg^{-1}Hz] $\simeq 25.6$, indicating that these galaxies have intense radiation fields. The ξ^{*}_{ion} values – that correspond to the intrinsic UV emission from the stellar population model that reproduces the data, computed before reprocessing by gas and before attenuation by dust – are larger than canonical values commonly used in reionization calculations (e.g., Kuhlen & Faucher-Giguère, 2012; Robertson et al., 2015; Bouwens et al., 2015a), and are also larger than the average ionizing photon production efficiencies ($\log_{10}\,\xi^{*}_{ion}$ [erg^{-1} Hz] $= 25.3$) recently derived in Bouwens et al. (2015c) for galaxies at $3.8 < z < 5.0$ (Fig. 5.17) and the average values derived at $z = 2.2$ ($\log_{10}\,\xi^{*}_{ion}$ [erg^{-1} Hz] $= 24.77$) by Matthee et al. (2015). If the extreme optical line emission of the Roberts-Borsani et al. (2016) galaxies is typical at $z > 7$, it would indicate that reionization-era systems likely have considerably larger ξ^{*}_{ion} values than previously thought, easing requirements on the escape fraction of ionizing radiation (e.g., Robertson et al., 2015; Bouwens et al., 2015a). The estimated values of $\xi_{\rm ion}$ are in the range $\log_{10}\,\xi_{\rm ion}$ [erg^{-1} Hz] $= 25.60$ and 25.73 for the three galaxies, larger than ξ^{*}_{ion} because of the effect of dust attenuation which lowers the observed UV flux density. The elevated ξ^{*}_{ion} values are consistent with those predicted from simulations of early star-forming galaxies (Wilkins et al., 2016).

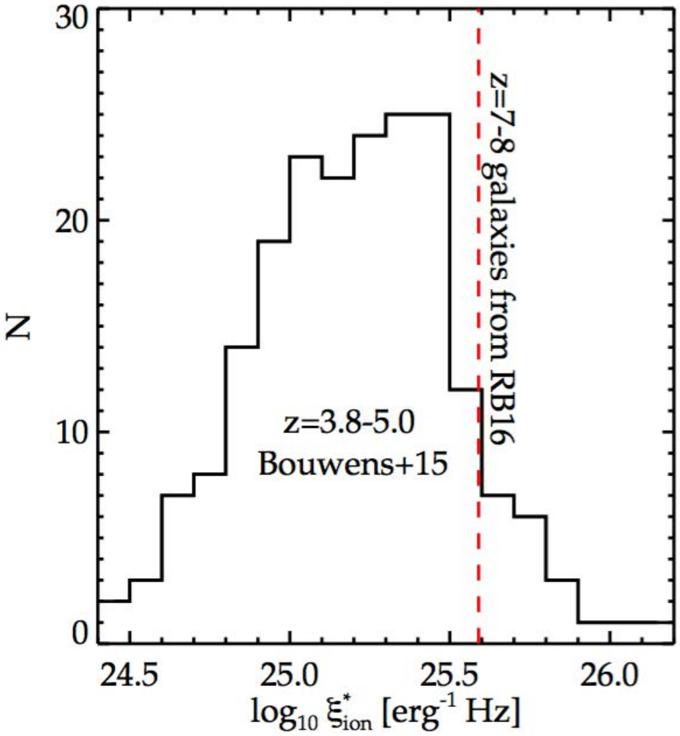

Figure 5.17: A comparison of the Lyman continuum production efficiency, ξ^*_{ion}, for galaxies at $3.8 < z < 5.0$ (histogram) to EGS-zs8-1. The selection of galaxies with IRAC color excesses picks out a population with high specific star formation rates and very large values of ξ^*_{ion}.

5.4.4 Conclusion

The IRAC 4.5μm flux excesses of the recent selection of the most luminous $z > 7$ galaxies in the CANDELS fields (Roberts-Borsani et al., 2016) are suggestive of extreme optical line emission; in particular, they are selected to have a large flux excess in the [4.5] IRAC filter, indicative of intense [O III]+Hβ emission. Photoionization models indicate that the data require very large specific star formation rates, moderately low metallicity, and large ξ^*_{ion} (Table 5.8), suggesting efficient LyC production rates. We consider the requirements to match the broadband SEDs and UV metal line properties of the Roberts-Borsani et al. (2016) galaxies using the new BEAGLE tool (Chevallard & Charlot, 2016). The red IRAC colors require the presence of an hard ionizing spectrum ($\log_{10} \xi^*_{\rm ion} \simeq 25.6$) in all of the galaxies, while the detection of intense C III]$\lambda\lambda$1907, 1909 emission in EGS-zs8-1 additionally requires models with reasonably low metallicity (0.11 $Z_{\odot}$).

These initial results provide the context for understanding why Lyα appears so frequently in the luminous sample of galaxies discovered in Roberts-Borsani et al. (2016). The observability of Lyα at $z > 7$ depends on the transmission through both the galaxy and the IGM. We argue that the product of both quantities is maximized in the Roberts-Borsani et al. (2016)

sample. The pre-selection of galaxies with extremely large equivalent width [O III]+Hβ emission picks out systems with very massive, young stellar populations. Based on results at lower redshift, we suggest that the hard radiation field of these galaxies likely increases the production rate of Lyα and may also decrease the covering fraction of neutral hydrogen in the circumgalactic medium, boosting the transmission of Lyα through the galaxy.

5.5 Conclusion

The reionization of intergalactic hydrogen is an important milestone in early cosmic history, marking the point at which nearly every baryon in the Universe was affected by the growth of structure. How and when reionization occurs encodes unique insight into the nature of the first luminous objects, motivating a number of dedicated observational efforts aimed at studying the process. Significant progress has been made in the last decade.

Photoionization models provide us with a valuable means of investigating the emission-line properties of galaxies at high redshift in terms of constraints on their physical properties, in particular their amount of star formation and nuclear activity. We have presented various spectral analyses of different samples of high-redshift galaxies recently observed, which exhibit prominent ultraviolet and optical emission lines, and we have used the model grid I have build in this thesis to investigate what range of properties are able to reproduce these high-redshift data. We have demonstrated that the ionizing spectra in these galaxies and large equivalent widths of optical nebular emission lines tend to require models with large ionization parameters, metal-poor gas, sub-solar C/O ratios, and a hard radiation field from moderately metal-poor and young massive stars. In particular, we have shown that, via our detailed modelling, measurements of rest-frame ultraviolet lines can provide unique information about important physical properties of galaxies during the reionization era, including the ionization parameters, metallicities and star formation histories, which remain degenerate when interpreting SEDs based on broad-band photometry alone. Hence, we have analyzed recent observations by fitting line strengths together with the broadband SED, allowing us to better constraint the ionizing output of galaxies in the reionization era.

CHAPTER 6

Conclusions

In this thesis, I have designed a new model to compute the emission from the photoionized interstellar gas in star-forming galaxies. To achieve this, I combined a stellar population synthesis model (GALAXEV; Bruzual & Charlot 2003, with recent updates) – to compute the spectral evolution of stellar populations inside galaxies – with a photoionization code (CLOUDY; Ferland et al. 2013) – to account for the transmission of stellar radiation through the gas ionized by hot massive stars. This combination allows me to compute in a reliable way complete (i.e., including continuum and line radiation) spectral energy distributions of galaxies. I point out that both codes are used in their very latest versions, including new improvements particularly valuable for the study of high-redshift galaxies, such as recent important progress in the treatment of the interiors and atmospheres of hot massive stars, including Wolf-Rayet stars, as well as of AGB stars.

In this approach, the ensemble of H II regions and the diffuse gas ionized by young stars throughout a galaxy are described by means of effective (i.e. galaxy-wide) parameters. The main adjustable parameters describing the stellar ionizing radiation are the stellar metallicity, Z, the IMF (whose upper mass cutoff can reach $m_{\rm up} = 300\,{\rm M}_\odot$) and the star formation history; those describing the ISM are the interstellar metallicity, $Z_{\rm ISM}$ (taken to be the same as that of the ionizing stars), the zero-age ionization parameter of a newly born H II region, $U_{\rm S}$, the dust-to-metal mass ratio, $\xi_{\rm d}$, the hydrogen gas density, $n_{\rm H}$, and the carbon-to-oxygen abundance ratio, C/O. Regarding the latter, a main feature of this model is the self-consistent yet versatile treatment of element abundances and depletion onto dust grains, which allows one to relate the observed nebular emission from a galaxy to both gas-phase and dust-phase metal enrichment, over a wide range of chemical compositions. This feature was enabled by a careful exploration of the solar relative ratios of C, N and O to reproduce the optical emission-line ratios of a large sample of nearby SDSS galaxies. In this model, I appeal to an analytic relation to describe the dependence of the N/O ratio on metallicity. While the C/O ratio does not have a specific dependence on metallicity, I consider models with reduced (and even enhanced) C abundance at fixed metallicity, to describe the delayed release of C by intermediate-mass stars relative to shorter-lived massive stars, which are the main production sites of O (and also produce C) in young galaxies. The solar values I adopt for these ratios are $(\mathrm{C/O})_\odot$=0.44 and $(\mathrm{N/O})_\odot$=0.07. Exploring wide ranges in the above parameters allows me to consistently compute a large grid of complete (i.e. continuum+line) spectra of star-forming galaxies, and in particular of high-redshift galaxies, in which the abundance ratios of heavy elements are expected to be non-solar.

The comprehensive grid of models I computed in this way allows systematic investigations of emission line-ratio diagrams, which are crucial to understand the sensitivity of individual emission-line intensities to the nature of the ionizing radiation and the physical parameters of interstellar gas. To explore this, I have selected four optical line-ratio diagnostic diagrams involving the six prominent optical lines [O II]λ3727, Hβ, [O III]λ5007, Hα, [N II]λ6584 and [S II]$\lambda\lambda$6717, 6731, and four ultraviolet diagnostic diagrams involving the six ultraviolet lines N V λ1240, C IV λ1550, He II λ1640, O III]λ1666, C III]$\lambda\lambda$1907, 1909 and Si III]λ1888. I showed that the models I built can reproduce available observations of star-forming galaxies at various cosmic epochs simultaneously in these different line-ratio diagrams. I also find that the sensitivity to parameters such as the C/O ratio, the hydrogen gas density, n_H, the upper IMF cutoff, m_up, and the dust-to-metal mass ratio, ξ_d, is more pronounced for ultraviolet emission lines than for optical ones. This implies that spectroscopic studies of the redshifted rest-frame ultraviolet emission of galaxies out to the reionization epoch should provide valuable clues about the nature of the ionizing radiation and early chemical enrichment of the ISM. This is all the more important in that future large telescopes with efficient infrared spectroscopic capabilities, such as the *JWST* (0.6 and 5 μm), will sample the rest-ultraviolet emission of high-redshift galaxies near the reionization epoch. More generally, the exhaustive grid of models I have computed, and their ability to describe the spectral properties of young galaxies with non-scaled solar element abundance ratios, should be useful in the context of a rapidly growing number of spectroscopic observations of very distant galaxies.

Interestingly, this comprehensive model grid also allows a proper investigation of the reliability of standard recipes, based on the direct-T_e method, to measure element abundances from emission-line luminosities in star-forming galaxies. I find that, while existing, widely used formulae allow one to constrain relatively faithfully ionic abundance ratios of oxygen and the C/O ratio from ultraviolet and optical emission-line luminosities at solar to sub-solar gas-phase metallicities, the recipes break down at lower and higher metallicities. To overcome this limitation, a self-consistent model of the type I have developed is required to interpret the observed nebular emission, in particular from chemically young galaxies.

I also could combine my predictions of the nebular emission from star-forming galaxies with a model of the nebular emission from narrow-line emitting regions of active galaxies, which is a crucial step to explore new line-ratio diagnostics of photoionization by nuclear activity versus star formation in galaxies. In practice, we have computed a large grid of photoionization models of AGN narrow-line regions using the same code and a similar parameterization to that I have developed to compute models of nebular emission from star-forming galaxies. This allowed us to confirm existing, widely used observational criteria to separate active from inactive galaxies in optical line-ratio diagrams, but also to exhibit new ultraviolet spectral diagnostics of the nature of ionizing radiation. Such diagnostics will be particularly useful to interpret the rest-frame ultraviolet emission from high-redshift galaxies soon observable with the *JWST* and other future facilities. Specifically, we find that combinations of a collisionally excited metal line or line multiplet with the He II λ1640 recombination line are good discriminants of the nature of the ionizing source and allow one to consistently constrain interstellar gas parameters and the shape of the ionizing radiation. We also identified valuable diagnostic diagrams involving Ne-based emission lines. These results can be used to derive the physical conditions of the ionized gas and to identify the sources of photoionization in distant galaxies, based on the observed ultraviolet and optical nebular emission.

The ensemble of models described above allow one to prepare future observations by focusing on some of the most useful diagnostics to constrain galaxy physical parameters: prominent emission lines, which will be the most easily detectable spectral signatures of the first galaxies to glow in the Universe at the end of the Dark Ages. I have presented examples of observational applications we could perform based on current data, which are paving the way toward these future studies. Specifically, we have used successfully the models to interpret observations of distant star-forming galaxies, over the redshift range $2 \lesssim z \lesssim 9$, to constrain the nature of the ionizing radiation and ISM parameters. This have been achieved by adopting a Bayesian approach to derive physical galaxy parameters, based on observed ultraviolet and optical emission-line properties, and in some cases additional constraints from the spectral continuum shape. We find that, in the various spectral analyses of high-redshift galaxy samples we performed, our modelling allows consistent constraints on galaxy physical properties, in particular in terms of star formation and nuclear activity. The typically large equivalent widths of optical nebular emission lines and prominence of high-ionization ultraviolet lines in these galaxies require photoionization models with large ionization parameters, metal-poor gas, sub-solar C/O ratios, and a hard radiation field from moderately metal-poor and young massive stars.

To optimize interpretations of the observed nebular emission from galaxies in future applications, the photoionization models I have developed have now been incorporated into the sophisticated spectral analysis tool BEAGLE (Chevallard & Charlot, 2016). This allows one to interpret in a flexible and physically consistent way the production of stellar radiation in galaxies as well as its transfer through the interstellar and intergalactic media, while accounting for attenuation by dust and different instrumental effects, such as spectroscopic flux calibration and line spread function.

I note that I have presented in this thesis ionization-bounded models of galaxies, but this work is currently being extended to allow the exploration of density-bounded galaxies and investigate the spectral signatures of the escape of ionizing photons into the intergalactic medium. Also, an ultimate goal of this work is to combine these spectral modeling techniques with simulations of early galaxy formation in a cosmological context, including spatially resolved zoom simulations of primeval galaxies, to explore the observational signatures of early star formation and black-hole growth, and how future observations will help elucidate the relation between these physical processes.

Acknowledgments

Tout d'abord, je tiens à remercier mon directeur de thèse Stéphane Charlot pour ses précieux conseils, son aide et sa disponibilité permanente tout au long de ma thèse. Stéphane, merci pour ta patience et tout ce que tu m'as appris !

Je remercie également les autres membres de la formidable équipe NEOGAL dans laquelle j'ai évoluée ces trois dernières années ; merci à tous pour les très bons moments passés au travail mais aussi en dehors : David l'homme de l'équipe venu des USA, Emma l'anglaise toujours souriante, Michaela la danseuse germanique, Aida la super maman franco-mexicaine, Alba ma charmante amie espagnole, et surtout, un immense merci à Anna, le rayon de soleil italien, qui m'a réellement aidée et soutenue tout au long de cette thèse. Vraiment, *grazie mille* Anna, je te dois beaucoup !!

Je remercie bien sûr mes rapporteurs Alessandro Bressan et Bruno Guiderdoni pour avoir relu attentivement mon travail et pour m'avoir fait part de leur précieux commentaires, ainsi que les autres membres de mon jury Patrick Boissé, Jarle Brinchmann et Elisabetta Caffau.

Merci aussi à Dan Stark, Brent Groves et Gustavo Bruzual pour nos discussions très utiles dans l'avancée de ma thèse.

Un très grand merci à toute l'équipe administrative et informatique de l'IAP : Chantal (pour son efficacité et sa disponibilité), Sopharith (pour les bons croissants et l'aide dans l'organisation du colloque IAP), Carlos (pour sa réactivité au moindre problème des machines neogal), Madeleine, Christophe, Roselys, Valérie, Lionel, et tous les autres !

Je remercie aussi grandement toute l'équipe des exoplanètes de la mezzanine pour les chouettes moments chocolatés partagés sur leurs canapés, juste en haut de l'escalier... !

Merci aussi à Ange Ansour pour le merveilleux monitorat que j'ai effectué grâce à elle ; enseigner l'astrophysique durant ces trois années auprès de classes primaires a été une véritable révélation pour moi. J'en profite aussi pour remercier Elisabeth Vangioni pour ses conseils en vulgarisation scientifique et pour le prêt de son matériel.

Évidemment, qu'aurais-je été sans tous les merveilleux doctorants de l'IAP et tout le temps passé quotidiennement avec eux depuis trois ans. Sincèrement, merci pour l'équipe soudée que nous formons tous et pour la bonne ambiance permanente, c'était un réel plaisir de tous vous retrouver chaque matin. Merci à ceux que j'ai particulièrement côtoyés : Erwan (mon renard bleu préféré), Laura (j'ai adoré nos supers discussions de la cantine, cinématographique comme footballistique, malheureusement), Tanguy (ce faux basque toujours motivé et partant pour tout), Clément (l'ami bavard et toujours là pour les autres), Vivien (le post-doc qui restera toujours doctorant dans nos coeurs, et surtout, une très belle rencontre), Rebekka (ma suisse préférée, initiatrice de yoga en salle entresol à ses heures perdues), Oscar (la joie de vivre chilienne), Caterina (la super organisatrice des sorties), Nicolas (qui a eu de la chance que je n'ai découvert ses talents de geek informatique qu'à la fin de ma thèse !), Thomas (merci pour tous tes conseils), Céline, Jesse, Tilman, Federico, Sebastien, Clotilde, Florian, Siwei, JB, Luciana, mais aussi tous les plus anciens que je n'oublie pas, Leandro, Long, Nicolas, Flavien, Vincent, Florent, Alice. Je vous souhaite à tous le meilleur pour la suite ! Enfin, je remercie bien évidemment mes deux âmes soeurs de thèse Mélanie et Alba avec qui j'ai partagé le même bureau pendant l'intégralité de ces trois années (et même depuis le début de l'université avec mon inséparable Mélachou :)) Notre “trinité infernale” de l'IAP a été d'un constant soutien et a rempli ma vie de thèse de souvenirs absolument mémorables et de fous rires toujours plus intenses chaque jour. Je vous remercie tellement pour tout ce que vous m'avez apporté pendant ces 1095 jours de thèse où l'on s'est vu quotidiennement... Que de choses à raconter avec ces deux véritables amies, j'en ferais une deuxième thèse à l'occasion !

Enfin, je tiens à remercier ces personnes extérieures qui m'apportent tant, toujours, et qui font que je n'aurai jamais envie de quitter ma ville, Paris...

Je remercie du fond du coeur ma famille sur qui j'ai toujours pu compter toute ma vie. Merci à ma mère que j'aime si fort pour tout ce qu'elle m'apporte depuis toujours, sa vivacité et sa générosité sans limite (et ma tante bien sûr, ça va de pair !); merci à mon père pour son aide constante et tout ce qu'il m'a transmis, dont le goût des sciences, mais aussi pour la patience dont il a su faire preuve face à moi pendant toutes ces années d'études ! Merci aussi à mon frère, pour tous ses conseils que j'ai pris le soin de ne bien sûr jamais suivre ;-)

Je n'oublie pas tous mes amis avec qui j'ai toujours pu me changer les idées pendant cette période intense qui n'a pas toujours été facile, et qui ont réellement été là pour moi : Anne-Sophie, Camille, Maëlle, et la liste exhaustive - presqu'autant que mes modèles - de tous les autres !

Bien sûr, je termine par remercier tout particulièrement et avec beaucoup d'amour mon futur mari Pierre-Alban, pour tout, sa patience, son soutien, son amour.

— Paris, Septembre 2016.

Appendices

APPENDIX A

Nebular emission files

The entire grid of photoionization models I have developed in this thesis is available electronically from http://www.iap.fr/neogal/models.html. I provide one file per metallicity – and then 15 files are available, each containing 18 emission-line luminosities in both optical and ultraviolet ranges, for all the different models of the wide space parameters. I detail here the content of these nebular emission files we provide online.

The file "nebular_emission_gutkin16.tar.gz" in this directory contains the values of some of the most commonly used optical and ultraviolet emission-lines predicted by models of nebular emission from star-forming galaxies (presented in this thesis). These models have been computed combining the updated version of the stellar population synthesis code GALAXEV (Bruzual & Charlot, 2003) with the latest version of the photoionization code CLOUDY (Ferland et al., 2013).

Description of the files "nebular_emission_gutkin16.tar.gz" contains 14 files, each corresponding to given value of the interstellar gas metallicity Z, specifically: Z= 0.0001, 0.0002, 0.0005, 0.001, 0.002, 0.004, 0.006, 0.008, 0.010, 0.014, 0.017, 0.020, 0.030 and 0.040.

The file names are built as follows: "nebular_emission_Zaaa.txt", where aaa are the digits after the decimal point of the value of the interstellar gas metallicity, for example: "nebular_emission_Z017.txt" corresponds to Z=0.017.

Each model file contains 23 columns:

column 1 logU_S, logarithmic value of the ionization parameter

column 2 ξ_d, dust-to-metal mass ratio

column 3 n_H, hydrogen gas density

column 4 C/O/(C/O)$_\odot$, carbon-to-oxygen abundance ratios scaled to the solar value (C/O)$_\odot$=0.44

column 5 m_up, upper mass cutoff of the IMF

columns 6 to 23 predicted intensities of 18 optical and ultraviolet emission-lines (in units of erg/s/Lsol per unit SFR) for an age of 10^8 yr, specifically: [O II]λ3727, Hβ, [O III]λ4959, [O III]λ5007, [N II]λ6548, Hα, [N II]λ6584, [S II]λ6717, [S II]λ6731, N V λ1240, C IV λ1548, C IV λ1551, He II λ1640, O III]λ1661, O III]λ1666, [Si III]λ1883, Si III]λ1888 and C III]λ1908.

Bibliography

Abazajian K., Survey f. t. S. D. S., 2008, The Seventh Data Release of the Sloan Digital Sky Survey. arXiv e-print 0812.0649, astrophys.J.Suppl.182:543-558,2009

Abel T., Bryan G. L., Norman M. L., 2000, The Astrophysical Journal, 540, 39

Abel T., Bryan G. L., Norman M. L., 2002, Science, 295, 93

Akerman C. J., Carigi L., Nissen P. E., Pettini M., Asplund M., 2004, Astronomy and Astrophysics, 414, 931

Alexandroff R. et al., 2013, Monthly Notices of the Royal Astronomical Society, 435, 3306

Allard F., Homeier D., Freytag B., Sharp C. M., 2012, in , eprint: arXiv:1206.1021, pp. 3–43

Allen M. G., Dopita M. A., Tsvetanov Z. I., 1998, The Astrophysical Journal, 493, 571

Allen M. G., Groves B. A., Dopita M. A., Sutherland R. S., Kewley L. J., 2008, The Astrophysical Journal Supplement Series, 178, 20

Aller L. H., 1942, The Astrophysical Journal, 95, 52

Aller L. H., 1984, in

Aller L. H., Liller W., 1959, The Astrophysical Journal, 130, 45

Anders P., Fritze-v. Alvensleben U., 2003, Astronomy and Astrophysics, 401, 1063

Antonucci M., Talavera A., Vagnetti F., Trevese D., Comastri A., Paolillo M., Ranalli P., Vignali C., 2015, Astronomy and Astrophysics, 574, A49

Arimoto N., Yoshii Y., 1987, Astronomy and Astrophysics, 173, 23

Ascasibar Y., Guidi G., Casado J., Scannapieco C., Díaz A. I., 2016, ArXiv e-prints, 1602, arXiv:1602.08474

Atek H. et al., 2015, The Astrophysical Journal, 800, 18

Baldwin J. A., Phillips M. M., Terlevich R., 1981, Publications of the Astronomical Society of the Pacific, 93, 5

Baskin A., Laor A., 2005, Monthly Notices of the Royal Astronomical Society, 358, 1043

Bayliss M. B., Rigby J. R., Sharon K., Wuyts E., Florian M., Gladders M. D., Johnson T., Oguri M., 2014, The Astrophysical Journal, 790, 144

Bertone E., Buzzoni A., Chávez M., Rodríguez-Merino L. H., 2008, Astronomy and Astrophysics, 485, 823

Binette L., Magris C. G., Stasińska G., Bruzual A. G., 1994, Astronomy and Astrophysics, 292, 13

Binette L., Wilson A. S., Storchi-Bergmann T., 1996, Astronomy and Astrophysics, 312, 365

Blanc G. A., Kewley L., Vogt F. P. A., Dopita M. A., 2015, The Astrophysical Journal, 798, 99

Bonzini M., Padovani P., Mainieri V., Kellermann K. I., Miller N., Rosati P., Tozzi P., Vattakunnel S., 2013, Monthly Notices of the Royal Astronomical Society, 436, 3759

Bouwens R. J. et al., 2014, The Astrophysical Journal, 795, 126

Bouwens R. J., Illingworth G. D., Oesch P. A., Caruana J., Holwerda B., Smit R., Wilkins S., 2015a, The Astrophysical Journal, 811, 140

Bouwens R. J. et al., 2015b, The Astrophysical Journal, 803, 34

Bouwens R. J., Smit R., Labbe I., Franx M., Caruana J., Oesch P., Stefanon M., Rasappu N., 2015c, ArXiv e-prints, 1511, arXiv:1511.08504

Bowler R. A. A. et al., 2014, Monthly Notices of the Royal Astronomical Society, 440, 2810

Bradley L. D. et al., 2012, The Astrophysical Journal, 747, 3

Bradley L. D., CLASH Team, 2013, in , p. 304.03

Bressan A., Chiosi C., Fagotto F., 1994, The Astrophysical Journal Supplement Series, 94, 63

Bressan A., Marigo P., Girardi L., Salasnich B., Cero C. D., Rubele S., Nanni A., 2012, PARSEC: stellar tracks and isochrones with the PAdova and TRieste Stellar Evolution Code. arXiv e-print 1208.4498, monthly Notices of the Royal Astronomical Society, Volume 427, Issue 1, pp. 127-145 (2012)

Brinchmann J., Charlot S., Kauffmann G., Heckman T., White S. D. M., Tremonti C., 2013, Monthly Notices of the Royal Astronomical Society, 432, 2112

Brinchmann J., Charlot S., White S. D. M., Tremonti C., Kauffmann G., Heckman T., Brinkmann J., 2004, Monthly Notices of the Royal Astronomical Society, 351, 1151

Brinchmann J., Pettini M., Charlot S., 2008, Monthly Notices of the Royal Astronomical Society, 385, 769

Broadhurst T. et al., 2005, The Astrophysical Journal, 621, 53

Bromm V., Coppi P. S., Larson R. B., 1999, The Astrophysical Journal Letters, 527, L5

Bruzual G., Charlot S., 2003, Monthly Notices of the Royal Astronomical Society, 344, 1000

Bruzual A. G., 1983, The Astrophysical Journal, 273, 105

Bruzual A. G., Charlot S., 1993, The Astrophysical Journal, 405, 538

Butler S. E., Heil T. G., Dalgarno A., 1980, The Astrophysical Journal, 241, 442

Buzzoni A., 1989, The Astrophysical Journal Supplement Series, 71, 817

Caffau E., Ludwig H.-G., Steffen M., Freytag B., Bonifacio P., 2010, arXiv:1003.1190 [astro-ph], arXiv: 1003.1190

Cai Z.-Y., Lapi A., Bressan A., De Zotti G., Negrello M., Danese L., 2014, The Astrophysical Journal, 785, 65

Calzetti D., Armus L., Bohlin R. C., Kinney A. L., Koornneef J., Storchi-Bergmann T., 2000, The Astrophysical Journal, 533, 682

Cardelli J. A., Clayton G. C., Mathis J. S., 1989, in , pp. 5–10

Castelli F., Kurucz R. L., 2004, ArXiv Astrophysics e-prints, arXiv:astro

Cenarro A. J. et al., 2007, Monthly Notices of the Royal Astronomical Society, 374, 664

Chabrier G., 2003, Publications of the Astronomical Society of the Pacific, 115, 763

Charlot S., Bruzual A. G., 1991, The Astrophysical Journal, 367, 126

Charlot S., Fall S. M., 1993, The Astrophysical Journal, 415, 580

Charlot S., Fall S. M., 2000, The Astrophysical Journal, 539, 718

Charlot S., Longhetti M., 2001, Monthly Notices of the Royal Astronomical Society, 323, 887

Chen Y., Bressan A., Girardi L., Marigo P., Kong X., Lanza A., 2015, Monthly Notices of the Royal Astronomical Society, 452, 1068

Chen Y., Trager S., Peletier R., Lançon A., 2011, Journal of Physics Conference Series, 328, 012023

Chevallard J., Charlot S., 2016, ArXiv e-prints, 1603, arXiv:1603.03037

Chevallard J., Charlot S., Wandelt B., Wild V., 2013, arXiv:1303.6631 [astro-ph]

Christensen L. et al., 2012, Monthly Notices of the Royal Astronomical Society, 427, 1953

Coe D. et al., 2013, The Astrophysical Journal, 762, 32

Coelho P., Barbuy B., Meléndez J., Schiavon R. P., Castilho B. V., 2005, Astronomy and Astrophysics, 443, 735

Collaboration P. et al., 2015, arXiv:1502.01589 [astro-ph], arXiv: 1502.01589

Conroy C., Gunn J. E., 2010, The Astrophysical Journal, 712, 833

Cooke R., Pettini M., Steidel C. C., Rudie G. C., Nissen P. E., 2011, Monthly Notices of the Royal Astronomical Society, 417, 1534

Cowie L. L., Barger A. J., Trouille L., 2009, The Astrophysical Journal, 692, 1476

Curtis-Lake E. et al., 2016, Monthly Notices of the Royal Astronomical Society, 457, 440

da Cunha E., Charlot S., Elbaz D., 2008, Monthly Notices of the Royal Astronomical Society, 388, 1595

Dale J. E., Ercolano B., Bonnell I. A., 2012, Monthly Notices of the Royal Astronomical Society, 424, 377

Dale J. E., Ercolano B., Bonnell I. A., 2013, Monthly Notices of the Royal Astronomical Society, 430, 234

Davidson K., Netzer H., 1979, Reviews of Modern Physics, 51, 715

Dopita M. A., Groves B. A., Sutherland R. S., Binette L., Cecil G., 2002, The Astrophysical Journal, 572, 753

Dopita M. A., Krauss L. M., Sutherland R. S., Kobayashi C., Lineweaver C. H., 2011, Astrophysics and Space Science, 335, 345

Dopita M. A., Sutherland R. S., Nicholls D. C., Kewley L. J., Vogt F. P. A., 2013, The Astrophysical Journal Supplement Series, 208, 10

Dors O. L., Cardaci M. V., Hagele G. F., Krabbe A. C., 2014, Monthly Notices of the Royal Astronomical Society, 443, 1291

Duncan K. et al., 2014, Monthly Notices of the Royal Astronomical Society, 444, 2960

Dunlop J. S. et al., 2013, Monthly Notices of the Royal Astronomical Society, 432, 3520

Ekström S. et al., 2012, Astronomy and Astrophysics, 537, 146

Eldridge J. J., Izzard R. G., Tout C. A., 2008, Monthly Notices of the Royal Astronomical Society, 384, 1109

Eldridge J. J., Stanway E. R., 2012, Monthly Notices of the Royal Astronomical Society, 419, 479

Ellis R. S. et al., 2013, The Astrophysical Journal Letters, 763, L7

Erb D. K., Pettini M., Shapley A. E., Steidel C. C., Law D. R., Reddy N. A., 2010, The Astrophysical Journal, 719, 1168

Ercolano B., Barlow M. J., Storey P. J., Liu X.-W., 2003, Monthly Notices of the Royal Astronomical Society, 340, 1136

Faber S. M., 1972, Astronomy and Astrophysics, 20, 361

Fan X., Carilli C. L., Keating B., 2006, Annual Review of Astronomy and Astrophysics, 44, 415

Feltre A., Charlot S., Gutkin J., 2016, Monthly Notices of the Royal Astronomical Society, 456, 3354

Feltre A., Hatziminaoglou E., Fritz J., Franceschini A., 2012, Monthly Notices of the Royal Astronomical Society, 426, 120

Ferguson J. W., Korista K. T., Baldwin J. A., Ferland G. J., 1997, The Astrophysical Journal, 487, 122

Ferland G. J., 1993, Hazy, A Brief Introduction to Cloudy 84

Ferland G. J., 1996, Hazy, A Brief Introduction to Cloudy 90

Ferland G. J., Kisielius R., Keenan F. P., van Hoof P. A. M., Jonauskas V., Lykins M. L., Porter R. L., Williams R. J. R., 2013, The Astrophysical Journal, 767, 123

Ferland G. J., Korista K. T., Verner D. A., Ferguson J. W., Kingdon J. B., Verner E. M., 1998, Publications of the Astronomical Society of the Pacific, 110, 761

Finkelstein S. L. et al., 2013, Nature, 502, 524

Finkelstein S. L. et al., 2012, The Astrophysical Journal, 756, 164

Fioc M., Rocca-Volmerange B., 1997, Astronomy and Astrophysics, 326, 950

Fiore F. et al., 2012, Astronomy and Astrophysics, 537, A16

Fontanot F., Cristiani S., Vanzella E., 2012, Monthly Notices of the Royal Astronomical Society, 425, 1413

Fosbury R. A. E. et al., 2003, The Astrophysical Journal, 596, 797

Frank A., Mellema G., 1994a, The Astrophysical Journal, 430, 800

Frank A., Mellema G., 1994b, Astronomy and Astrophysics, 289, 937

Frye B. L. et al., 2007, The Astrophysical Journal, 665, 921

Garcia-Vargas M. L., Bressan A., Diaz A. I., 1995, Astronomy and Astrophysics Supplement Series, 112, 35

Garnett D. R., 1992, The Astronomical Journal, 103, 1330

Garnett D. R., 2003, in , p. 197

Garnett D. R., Dufour R. J., Peimbert M., Torres-Peimbert S., Shields G. A., Skillman E. D., Terlevich E., Terlevich R. J., 1995a, The Astrophysical Journal Letters, 449, L77

Garnett D. R., Shields G. A., Peimbert M., Torres-Peimbert S., Skillman E. D., Dufour R. J., Terlevich E., Terlevich R. J., 1999, The Astrophysical Journal, 513, 168

Garnett D. R., Skillman E. D., Dufour R. J., Peimbert M., Torres-Peimbert S., Terlevich R., Terlevich E., Shields G. A., 1995b, The Astrophysical Journal, 443, 64

Georgy C. et al., 2013, Astronomy and Astrophysics, 558, A103

González V., Bouwens R., Illingworth G., Labbé I., Oesch P., Franx M., Magee D., 2014, The Astrophysical Journal, 781, 34

Grazian A. et al., 2015, Astronomy and Astrophysics, 575, A96

Gregg M. D. et al., 2004, in , p. 94.06

Grevesse N., Sauval A. J., 1998, Space Science Reviews, 85, 161

Groves B. A., Dopita M. A., Sutherland R. S., 2004a, The Astrophysical Journal Supplement Series, 153, 9

Groves B. A., Dopita M. A., Sutherland R. S., 2004b, The Astrophysical Journal Supplement Series, 153, 75

Groves B. A., Heckman T. M., Kauffmann G., 2006, Monthly Notices of the Royal Astronomical Society, 371, 1559

Gruenwald R., Viegas S. M., Broguière D., 1997, The Astrophysical Journal, 480, 283

Gräfener G., Koesterke L., Hamann W.-R., 2002, Astronomy and Astrophysics, 387, 244

Guaita L., Francke H., Gawiser E., Bauer F. E., Hayes M., Östlin G., Padilla N., 2013, Astronomy and Astrophysics, 551, A93

Guiderdoni B., Rocca-Volmerange B., 1987, Astronomy and Astrophysics, 186, 1

Gustafsson B., Bell R. A., Eriksson K., Nordlund A., 1975, Astronomy and Astrophysics, 42, 407

Gustafsson B., Edvardsson B., Eriksson K., Jørgensen U. G., Nordlund A., Plez B., 2008, Astronomy and Astrophysics, 486, 951

Gustafsson B., Karlsson T., Olsson E., Edvardsson B., Ryde N., 1999, Astronomy and Astrophysics, 342, 426

Gutkin J., Charlot S., Bruzual G., 2016, Monthly Notices of the Royal Astronomical Society, 462, 1757

Haardt F., Salvaterra R., 2015, Astronomy and Astrophysics, 575, L16

Haffner L. M. et al., 2009, Reviews of Modern Physics, 81, 969

Hainich R., Pasemann D., Todt H., Shenar T., Sander A., Hamann W.-R., 2015, Astronomy and Astrophysics, 581, A21

Hainich R. et al., 2014, VizieR Online Data Catalog, 356

Hainline K. N., Shapley A. E., Greene J. E., Steidel C. C., 2011, The Astrophysical Journal, 733, 31

Hainline K. N., Shapley A. E., Kornei K. A., Pettini M., Buckley-Geer E., Allam S. S., Tucker D. L., 2009, The Astrophysical Journal, 701, 52

Hamann W.-R., Gräfener G., 2003, Astronomy and Astrophysics, 410, 993

Hamann W.-R., Gräfener G., 2004, Astronomy and Astrophysics, 427, 697

Hamann W.-R., Gräfener G., Liermann A., 2006, Astronomy and Astrophysics, 457, 1015

Hao J.-M., Yuan Y.-F., Wang L., 2015, Monthly Notices of the Royal Astronomical Society, 451, 1875

Harrington J. P., 1968, The Astrophysical Journal, 152, 943

Hauschildt P. H., Allard F., Baron E., 1999, The Astrophysical Journal, 512, 377

Hauschildt P. H., Allard F., Ferguson J., Baron E., Alexander D. R., 1999, The Astrophysical Journal, 525, 871

Hauschildt P. H., Baron E., 1999, Journal of Computational and Applied Mathematics, 109, 41

Hauschildt P. H., Baron E., Allard F., 1997, The Astrophysical Journal, 483, 390

Heger A., Woosley S. E., 2002, The Astrophysical Journal, 567, 532

Henry R. B. C., Edmunds M. G., Köppen J., 2000, The Astrophysical Journal, 541, 660

Henry R. B. C., Kwitter K. B., Bates J. A., 2000, The Astrophysical Journal, 531, 928

Hillier D. J., Miller D. L., 1998, The Astrophysical Journal, 496, 407

Hillier D. J., Miller D. L., 1999, The Astrophysical Journal, 519, 354

Hollenbach D. J., Tielens A. G. G. M., 1999, Reviews of Modern Physics, 71, 173

Hubeny I., Lanz T., 1995, The Astrophysical Journal, 439, 875

Humphrey A., Iwamuro F., Villar-Martín M., Binette L., Fosbury R., di Serego Alighieri S., 2007, Monthly Notices of the Royal Astronomical Society, 382, 1729

Hunt L. K., Hirashita H., 2009, Astronomy and Astrophysics, 507, 1327

Hunter D. A., Gallagher, III J. S., 1990, The Astrophysical Journal, 362, 480

Iben, Jr. I., Renzini A., 1983, Annual Review of Astronomy and Astrophysics, 21, 271

Inoue A. K., Shimizu I., Iwata I., Tanaka M., 2014, Monthly Notices of the Royal Astronomical Society, 442, 1805

Izotov Y. I., Stasińska G., Meynet G., Guseva N. G., Thuan T. X., 2006, Astronomy and Astrophysics, 448, 955

Izotov Y. I., Thuan T. X., 1999, The Astrophysical Journal, 511, 639

James B. L. et al., 2014, Monthly Notices of the Royal Astronomical Society, 440, 1794

Jehin E., Bagnulo S., Melo C., Ledoux C., Cabanac R., 2005, in , pp. 261–262

Juneau S. et al., 2014, The Astrophysical Journal, 788, 88

Kallman T., 1999, Astrophysics Source Code Library, ascl:9910.008

Kauffmann G. et al., 2003, Monthly Notices of the Royal Astronomical Society, 346, 1055

Keenan F. P., Aller L. H., Ramsbottom C. A., Bell K. L., Crawford F. L., Hyung S., 2000, Proceedings of the National Academy of Science, 97, 4551

Kennicutt, Jr. R. C., 1983, The Astrophysical Journal, 272, 54

Kennicutt, Jr. R. C., 1998, Annual Review of Astronomy and Astrophysics, 36, 189

Kennicutt, Jr. R. C., Bresolin F., Garnett D. R., 2003, The Astrophysical Journal, 591, 801

Kewley L. J., Dopita M. A., 2002, The Astrophysical Journal Supplement Series, 142, 35

Kewley L. J., Dopita M. A., Leitherer C., Dave R., Yuan T., Allen M., Groves B., Sutherland R., 2013a, Theoretical Evolution of Optical Strong Lines across Cosmic Time. arXiv e-print 1307.0508

Kewley L. J., Dopita M. A., Sutherland R. S., Heisler C. A., Trevena J., 2001, The Astrophysical Journal, 556, 121

Kewley L. J., Ellison S. L., 2008, The Astrophysical Journal, 681, 1183

Kewley L. J., Groves B., Kauffmann G., Heckman T., 2006, Monthly Notices of the Royal Astronomical Society, 372, 961

Kewley L. J., Maier C., Yabe K., Ohta K., Akiyama M., Dopita M. A., Yuan T., 2013b, The Astrophysical Journal Letters, 774, L10

Kimm T., Cen R., 2014, The Astrophysical Journal, 788, 121

Kobulnicky H. A., Kennicutt, Jr. R. C., Pizagno J. L., 1999, The Astrophysical Journal, 514, 544

Kobulnicky H. A., Skillman E. D., 1996, The Astrophysical Journal, 471, 211

Koleva M., Vazdekis A. V., 2012, Astronomy & Astrophysics, 538, A143, arXiv: 1111.5449

Kraemer S. B., Ruiz J. R., Crenshaw D. M., 1998, The Astrophysical Journal, 508, 232

Kroupa P., 2001, Monthly Notices of the Royal Astronomical Society, 322, 231

Kroupa P., Tout C. A., Gilmore G., 1993, Monthly Notices of the Royal Astronomical Society, 262, 545

Kuhlen M., Faucher-Giguère C.-A., 2012, Monthly Notices of the Royal Astronomical Society, 423, 862

Kurucz R. L., 1970, SAO Special Report, 309, 309

Kurucz R. L., 1979, The Astrophysical Journal Supplement Series, 40, 1

Kurucz R. L., 2005, Memorie della Societa Astronomica Italiana Supplementi, 8, 14

Kwan J., 1984, The Astrophysical Journal, 283, 70

Labbé I. et al., 2013, The Astrophysical Journal Letters, 777, L19

Lanz T., Hubeny I., 2003, The Astrophysical Journal Supplement Series, 146, 417

Lanz T., Hubeny I., 2007, The Astrophysical Journal Supplement Series, 169, 83

Le Borgne J.-F. et al., 2003, Astronomy and Astrophysics, 402, 433

Leitherer C., Heckman T. M., 1995, The Astrophysical Journal Supplement Series, 96, 9

Leitherer C., Ortiz Otálvaro P. A., Bresolin F., Kudritzki R.-P., Lo Faro B., Pauldrach A. W. A., Pettini M., Rix S. A., 2010, The Astrophysical Journal Supplement Series, 189, 309

Lequeux J., 2005, The Interstellar Medium

Lusso E., Worseck G., Hennawi J. F., Prochaska J. X., Vignali C., Stern J., O'Meara J. M., 2015, Monthly Notices of the Royal Astronomical Society, 449, 4204

Maeder A., 1992, Astronomy and Astrophysics, 264, 105

Maiolino R., Marconi A., Oliva E., 2001, Astronomy and Astrophysics, 365, 37

Maraston C., 1998, Monthly Notices of the Royal Astronomical Society, 300, 872

Maraston C., 2005, Monthly Notices of the Royal Astronomical Society, 362, 799

Maraston C., Strömbäck G., 2011, Monthly Notices of the Royal Astronomical Society, 418, 2785

Marigo P., 2001, Astronomy and Astrophysics, 370, 194

Marigo P., 2002, Astronomy and Astrophysics, 387, 507

Marigo P., Bressan A., Chiosi C., 1996, Astronomy and Astrophysics, 313, 545

Marigo P., Bressan A., Chiosi C., 1998, Astronomy and Astrophysics, 331, 564

Marten H., Schoenberner D., 1991, Astronomy and Astrophysics, 248, 590

Marten H., Szczerba R., 1997, Astronomy and Astrophysics, 325, 1132

Martin C. L., 1997, The Astrophysical Journal, 491, 561

Martin P. G., Rouleau F., 1991, p. 341

Martins L. P., González Delgado R. M., Leitherer C., Cerviño M., Hauschildt P., 2005, Monthly Notices of the Royal Astronomical Society, 358, 49

Mathis J. S., Rumpl W., Nordsieck K. H., 1977, The Astrophysical Journal, 217, 425

Matsuoka Y., Oyabu S., Tsuzuki Y., Kawara K., 2007, The Astrophysical Journal, 663, 781

Matthee J., Sobral D., Santos S., Röttgering H., Darvish B., Mobasher B., 2015, Monthly Notices of the Royal Astronomical Society, 451, 400

McLean I. S. et al., 2012, in , p. 84460J

McLure R. J. et al., 2013, Monthly Notices of the Royal Astronomical Society, 432, 2696

Mellema G., 1995, Monthly Notices of the Royal Astronomical Society, 277, 173

Mellema G., Frank A., 1995, Monthly Notices of the Royal Astronomical Society, 273, 401

Mignoli M. et al., 2013, Astronomy and Astrophysics, 556, A29

Mihalas D., 1972, Non-LTE model atmospheres for B and O stars.

Miller G. E., Scalo J. M., 1979, The Astrophysical Journal Supplement Series, 41, 513

Miniati F., Ferrara A., White S. D. M., Bianchi S., 2004, Monthly Notices of the Royal Astronomical Society, 348, 964

Mink D. J., Wyatt W. F., 1995, in , p. 496

Morisset C., 2006, Proceedings of the International Astronomical Union, 2, 467, arXiv: astro-ph/0605400

Mouhcine M., Contini T., 2002, Astronomy and Astrophysics, 389, 106

Munari U., Sordo R., Castelli F., Zwitter T., 2005, Astronomy and Astrophysics, 442, 1127

Nagao T., Maiolino R., Marconi A., 2006, Astronomy and Astrophysics, 447, 863

Nanayakkara T. et al., 2016, arXiv preprint arXiv:1607.00013

Negrete C. A., Dultzin D., Marziani P., Sulentic J. W., 2014, The Astrophysical Journal, 794, 95

Netzer H., 2013, The Physics and Evolution of Active Galactic Nuclei

Nieva M.-F., Przybilla N., 2012, Astronomy and Astrophysics, 539, 143

Och S. R., Lucy L. B., Rosa M. R., 1998, Astronomy and Astrophysics, 336, 301

O'Connell R. W., 1976, The Astrophysical Journal, 206, 370

Oesch P. A. et al., 2010, The Astrophysical Journal Letters, 709, L16

Oesch P. A. et al., 2014, The Astrophysical Journal, 786, 108

Oesch P. A. et al., 2015, The Astrophysical Journal Letters, 804, L30

Oey M. S., Kennicutt, Jr. R. C., 1993, The Astrophysical Journal, 411, 137

Oey M. S., Kennicutt, Jr. R. C., 1997, Monthly Notices of the Royal Astronomical Society, 291, 827

Oke J. B. et al., 1995, Publications of the Astronomical Society of the Pacific, 107, 375

Ono Y. et al., 2013, The Astrophysical Journal, 777, 155

Ono Y. et al., 2012, The Astrophysical Journal, 744, 83

Osmer P. S., Smith M. G., 1976, The Astrophysical Journal, 210, 267

Osterbrock D. E., Ferland G. J., 2006, Astrophysics of gaseous nebulae and active galactic nuclei

Ouchi M. et al., 2009, The Astrophysical Journal, 706, 1136

Pacifici C., Charlot S., Blaizot J., Brinchmann J., 2012, Monthly Notices of the Royal Astronomical Society, 421, 2002

Pagel B. E. J., Edmunds M. G., Blackwell D. E., Chun M. S., Smith G., 1979, Monthly Notices of the Royal Astronomical Society, 189, 95

Pagel B. E. J., Simonson E. A., Terlevich R. J., Edmunds M. G., 1992, Monthly Notices of the Royal Astronomical Society, 255, 325

Panagia N., 1973, The Astronomical Journal, 78, 929

Panuzzo P., Bressan A., Granato G. L., Silva L., Danese L., 2003, Astronomy and Astrophysics, 409, 99

Pauldrach A., Puls J., Kudritzki R. P., 1986, Astronomy and Astrophysics, 164, 86

Pauldrach A. W. A., Hoffmann T. L., Lennon M., 2001, Astronomy and Astrophysics, 375, 161

Peimbert M., 1967, The Astrophysical Journal, 150, 825

Peimbert M., Costero R., 1969, Boletin de los Observatorios Tonantzintla y Tacubaya, 5, 3

Pequignot D., Stasińska G., Aldrovandi S. M. V., 1978, Astronomy and Astrophysics, 63, 313

Pettini M., Pagel B. E. J., 2004, Monthly Notices of the Royal Astronomical Society, 348, L59

Pickles A. J., 1998, Publications of the Astronomical Society of the Pacific, 110, 863

Prantzos N., Vangioni-Flam E., Chauveau S., 1994, Astronomy and Astrophysics, 285

Prugniel P., Soubiran C., 2001, Astronomy and Astrophysics, 369, 1048

Prugniel P., Soubiran C., Koleva M., Borgne D. L., 2007, arXiv:astro-ph/0703658, arXiv: astro-ph/0703658

Prugniel P., Vauglin I., Koleva M., 2011, Astronomy & Astrophysics, 531, A165, arXiv: 1104.4952

Puls J., Urbaneja M. A., Venero R., Repolust T., Springmann U., Jokuthy A., Mokiem M. R., 2005, Astronomy and Astrophysics, 435, 669

Pâris I. et al., 2012, Astronomy and Astrophysics, 548, A66

Pâris I. et al., 2014, Astronomy and Astrophysics, 563, A54

Péquignot D. et al., 2001, in , p. 533

Rauch T., 2002, in , pp. 150–151

Rayner J. T., Cushing M. C., Vacca W. D., 2009, The Astrophysical Journal Supplement Series, 185, 289

Reddy N. A., Pettini M., Steidel C. C., Shapley A. E., Erb D. K., Law D. R., 2012, The Astrophysical Journal, 754, 25

Rich J. A., Kewley L. J., Dopita M. A., 2011, The Astrophysical Journal, 734, 87

Richard J. et al., 2014, Monthly Notices of the Royal Astronomical Society, 444, 268

Richard J., Jones T., Ellis R., Stark D. P., Livermore R., Swinbank M., 2011a, Monthly Notices of the Royal Astronomical Society, 413, 643

Richard J., Kneib J.-P., Ebeling H., Stark D. P., Egami E., Fiedler A. K., 2011b, Monthly Notices of the Royal Astronomical Society, 414, L31

Richard J. et al., 2007, The Astrophysical Journal, 662, 781

Richardson C. T., Allen J. T., Baldwin J. A., Hewett P. C., Ferland G. J., 2014, Monthly Notices of the Royal Astronomical Society, 437, 2376

Roberts-Borsani G. W. et al., 2016, The Astrophysical Journal, 823, 143

Robertson B. E., Ellis R. S., Furlanetto S. R., Dunlop J. S., 2015, The Astrophysical Journal Letters, 802, L19

Robertson B. E. et al., 2013, The Astrophysical Journal, 768, 71

Rodriguez-Gaspar J. A., Tenorio-Tagle G., 1998, Astronomy and Astrophysics, 331, 347

Rodríguez-Ardila A., Viegas S. M., Pastoriza M. G., Prato L., Donzelli C. J., 2002, The Astrophysical Journal, 572, 94

Rodríguez Espinosa J. M. et al., 2014, Monthly Notices of the Royal Astronomical Society, 444, L68

Rodríguez-Merino L. H., Chavez M., Bertone E., Buzzoni A., 2005, The Astrophysical Journal, 626, 411

Rogers A. B., McLure R. J., Dunlop J. S., 2013, Monthly Notices of the Royal Astronomical Society, 429, 2456

Rubin R. H., 1968, The Astrophysical Journal, 153, 761

Rubin V. C., Burstein D., Ford, Jr. W. K., Thonnard N., 1985, The Astrophysical Journal, 289, 81

Salmon B. et al., 2015, The Astrophysical Journal, 799, 183

Salpeter E. E., 1955, The Astrophysical Journal, 121, 161

Sander A., Hamann W.-R., Todt H., 2012, Astronomy and Astrophysics, 540, A144

Sanders R. L. et al., 2016, The Astrophysical Journal, 816, 23

Santos M. R., Ellis R. S., Kneib J.-P., Richard J., Kuijken K., 2004, The Astrophysical Journal, 606, 683

Sarangi A., Cherchneff I., 2015, Astronomy and Astrophysics, 575, A95

Savage B. D., Sembach K. R., 1996, Annual Review of Astronomy and Astrophysics, 34, 279

Scalo J. M., 1986, Fundamentals of Cosmic Physics, 11, 1

Schaerer D., 2003, Astronomy and Astrophysics, 397, 527

Schaerer D., de Barros S., 2009, Astronomy and Astrophysics, 502, 423

Schaerer D., Hayes M., Verhamme A., Teyssier R., 2011, Astronomy and Astrophysics, 531, A12

Schaerer D., Vacca W. D., 1998, The Astrophysical Journal, 497, 618

Schenker M. A., Ellis R. S., Konidaris N. P., Stark D. P., 2014, The Astrophysical Journal, 795, 20

Schenker M. A. et al., 2013, The Astrophysical Journal, 768, 196

Schenker M. A., Stark D. P., Ellis R. S., Robertson B. E., Dunlop J. S., McLure R. J., Kneib J.-P., Richard J., 2012, The Astrophysical Journal, 744, 179

Schirmer M., Diaz R., Holhjem K., Levenson N. A., Winge C., 2013, The Astrophysical Journal, 763, 60

Schmidt-Voigt M., Koeppen J., 1987, Astronomy and Astrophysics, 174, 211

Schmidt-Voigt M., Koppen J., 1987, Astronomy and Astrophysics, 174, 223

Schneider R., Ferrara A., Natarajan P., Omukai K., 2002, The Astrophysical Journal, 571, 30

Schneider R., Ferrara A., Salvaterra R., 2004, Monthly Notices of the Royal Astronomical Society, 351, 1379

Shapley A. E. et al., 2015, The Astrophysical Journal, 801, 88

Shapley A. E., Steidel C. C., Pettini M., Adelberger K. L., 2003, The Astrophysical Journal, 588, 65

Shaw R. A., Dufour R. J., 1995, Publications of the Astronomical Society of the Pacific, 107, 896

Shibuya T., Kashikawa N., Ota K., Iye M., Ouchi M., Furusawa H., Shimasaku K., Hattori T., 2012, The Astrophysical Journal, 752, 114

Shields J. C., Kennicutt, Jr. R. C., 1995, The Astrophysical Journal, 454, 807

Shim H., Chary R.-R., Dickinson M., Lin L., Spinrad H., Stern D., Yan C.-H., 2011, The Astrophysical Journal, 738, 69

Shimizu I., Inoue A. K., 2013, Publications of the Astronomical Society of Japan, 65, 96

Shirazi M., Brinchmann J., Rahmati A., 2014, The Astrophysical Journal, 787, 120

Silva L., Granato G. L., Bressan A., Danese L., 1998, The Astrophysical Journal, 509, 103

Smit R., Bouwens R. J., Franx M., Illingworth G. D., Labbé I., Oesch P. A., van Dokkum P. G., 2012, The Astrophysical Journal, 756, 14

Smit R. et al., 2014, The Astrophysical Journal, 784, 58

Sobral D., Matthee J., Darvish B., Schaerer D., Mobasher B., Röttgering H. J. A., Santos S., Hemmati S., 2015, The Astrophysical Journal, 808, 139

Song M., Finkelstein S. L., Livermore R. C., Capak P. L., Dickinson M., Fontana A., 2016, ArXiv e-prints, 1602, arXiv:1602.02160

Spinrad H., Taylor B. J., 1971, The Astrophysical Journal Supplement Series, 22, 445

Spitzer L., 1978, Physical processes in the interstellar medium

Stark D. P. et al., 2016, ArXiv e-prints, 1606, arXiv:1606.01304

Stark D. P. et al., 2015a, Monthly Notices of the Royal Astronomical Society, 450, 1846

Stark D. P. et al., 2014, Monthly Notices of the Royal Astronomical Society, 445, 3200

Stark D. P., Schenker M. A., Ellis R., Robertson B., McLure R., Dunlop J., 2013, The Astrophysical Journal, 763, 129

Stark D. P. et al., 2015b, Monthly Notices of the Royal Astronomical Society, 454, 1393

Stasińska G., 1980, Astronomy and Astrophysics, 85, 359

Stasińska G., 1990, Astronomy and Astrophysics Supplement Series, 83, 501

Stasińska G., 2005, Astronomy and Astrophysics, 434, 507

Stasińska G., Leitherer C., 1996, The Astrophysical Journal Supplement Series, 107, 661

Steidel C. C., Hunt M. P., Shapley A. E., Adelberger K. L., Pettini M., Dickinson M., Giavalisco M., 2002, The Astrophysical Journal, 576, 653

Steidel C. C. et al., 2014, The Astrophysical Journal, 795, 165

Steidel C. C., Strom A. L., Pettini M., Rudie G. C., Reddy N. A., Trainor R. F., 2016, arXiv preprint arXiv:1605.07186

Storey P. J., 1981, Monthly Notices of the Royal Astronomical Society, 195, 27P

Stoughton C. et al., 2002, The Astronomical Journal, 123, 485

Strömgren B., 1939, The Astrophysical Journal, 89, 526

Sutherland R. S., Dopita M. A., 1993, The Astrophysical Journal Supplement Series, 88, 253

Sánchez-Blázquez P. et al., 2006, Monthly Notices of the Royal Astronomical Society, 371, 703

Tarter C. B., Salpeter E. E., 1969, The Astrophysical Journal, 156, 953

Tilvi V. et al., 2014, The Astrophysical Journal, 794, 5

Tilvi V. et al., 2013, The Astrophysical Journal, 768, 56

Tinsley B. M., 1978, The Astrophysical Journal, 222, 14

Todt H., Sander A., Hainich R., Hamann W.-R., Quade M., Shenar T., 2015, Astronomy and Astrophysics, 579, A75

Tremonti C. A. et al., 2004, The Astrophysical Journal, 613, 898

Turnrose B. E., 1976, The Astrophysical Journal, 210, 33

Tylenda R., 1979, Acta Astronomica, 29, 355

Valdes F., Gupta R., Rose J. A., Singh H. P., Bell D. J., 2004, The Astrophysical Journal Supplement Series, 152, 251

van den Hoek L. B., Groenewegen M. A. T., 1997, Astronomy and Astrophysics Supplement Series, 123

Vanden Berk D. E. et al., 2001, The Astronomical Journal, 122, 549

Vanzella E. et al., 2011, The Astrophysical Journal Letters, 730, L35

Vassiliadis E., Wood P. R., 1993, The Astrophysical Journal, 413, 641

Vazdekis A., 1999, The Astrophysical Journal, 513, 224

Veilleux S., 2002, in , eprint: arXiv:astro-ph/0201118, p. 111

Veilleux S., Osterbrock D. E., 1987, The Astrophysical Journal Supplement Series, 63, 295

Villar-Martin M., Tadhunter C., Clark N., 1997, Astronomy and Astrophysics, 323, 21

Villar-Martín M., Cerviño M., González Delgado R. M., 2004, Monthly Notices of the Royal Astronomical Society, 355, 1132

Volonteri M., Gnedin N. Y., 2009, The Astrophysical Journal, 703, 2113

Walborn N. R., Panek R. J., 1984, The Astrophysical Journal, 286, 718

Wang J., Heckman T. M., Lehnert M. D., 1997, The Astrophysical Journal, 491, 114

Wild V. et al., 2011, Monthly Notices of the Royal Astronomical Society, 410, 1593

Wilkins S. M., Bunker A. J., Stanway E., Lorenzoni S., Caruana J., 2011, Monthly Notices of the Royal Astronomical Society, 417, 717

Wilkins S. M., Feng Y., Di-Matteo T., Croft R., Stanway E. R., Bouwens R. J., Thomas P., 2016, Monthly Notices of the Royal Astronomical Society, 458, L6

Willott C. J. et al., 2010, The Astronomical Journal, 139, 906

Wofford A. et al., 2016, Monthly Notices of the Royal Astronomical Society, 457, 4296

Worthey G., 1994, The Astrophysical Journal Supplement Series, 95, 107

Wu Y., Singh H. P., Prugniel P., Gupta R., Koleva M., 2011, Astronomy & Astrophysics, 525, A71, arXiv: 1009.1491

Wyithe J. S. B., Mould J., Loeb A., 2011, The Astrophysical Journal, 743, 173

Yu N., Wang J.-J., Li N., 2015, Monthly Notices of the Royal Astronomical Society, 446, 2566

Yuan T.-T., Kewley L. J., Sanders D. B., 2010, The Astrophysical Journal, 709, 884

Zackrisson E., Bergvall N., Olofsson K., Siebert A., 2001, Astronomy and Astrophysics, 375, 814

Zaritsky D., Kennicutt, Jr. R. C., Huchra J. P., 1994, The Astrophysical Journal, 420, 87

Zheng W., Kriss G. A., Telfer R. C., Grimes J. P., Davidsen A. F., 1997, The Astrophysical Journal, 475, 469

Zheng W. et al., 2012, Nature, 489, 406

Zitrin A., Ellis R. S., Belli S., Stark D. P., 2015, The Astrophysical Journal Letters, 805, L7

Zitrin A. et al., 2012, The Astrophysical Journal Letters, 747, L9